Oversized Elements For High Efficiency Extremely High Frequency Boresight Array

by Derek Gray

A Thesis Submitted to the Faculty of

Graduate Studies in Partial Fulfillment of the

Requirements for the Degree of Doctor of

Philosophy in Electrical Engineering

University of Manitoba

Department of Electrical and Computer Engineering

Winnipeg, Manitoba

Canada

December, 2000

THE UNIVERSITY OF MANITOBA

FACULTY OF GRADUATE STUDIES

*****

COPYRIGHT PERMISSION PAGE

Oversized Elements for High Efficiency Extremely High Frequency Boresight Array

BY

Derek Gray

A Thesis/Practicum submitted to the Faculty of Graduate Studies of The University of Manitoba in partial fulfillment of the requirements of the degree of Doctor of Philosophy

Abstract

High gain, planar array antennas which operate at millimetre wave frequencies, and can be mass produced at low cost, are desired by industry. The design of such arrays continues to be academically challenging. A literature review was conducted covering patents and papers describing antenna arrays either operating at, or suitable for operation at, millimetre wave frequencies. Four presently under exploited technology types were identified. Two of the under exploited technologies were investigated.

Both small and medium sized arrays of non-radiating edge fed microstrip patches were built up in a consistent process. The design of the patch and 1x2 subarray were shown to affect the radiation pattern behaviour of 16x16 arrays. The placement of nulls in the 2x2 subarray radiation patterns proved critical to the mitigation of grating lobes, which were a source of directivity loss. A considerable difference in directivity characteristics across 10% bandwidth was found between in phase and 180° feeding within the 2x2 subarrays. An optimised 180° fed 4x4 subarray presented an improvement over prior work.

Changing the boundary conditions at the juncture of the base and rim of the cavity of short backfire antennas was found to alter the directivity. Large diameter short backfire antennas with choked, inclined and curved junctures produced high directivity. A readily machinable design was used in a small array, to demonstrate its utility as a high aperture efficiency array element.

The results are of importance to the future development of low cost, planar or quasi-planar antenna arrays, particularly at millimetre wave frequencies.

Acknowledgements

Dedicated to the memory of
Mr. David Barford
good friend and mentor

Firstly, I must apologise to my friends and family for having being absent from home for such an extended period. I must especially thank Tamaki Hirai for her tolerance in this respect, additionally thank her for her help with building silly, fiddly, little things.

Thanks must go to Dr. Jun Wei Lu, Dr. David Thiel and Dr. Steven O'Keefe for getting me started ten years ago, and their ongoing encouragement. I should additionally thank Dr. Achilles Leontanakis for his conviction that that drain-pipe waveguide stuff is still useful for something.

More specific to this thesis, I thank Dr. Lot Shafai for his guidance over the last four and a half years. Thanks likewise goes to George Squires and the staff of TRLabs Wireless Calgary for the provision of support, and the suggestion of the topic herein studied, without either of which nothing would have happened. I thank Dr. Misao Haneishi, Dr. Derek Oliver, Alex Gill, {not yet Dr.} Tomaz Blach and Dr. Kazuo Nakayama for their useful discussions, and good humor, over the course of the four and half years. Likewise, I thank Dr. C.B. Ravipati and Dr. Michel Clenet. As far as the practicalities of actually doing anything, let alone research, at the University of Manitoba, I am greatly indebted to Brad Tabachnick, Ken Biegun, Mout-first Ng, Guy Jonatschick and Al Symmons. I would also like to thank my committee members, Dr. Ernie Bridges, Dr. Attahiru Alfa and Dr. Jack Cahoon, for their useful discussions. I would also like to thank Dr. Jim Wight for taking the time, and braving the cold, to attend my oral defense.

Table of contents

List of Figures

List of Tables

Glossary and list of acronyms

DBS	Direct Broadcast Satellite television service
EHF	Extremely High Frequency (30 - 300GHz)
HFSS	a commercially available Finite Element Method numerical tool
IE3D	a commercially available Method of Moments numerical tool
LMCS	Local Multipoint Communication System; a proposed millimetre wave, civil communications system to provide interactive television, internet and telephony service to businesses and domestic dwellings
NRE	non-radiating edge fed microstrip patches; not commonly used as a cross-polarised mode is excited before the desired co-polarised mode
RE	radiating edge fed microstrip patches; commonly used configuration
SBA	short backfire antenna
2^n grating lobe	grating lobe generated by 2x2 microstrip patch array, due to non-uniform aperture distribution
scaled directivity	gain + mismatch loss

CHAPTER 1: PLANAR ARRAY CANDIDATES

1.1 Introduction and literature survey

1.1.1 Requirement for medium gain planar arrays

Many modern, and future, civil sector communications services require medium gain antenna arrays. These applications differ greatly in system requirements of the antennas employed, but the features of low cost and ease of manufacture, low noise temperature, durability and asthetic appeal are common. In addition, low profile is often preferred, or demanded, which enables fitting of the antenna to, or within, building walls. Some such applications are automotive collision avoidance radar, personal identification systems, wireless office and short distance communications links. Thus, there is a need for planar antenna arrays.

In the literature review (sections 1.2-1.4), problems with existing planar and quasi-planar antenna array types are identified. The need to improve upon the present designs is concluded in section 1.5. Thus, the purpose of this work is to improve upon the present planar antenna array technology. To this end, extensive parametric studies of microstrip patch arrays are undertaken in Chapter 2. Similarly, short backfire antennas are studied in Chapter 3. In Chapter 4, experimental studies of short backfire antennas were undertaken, and a small array is presented.

1.1.2 Some modern, civil sector, EHF communications systems

Civil sector, short range wireless communications systems operating at millimetre frequencies have been under development since the mid 1970s [1]. Early applications included business data links (38.6-40GHz), video conferencing (38.6-40GHz) and inter-office telephone and data (25.25-27.5GHz) [1], while more recent services have grown beyond the business sector to encompass interactive television and internet to private dwellings. The North American Local Multipoint Distribution Systems (LMDS) operates across the frequency ranges 27.5-28.35GHz, 29.1-29.25GHz and 31.0-31.3GHz [2, 3], Local Multipoint Communications Systems (LMCS) across 25.35-28.35GHz [4], and upper band Millimetre Distribution System (MMDS) across 27.5-28.35GHz [5]. The advantages of these systems include the avoidance of cable laying costs (low infrastructure costs), reduction of congestion in cable ducts, readily scalable systems, high data rate capacity, and the facility to be able to relocate subscriber terminals at short notice and little expense [1,6].

The terminal link between the user and base station must be economically constructed and maintained, as it would be used exclusively by a single user [1]. Long haul links between base stations would be shared by numerous users. Use of higher frequencies has allowed for miniaturisation of the equipment to facilitate terminal links that enable prompt service initiation [1]. Small equipment can be easily transported, assembled and installed either indoors or outdoors. An essential but bulky component of the subscriber transponder is the high gain antenna. All early antennas were based upon parabolic dish reflectors, which could be mass produced at low cost. These antennas provide excellent performance but are considered to be bulky, difficult to camouflage, prone to wind strain, and often require complex mounting structures. Thus, there is pressure to design planar or quasi-planar antennas with a much lower profile (say 1 λ_o instead of

8 λ_o for parabolic antennas) that can be mounted flat against a wall or set into a wall, avoiding wind strain and providing greater camouflage. However, the design and manufacture of low cost planar array antennas for these applications has proven to be both difficult and challenging. As will be discussed below, the main difficulties relate to power distribution across the antenna and finding types of antenna that can be produced economically. There is a large resource of planar antenna designs that have been used successfully for DBS television subscriber terminals, some of these designs may be adaptable to millimetre wave operation. There is also scope for the development of novel antenna designs to meet these needs.

In summary, an antenna suitable for use in a modern civil communications service will exhibit characteristics such as found in Table 1.1. It is presumed that any terminal antenna proposed for these systems can be scaled for use in 40.5-42.5GHz systems as used in some European countries (Great Britain, Germany, etc) [5, 7]. Likewise, these antennas may have wide applicability in personnel identification systems, mobile communications, automotive collision avoidance, and millimetre radar imaging.

Table 1.1: Presumed requirements for LMDS/LMCS subscriber antenna

Quantity	Value
gain	30-35dBi
frequency band	25.35-31.3GHz
bandwidth	500MHz increments (full band desirable)
3dB beamwidth	4-6°
polarisation	linear (dual linear desirable)
lateral size	230-500cm^2
topology	planar/quasi-planar
cost of manufacture	as low as possible
operating thermal range	outdoor (-30 to 100°C)
other features	aesthetically unobtrusive

data quoted from Table 1 in [4]

1.2.1 Planar aperture illumination

Currently, there are no low profile antennas that have the lateral dimensions to achieve the required gain level for the envisioned subscriber antenna. This suggests that a number of smaller planar antennas could be grouped together to cover the required area, yielding the desired gain level. These individual antennas would be supplied with power through a planar feeding network. Higher aperture efficiency means that smaller arrays can achieve a required gain. This also means that noise effects from losses will be reduced. In order to construct an antenna array with high aperture efficiency, a number of characteristics must be minimized. These include losses from phase errors in element illumination, grating lobe losses from element spacing, and radiation and ohmic losses within the feeding network. This section focuses on choosing an appropriate transmission line to illuminate the array elements.

For systems integration reasons, an array antenna and its supporting subsystems must have a single feeding point [8]. Thus, a feeding network is required to distribute the power from the terminal feeding point to the individual radiating elements and any supporting circuitry. The feed network must satisfy the amplitude and phase distributions for each radiator prescribed by the array configuration. As a result, suitable feed networks are geometrically complex and consist of long lengths of transmission line relative to the guided wavelength. This makes them difficult and expensive to manufacture. The long lengths of transmission line are of concern as all transmission lines are dissipative to some degree; the longer the transmission line, the greater the dissipation of power. This loss mechanism reduces the achievable gain and aperture efficiency of the array, and increases the noise temperature of the final communications system. This is of particular concern at millimetre wave frequencies where most transmission line types are highly lossy. Losses from discontinuities in transmission lines are also a source of concern. As a result, all potential transmission line types must be compared in terms of:

lateral space

thickness

dissipative losses per guided wavelength

discontinuity and radiation losses

cost of production

weight

mechanical strength/rigidity

behaviour with temperature/thermal stability

achievable bandwidth

ease of integration (of circuit components and terminal feed)

power handling capability

A number of studies have considered these aspects of a wide range of transmission line types [8, 9, 10]. Some of these have made particular reference to planar and quasi–planar transmission lines for 30GHz operation [8,10].

The choice of the best general transmission line in terms of power handling capability, size, weight, etc. for use around 30GHz is not clear. For optimal performance, the choice should be based upon the particular requirements and constraints imposed by the application [10]. The proposed millimetre wavelength subscriber antenna will usually be mounted on the outside of a building, exposing it to climatic temperature variations. Thus, the antenna would be expected to operate between temperature extremes of –30 to 100°C. To accomplish this, all components of the array antenna will need to have similar thermal expansion coefficients throughout this temperature range to avoid thermal stress and fracture. Similarly, the dielectrics within the transmission lines must have constant electrical characteristics across this temperature range to guarantee a consistency of performance. Such dielectric substrates are available but are relatively expensive, and are generally reserved for military and space applications. These would be unsuitable for mass

production civil application due to the high cost of the unprocessed dielectric stock. Given the choice between cheap but unacceptably poor performance dielectrics and unacceptably expensive but well behaved dielectric substrates, it seems simpler to avoid the use of dielectrics within the feeding network all together. This suggests the use of air-filled rectangular waveguides. Air-filled rectangular waveguide have additional advantages, including very low conductor losses, no dielectric losses (as dielectrics are absent). They can act as heat sinks, manufacturing tolerances are not as strict as other transmission line types, and they are mechanically rigid. For example, typical loss figures at 35GHz are 0.5dB/m and 25dB/m respectively, for a rectangular waveguide (WR-28) and a microstrip line (50Ω) [8]. For an array antenna with 0.1m transmission lines, 2.45dB more power would be available for radiation with waveguide feeding as compared to microstrip line feeding (a difference of 76% in aperture efficiency). Although there are considerable differences between rectangular waveguide and microstrip line efficiencies, it should be noted that active components have been used in microstrip line feeding networks to improve signal to noise ratio [11]. However, this adds more components, further complicating the assembly, increasing the cost of manufacture (in terms of time and money) and providing additional sources of failure.

In addition to the advantages noted above, if the rectangular waveguide feed network is cast in a metal block or molded in plastic which is later metallised, it will form a rigid piece to which other array components can be added and held flat. Following this reasoning, such rectangular waveguide feed networks have been employed by many previous investigators [12-16]. It has been shown that the choice of a rectangular waveguide for the majority of signal distribution within the proposed antenna array is prudent. This is because the configuration exhibits low losses, mechanical rigidity, constancy of behaviour over the required temperature range, and amenability to low cost manufacture by casting or molding. The exact nature of the waveguide feed network and some inherent disadvantages are discussed in the next section.

1.2.2 Planar waveguide feed networks

The gain bandwidth limitations associated with series feeding large numbers of array elements brought about by phase errors will be discussed in the next section. It is presumed that the low loss, large scale waveguide feeding network will be corporate, so that all array elements are fed with equal amplitude and phase across the operable bandwidth of the feeding network.

Both rectangular and radial waveguides have been used to build up corporate feed networks. Corporate feeds of radial waveguide have been rarely used, have increasing thickness as more layers are added to cover increasing lateral dimensions and appear to be relatively difficult to construct [17, 18]. By contrast, rectangular waveguide corporate feed networks for a single polarisation can be fabricated on a single layer. In this process, three sides of the rectangular waveguide are cast into the upper face of a metal block, so that the antenna layer will sit upon adding the fourth wall, completing the rectangular waveguide.

The most common, or favored, type of cast rectangular waveguide feed network has consisted of H-plane bends in the lateral plane with E-plane bends used to "turn up" normal to the plane of the feed network, feeding into the array elements. This means that the troughs in the metal block have greater width than depth and are amenable to casting. Furthermore, matching stubs [14] or flanges [19-21] can be easily formed by casting. The simplest form is shown in Figure 1.1A, with each 2x2 subunit having three H-plane T-junctions and four E-plane bends. However, as illustrated, the phase of the upper and lower pairs of waveguide mouths is 180° out of phase. This explains the absence of this particular configuration from the literature, though it may prove useful for feeding some of the oversized microstrip patch antennas mentioned later where the phase reversal can be exploited for higher order mode elimination.

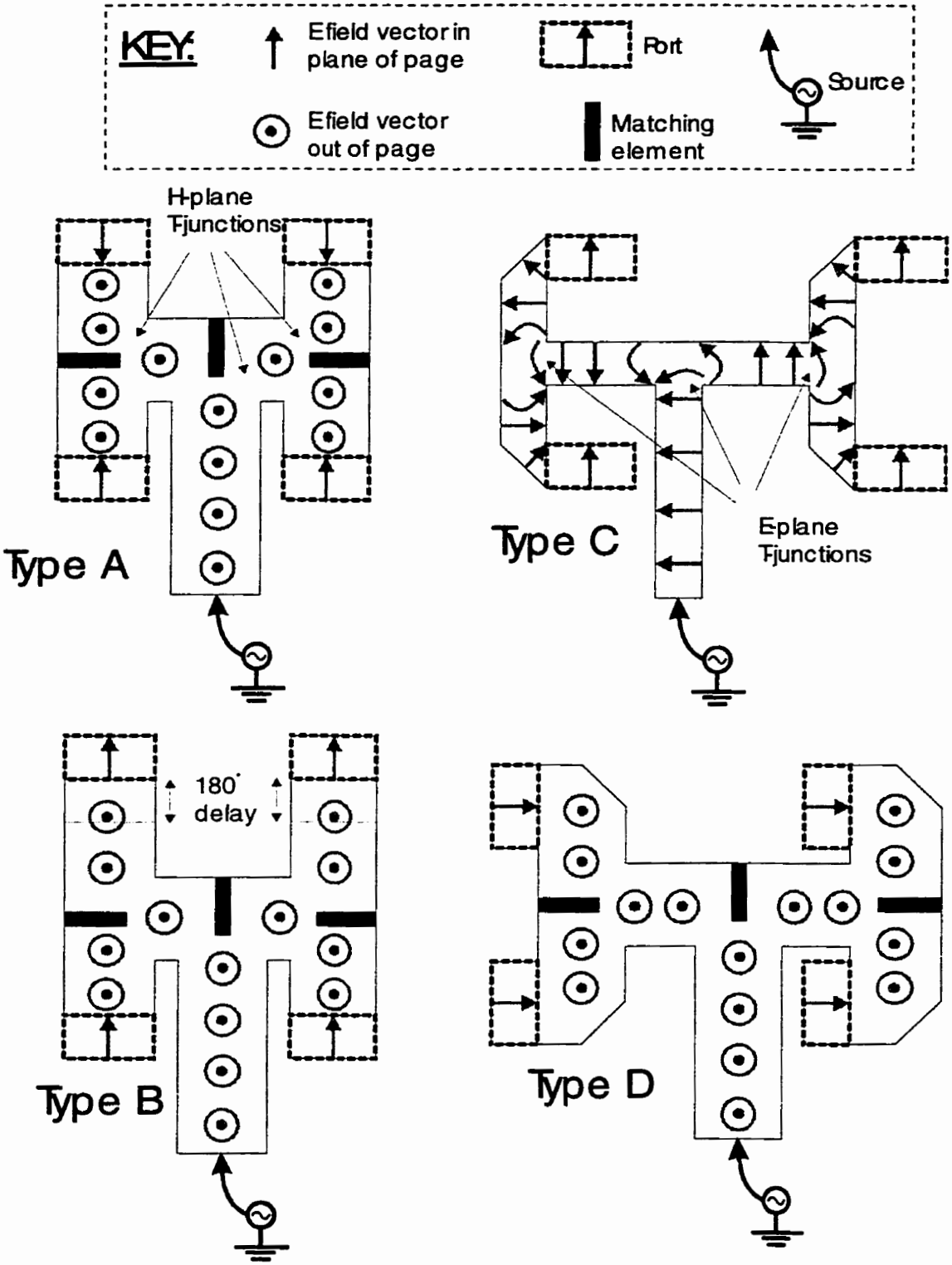

Figure 1.1: Single layer, rectangular waveguide corporate feed networks.

By adding 180° delay lines to the upper pair of waveguide mouths the configuration shown as Figure 1.1B is obtained [14, 19-21]. At the centre frequency all four waveguide mouths, or ports, in each 2x2 subunit will be in phase. Within the 11.0% bandwidth studied the phase error that occurs away from the centre frequency does not appear to have severely compromised the gain bandwidth of a wide band array antenna [14]. An E-plane port-to-port spacing of 1.8 λ_o has been achieved, showing this configuration to be a relatively compact feed network [14, 19-21]. However, this required an oversized array element with a repetition distance of 1.8 λ_o. This was done to avoid radiation pattern losses into grating lobes, which become apparent with interelement spacings greater than 1 λ_o. This highlights the principal disadvantage of rectangular waveguides; this type of transmission line occupies much more lateral space than any of the other types of transmission line available for use at millimetre wave frequencies [8, 10]. As a practical example, microstrip lines can be used to feed individual microstrip patches having an inter-element spacing of 0.8 λ_o, while rectangular waveguides can not. The relatively large lateral dimensions of rectangular waveguide create port spacings greater than 1 λ_o, which is a disadvantage in terms of grating lobe generation. However, the larger lateral dimensions are an advantage with respect to manufacturing tolerances [8]. In the 30GHz range, a 100Ω characteristic impedance microstrip line is 0.3mm wide, while a TE_{10} mode rectangular waveguide with a cut off frequency of 27GHz be about 5.5mm wide.

The problem of grating lobe losses caused by rectangular waveguide bulkiness was overcome by two further methods in addition to the specially designed oversized array elements mentioned earlier [14,19-21]. Both methods avoided the grating lobe generation due to an inter-element spacing of 1 λ_o by reducing the lateral dimensions of the rectangular waveguide. The first method [22] simply involved tipping the rectangular waveguide onto its side, and forming the feed network from E-plane T-junctions and E-plane bends, with H-plane bends turning up to feed the

ports (Figure 1.1C). As this type was fully corporate, having no 180° delay lines, all four ports had identical phase and amplitude across a wide bandwidth. The disadvantages were an increased thickness (as the longer dimension of the waveguide was in the vertical plane), narrower channels to cast. The second method exploited a ridged waveguide with smaller dimensions than normal rectangular waveguide [9], i.e. a more compact feed network [23]. A typical corporate feed network was used for the layout (Figure 1.1D) and a port to port spacing of 1 λ_o was achieved, mitigating grating lobe generation [23]. Again, the feed network was harder to cast than a normal rectangular waveguide feed network due to the reduced dimensions and added complexity of the ridge at the centre of the modified guide. Additionally, ridged waveguide had higher losses than normal waveguide [9].

Dual polarisation can be achieved by either laminating an orthogonal but otherwise identical feed network below that for a single linear polarisation [24], or by building up a feed network of square waveguide which treats both polarisations identically [25-27]. Either method would require two cast blocks to form the waveguide feeding network, and are thus roughly equal in complexity of manufacture.

Some of the issues relating to the production and use of low loss rectangular waveguide corporate feed networks have been introduced. The main disadvantage appears to be the large lateral dimensions of such feed networks which result in port-to-port spacings greater than 1 λ_o, causing radiation losses into grating lobes. Three methods of mitigating this problem have been identified, two of these involved means of shrinking the dimensions of the feed network. The last entailed the design of novel radiating elements which placed a far field radiation pattern null in the direction of the grating lobes or incorporated novel elements incorporating smaller radiating elements. Having described the type of quasi-planar feeding network that is most economical to

produce , and the need for radiating elements with dimensions on the order of 1-1.8 λ_o or greater, some potential radiating element candidates for millimetre wave operation will be introduced and discussed.

1.3.1.1 Series-fed planar arrays

Types of metallic waveguides suitable for illuminating large planar arrays were identified as having low manufacturing cost and low losses [28-30]. Little manufacturing complexity is added to the production of waveguide components if efficient slot radiating elements are added to the upper wall of a metallic waveguide. This is regardless of whether the slots are added by stamping or etching process. As a result, slotted waveguide arrays are leading candidates for prototype high gain flat antennas because they are capable of achieving very high aperture efficiency at high frequencies [28]. Radial and various widths of rectangular waveguide have been studied extensively. It should be noted that the phase path length for each array element is unique, resulting in complicated design procedures. Good performance has often been achieved at the design frequency. However, for all other frequencies, phase errors will exist between the array elements causing degradation of overall performance, i.e. an intrinsic narrow band performance.

1.3.1.2 Slotted radial waveguide

Large arrays of slots fed by centre-excited, dielectric-filled radial waveguide have been used successfully around 17GHz and 35GHz for high gain, good quality, pencil beam radar

application [31, 32], Figure 1.2. The radial waveguide was formed by the copper cladding on both sides of a thin, low loss dielectric substrate. Concentric rings of slots were etched into the copper cladding on one side of the low loss dielectric. Along with a pin, a centred circular hole was in the reverse side served as a feed for the radial waveguide. The lowest order TM mode was excited within the radial waveguide by a proper choice of ground plane spacing and a coaxial TEM mode excitation between the feed pin and circular hole. The resultant current flow is radial, with the slot rings intercepting the current flow and producing a radiation pattern [31, 32], Figure 1.2. The feeding connection to the probe can be microstrip line, coaxial line or waveguide, depending on the available transceiver interface [31, 32]. A circularly polarised array using slot pairs as the radiators with a peak gain of 36.5dBic (84% aperture efficiency) has been investigated for DBS satellite subscriber use at 11.875GHz [33]. Despite displaying a return loss of ≤ -20dB across a wide range of frequencies, this array had a 1dB gain bandwidth of only 3.4% resulting from the aforementioned phase errors. These single layer slotted radial waveguide designs have also been investigated in the 60GHz band [28, 29]. Some work has been reported on slotted radial waveguides excited at the circumference instead of the centre [34]. The circumference excitation was achieved via centre feeding to a lower radial waveguide, the circumference of which fed the upper slotted waveguide. Such an arrangement adds greatly to the manufacturing complexity if compared to the single-layer arrays. The double-layer radial waveguide concept has been used successfully for dual polarisation operation [35]. A further form of radial waveguide fed array that has been investigated employed probe excited microstrip patches instead of slots [36]. This allows for a greater flexibility in polarisation control than the slotted arrays [37]. Approximately 90% peak aperture efficiency was obtained by a 288 element array. This array had a peak gain of 31.5dBic and a 1dB gain bandwidth of about 5.9%. Studies of the use of microstrip antennas as radiating elements indicate that these antennas have greater flexibility in polarisation control and resulted in wider gain bandwidth. The major source of additional complexity in the manufacture of

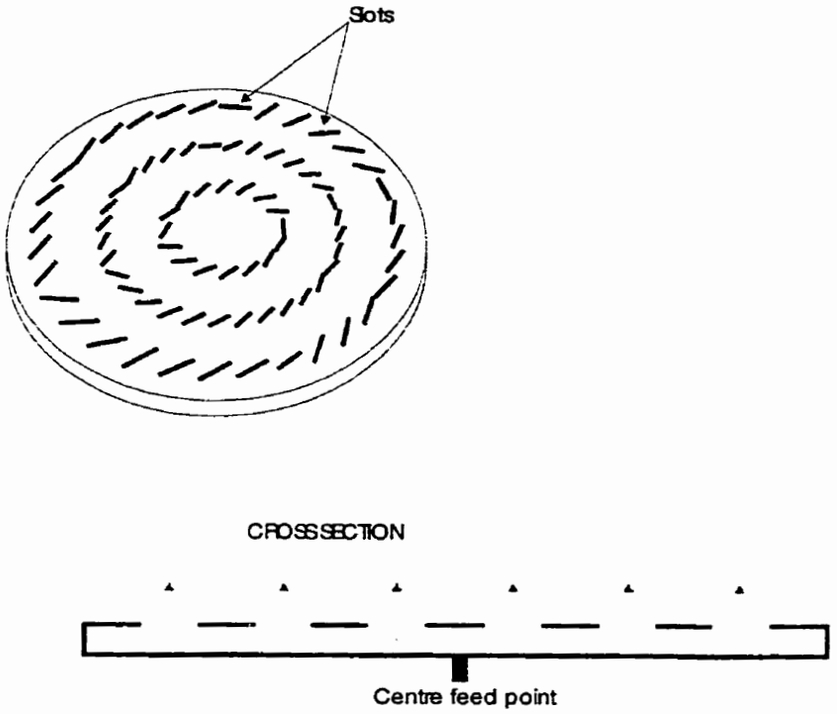

Figure 1.2: Single layer slotted radial waveguide [31, 32]

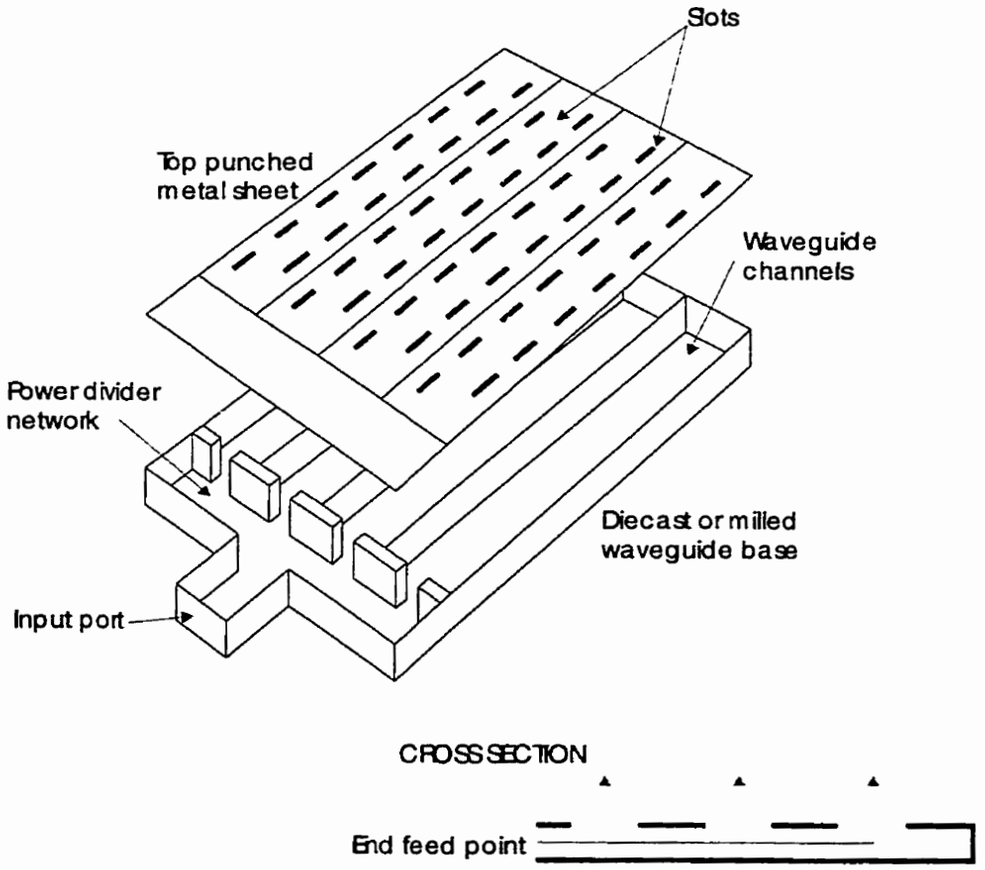

Figure 1.3: Slotted rectangular waveguide [39]

this last type of radial waveguide fed array was the placement of the probes, and some work has been done to overcome this problem [38].

1.3.1.3 Slotted rectangular waveguide

Slotted rectangular waveguides have also been investigated extensively for high gain application at millimetre wavelengths. Two reasonably distinct classes exist; those having multiple narrow rectangular waveguides and a simpler form employing a single wide rectangular waveguide, Figure 1.3.

A high-gain and high-efficiency single-layer slotted waveguide array was constructed for use in the 22GHz band [39]. Construction of this array required the joining of only two parts; a slotted plate made by printing technology and a grooved structure made by die casting, Figure 1.3. Manufacturing was thus simple and cost effective. This array consisted of 24 waveguides, each having 25 radiating slots, and was fed by a cascade of rectangular waveguide π-junctions. A peak aperture efficiency of 75.6% and gain of 35.9dBi were reported at 22.15GHz. However, the 1dB gain bandwidth was very narrow (1.5%), showing the bandwidth limitations of this design. A variant using alternate phase feeding for neighbouring waveguides within the array did not require full electrical contact between the slot plate and the narrow walls of the waveguides [40]. This greatly reduced the number of laser welds required to bond the slot plate to the grooved plates, simplifying construction, but narrowed the gain bandwidth further [40]. The benefits of increased aperture efficiency from filling the waveguides with dielectrics of ε_r=2 has been noted [28]. This work has proposed alternative methods for manufacturing this type of array using plated holes in close proximity to form the waveguide walls [41,42]. This has been shown to be a successful

method of manufacture for frequencies as high as 76GHz [41]. Similar arrays have also been built up from slotted leaky wave rectangular waveguide array antennas [43].

As noted above, reducing the number of laser weld strokes required to bond the plates reduces construction cost and time [28]. The second class of rectangular waveguide excited slot array employs a single wide guide, dispensing with the need for all but the outer most walls [44]. A tapered segment was required for the transition from the normal width feeding waveguide and the wide slotted radiating section. A dielectric lens was fitted at the boundary of the tapered guide and the slotted guide to correct for the phase error that develops along the tapered guide [44, 45]. The addition of tabs, projecting into the rectangular waveguide, on the sides of the radiating slots removed the need to offset the slots and allowed an increase in gain [46]. Likewise, for an array of full waveguide width slots, matching grooves cut into the bottom of the rectangular waveguide improved performance [47]. The slotted rectangular waveguide arrays mentioned above were only fed a one end. Variable polarisation, and perhaps wider bandwidth, arrays have been demonstrated by feeding all four sides of a slotted rectangular waveguide [48].

1.3.1.4 Dielectric waveguide and microstrip line excited arrays

In a similar fashion to the slotted radial waveguide arrays, dielectric guides have been used to distribute power radially from a centre feed to concentric rings of radiating elements [49]. These arrays have typically been fed by circular waveguide, terminated in a metal cap which transfers the power to the radial dielectric image line [49]. The radial wavefront propagates away from the centre cap to illuminate concentric rings or dipole elements etched on the upper surface of the image guide [49]. An improved surface wave launcher incorporating quarter wave chokes has been demonstrated for operation at 47GHz [50]. In terms of manufacturing complexity, these arrays are

comparable to the slotted radial waveguide arrays, but will suffer from a higher noise temperature due to dielectric losses.

Various dielectric waveguides have been tested as alternatives to rectangular waveguide [51-53]. Comparing these dielectric guide illuminated arrays to the rectangular waveguide arrays, a major disadvantage is the considerable increase in manufacturing complexity. For instance, a non-radiating dielectric waveguide excited arrays [53], requires the additional manufacture and careful placement of the dielectric slab within the rectangular cavity, the equivalent rectangular waveguide does not require [39]. Additionally, the top slotted plate cannot be affixed by high speed laser welding as the dielectric guide would be distorted and/or ignited by the heat.

Microstrip technology offers easy-to-manufacture, low-profile feeding networks and radiating elements [30]. Traveling wave arrays of microstrip patches have been identified as having the minimised feed line lengths, reducing spurious radiation and line losses [31]. Analysis of the loss mechanisms within linear and parallel fed microstrip patch arrays has shown that parallel fed arrays suffer from poor radiation pattern control, high feed line losses and significant changes in polarisation due to radiation from the complicated feeding network [30]. Thus, series fed arrays are more useful for higher gain applications, which do not need considerable feed line lengths to disperse power effectively, and have good radiation patterns and impedance control characteristics [30].

1.3.1.6 Conclusions

Series fed arrays suffer from narrow gain bandwidth, despite being capable of very high aperture efficiencies. This results from the phase errors that occur away from the design frequency. A hybrid arrangement of parallel feeding to small linear fed subarrays may be a means of overcoming the narrow gain characteristics of the large series fed arrays.

1.4.1 Parallel fed planar arrays

This type of planar array is characterised by an equal length of transmission line from the source point to each array element, giving equal phase path length and thus potentially wider bandwidth operation than the series fed arrays.

1.4.2 Microstrip arrays

Microstrip antennas are probably now the most well known and used antenna type for modern applications requiring low profile antennas. This type of antenna is also readily made conformal to vehicle chassis, and frangible, as is required for smart munitions application [184]. The typical microstrip antenna consists of a printed metallic pattern on a thin dielectric material (usually less than $\lambda_o/10$ in thickness), which has a solid metallic sheet backing. The simplest means of feeding an array of microstrip patch antennas is to use a microstrip line feeding network. Such an array only requires single sided etching and installation of a transition to the support

circuitry. As a result manufacturing is reasonably simple and low cost. Disadvantages include the high cost of the dielectric substrate, distortions to the dielectric when the metalisation is removed from one side unless measures are taken to prevent this [15, 54]. Furthermore, unwanted radiation due to microstrip line discontinuities and the lossy nature of microstrip line not only affects the gain level and aperture efficiency, but also the noise temperature. The microstrip line losses resulting from various manufacturing methods have been discussed in detail [184]. However, microstrip line loss can be avoided to some degree by only using short lengths within a subarray (fed by waveguide or coaxial line), or completely avoided by using parasitic coupling to distribute power across the array area.

1.4.2.1 Single layer configurations

Single layer microstrip patch antenna arrays are the lowest profile candidate for large planar arrays. This is due to both the radiator and the interconnecting transmission lines been on one side of a thin dielectric substrate sheet, Figures 2.1 & 2.15. Production is usually quite simple, requiring only the photolithographic etching of one side of the dielectric; a standard printed circuit board process. However, there are a number of operational disadvantages resulting from this simple construction, as mentioned earlier.

The methodology in designing a large corporate fed microstrip patch antenna array is to take a modular approach [55]. A 2x2 subarray of identical microstrip patch antennas with 0.8 λ_o spacing was deigned for optimal gain and input impedance matching at the desired frequency of operation. The 2x2 array (without modification) was used as a subarray for a 4x4 array. In turn, this was used as a subarray for a 8x8 array [55]. Interconnection between the patches was by H

shaped networks of 100Ω, 200Ω and 140Ω λ/4 transformers. The majority of the feed network was 200Ω line which was the highest achievable characteristic impedance line (0.2mm width) that could be implemented on the substrate used. It was therefore chosen to minimise the radiation losses from the feed network [55]. A 50Ω probe feed placed at the centre of the central 100Ω trunk line was used to drive the arrays. As the phase length from this central feed point through the feed network to each patch was identical, frequency sensitivity of the array radiation pattern was reduced. A further advantage of the H-shaped corporate feed used was that the currents propagating away from each T junction were opposed in direction. Thus, they contributed to the radiation pattern 180° out of phase in the boresight, canceling at boresight [55].

A series of arrays consisting of 4, 8, 16 and 64 microstrip patch antennas have been built and studied for operation at 9GHz [55]. Mutual coupling between neighbouring patches appeared to be insignificant, it was not necessary to retune the impedances of the 4x4 subarray when it was used in successively larger arrays. As expected, the main lobe beamwidth was found to halve in width in the plane in which the array size had been doubled, as was expected. However, doubling the array size did not double the gain (3dB increase) as expected. For example, the measured gain difference between the 64 element and 16 element arrays was only 4dB. As this involved a four fold increase in area, the difference was expected to be 6dB, i.e. a 2dB loss occurred. Theoretical consideration of the dielectric and copper losses within these arrays suggested that a loss of 1.2dB was to be expected, leaving 0.8dB unaccounted for [55]. The radiation patterns of all arrays are presented, showing all the H-plane radiation patterns for all arrays to be more or less symmetrical except that of the 64 element array. H-plane pattern symmetry is to be expected as the array topology was perfectly symmetrical in that plane. However the lack of symmetry and presence of a high sidelobe on only one side points to a problem either with distortion of the array and/or damage to some part of the feed network leading to uneven illumination. This may also account for the

0.8dB loss in the 64 element array. None of the E-plane patterns for any of the array sizes are symmetrical, as was to be expected as the arrays were not symmetrical in that plane. The 1dB gain bandwidth for the four arrays was about 7.2%.

An example of a 64 element, corporate fed array of microstrip patch antennas which was built up by a modular subarraying method has been discussed [55], identifying the associated problems of dielectric losses, copper losses and distortion of the thin dielectric substrate sheet. The counteracting effects of increased directivity and increased feed network losses resulting from increasing the area of a 2^n element, square sided, corporate fed microstrip array are expressed in equation 1.1 [56].

$$G = 10 \log_{10} 4\pi L^2 - \alpha L - C \qquad (1.1)$$

where G is the gain

L is the length of one side of the aperture in wavelengths

α is the loss per unit wavelength

C constant due to other loss mechanisms independent of feed line length

Application of equation 1.1 to a 16x16 35GHz array yielded a gain figure within 0.5dB of the experimental figure [57]. The discrepancy was probably mostly due to the power lost into a relatively high sidelobe on one side of the E-plane pattern, due to the intrinsic lack of symmetry in the E-plane of the array.

A more detailed analysis of losses within corporate fed microstrip patch arrays has been conducted [58,59]. This study considered all aspects of losses occurring within a corporate fed microstrip array. These covered the coaxial to microstrip transition, substrate height effects upon

aperture efficiency, substrate surface wave scattering, design and production tolerances, and radiation losses from the various elements of the corporate feed network. It was shown that as the substrate thickness was decreased, the radiation loss from the coaxial to microstrip transition decreased, the aperture efficiency increased and the input impedance decreased [58, 59]. Loss contributions from surface waves, bends within the feed network and the input coaxial to microstrip transition are constants as the array size was increased in the 2^n manner described above. As the size was increased from 2 to 64 elements, the line losses and losses from T-junctions increased exponentially, becoming the dominant loss mechanisms within the larger arrays. The contribution of spurious radiation from the feed network to the radiation pattern was given considerable attention. Feed discontinuities close to the patches were identified as causing the most pattern perturbation, and it was recommended that particular care be taken in design at that point. A bend radius of 0.5 λ_o for all 90° bends and T-junctions was recommended. Substrate effects on patch operation were identified as posing contradictory design requirements to those for low feed network radiation losses. A low dielectric constant will result in patch antennas with wider input impedance bandwidth but increased array losses, and the use of thin substrates will lead to all round array benefits at the cost of narrow input impedance bandwidth [58, 59].

Table 1.2: Optimal substrate parameter choice for microstrip patch arrays

Parameter	dielectric constant	substrate thickness
low feed radiation	high	thin
low surface waves	low	thin
low mutual coupling	low	thin
wide patch input impedance BW	low	thick
good tolerance control	low	thin

applicable for $1<\varepsilon_r<2.5$; $0.01<h/\lambda_o<0.1$; after table 3 of [59]

A similar study the losses within the feed networks for 2^n array architectures concluded that array sizes beyond 32x32 are impractical if reasonable aperture efficiencies are required [60]. The recommendation was made that novel means are required to overcome the dielectric and conductor losses in the long lengths of microstrip line interconnecting the subarrays should be used [60]. The common solution has been to replace longer sections of the microstrip line feed network with an equivalent network based on a lower loss transmission media. Both rectangular waveguide [15,16] and coaxial cable [61] have been used successfully to replace the main trunk lines between subarrays within large arrays. For example, a rectangular waveguide was used to feed four subarrays of 16x16 elements to form a 32x32 array for 38GHz operation [15]. The rectangular waveguide network was milled out of the thick aluminum backing plate that the array was affixed to [15]. Other than overcoming some of the feed line losses, there was the added benefit of the backing plate holding the substrate flat, thus preventing distortion. The transfer of power from the waveguide to the microstrip line was accomplished by a probe transition [15,16] but this wastes the advantages of slot coupling which provides a wideband 180° phase shift [62], which would be more suited for mass production. Slot coupling would be more suitable for mass production as it does not require the careful placement of the probe pin, which itself requires high tolerances. Some consideration has been given to coupling waveguide via slot to microstrip patches [63] or line [64].

The benefits of feeding a pair of neighbouring microstrip patches both electrically and physically 180° out of phase have been identified by theoretical [65] and experimental studies [66]. In the theoretical study, 180° feeding cancelled the cross-polar component in the E-plane radiation pattern, and significantly reduced that in the H-plane pattern [65]. The experimental study showed similar results, with the E-plane cross-polar radiation having been undetectable (at noise level) and the H-plane cross-polar level about –35dB [66]. Surprisingly, no further cases of 180° feeding to patch antenna arrays have been found in the literature, let alone the use of a slot in a rectangular

waveguide endwall been used to produce a wideband 180° central feed for a 4x4 microstrip patch subarray within, say, a 32x32 array. Thus, a theoretical and/or experimental investigation of such a hybrid array would be a useful contribution to the field of low profile high gain planar arrays. Expected benefits are the creation of the 180° phase shift at the centre of the feed network of a subarray, the elimination of the 0.6dB that occurs at a probe feed to microstrip line [58], and the removal of the long feed lines connecting the subarrays. Removing the longer lengths of microstrip line within a large array results in the removal of the considerable line losses, another manufacturing advantage associated with large scale corporate fed microstrip arrays.

For the satisfactory production of a corporate fed microstrip array, a reasonable level of accuracy is required in the photolithographic mask for the accurate rendering of the features of the design. Furthermore, an equal rate of etching across the entire array is needed, despite this being hard to achieve across a large array. As an example of the electrical dimensions involved, a 32x32 array has a side length of approximately 28 λ_o. The interconnecting microstrip lines are typically of high impedance (100-200Ω) and are relatively thin. If the etch rate is uneven across such a large array, achieving long thin lines without variations in width is extremely difficult. Any variations in line width will cause impedance mismatches leading to uneven illumination across the array and unwanted radiation from the localities of the mismatches. Uneven aperture illumination might explain the uneven H-plane radiation pattern from the 8x8 array described above [55]. This array design was highly susceptible to this problem as it employed 200Ω characteristic impedance microstrip line (0.2mm width) for the corporate feed network. It appears no consideration has been given to this problem in the literature, but the replacement of the long lengths of microstrip line in medium and large scale arrays with electrically equivalent rectangular waveguide would successfully mitigate this problem.

Another promising method for mitigation of losses within the long lengths of microstrip line within large corporate feed microstrip arrays is to place an air filled channel beneath the microstrip line to form grooved line [67]. Insertion of a lengthwise air pocket under a microstrip line modifies it to form a grooved microstrip line. Grooved lines have been shown to reduce both conductor and dielectric losses by approximately 3dB/m at 30GHz [67], compared to a microstrip lines of identical characteristic impedance. Employing grooved lines would produce a total reduction in losses of approximately 6dB per metre. Further reductions in loss would result from the reduction in the effective relative permittivity of the line when compared to a microstrip line of identical characteristic impedance. This would cause the wavelength to increase, reducing the losses due to surface roughness, as these would be electrically smaller with respect to the guided wavelength. The reduction of the losses would give an improvement in the noise temperature of the antenna. An efficient and low cost means of manufacturing grooved line using the commercially available dielectric substrates commonly used for microstrip antenna has still to be developed, and is the only impediment to its wide spread adoption. However, it should be noted that the thin substrates used at millimetre wavelengths will be more difficult to handle with a machined groove. Further, the radiation losses from grooved line have not been studied, and may prove to be higher than from a conventional microstrip line as the effective relative permittivity is reduced by the insertion of the air pocket. A disadvantage of grooved line fed arrays would be that the 180° phase shifter from the slot will not be available. Additionally, the losses in grooved line are still higher than those in rectangular waveguide, so the noise temperature will be higher and the aperture efficiency lower. The problem of etching of long thin microstriplines also plagues grooved line. However, unlike a rectangular waveguide feed network, the implementation of grooved line would not be at the expense of making the total array any thicker than the dielectric substrate.

The remainder of this section is dedicated to introducing an number of unusual microstrip patch antenna structures and topologies for small scale arrays.

By using increased width microstrip patches, the supporting corporate feed network can be simplified. This has been demonstrated using patches wide enough to cover the space usually occupied by two patches side by side [68] and four patches side by side [69]. Any advantages in terms of aperture efficiency or input impedance compared to typical patches were not commented upon.

Several unconventional feeding networks have been proposed which have been claimed to offer some advantages over the commonly used feed network topology described above. Small series fed arrays have been used to simplify the feed network of 2x2 subarrays [70, 71]. Reduction of the number of discontinuities reduces the losses within the 2x2 subarray but no comments were made on the gain bandwidth [71]. An alternate method of corporate feeding within a 2x2 subarray which offers a reduction in the number of bends and reduces the length of the lines entails non-radiating edge feeding to the patches, instead of conventional feeding to the radiating edges [72]. The disadvantage of this feeding method has been identified as the generation of high cross polarised radiation components, leading to losses of power into the undesired polarisation. A theoretical study of a single element has shown that with careful choice of the ratio of patch width to resonant length, a patch which radiates a minimum of cross polarised component can be designed [72]. Additionally, the H-plane symmetry of the array design should lead to decreased cross polar radiation in the boresight direction; exciting a patch on the opposing side to its lateral neighbour, so that some of the higher order modes will also be opposed in direction.

An obvious alternative to the difficulties of complex feeding networks, for distribution of power across an aperture, is not to use a feed network at all. To this end, parasitic coupling

between coplanar microstrip patches has been used to replace a feeding network [73]. This technique was taken to an extreme in a 7x1 array [74] suitable for excitation by a centrally placed waveguide feed [63]. Aperture coupling to the smaller variety of coplanar parasitically coupled patch arrays has been demonstrated successfully [75-77]. Three parasitically coupled patches were placed on either side of a driven patch antenna, in its E-plane. This resulted in a symmetrical E-plane radiation pattern, in contrast to the asymmetrical radiation patterns innate to corporate feed arrays. The total length of this parasitically coupled array was 4.3 λ_o [74], which leaves more than sufficient inter-subarray spacing to accommodate a rectangular waveguide corporate feed, below the ground plane as discussed above. An oversized square slotted patch, having a side length of 1.32 λ_o, has been investigated experimentally [78]. This oversized patch offers a means of replacing a 2 x 2 subarray with a single element of equal lateral dimensions, and has the advantage of lacking the corporate feed network of a 2x2 subarray. Although the design presented was probe fed, it was envisioned to be slot coupled [78], and could be readily adapted to the above proposed slotted endwall rectangular waveguide feed. An 8.5 λ_ox8 λ_o grid array, having 128 grid cells, has been investigated on a low relative permittivity, 0.05 λ_o thick substrate [79]. This array has been investigated using two central feed types; a probe feed and balanced form of excitation such as would be produced by slot excitation. The balanced feed type gave a higher gain, of about 30dBi, and a 1dB gain bandwidth of 1.7% [79]. The interesting feature of this array was that such a low dielectric substrate ($\varepsilon_r \cong 1$) has been used successfully. This maybe useful for simplification of manufacture of the parasitically coupled arrays and oversized patch designs discussed previously.

In summary, a number of comprehensive studies of microstripline fed microstrip patch arrays have been identified and introduced, and it has been confirmed that the aperture efficiency decreased as the array size was increased; the microstrip line feed network lengths became longer as the array size was increased and the dielectric and conductor losses in those lines further

compounded. These losses would affect the operational noise temperature of a system employing such an antenna array. The long line lengths have a further problem related to uneven etching during manufacture, which has been shown to cause uneven illumination across an array. A corporate feed network of rectangular waveguide to interconnect small scale subarrays has been proposed to mitigate these and other problems that were identified. Single layer microstrip technology offers the lowest profile of all the candidates considered, and most of this technology's operational disadvantages could be over come by a change of media for the majority of the feed network.

1.4.2.2 Multilayer and miscellaneous configurations

It has been noted that choice of optimal substrate characteristics for a high gain, wide bandwidth microstrip patch antenna array faces several contradictions [58, 59]. For example, use of a thin substrate improves array efficiency due to decreases in feed network losses, but will also decrease the input impedance bandwidth of the patch radiators. This leads to the need for a compromise in coplanar designs, as described in the previous section. However, the addition of further layers of low relative permittivity substrates, supporting parasitic microstrip patch antennas, offers a means of increasing the input impedance bandwidth of the patch antenna elements of an array. This has been trialed using a conventional corporate feed [80], and with the simplified corporate feed to the non-radiating edge fed patches described above [81]. Both studies showed an increase in input impedance bandwidth, approximately doubled, and, in case of the former, a 1dB increase in gain for an 8x8 array when the layer of parasitic patches was added. A variation of this concept with the lower driven patches removed has been trialed for a 2x2 subarray [82]. The power was transferred from the resonant feed network to the patches on an over-laying layer by electromagnetic coupling. One pair of patches were fed both electrically and physically

180° out of phase with the other pair, which gave decreased cross-polarised radiation and symmetrical radiation patterns in both planes [82]. The 1dB gain bandwidth for this small array was 11.2%. The structure is suitable for centre feeding by a slot. A further variation upon the stacked patch concept has been to place four parasitic patches over the driven patch, instead of the usual single driven patch [83]. As the interelement spacing of this array is greater, the array is thinner and the feed network simpler. No comment was made in any of these papers about problems related to satisfactory lamination of the different substrate layers. Air pockets between the layers and other lamination problems may prevent high volume, inexpensive manufacture of these multi-layer microstrip antenna designs at millimetre wave frequencies using conventional substrates. However, manufacture by present day microelectronic process should have a high, if costly, yield.

A novel multi-layer microstrip array has been investigated, in which the feeding network was replaced by a cavity [85]. The cavity offers a low loss alternative to microstrip line feeding, and would be produced by casting [85]. Despite these advantages, and the completed array still having a much lower profile than a reflector antenna, the 3dB gain bandwidth obtained was incredibly narrow at 3.1%.

A number of dielectric sphere overlaid microstrip patch arrays have been investigated at 90GHz [86 & 184]. The partially truncated dielectric sphere overlaying each microstrip antenna acted as a lens and increased the directivity of each individual radiator, but at the expense of greater manufacturing complexity, increased lateral dimensions and a considerably increased thickness. Addition of the spheres increased the gain of a 16x16 array with inter-element spacing of 0.95 λ_o by 3dB, and by 12dB for an 8x8 array with 1.90 λ_o inter-element spacing [86]. Additional benefits of the increased inter-element spacing was to decrease the complexity of the microstripline feed network for passive arrays, and to provide sufficient space for active devices

for phased arrays [184]. It is interesting to note that when a lens of the optimal radius of about 1.5 λ_o was fitted to an open rectangular waveguide mouth, a gain of 19.5dBi was obtained, been 3dB higher than that from patch excitation [87]. This suggests that may have been better to produce a corporate fed array of open waveguide mouths by casting, and overlay the lenses. The waveguide array would, however, have had a higher profile than the microstrip patch array.

A number of multi-layer microstrip array types have been introduced, and the electrical performance improvements over coplanar microstrip array types briefly discussed. The successful implementation of these multilayer types at millimetre wave frequencies was noted to depend largely upon the development of a suitable manufacturing process. The benefits of simplification of the array feeding network resulting from greater inter-element spacing has also been introduced. Another element size increase technique involves fitting a partially reflective screen over widely spaced patches to form Fabry-Perot resonators.

A Fabry-Perot resonator consists of two parallel, partial reflectors separated by some set distance [88-90]. These structures have found widespread use as interferometers, and have also been used as antennas. Two categories exist, discrimination due to the reflector separation been a fixed distance or variable across the extent of the reflectors [88]. Typical Fabry-Perot reflectors used at submillimetre wavelengths are grids, meshes, perforated metallic sheets and arrays of square patches [90]. When used as antennas, an open rectangular waveguide projecting through the back reflector could be used to excite the cavity [89], although microstrip patch antennas have been used in published examples. The constant separation-distance type of reflector have used solid metal ground planes as the backing reflector, while the partially reflective upper reflector has been either widely spaced metal patches [91-93] or sparsely slotted metal sheet [94]. The metal patches are located 0.5 λ_o above the exciting microstrip patch antennas, forming an array of short

backfire antennas [91-93]. A maximum gain of 13dBi was obtained for a single subunit having a 2 λ_o diameter back reflector, and increasing the diameter did not increase the gain [92]. Some what lower gain, approximately 10dBi, was measured for the type with a sparsely slotted upper reflector, and the 1dB gain was narrow at about 3% [94]. A spherical upper reflector of radius 33 λ_o was used for a 6.1 λ_o sided antenna, which radiated a Gaussian beam [95]. The centre section of the upper reflector was partially reflective mesh, through which the radiation escaped the cavity. A radiation efficiency of 95% was estimated, and input impedance bandwidth of 7% was measured [95]. Excitation of the driving patch antenna by a rectangular waveguide with endwall slot was suggested [95]. Further work has concentrated upon the application of modern numerical techniques to the design of this type of antenna [96].

A number of variations to the basic microstrip patch antenna array concept have been introduced, and briefly discussed. The benefits of these variations are improved input impedance bandwidth, improved directivity and array thinning, which allows for a simplification of the feeding network. All these improvements have come at the cost of increased manufacturing complexity, and are mostly very dependant upon the ability to laminate multiple layers of thin dielectric substrates successfully.

1.4.3 Triplate arrays

Triplate antenna arrays are characterised by the use of flat metallic ground planes on the other sides of two layers of a low relative permittivity dielectric substrate. Between these is a thin film supporting the feeding network (usually etched as per a microstrip antenna), Figure 1.4. A square aperture (approximately 0.6 λ_o) is cut in the upper group plane form the fundamental

radiating element, which is excited by a probe or patch on the feeding layer. However, the radiating aperture creates a discontinuity in the triplate transmission media which generates a parallel plate mode (PPM) between the ground planes [97,98]. Management of the PPM, as discussed later, is essential to the production of an efficient antenna array. The typical triplate antenna array is a lamination of 5 layers which is more complex to manufacture than a single layer microstrip patch array requiring careful alignment of the various layers and is thicker than microstrip designs. However, the advantages of lower losses and greater input impedance bandwidth have made this type of array immensely popular for DBS satellite subscriber terminal application in Japan (12GHz) and Europe (10GHz). Patch fed triplate arrays have also been investigated at 59.6GHz as a candidate for automotive collision avoidance radar giving 60% aperture efficiency as a 4x4 array [99]. As will be discussed, triplate arrays have been used for applications requiring single linear polarisation, dual linear polarisation, single circular polarisation, dual circular polarisation, and a 45° offset linear polarisation for low sidelobes in the principal planes [100].

Due to triplate arrays been so suited to application as planar DBS subscriber antennas, this type of array has been studied extensively. Almost every aspect of triplate arrays has been studied in such depth that there appears that there is little that has not been done. Placing a large number of via posts about the transition from triplate transmission line to radiating element insures that little power is lost into a parallel plate mode (PPM) between the upper and lower ground planes [101]. This technique of PPM mitigation has been shown to be highly effective, but come at the cost of greater manufacturing complexity and thus lower process yield. For a mass produced and inexpensive product, the simplest possible construction is desirable. To this end, triplate arrays without PPM suppression vias have been studied, resulting in high aperture efficiency designs that can be snapped together [102]. The source of PPM has been studied in detail [97,98]. For a symmetrical triplate line there is no PPM generation as long as there are no abrupt discontinuities

in the transmission line. Likewise, if the upper and lower ground planes along the course of a feed line are perforated identically no PPM is generated [97,98,103-108]. However, having identical slots in both ground planes will form a bidirectional antenna, for which there are few applications. Two methods of dealing with the PPM, which can potentially trap considerable amounts of power, have proven successful. The first method has been to suppress the PPM, and the second to manage it effectively. Both techniques have been applied to large scale linearly polarised, dual polarised and circularly polarised triplate arrays.

A comprehensive study of triplate antennas has shown that placing a cavity under each aperture element will suppress the generation of PPM [97,103-108]. Addition of the underlying cavity to a square triplate element increased the radiation efficiency from 55% to 90%, and improved the gain from 5dBi to 6.75dBi. The increase in radiation efficiency shows the effectiveness of this means of suppression of PPM. Circular cavities have also been investigated, showing similar improvements [103]. The disadvantage was the addition of the cavity depth to the overall thickness of a triplate array. The bottom ground plane could be commercially produced by casting, or stamped by numerically controlled mill. The same study also investigated the use of walls around the aperture edges in dual polarised arrays, and 180°, electrical and physical, out of phase feeding within 2x2 subarrays. Similar structures have been investigated where the underlying cavity has greater lateral dimensions than the aperture, so that the cavity undercuts the edge of the ground plane [109]. No comment was made on the effect of the undercut, but it may offer a further improvement over that obtained with the fitted cavity. Similar cavities have also been fitted to a hybrid triplate/CPW fed array, and shown to be as effective [110-112]. An alternative method of PPM generation mitigation has been to place concentric rings of slots about the aperture of a triplate element [113]. No comments were made upon the effectiveness of this technique. However, line losses accounted for almost all the losses in a 32x32 array of similar elements, showing little loss from PPM [114].

A number of comprehensive, and wide ranging, studies have considered careful spacing of the triplate elements to effectively manage the PPM, instead means of suppressing it [94, 115-134]. It has been shown that radiation efficiency and gain of triplate arrays are highly dependant upon the inter-element spacing. The spacing at which the PPM exits the apertures in phase with the power from the probes exciting the apertures was typically 0.85-0.9 λ_o, been a guided wavelength in the foam substrate between the ground planes [94]. The dependence of PPM power upon aperture size has also been studied experimentally [94]. These techniques, combined with removal of the foam under the elements, have been successfully used to produce a 4x4 array with 61.3% aperture efficiency operating at 59.5GHz for automotive radar [99]. Peak aperture efficiencies of 70-75% have been typical for linearly polarised, circularly polarised and double layered dual polarisation arrays operating around 12GHz for DBS satellite television reception. Small tabs on the edges of the apertures covering the transition of the probe from triplate region to open aperture have been shown to improve aperture efficiency, by decreasing a large first sidelobe on one side of the E-plane radiation pattern [116]. Another comprehensive study has covered generation of cross polar components, the influence of ground plane separation upon element Q and bandwidth, the presence of patches either in the aperture or on the probe layer, random perforation of the foam, coaxial to triplate transitions for feeding arrays, radome effects, arrays of non-uniform elements, partially exposed feedline at aperture edge, and noise figures [119-134]. The best results from this study were from a linearly polarised 16x16 array using pairs of slots as elements, instead of large single apertures as above, which was fitted with an overlaying polariser which converted linearly polarised radiation to circular [131]. The measured gain was above 32dBic from 11.5-12.5GHz (8.5% bandwidth) with aperture efficiencies ranging from 83-96% [131]. No results were presented showing the effect of addition of the polariser upon the PPM, although the aperture efficiency was some 15-25% (0.5-1dB in gain) higher than that of a triplate array using normal circularly polarised elements, and having no overlaying parasitic layer [131]. The addition of a layer of parasitic dipoles or patches above the radiating apertures of triplate

arrays have been investigated by other authors [113,117,118,135]. A layer of small parasitic patches added to a 4x4 array of patch-probe excited square aperture elements improved the aperture efficiency by 10% at the centre frequency. These designs produced a very constant aperture efficiency (80%) across at least 8% bandwidth, and improved the input impedance to be of the order of 8% [117]. Whether these various types of parasitic elements decrease the generation of PPM or ease its exit out of the apertures has not been investigated. The disadvantages of the addition of the layer of parasitic elements were an increase in thickness from the extra foam layer and the need for careful alignment of the parasitic elements, but these additional costs may be merited the improvement in performance. High cross polar radiation, of about −15dB, in the H-plane pattern has been identified as a failing of arrays of large aperture square elements and various meshes have been trialed in the aperture mouths or on the probe layer to minimize this [136,137].

Further possible work on triplate arrays could investigate the cause of the improvements resulting from the addition of parasitic elements, alternate methods for realising the parasitic elements that do not require the addition of an extra foam and alignment of the extra parasitic patch layer, element types that innately generate less PPM and easier means of integrating rectangular waveguide feeds to triplate arrays. At present, a centrally placed rectangular waveguide feed has required removal of one radiating element, and its replacement by an equivalent load. An open waveguide mouth in the lower ground plane coupling to the triplate line would be much simpler to manufacture.

1.4.4 Miniature horn arrays

Miniature horn antennas are formed by a cylindrical cavity (short length of circular waveguide terminated by a short circuit) with a chamfered open mouth which radiates. This gives an antenna element with small lateral dimensions, comparable to a microstrip patch antenna, but potentially having a higher radiation efficiency [138]. These antennas are typically fed by channel suspended line or triplate network. Structurally, a miniature horn array can perhaps be thought of as a transition between triplate and horn arrays. Miniature horn arrays are structurally robust been composed of two shaped metal blocks, or metallised molded plastic to reduce weight. Recently, work has been undertaken to extend miniature horn arrays to phased array application at 60GHz [139]. This type of array element is adjudged to be more appropriate for phased array application, as it is probably better to have larger elements for broadside arrays which result in an overall simpler structure. Cutting and placing the dielectric strips for the channel suspended line would add significantly to the cost of production. No further consideration will be given to this type of radiating element.

1.4.5 Horn arrays

Rectangular horn antennas as array elements in combination with waveguide feed networks offer means of producing large scale arrays with very low loss [25], Figure 1.5. Horn antennas have been used in large dual linearly polarised arrays [24, 25], and large scale linearly polarised arrays [12, 13, 19-21]. Various types and sizes of horn have been used ranging from simple designs with 1 λ_o sided mouths to 1.8 λ_o sided box horns with radiation pattern nulls carefully placed to cancel the grating lobes resulting from the large inter-element spacing. These arrays

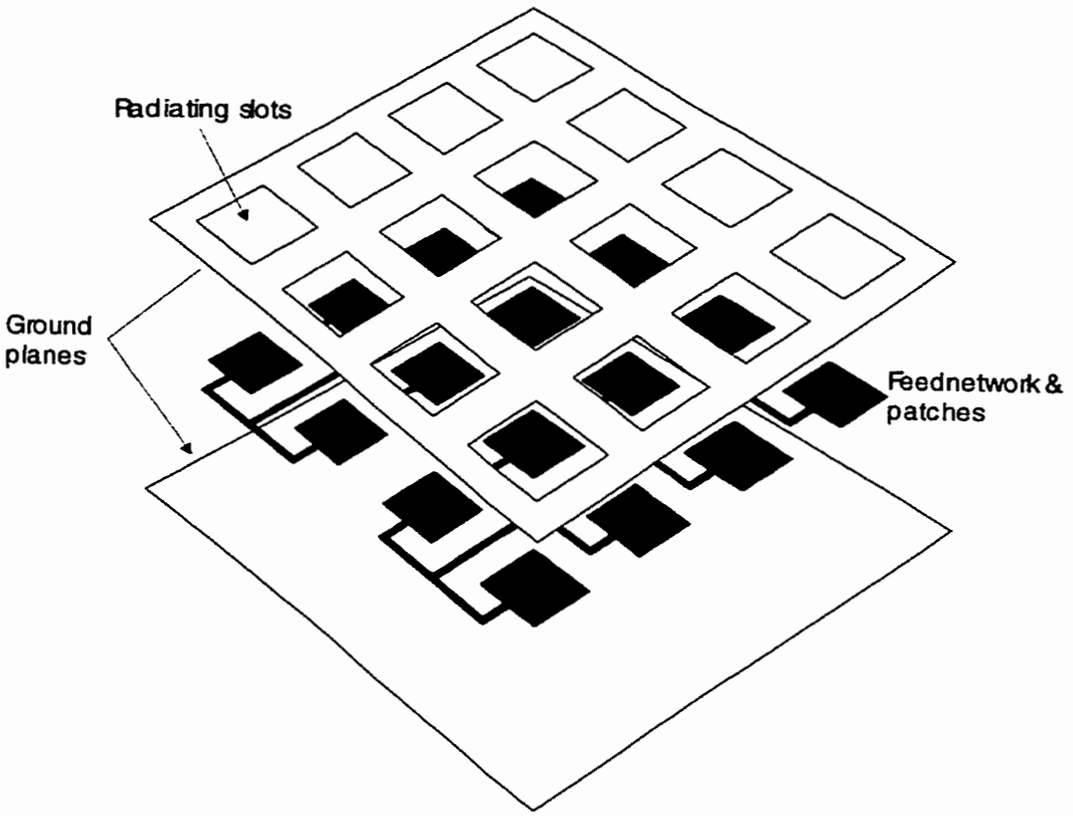

Figure 1.4: **Triplate array.**

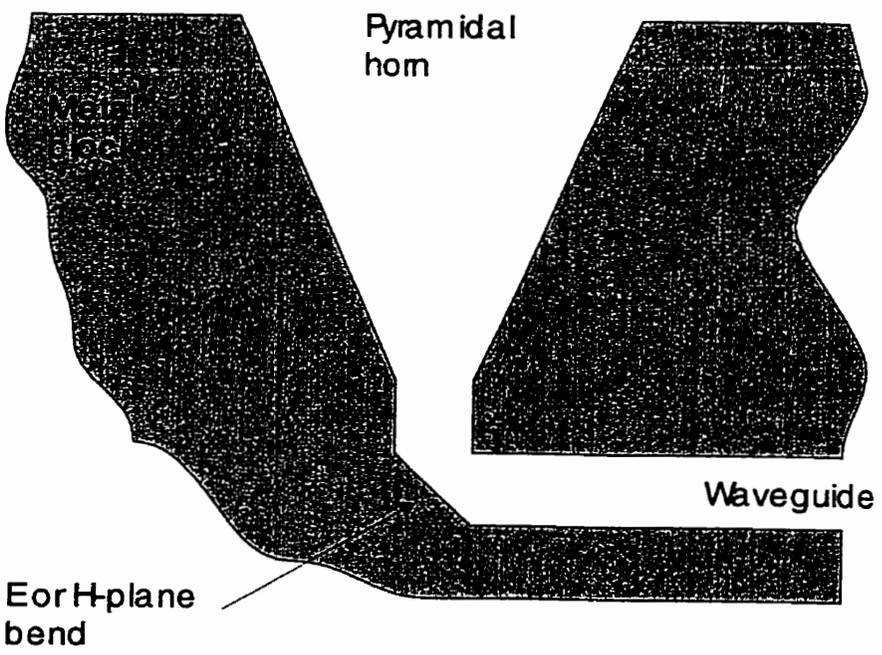

Figure 1.5: **Horn array element.**

appear to be easily mass-produced by casting two or three metal blocks with channels and cavities forming the waveguide feeding network, which are merely bolted together to form the final array antennas. Such arrays should be relatively inexpensive to manufacture, and if cast from like metals ought not to be susceptible to thermal stresses and degradation if used outdoors. The main disadvantage of using horn antennas is the considerable height of this type of antenna which is in excess of 1 λ_o. A completed array of box horns for operation at 39GHz had a total thickness of 4.0cm [19], been about 5 λ_o, two thirds of which was probably the length of the horns. However, due to the small dimensions of antennas at millimetre wave frequencies, having a thickness of multiple λ_o may not be a great disadvantage unless a very low profile is required, Figure 1.5. In conclusion, rectangular waveguide fed horn antenna arrays have been well investigated for use at millimetre wave frequencies, although no means of phase error correction by either lenses, interfering objects [140] or dielectric liners [141] have been trialed.

1.4.6 Anulus parallel slot array

Radial waveguide has been used to feed an efficient and broadband array of concentric circular slots [17], Figure 1.6. The radial waveguide is used to spread power from the central feed point out to its rim, from which a number of junctions and further sections of radial waveguide transfer power to the slot radiators. In stark contrast to the series fed radial waveguide arrays considered above [28, 29, 36], the phase distance from the feed centre to each slot radiator is identical [17], Figure 1.6.

If equal impedance radial waveguides (equal impedance) are used after each Y-junction, equal power will be delivered to each slot, Figure 1.6. Due to the difference in the circumference

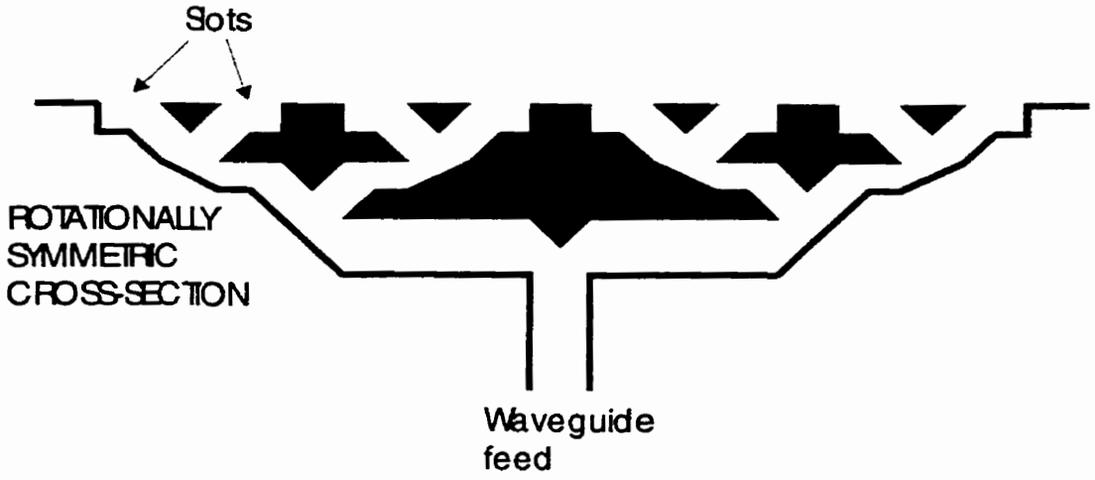

Figure 1.6: Annulus parallel slot array.

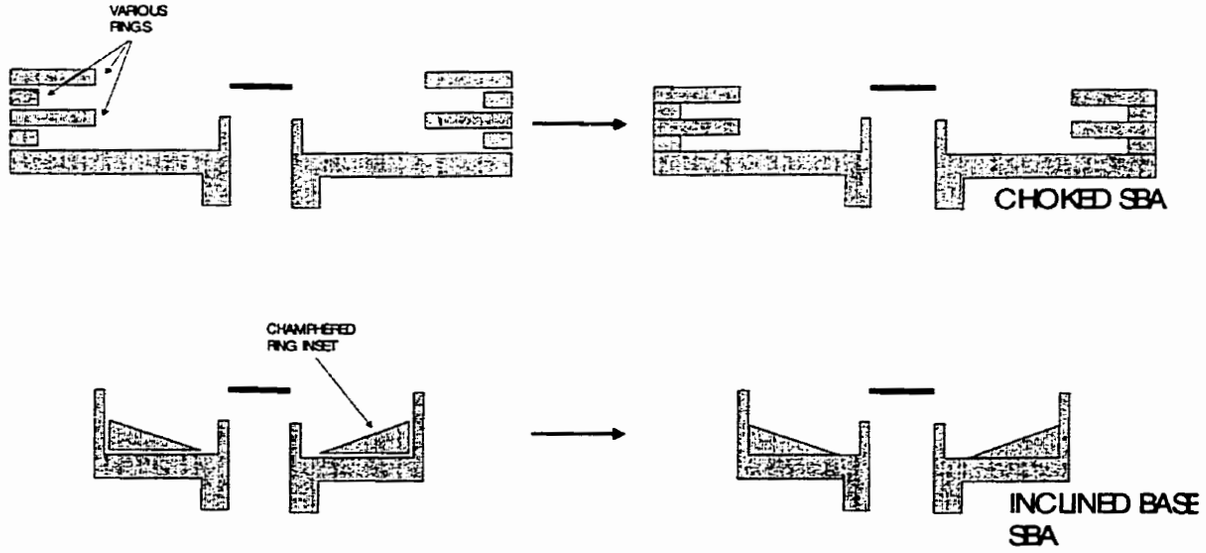

Figure 1.7: Possible sources of airgaps in novel short backfire antennas.

of each concentric slot, the power density on each slot decreases away from the array centre [17]. Thus there will be a radially dependent amplitude taper in such an array. For example, a 4 slot array with 0.7 λ_o slot spacing will have slot circumferences of 2.51 λ_o, 7.54 λ_o, 12.57 λ_o and 17.59 λ_o; all slot circumferences are odd multiples of the innermost slot circumference. Equalising the power density on each slot is a matter of using those odd multiples to scale the impedances at each of the Y-junctions. For the example, the impedance of the final radial waveguide feeding the outermost slot must be 1/7 of the impedance of the last segment feeding the innermost slot. Similarly other power distributions could be designed, which will have broadband performance.

This structurally simple antenna array, which could be built up from a shaped metal base, 4 stamped foam O-rings and 4 circular metal pieces. Assembly would merely involve dropping the 8 pieces into the base. This, may, however be too complicated and time consuming for viable mass production. If struts could be added between the outer rim and the inner slot separation plates, the need for the foam separators would be eliminated, and construction greatly simplified. The inclusion of struts, across the slot mouths, to induce circular polarisation has been hinted at [17], and could certianly be adapted for structural support instead.

The total thickness of the array is approximately 3/4 λ_o [17]. The afore mentioned 4 slot array with 0.7 λ_o spacing would have a side length of 6.4 λ_o (5.6 λ_o radius), which is sufficient inter-subarray spacing to allow the use of a H-plane rectangular waveguide corporate feed network.

A means of minimizing the currents induced upon the metallic slot separation plates has been suggested [18]. These unintended currents contribute to the cross-polar radiation of the array. Introduction of radially aligned teeth, or slots, to the slot separation plates will effectively block

the current flow [18]. Introduction of the teeth would not increase the manufacturing complexity of the array.

The E and H plane patterns of a 4 slot array are not identical, Figures 4 and 5 of [17]. The E-plane pattern has higher sidelobes than the H-plane. Distorting the present circular array shape into a slight ellipse, having a E-plane slot separation less than in the H-plane, would reduce the level of the E-plane sidelobes, and add no further complexity to the array design. This type of array has not been used as an array element, so any mutual coupling effects upon performance are unknown.

1.4.7 Short backfire antenna arrays

Short backfire antennas are a low profile alternative to horns as elements for planar array application [142, 143], Figure 4.2. A further advantage over horn antennas is a considerable reduction in weight [142]. A common reflector 2x2 array of short backfire antennas has been shown to have comparable directivity to a horn having an identical aperture area (4.5 λ_o) [143]. The short backfire array has the advantage of being much shorter in length (0.6 λ_o) as opposed to the horn antenna (4.6 λ_o), saving some 4 λ_o in length. Comparable pattern shape and gain (15dBi) to a 5.5 λ_o long Yagi-Uda array was achieved with a rimmed, 0.5 λ_o length, dipole excited short backfire antenna [144].

Addition of a rim to the main reflector has been shown to increase the directivity and reduce the side and backlobe levels of the antenna [142]. The rimmed main reflector forms a cavity, which can be manufactured from sheet metal or set into a solid metal block, Figure 5.1.

The latter method is suited to casting, making for easy production of large arrays of cavities, Figure 4.1. The subreflectors could be etched on a thin dielectric layer and laid over the array of cavities, Figure 4.2.

All early antenna designs were excited by dipoles. Excitation by waveguide instead of dipole provides high gain, high power handling capability and a simplification of construction for microwave band operation [143]. Waveguide excitation was first trialed soon after the invention of this type of antenna [145]. Further advantages of waveguide feeding are the use of a low loss feed system, improved impedance bandwidth over a simple dipole feed, easier design and construction at higher frequencies (stringent mechanical tolerances of the dipole eliminated), and weather protection and air pressure sealing measures can easily be built into the antenna [142]. Two positions within the cavity at which the rectangular waveguide feed will impart a high directivity have been identified [142]. These are a flush mounting and when the mouth is inset midway between the main reflector and the subreflector [142], Figure 4.2. It has been shown for an antenna with a 2 λ_o diameter, 0.25 λ_o deep cavity, 0.6 λ_o height 0.5 λ_o diameter subreflector, that the use of the inset waveguide mouth gave 1.3dB higher gain compared to an identical antenna using the flush waveguide mouth [142]. This increase in gain was mostly due to a narrowing of the E-plane pattern [142]. There is also some improvement in input impedance matching. Use of an inset rectangular waveguide feed will not inhibit production by casting.

The majority subreflectors used have been circular disks, Figure 5.1. A diameter of 0.5 λ_o has been shown to give the highest directivity, and has been widely used [142]. Square subreflectors have also been suggested [146, 147]. However, higher gain and reduced E-plane beamwidths can be obtained using subreflectors which are either rectangular or elliptical rather than circular in shape [142]. A rectangular subreflector of 0.4 λ_o E-plane width and 0.9 λ_o H-plane

width (mirroring the shape of the rectangular waveguide mouth) increased the gain of an inset rectangular waveguide fed antenna by 1dB over that of the same antenna with a 0.5 λ_o diameter circular disk subreflector [142]. This antenna held its pattern shape well across 10% bandwidth.

The subreflector need not be restricted to a planar nature [147]. Conical and spherical subreflectors maybe used [147], but this will complicate manufacture as the subreflector can no longer simply be etched onto the overlaying thin dielectric sheet using standard photolithographic methods. The use of paraboloidal, or spherical, reflectors are suggested also [147]. Interestingly, all short backfire antenna configurations pictured in [147] have a short extension of the waveguide feeder into the cavity, although no comment was made about it. Presumably this was for fixing the phase centre of the waveguide feed as discussed by [148].

Various soft surfaces have been successfully employed to improve the radiation characteristics of horn antennas. These techniques have also been trialed on the rims of short backfire antennas. Quarter wave chokes were first trialed on the rim of a dipole excited 2.5 λ_o diameter cylindrical cavity antenna [149]. This technique was then used on a similarly-sized rectangular waveguide excited antenna [150], Figure 1.7. The rim in both cases was 0.5 λ_o in height, and had two $\lambda/4$ chokes of approximately 0.13 λ_o height set into it, Figure 1.7. Additionally, these antennas were compared to equal diameter antennas (3 λ_o), an it was found that the quarter wave chokes gave a gain improvement of 3-5.5dB. The gain improvement steams from an increase in the directivity. This comparison is a little misleading, as a 2.5 λ_o diameter antenna gives a considerably higher gain than a 3 λ_o diameter antenna, even without the chokes. If the addition of chokes do in fact improve the characteristics of 2.5 λ_o diameter antennas, then the technique is of some value. The use of the quarter wavelength chokes has been extended to 34GHz and also has been successfully used in the common rim of a 2x2 common reflector array [151]. However, in all cases, the cavity walls were built up by laminating rings of various diameters

instead of milling the chokes out of solid metal block, Figure 1.7. Consequently, the observed effects may have been the result of a combination of both the chokes and incomplete electrical contact between the laminated rings. In either case, changing the boundary conditions along the walls of the cavity affected antenna performance. The addition of a low relative dielectric constant liner has also been shown to increase the gain of a 3 λ_o diameter short backfire antenna by approximately 2dB [152]. This technique has also been successfully extended to the common rims of a 2x1 and a 2x2 common reflector arrays. Comparisons were made between the antennas with and without the dielectric liner, and are thus reasonable. No explanation was given for the intentions behind this modification. The relative permittivity of the liner was 3.1 at 1MHz [153], but is unknown at 34GHz, the design frequency of the antenna. It is likely that the relative permittivity will be much lower at 34GHz than at 1MHz, and the loss tangent possibly higher. The liner thickness used is approximately 0.2 λ_o, and some air gaps between the layers of the material are clearly visible in the published photographs [152]. These observations lead to the speculation that liner did not affect the currents on the rim (adherence to the rim was not important), but forced the aperture distribution to be more uniform, as has been demonstrated in dielectric loaded horns [141, 154]. A more uniform aperture distribution yields a higher aperture efficiency.

Surprisingly little work has been done on shaping of the main reflector or cavity. Inclination of the base of a dipole excited 2.05 λ_o diameter, 0.25 λ_o rimmed cylindrical short backfire antenna, with two subreflectors (at 0.66 λ_o above the main reflector), has been shown to improve the input impedance bandwidth to 20% for VSWR=1.5, compared to 3% for the standard antenna [155, 156]. Follow-up work has been done with rectangular waveguide excited, 2.5 λ_o diameter, 0.5 λ_o rimmed cylindrical short backfire antennas, with single subreflector (at 0.5 λ_o above the main reflector), showing that the principal is also applicable to this alternate style of

excitation [157,158], Figures 1.7 & 4.8C. In all three cases, the gain was also increased by 0.3-0.8dB, by the inclination of the base. In the latter case, 5°, 10°, 15° and 20° rings were added to a normal flat based antenna [157], Figure 1.7. The 15° inclination was found to be best in terms of both gain and input impedance, in agreement with the findings from the dipole excited antennas. In contrast to the dipole excited antennas where the cavity was one solid piece, rings were retrofitted to a rectangular waveguide fed flat based antenna and, as a results, may have been the source airgaps, Figure 1.7. Curved (possibly paraboloidal) main reflectors have also been suggested, but the behaviour of these in comparison to similarly sized flat based reflectors is unknown [147,159,160]. Generally, the main reflector has been circular, though square [146,147,156] and octagonal [161,162] shapes have been used. A comparison of an antenna with a circular cavity to an otherwise identical antenna with an octagonal cavity of nearly identical base area, showed a higher gain by 0.7dB for the circular cavity [162]. Perhaps to the contrary, it has been claimed that an inclined base square cavity antenna was identical in performance to a similar antenna having an inclined base circular cavity [156]. Beyond this, nothing has been done. Given that a large array of short backfire antennas would likely be produced by casting, Figure 4.1, virtually any arbitrarily chosen shape could be manufactured with no more impediment than production of antennas with flat based cylindrical cavities. Little consideration has been given to the aperture distributions of short backfire antennas, although some work was done on an allied structure, a cavity backed dipole [163].

An alternative to the subreflectors used in all the above described antennas is a high dielectric radome [164], Figure 4.8D. A half guided wavelength radome is typically used on antennas requiring some protection from the surrounding environment, but for this class of short backfire antenna a slightly less than quarter wave length thick radome is used. It has been shown that higher relative permittivity, ε_r=10.2, are preferable than lower values, ε_r=3.0 [164]. To date, only microstrip patches on the floor of the cavity have been used to excite this class of short

backfire antenna. The use of a patch as an exciter is unsuitable for mass production, as placing the patch on a dielectric puck on the floor of the cavity requires considerable care, and there is also some difficulty in feeding the patch. Waveguide excitation would greatly simplify construction, but the high relative permittivity radome is still expected to be prohibitively expensive.

Dipole excited short back antennas have been used as array elements [165-168], as have waveguide excited antennas [1 43,146,147,151,152,169]. Both excitation configurations have been used as array elements in two ways; either by arraying individual short backfire antennas or by arraying the feeds and subreflectors over a common oversized reflector having a boundary rim only. No study has been undertaken to compare the arraying of individual antennas to arraying over a common reflector. The only published figure for mutual coupling between adjacent short backfire antennas within an array is from an array of dipole excited individual antennas and was below –40dB [166]. No consideration appears to have been given to the systematic elimination of grating lobes by careful null placement. As short backfire antennas are much greater in diameter than 1 λ_o, grating lobes will be close to be main beam direction, and measures will have to be taken for the mitigation of this effect if a high efficiency array is to be built.

The work described above on short backfire antennas was purely experimental, and often done for only one reflector depth and diameter. A few numerical studies have been undertaken [170-175], but none appear to have made any solid contribution to the study of this type of antenna. However, it should be noted that modern numerical modeling methods could be used to undertake a useful and wide ranging parametric studies for antennas of this type at less expense than doing it experimentally. It should also be possible to use these numerical methods in combination with other techniques to arrive at an optimised design for some given application [175].

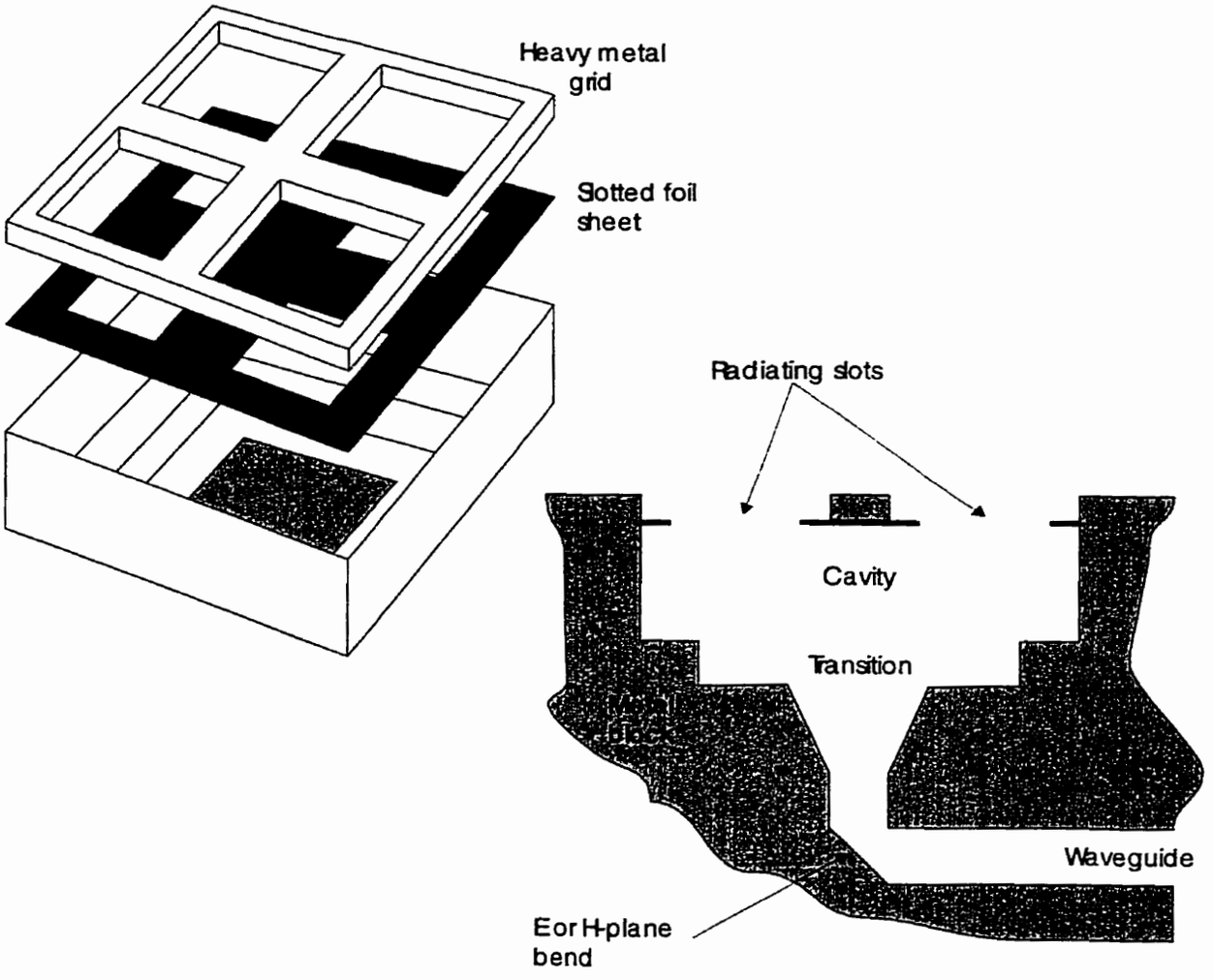

Figure 1.8: Isometric and cross section views of broadband cavity antenna array [14,177].

1.4.8 Broadband cavity antenna array

A vaulted cavity antenna array has been successfully built and tested for operation around 12GHz [14, 176, 177], Figure 1.8. The array studied is fed by rectangular waveguide and air filled cavities, and thus does not suffer from either dielectric or significant conductor losses. This, combined with high efficiency and wideband high quality impedance matching, made it suitable for high-power applications, such as transmit antennas. Given that the array is composed entirely of shaped metal blocks, it is structurely robust, and should be able to withstand wide variations in temperature. Additionally, the structure is suited to manufacture by low cost casting [14,176,177].

The 16 element array consisted of 4 subarrays of 2x2 aperture elements of 0.8 λ_o spacing. Each subarray unit has a stepped section and a cavity. The stepped section had the function of both overmoding and impedance matching. A lattice frame overlays each cavity forming the 2x2 subarrays of apertures, Figure 1.8. By separating the apertures, the frame improves matching of the cavities to free space. A compact H-plane rectangular waveguide corporate feed incorporating a 180° delay line (type B of Figure 1) was used to distribute power to the cavities.

The measured return loss is better than −10dB from 10.25-14.5GHz, and better than −20dB from 11.9-13GHz (9% bandwidth). The aperture efficiency calculated from the measured gain was 80% or better from 11.5-13GHz (−4% to +8% of the design frequency). The drop in aperture efficiency from 90% to 80% that occurs at 12.5GHz maybe be a result of phase errors in the 180° delay line away from its design frequency.

Several variations of this antenna have been investigated [14, 177]. The boresight gain of the single 2x2 aperture cavity were improved over those of the original antennas [14] by adding a

heavy metal grid over the thin metal plates separating the radiating elements [177], Figure 1.8. The stepped section and radiating aperture size were modified and the effects upon input impedance matching and gain bandwidth were also presented. These improved 2x2 arrays have been used as a subarray for a 64 element array, having a side length of 173.8mm [14]. The electrical characteristics of the 64 element array were impressive, having an aperture efficiency over 80% for 11.0% bandwidth, and over 90% for 5.8% bandwidth [14]. The return loss was ≥14dB over 16% bandwidth, and ≥20dB over 8.4%.

Some larger size cavity antennas, having a greater number of radiating elements, have been investigated, but appear not to operate as well as the smaller cavity antennas, due to the closeness of desired and unwanted modes in larger cavities [153, 178]. Some theoretical consideration have been given to the modal distribution in the cavities [153, 178].

It should be noted that the cavities have a depth of about 0.5 λ_o, and the stepped matching section is somewhere between 0.25-0.5 λ_o. The high efficiency 64 element array had a total thickness of 38mm, or 1.52 λ_o [14]. Increasing the size of this type of array to 128 (=30.5dBi) or 256 (=33.5dBi) elements will not add any further thickness to an array of this type. Other than having a relatively high thickness, the reported structural characteristics, and electrical performance, of this type of array is the best of all candidate antenna types considered here.

Table 1.3: Summary of candidate technologies for large array element.

Technology	Profile & area	Manufacturing requirements	Electrical performance	Comments
Single layer microstrip	low 0.05-0.1 λ_o 4x4 array ≈ 3λ_o side	high precision photolithography etched substrate affixed to a metal plate	have to compromise between impedance BW and feed line losses/gain/ aperture efficiency	no centre fed by waveguide, no topology surveys. line losses low enough in small arrays to be practical. maybe possible to make very good small corporate fed array. 180° feeding may be beneficial for elimination of higher order modes.
Triplate	low 0.1-0.2 λ_o 4x4 array≈ 3λ_o side 8x8 array ≈ 6λ_o side	2 or 3 high precision photolithography etched thin film layers. possibly 1 stamped thin metal sheets. lamination of these layers and interleaving foam sheets onto metal plate	high aperture efficiency & good impedance bandwidth	no simple centre feeding by waveguide. PPM suppression and management techniques well known but not fully understood. 180° feeding maybe beneficial for elimination of higher order modes. parasitic patches and underlying cavities worthy of further investigation for aperture efficiency enhancement
Short backfire antenna	medium 0.5-0.6 λ_o 1 unit ≈ 2.5λ_o side	subreflector etched on thin dielectric substrate overlaying cast metal block with inset cavities	high aperture efficiency & impedance bandwidth might be sufficiently wide	no wide ranging structural survey. little work on shaping the main reflector. chokes and liners not well understood. need to investigate shapes more amenable to casting
Anulus	medium 0.75-1.0 λ_o 1 unit ≈ 4.9λ_o side	presently complex; 4 metal rings & 4 foam o-rings sitting in insets in cast plate	high aperture efficiency & wide impedance bandwidth	manufacture needs simplification. no topology surveys

1.5.1 Conclusions

A brief review of the present literature on millimetre wave planar array antennas has identified the need for an oversized, high efficiency, high directivity planar radiating element, which will be fed by rectangular waveguide. Specifically, a linearly polarised element having 1-3 λ_o side is sort that has 10% bandwidth on impedance and high aperture efficiency, null placement for grating lobe suppression or some other technique for grating lobe suppression. Many of the array element candidates identified have not been investigated rigorously to identify the effects of most parameters, thus the undertaking of such parametric studies is of some value. The four potentially most promising technologies with comments on possible research directions are summarised in Table 1.3. Many commercial software tools have recently become available which are suited to the undertaking of such parametric studies.

In summary, a linearly polarised, 30dBi gain, 30GHz antenna array with 10% bandwidth is required for a modern application. A number of suitable array element types have been introduced, and will be investigated within the setting of a large array environment using modern commercial software and experimental techniques, which has not been done previously. There is also scope for the design of novel planar antennas built up about open waveguide mouths.

CHAPTER 2: Microstrip subarrays for wideband operation

2.1 Introduction

As described in Chapter 1, there is a need to develop 2.5-3.5λ_o sided, planar, linearly polarised, waveguide fed sub-arrays or large diameter array elements for use in LMCS band high gain arrays. Single layer microstrip array is the lowest profile candidate for this application, and requires only one step etching as the elemental radiators and feed network are on the same layer of copper pattern. There is no need for costly, yield lowering alignment or bonding of laminar layers. Also, there is sufficient space between the microstrip patch radiators at the optimal spacing for highest directivity ($\approx 0.75\lambda_o$) to allow the use of parallel/corporate feed networks which deliver equal power amplitude and phase to all array elements irrespective of frequency. This satisfies the need for 10% bandwidth at LMCS band. As identified in Chapter 1 from the work of Weiss [15] and Ashkenazy [55], there are two aspects of waveguide fed microstrip arrays that require improvement. These are to increase the gain bandwidth of the microstrip arrays and the development of a easily-constructed waveguide to microstrip transition. This chapter is focused on increasing the gain bandwidth, while the transition and its effects upon the microstrip subarray are left for future work. The gain bandwidth was increased by using non-radiating edge fed (NRE) patches [71,72,181] instead of the conventional radiating edge fed (RE) patches [15,55] within the microstrip arrays. The present work was a continuation at LMCS band from work undertaken by the author and a post-doctoral fellow at 12GHz [181].

An initial study of NRE patch aspect ratio influence upon cross-polar radiation levels by prior investigators was only done for dielectric substrates of the order of a few hundredths of a

wavelength thick using the theoretical cavity model [71]. In the current work, it was necessary to use a substrate about $\lambda_g/10$ thickness to obtain good input impedance bandwidth and to allow sufficient spacing between each 1x2 pair of patches for two impedance transformers. A NRE patch side length aspect ratio study using IE3D for the thicker substrates showed that, as with the thin substrates [71], an aspect ratio of about 1.5 produced the lowest cross-polarised radiation.

As the boresight cross-polarised radiation levels of NRE patches on the thick substrate was found to be relatively high, two methods of cross-polar level reduction were trialed in the corporate fed 2x2 subarrays of NRE patches. Both opposed patch 1x2 arraying and 180° feeding were found to be successful, but both generated 2^n grating lobes due to non-identical excitation of neighbouring patches, as previously noted from probe fed RE patch arrays [65]. These grating lobes proved to be the determining factor in the scaled directivity (gain + mismatch loss) bandwidths of the NRE patch arrays. Where the grating lobes were successfully suppressed by careful null placement in the 2x2 subarray radiation patterns, reasonably wide bandwidth scaled directivity was obtained. Where nulls were improperly placed, the bandwidth was narrowed due to the loss in directivity due to the high level of the grating lobes. The best experimentally tested NRE 4x4 patch subarray gave of the order of 75% aperture efficiency between 28.5 and 29.5GHz, which are considered to be excellent results in comparison to those obtained by previous investigators using RE patch arrays [15, 55].

Thus, NRE microstrip patches were investigated on practical thick substrates, and successfully used within both small and medium sized arrays at LMCS band. Some of the peculiarities of using NRE patches within single layer, corporate fed arrays were gleaned, such as creation of a second input impedance resonance when neighbouring 1x2 subarrays were fed through a pair of $\lambda/4$ transformers. In addition to the scientific value of these findings, the

methodology to be presented was that of a logical and consistent procedure for the design of a successful large scale microstrip patch array.

2.2 Non-radiating edge fed microstrip patches for LMCS subarray

The study of various radiating edge (RE) and non-radiating edge (NRE) fed 12GHz 4x4 patch arrays [181] showed that higher directivity and better radiation pattern shape fidelity across 10% bandwidth can be obtained with the NRE designs. Thus the NRE patch arrays were chosen for further investigation as LMCS band subarrays. The radiation pattern characteristics of NRE patches, both singularly and as small array elements, were investigated in this section using the commercially available MOM software Zeland IE3D™.

The work of previous investigators showed that a NRE patch side length aspect ratio of about 1.5 gave the lowest cross-polar radiation from a single patch on a substrate a few hundredths of λ_o thick [72, 73]. That study used the theoretical cavity model. Unfortunately, the cavity model was not used to identify the modes on the NRE patch responsible for generation of the cross-polar radiation, which would have given some physical insight into the operation of this type of microstrip radiator. Also, although expected, there was nothing in the open literature to indicate that the 1.5 patch side length aspect ratio applies to NRE patches on thicker dielectric substrates. Thicker substrates were necessary to obtain wider input impedance bandwidths [58, 59], and to allow sufficient spacing between each 1x2 pair of patches for two impedance transformers. Thus, undertaking a theoretical or numerical study of NRE patches on practical substrates, 0.05-0.1λ_o thick, would be of some value, and it was necessary to do such a study before using these patches in a large array.

Three NRE patches were designed for use in six 4x4 array types, Tables 2.2 & 2.5. The patches of D and H suffix array types were identical, and are referred to as the D/H patch when the patches were considered singularly. The "E" and "F" prefixes were used to distinguish 180° physical and electrical or in-phase feeding of the 1x2 subarrays within each 2x2 subarray, Figure 2.10. A 100Ω characteristic impedance (0.31mm wide) microstripline was used for the feed networks, and the arrays were built on (or simulated with) 0.397mm thick Arlon Diclad substrate (ε_r=2.5). Where three 100Ω microstrip lines met at a T-junction, a 70.7Ω $\lambda/4$ impedance transformer was used. For all IE3D models the segmentation was 10 cells per λ_o at 31GHz, with 0.05mm edge elements.

The commercially available Method of Moments numerical tool IE3D was used to confirm the existing theory relating single NRE patch aspect ratio to cross-polar radiation performance, and to relate that to the radiation performance of the type E and F 2x2 subarrays.

2.2.1 Numerical assessment of patch aspect ratio

The length to width aspect ratio of a NRE patch was theoretically shown by prior investigators to be a critical parameter for reducing the cross-polar radiation level [72]. A theoretical approach was successful because the dielectric substrate was only 3.2% of λ_d thick. The substrate used for the three NRE patch designs here was 5.8% of λ_d at the lower end of the bandwidth studied (27.8GHz) and was 6.5% of λ_d at the upper end (30.8GHz). The commercially available numerical tool IE3D, which was used to model the full 4x4 subarrays, was used here to study the effects of NRE patch aspect ratio upon cross-polarised radiation over 10% bandwidth.

The IE3D models used for the aspect ratio study consisted of a rectangular polygon, with a 0.05mm edging of fine cells to accurately model the high currents on the edges of the patches and a localised source placed at the feed point on one of the NRE sides of the patch under consideration, Figure 2.1. Three patch designs were studied, each having a different resonant length L, Table 2.1. The length (L) and feed positions (f) of patches A, D/H and M were fixed. These dimensions were as specified in Table 2.1. The patch width (W) for each of the three designs was varied from L-2L in 0.3mm steps, with the peak cross-polarised component of the H-plane radiation patterns for the three frequencies of interest been noted. The cross-polar characteristics of the three patches across the three frequencies all showed similar behaviour to that observed by Ohberhart [72], Figures 2.2-2.4. For aspect ratios of about 1 and 2, the cross-polarised level was roughly equal to the co-polarised. For an aspect ratio in the range 1.4-1.6, the cross-polarised radiation was at its lowest level with respect to the co-polarised radiation, Figures 2.2-2.4. Thus, the general trend observed by Ohberhart [72] was found to hold true for a thicker substrate and across 10% bandwidth. However, the lowest cross-polarised component achieved here was not as low as that found on the thinner substrates. The lowest cross-polarisation level here was about −17dB whereas −21dB was achieved by Ohberhart [72], Figures 2.2-2.4. This shows that the cross-polarisation level was higher for thicker substrates.

For patch design A, the lowest H-plane peak cross-polar radiation levels occurred between aspect ratios of 1.35 and 1.5 across the 10% bandwidth studied. The lowest cross-polarised component occurred at 27.8GHz for 1.5, then at 1.425 for 29.3GHz and at about 1.35 for 30.8GHz, Figure 2.2 & Table 2.1. For this patch, the minimum achievable cross-polar level worsened with increasing frequency across the LMCS band. Shortening the patch length L from 3.1 to 3.0mm (changing from patch design A to D/H; Table 2.1) had the effect of moving the aspect ratios for

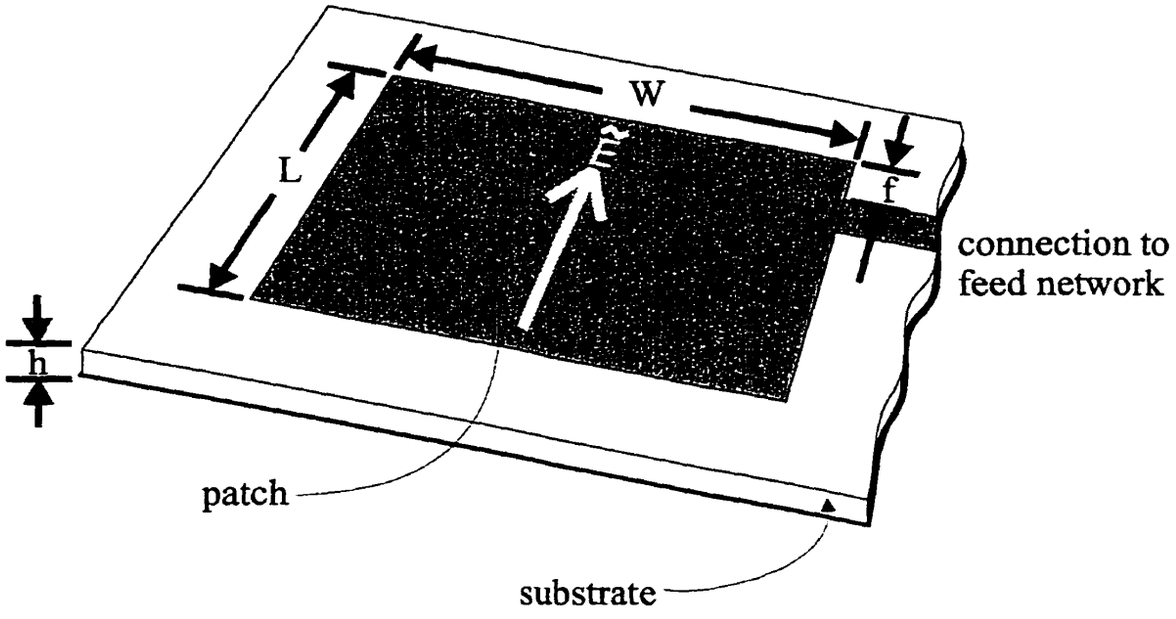

Figure 2.1: Geometry of a NRE microstrip patch antenna.

Table 2.1: Summary of single patch aspect ratio study.

Patch	L (mm)	Minimum peak cross-polarisation level at frequency with lowest peak cross-polarisation levels			Minimum peak cross-polarisation level at frequency with highest peak cross-polarisation levels		
		frequency (GHz)	level (dB)	aspect ratio	frequency (GHz)	level (dB)	aspect ratio
A	3.10	27.8	-15.8	1.5	30.8	-7.6	1.4
D/H	3.00	27.8	-18	1.55	30.8	-9.6	1.4
M	2.90	29.3	-17	1.5	30.8	-12	1.4

complementary to Figures 2.2-2.4

Table 2.2: Dimensions of LMCS band NRE microstrip patches.

Patch	L (mm)	W (mm)	Aspect ratio	f (mm)
A	3.10	4.48	1.44	0.36
D/H	3.00	4.48	1.50	0.31
M	2.90	4.38	1.52	0.26

dimension f determined by input impedance matching of patch in a 4x4 array

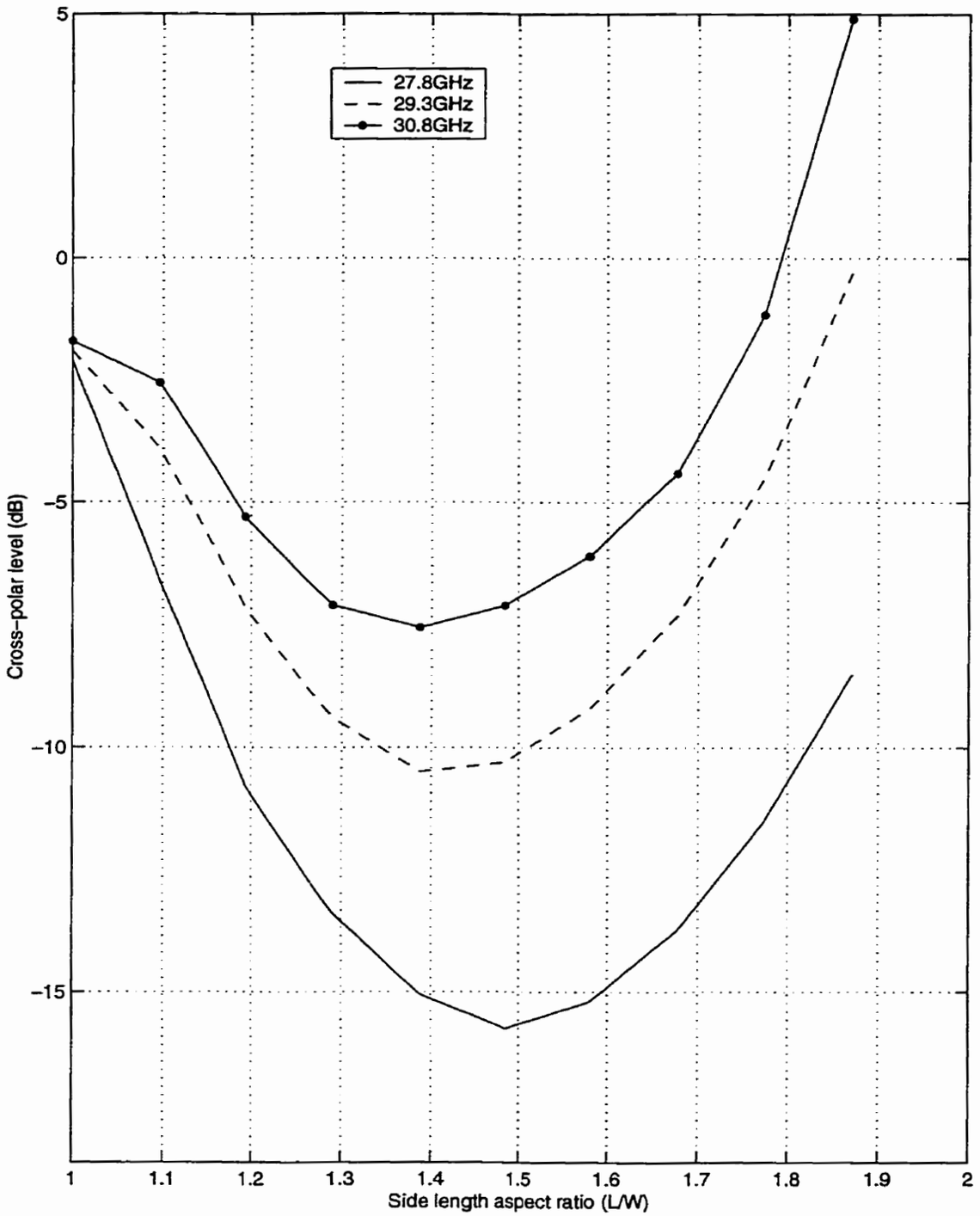

Figure 2.2: Effect of NRE patch aspect ratio upon single patch H-plane cross/co-polar ratio using IE3D (design A).

patch resonant length (L) & feed position (f) from Table 2.2

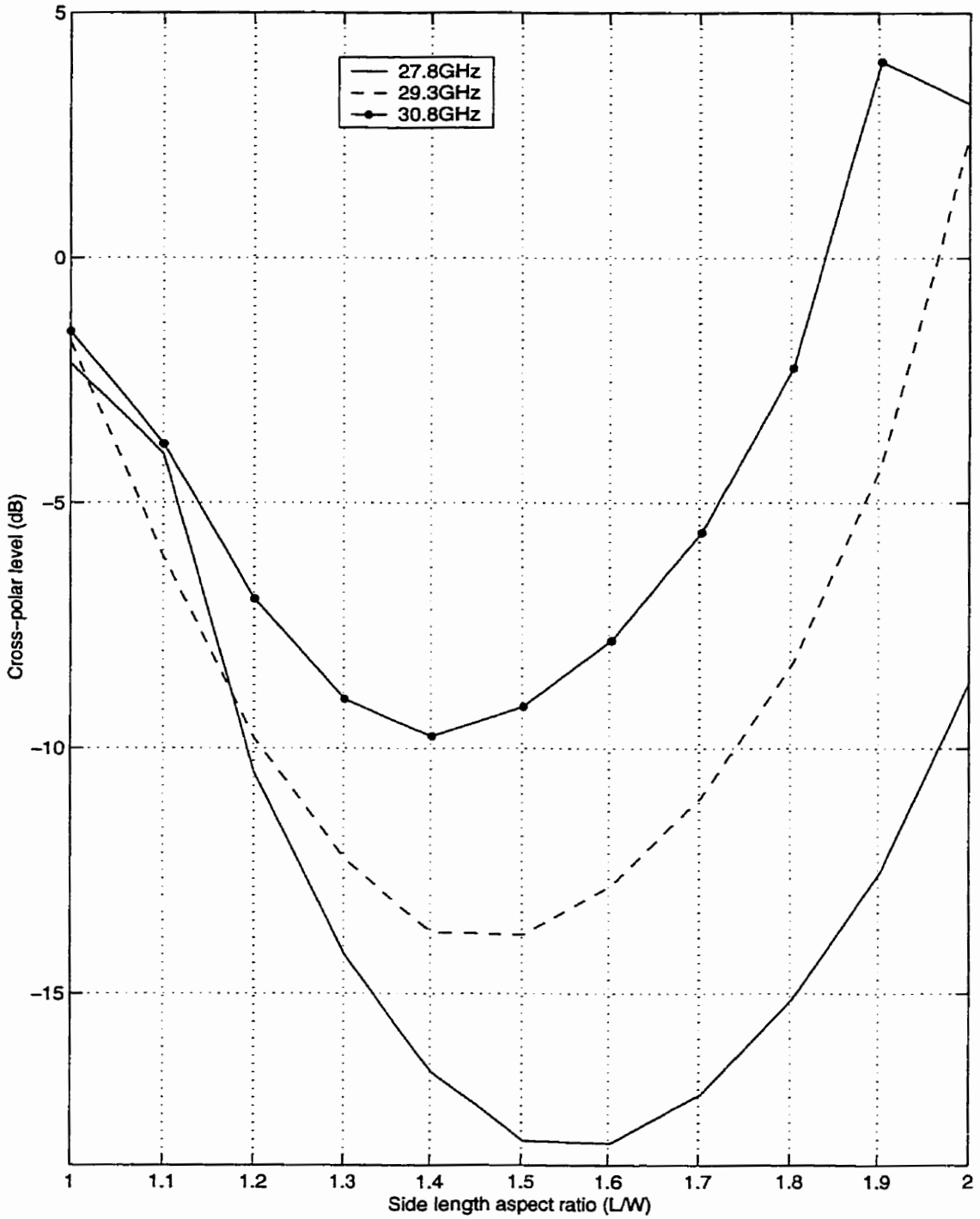

Figure 2.3: Effect of NRE patch aspect ratio upon single patch H-plane cross/co-polar ratio using IE3D (design D/H).

patch resonant length (L) & feed position (f) from Table 2.2

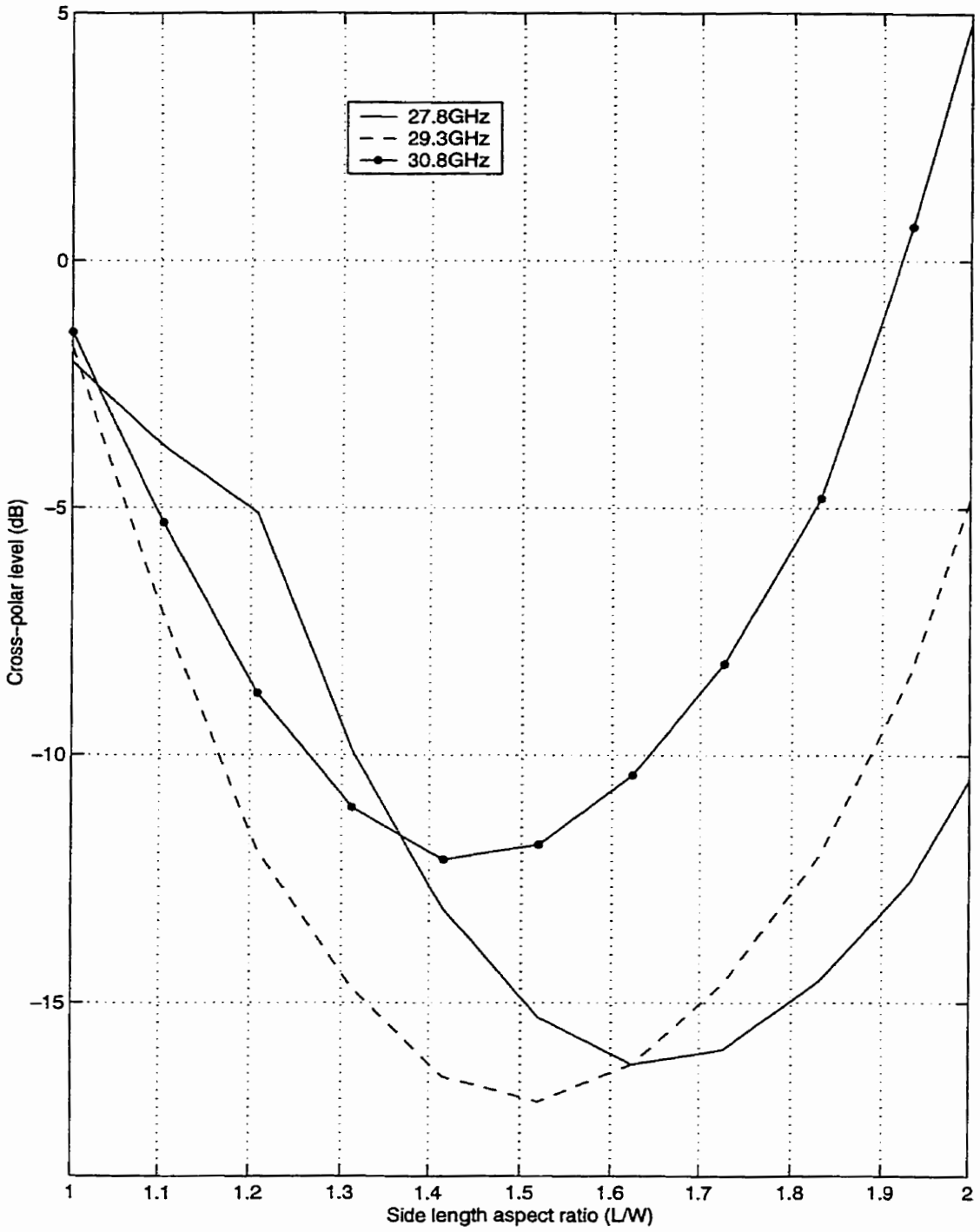

Figure 2.4: **Effect of NRE patch aspect ratio upon single patch H-plane cross/co-polar ratio using IE3D (design M).**

patch resonant length (L) & feed position (f) from Table 2.2

which the minimum cross-polarised component occurred to slightly greater aspect ratio values, Figure 2.3. Also, the minimum cross-polarisation level was overall decreased by about 2.5dB. Thus, patch type D/H gave lower cross-polarisation levels than type A across the LMCS band. These differences affected the performance of the 4x4 arrays discussed below. With L further shortened to 2.9mm, and the feed point moved yet closer to the nearest corner for input impedance matching purposes within a 4x4 array, patch type M gave its lowest cross-polarisation levels at 29.3GHz, Table 2.1 & Figure 2.4. With the lowest cross-polarisation at the centre of the band (29.3GHz), the extremities (27.8 and 30.8GHz) also gave low minimum cross-polarisation levels, Figure 2.4. Thus the patch with the shortest L of the three patch lengths studied gave the best overall low H-plane cross-polarisation levels. The optimal W for each of the three designs (A, DH and M) were chosen based upon a compromise between cross-polarisation level across the entire 10% bandwidth. However, it should be noted that the best NRE patch cross-polarisation performance here of −17.5dB is relatively high. This dictates the use of further cross-polarisation reduction techniques such as paired 1x2 arrays and 180° feeding when using NRE patches in an array. In subsequent subsections, the effects of these two cross-polarised component reduction techniques are considered.

2.2.2 Effect of patch size and impedance transformers upon far field radiation of 1x2 arrays

The simplest grouping of NRE patches within a large array environment was as 1x2 subarrays, Figure 2.5. Each 1x2 subarray consisted of a pair of identical NRE patches, arranged in the H-plane direction, which were fed on the inner NRE patch sides, Figure 2.5. This feeding arrangement was expected to put the TM_{01} and TM_{02} modes on each patch in phase opposition to its partner, creating a cross-polarised component null at boresight in the H-plane [181, 187, 188].

This was shown to be the case in the experimental results obtained by Ohberhart with both patches of aspect ratio 1 and of 1.5, Figure 3 of [72], although it was not commented upon at the time. The feeding method used for the 1x2 subarrays by prior investigators involved placing a very short length of microstrip feedline to connect the feeding points on the inner edges of the two NRE patches [72, 81]. The centre of the short microstrip feedline then connected to the remainder of the feed network. Here the H-plane spacing was increased considerably to about $0.75\lambda_o$, which was the patch to patch spacing giving the highest achievable directivity. This allowed incorporation of a pair of $\lambda/4$ (or similar impedance) transformers to feed each of the patches [181], Figure 2.5. This overcame the feed network crowding problem due to too small a patch spacing, Figure 1 of [81]. However, the presence of the impedance transformers between the patches fixed the 2T dimension. Each transformer was to match the 50Ω input impedance of each patch to 200Ω. With the 200Ω impedance from each of the two patches connected in parallel, the input impedance to each 1x2 was 100Ω, matching the characteristic impedance of the remainder of the corporate feed network. In this subsection, the H-plane radiation patterns of the 1x2 subarrays of the three NRE patch designs, with and without the $\lambda/4$ transformers, are discussed.

The IE3D H-plane radiation patterns of the four 1x2 subarrays built from the three NRE patch designs are discussed in this subsection. A 1x2 subarray was made using each of the patch types A and M, while the remaining two 1x2 subarray designs both used patch D/H, Table 2.3. The only difference between 1x2 subarray designs D and H was in the H-plane spacing, Table 2.3. The H-plane patch spacing of design H was 26% less than that of design D. Any differences between the two subarrays would be the result of that one dimensional difference. The input impedance of all four 1x2 subarray designs were matched within a full 4x4 array setting using IE3D. During this process, the two well matched designs using patch D/H were found. This

accounted for the effects of mutual coupling between patches and patch to feedline interaction. The input impedance is discussed in section 2.3.2.

The H-plane radiation patterns, Figures 2.6-2.9, of the four 1x2 subarrays across the three frequencies studied have many common features. The cross-polarised component always had a null at boresight showing the value of opposed feeding on the inner NRE edges of each 1x2 pair of patches. Thus, the radiation from the TM_{01} mode on each patch had equal amplitude, but opposite phase, to that from the other patch of the pair, as a result of the structural symmetry, Figure 2.5. In the far field at boresight, where the path length was identical, the radiation from the cross-polarisation modes added destructively to produce the null, Figures 2.6-2.9. Introduction of the transformers decreased the cross-polarised component peak about 20-40° off boresight, but increased the cross-polarisation level at wider angles. This was expected as the currents on each transformer were 180° out of phase with the TM_{01} mode on its associated patch.

The co-polarised radiation patterns had a main lobe, with a null and sidelobe on either side, Figures 2.6-2.9. Sidelobe levels increased with frequency because the electrical spacing between the two patches increased with the shortening of the wavelength increasing grating lobe contribution.

Comparing types A and D, these two had identical patch width (W) and $\lambda/4$ transformers (2T), Table 2.3. The only difference was the patch length (L), which was shorter for patch D/H, which pushed the cutoff frequencies of modes TM_{02} a little higher than those of patch A. This gave 1x2 array D lower sidelobes and lower cross-polarised component than array A, across the three frequencies studied, Figures 2.6 & 2.7. Reducing spacing 2T (and consequently the transformers) by 26% gave 1x2 array H wider null positioning, and 5dB (at 27.8GHz) to 2dB (at 30.8GHz) lower sidelobe levels compared to subarray D, Figures 2.7 and 2.8. Shorter than $\lambda/4$ transformers

also gave a good input impedance match in a 4x4 array; a point to be discussed later. The shorter transformers did not decrease the cross-polarised component near boresight in design H as much as the full length $\lambda/4$ transformers did for design D. However, the wider angle cross-polarised component was much lower in design H at 30.5GHz, Figures 2.7 & 2.8. These results suggest that the shorter transformers did not radiate as much as the full length $\lambda/4$ transformers did. As with the single patch, the type M 1x2 subarray had its minimum cross-polarised component at 29.3GHz, Figure 2.9. Due to the further reduced W and L of patch design M, the type M 1x2 array gave the lowest sidelobe level of the four types. This was a near optimal design for operation across the entire 10% bandwidth required for LMCS.

The radiation patterns of the four 1x2 subarrays as modeled in IE3D were briefly discussed. Feeding the inner NRE edges of each 1x2 subarray pair of patches was shown to reduce the H-plane cross-polarised component about boresight due to the null. The use of shorter than $\lambda/4$ transformers and smaller H-plane spacing were shown to greatly improve the performance of one of the 1x2 subarrays. The patch design M was found to have produced a near optimal 1x2 subarray across the entire 10% bandwidth of interest. However, the cross-polarisation level was still above –20dB, where 10dB lower cross-polarised component would be expected of a RE patch array. Thus, further measures for cross-polarisation reduction such as 180° feeding were necessary. This technique is evaluated in the next subsection.

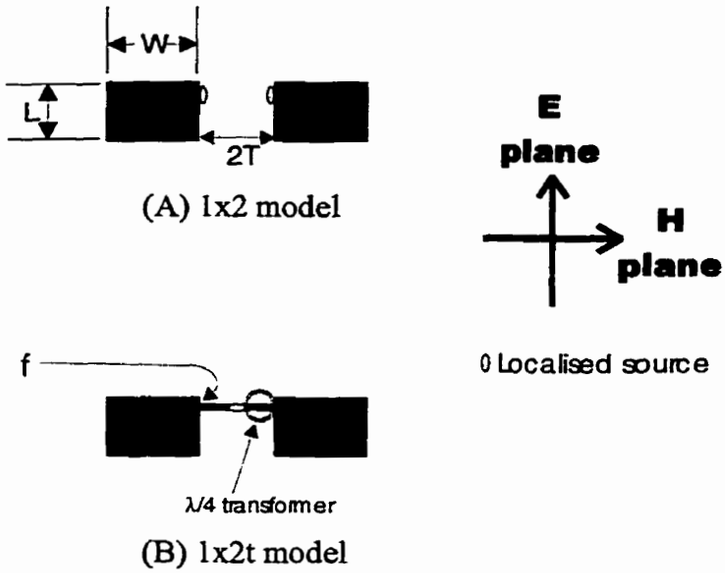

Figure 2.5: Geometries used for 1x2 array study

(A) "1x2" 1x2 dual-feed array,
(B) "1x2t" 1x2 single-feed array with associated impedance transformers

Table 2.3: Dimensions of 1x2 patch arrays

Array	patch type used	L (mm)	W (mm)	f (mm)	2T (mm)
A	A	3.1	4.48	0.36	3.82
D	D/H	3.0	4.48	0.31	3.82
H	D/H	3.0	4.48	0.31	2.82
M	M	2.9	4.38	0.26	3.32

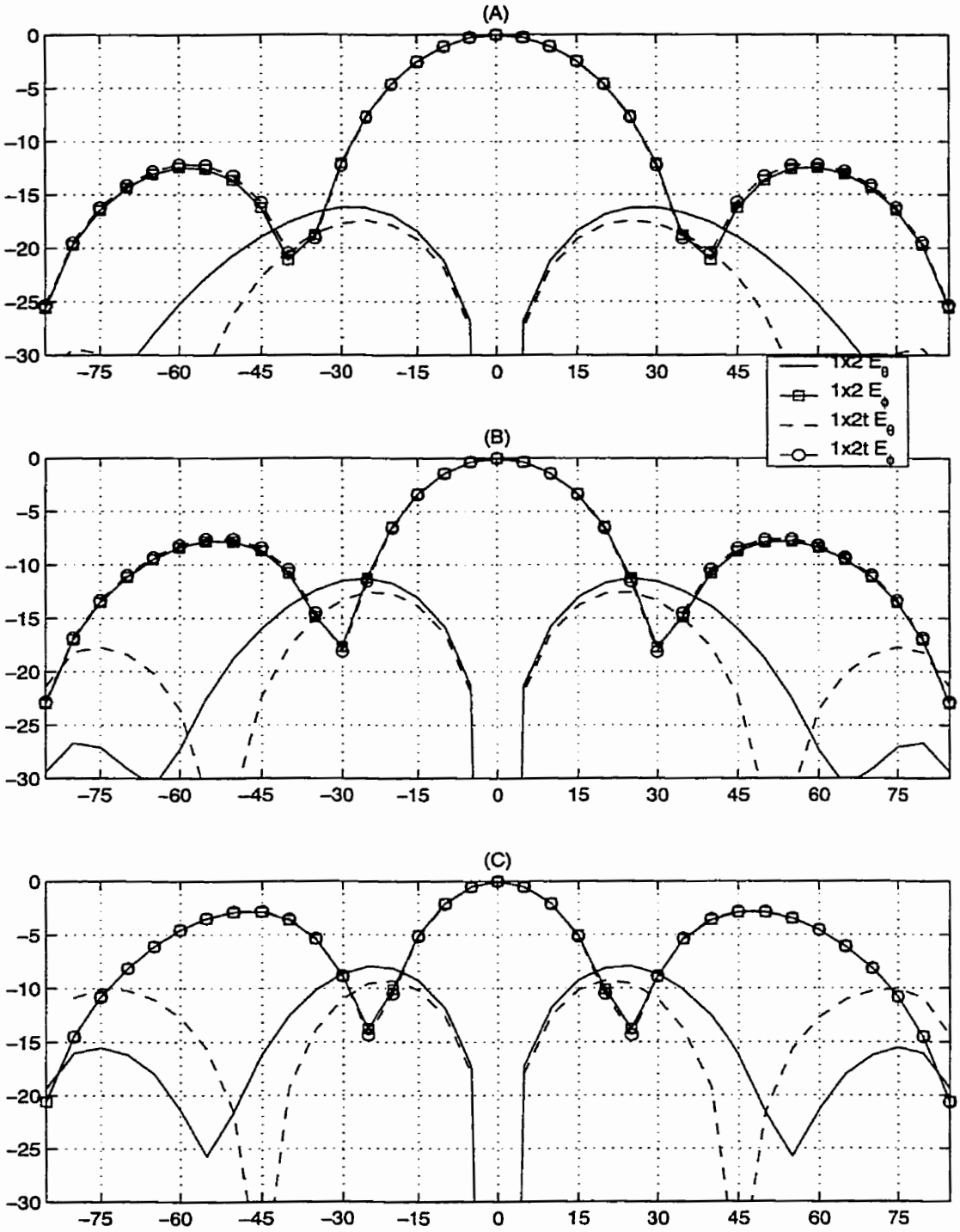

Figure 2.6: H-plane radiation patterns of type A 1x2 subarray using IE3D.

(A) 27.8GHz, (B) 29.3GHz, (C) 30.8GHz.
geometries from Table 2.3 & Figure 2.5
"1x2" 1x2 dual-feed array,
"1x2t" 1x2 single-feed array with associated impedance transformers

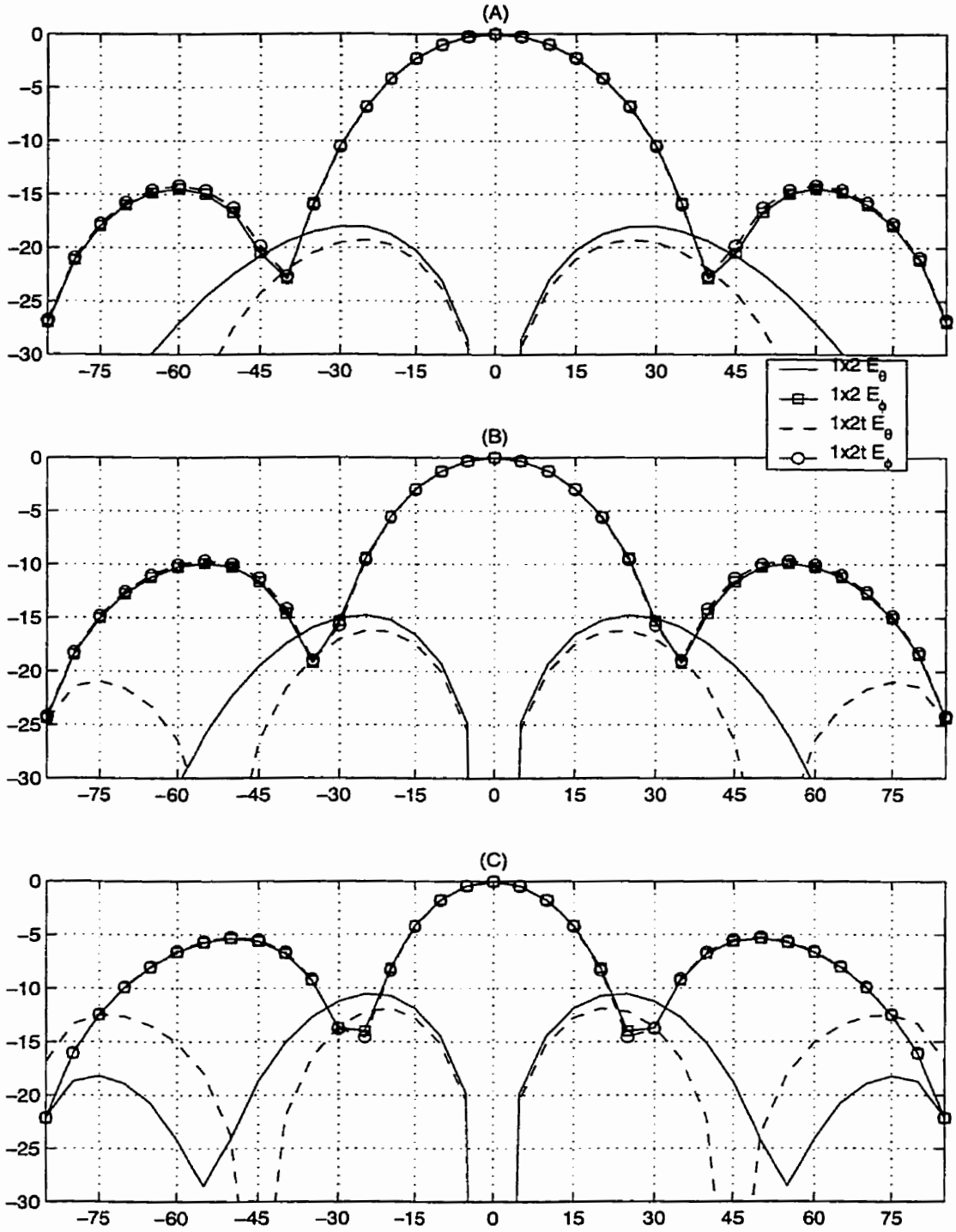

Figure 2.7: H-plane radiation patterns of type D 1x2 subarray using IE3D.

(A) 27.8GHz, (B) 29.3GHz, (C) 30.8GHz.
geometries from Table 2.3 & Figure 2.5
"1x2" 1x2 dual-feed array,
"1x2t" 1x2 single-feed array with associated impedance transformers
identical to geometry of Figure 2.6, except shorter patch length L

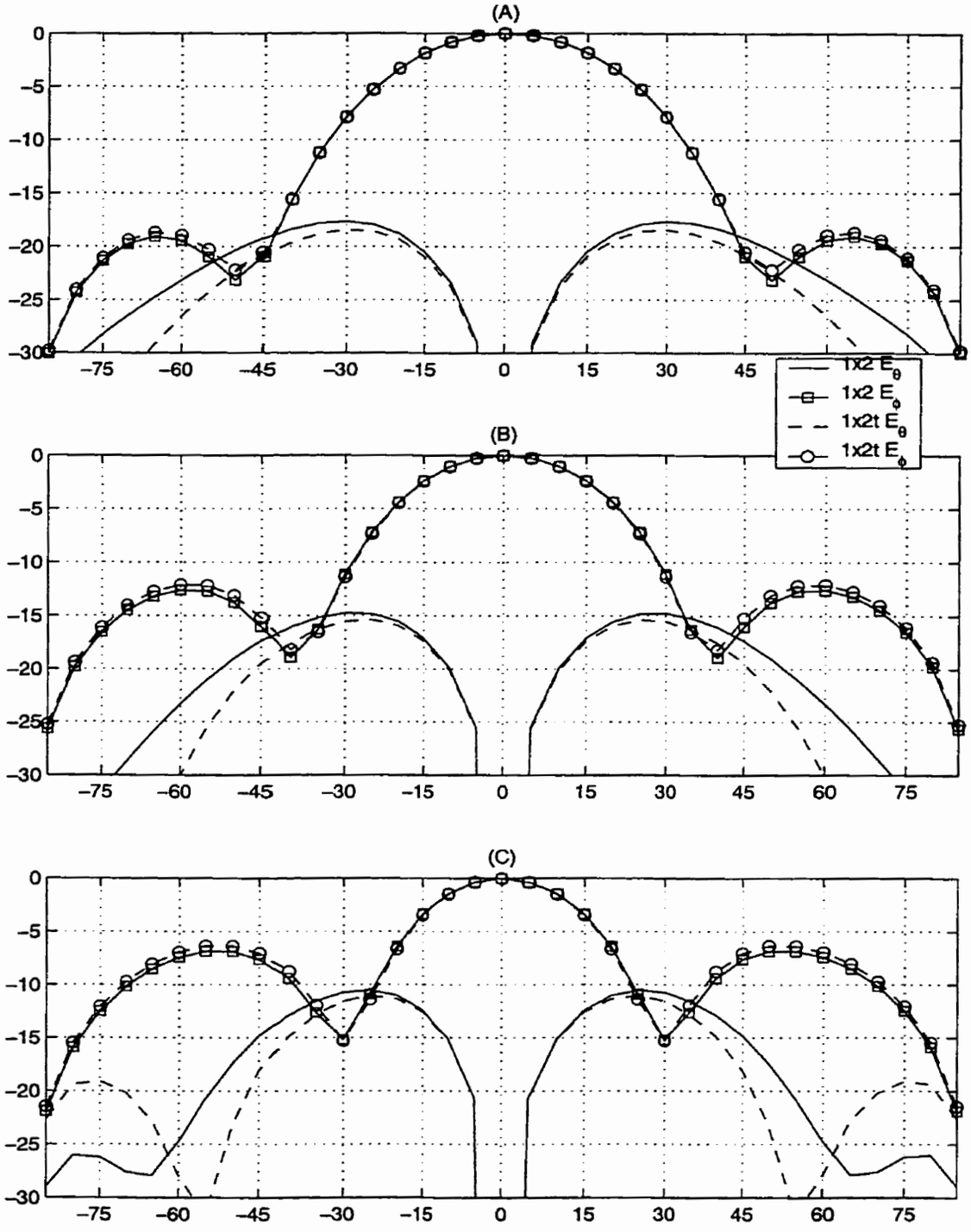

Figure 2.8: H-plane radiation patterns of type H 1x2 subarray using IE3D.

(A) 27.8GHz, (B) 29.3GHz, (C) 30.8GHz.
geometries from Table 2.3 & Figure 2.5
"1x2" 1x2 dual-feedarray,
"1x2t" 1x2 single-feed array with associated impedance transformers
identical to geometry of Figure 2.7, except shorter transformer length 2T

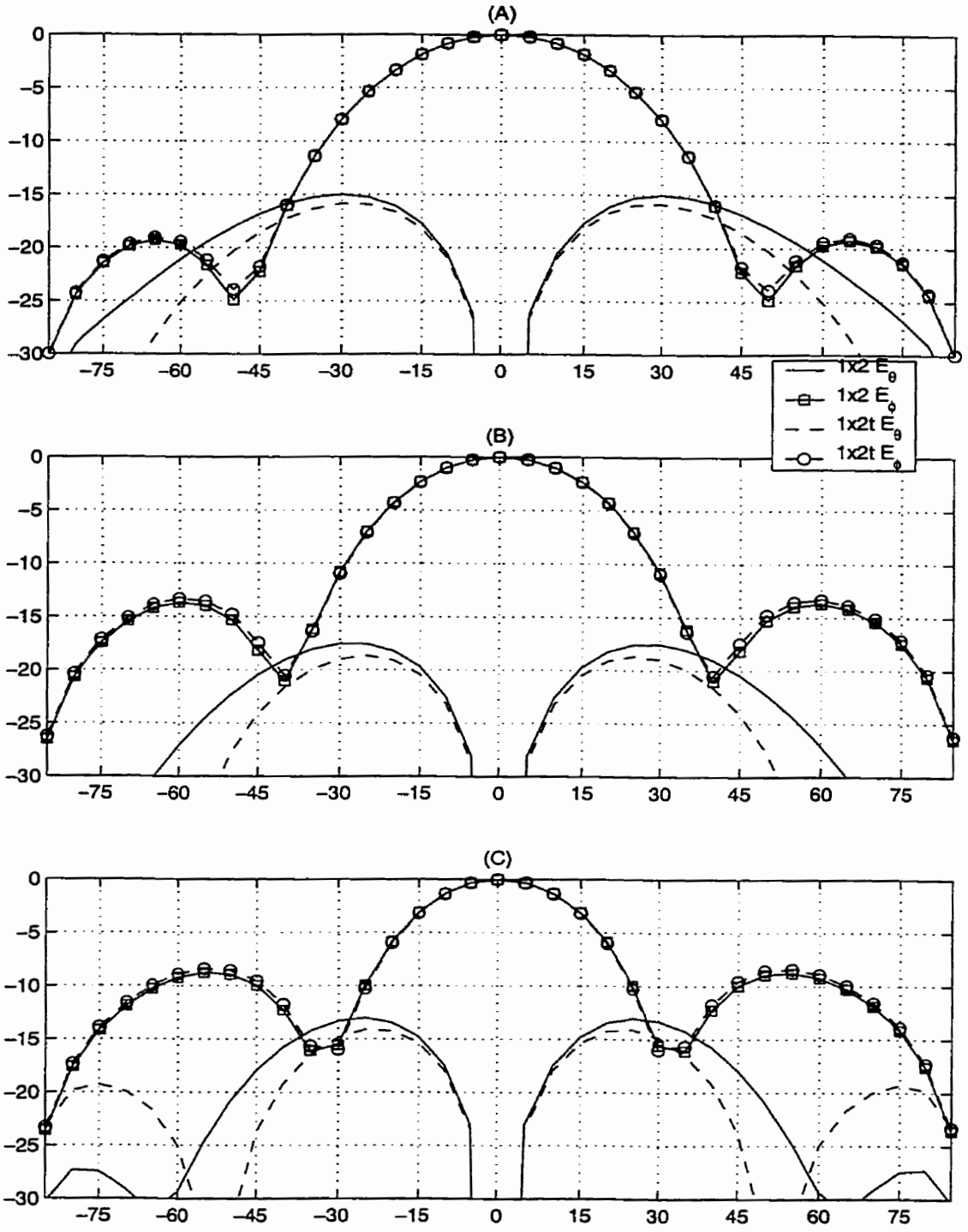

Figure 2.9: **H-plane radiation patterns of type M 1x2 subarray using IE3D.**

(A) 27.8GHz, (B) 29.3GHz, (C) 30.8GHz.
geometries from Table 2.3 & Figure 2.5
"1x2" 1x2 dual-feed array,
"1x2t" 1x2 single-feed array with associated impedance transformers

2.2.3 *Effect of different excitation schemes upon far field radiation of 2x2 arrays*

As noted in the previous subsection, the 1x2 NRE patch arrays had roughly 10dB higher minimum cross-polarisation levels than would be expected of RE patches. Thus, 180° electrical and physical excitation of the upper and lower 1x2 subarrays within each 2x2 array was examined here as a means of cross-polarised component reduction, especially in the H-plane radiation pattern. For brevity, only the type M 1x2 arrays were used. The only difference between the two 2x2 subarrays investigated here was the feeding technique used to excite the constituent 1x2 subarrays, and was thus the only factor responsible for the operational differences. IE3D was used to simulate the in-phase and 180° out of phase fed 2x2 arrays with and without the central feedline, Figure 2.10. Both E and H-plane radiation patterns from the three frequencies covering the 10% bandwidth of interest were examined.

Comparing the 2x2 arrays without the central feedlines, the co-pol radiation patterns of matching frequencies and planes from the in-phase and 180° fed were identical, Figures 2.11-2.14. This was not surprising as the two localised sources feeding to the transformer pair of each 1x2 subarray was ideally of an amplitude of 1 with a phase of 0° or 180° as appropriate. As a result the TM_{10} mode on each patch was perfectly in phase with its three fellows in either 2x2 array. This was noted by previous investigators for arrays of probe fed RE patches [65]. For the TM_{01} cross-polarisation mode there was a difference between the in-phase and 180° feeding to the 1x2 subarrays. With in-phase feeding, the TM_{01} modes on the patches and currents on the $\lambda/4$ transformers were symmetrically anti-phase in the H-plane, but in phase in the E-plane. This was a result of the structural symmetry in the E-plane and lack of symmetry in the H-plane, Figure 2.10A. This was shown in the H-plane where the cross-polarised component varied from −17dB to −13dB across the bandwidth studied, Figure 2.12. With 180° excitation of the 1x2 subarrays, the TM_{01} mode and transformer currents were symmetrically anti-phase in both E and H-planes, so the

cross-polarised radiation was suppressed below –25dB in the H-plane, Figure 2.14. So, in an ideal case, 180° physical and electrical feeding of the 1x2 subarrays within each 2x2 subarray had the advantage over in-phase excitation of reducing the cross-polarised component in the H-plane by more than 10dB. In the E-plane, for either excitation type, the cross-polarised component also cancels as the TM_{01} and transformer currents of each individual 1x2 subarray were symmetrical but antiphase in the H-plane, and thus the cross-polarised component was suppressed, Figures 2.12 & 2.14. However, it was not practical to feed every 1x2 subarray with a perfect source, and the introduction of the central feedline to each 2x2 subarray caused the radiation patterns to deviate from the ideal cases discussed here.

Introduction of the central feedline to the 2x2 subarrays affected the performance of both in-phase and 180° types. For the in-phase fed array type, the major effect of the introduction of the central feedline was in the E-plane, Figures 2.10 & 2.11. For the 180° fed type, the changes were in both E and H-plane radiation patterns, comparing the results of the 180° fed 2x2c and 2x2, Figures 2.13 & 2.14. The E-plane radiation patterns were no longer symmetrical, with the main lobe peak scanned up to 7.5° at 30.8GHz.

The sole function of the central feedline in the in-phase fed 2x2 arrays was to deliver equal amplitude and phase to the upper and lower 1x2 subarrays, Figure 2.10A. Addition of the central line (structure 2x2 to 2x2c of Figure 2.10A) caused the E-plane main lobe peak to scan 4° off boresight at 27.8GHz, Figure 2.11A. The E-plane sidelobes at all frequencies became asymmetric upon addition of the central feedline, Figure 2.11. There were no major changes in the H-plane patterns, Figure 2.12. The only asymmetry along the length of the central feedline, which could have caused the delivery of unequal amplitude and phase to the upper and lower 1x2 subarrays, was that the central line passes between the patches of the upper 1x2 subarray but not the lower,

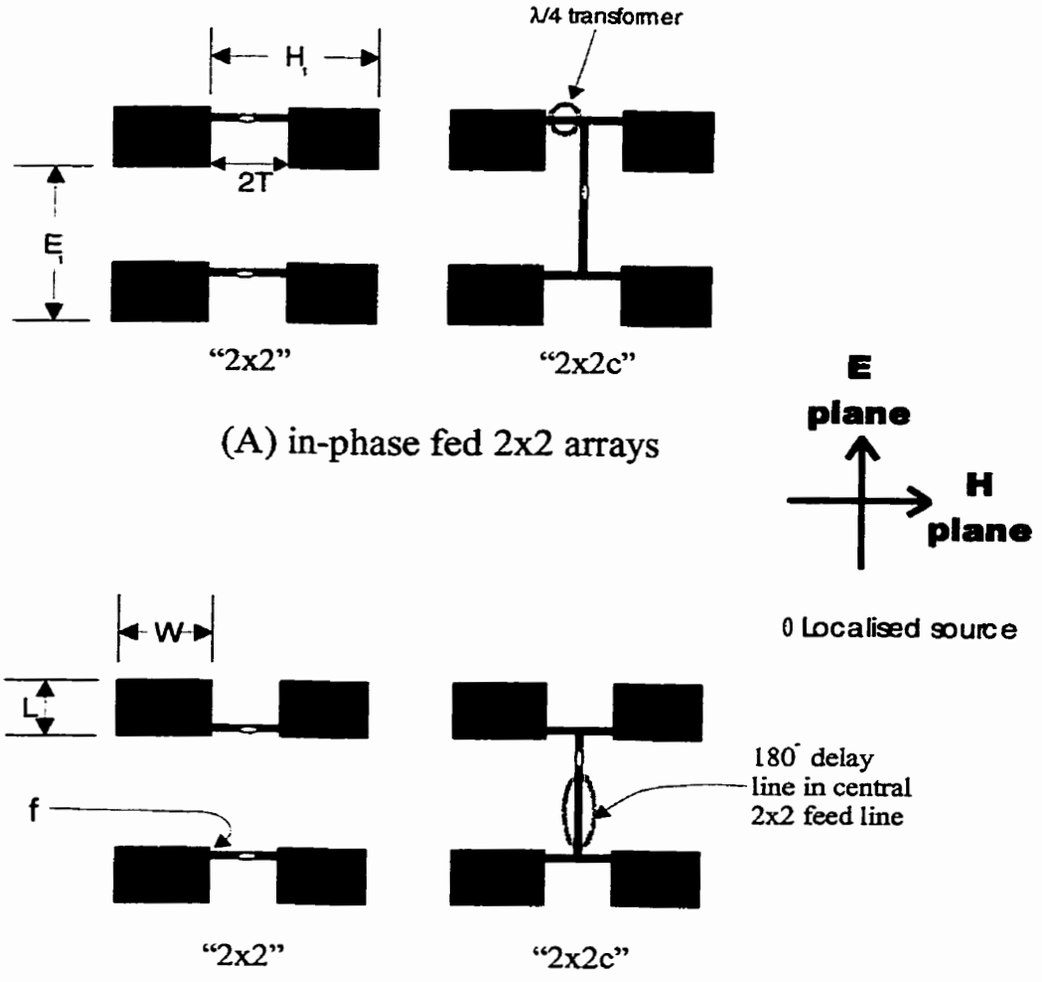

Figure 2.10: Geometries used for 2x2 array study

Table 2.4: Dimensions of 2x2 patch arrays

Array	Patch type used	L (mm)	W (mm)	2T (mm)	E_1 (mm)
in phase 2x2	M	2.9	4.38	3.82	8.73
in phase 2x2c	M	2.9	4.38	3.82	8.73
180° 2x2	M	2.9	4.38	3.32	8.73
180° 2x2c	M	2.9	4.38	3.32	8.73

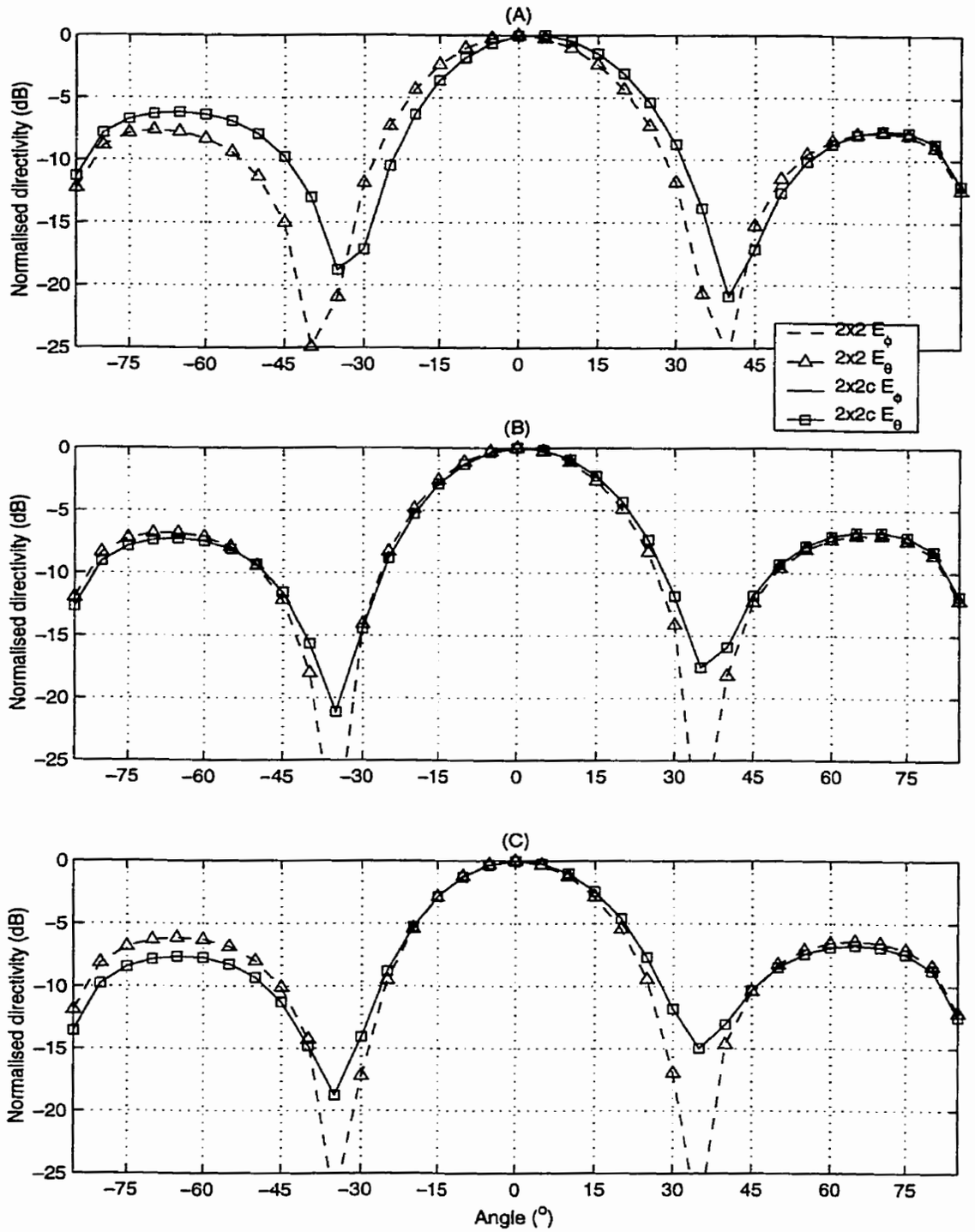

Figure 2.11: E-plane radiation patterns of in-phase fed 2x2 subarray.

(A) 27.8GHz, (B) 29.3GHz, (C) 30.8GHz.
"2x2" 2 of 1x2 subarrays, with individual sources
"2x2c" full 2x2 with central feedline, to which source was attached
patch dimensions and spacing taken from Table 2.4

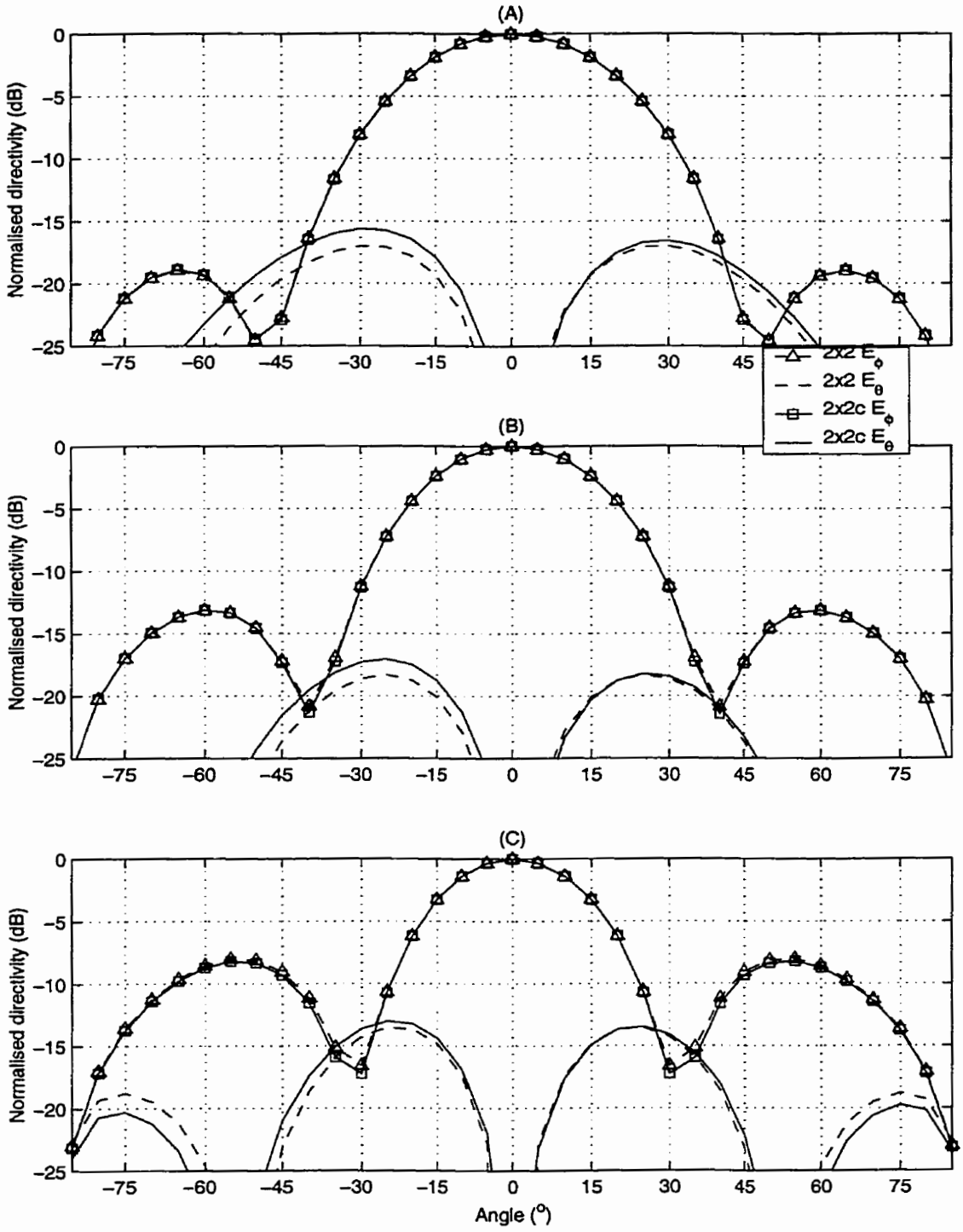

Figure 2.12: H-plane radiation patterns of in-phase fed 2x2 subarray.

(A) 27.8GHz, (B) 29.3GHz, (C) 30.8GHz.
"2x2" 2 of 1x2 subarrays, with individual sources
"2x2c" full 2x2 with central feedline, to which source was attached
patch dimensions and spacing taken from Table 2.4

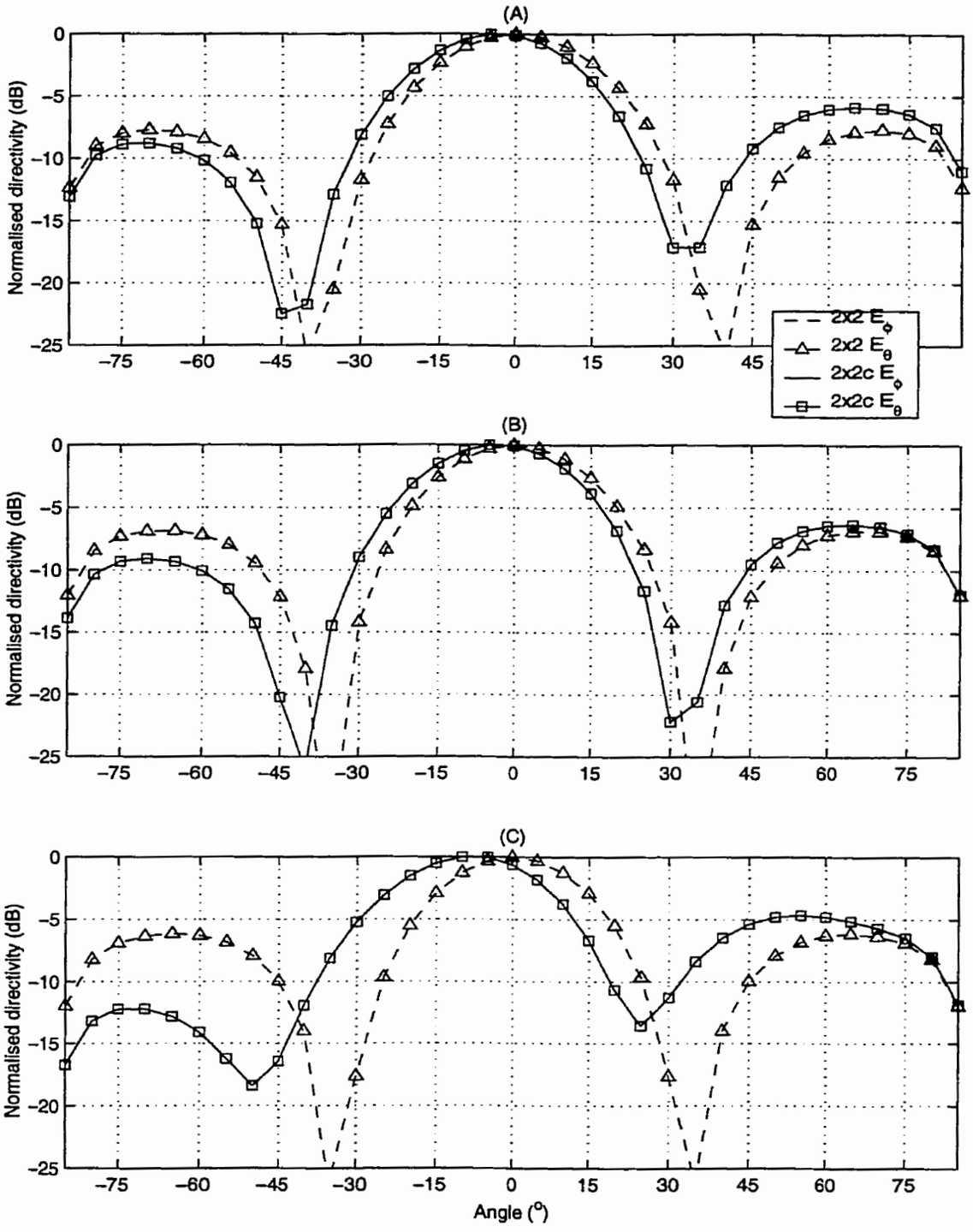

Figure 2.13: E-plane radiation patterns of 180° fed 2x2 subarray using IE3D.

(A) 27.8GHz, (B) 29.3GHz, (C) 30.8GHz.
"2x2" 2 of 1x2 subarrays, with individual sources
"2x2c" full 2x2 with central feedline, to which source was attached
patch dimensions and spacing taken from Table 2.4

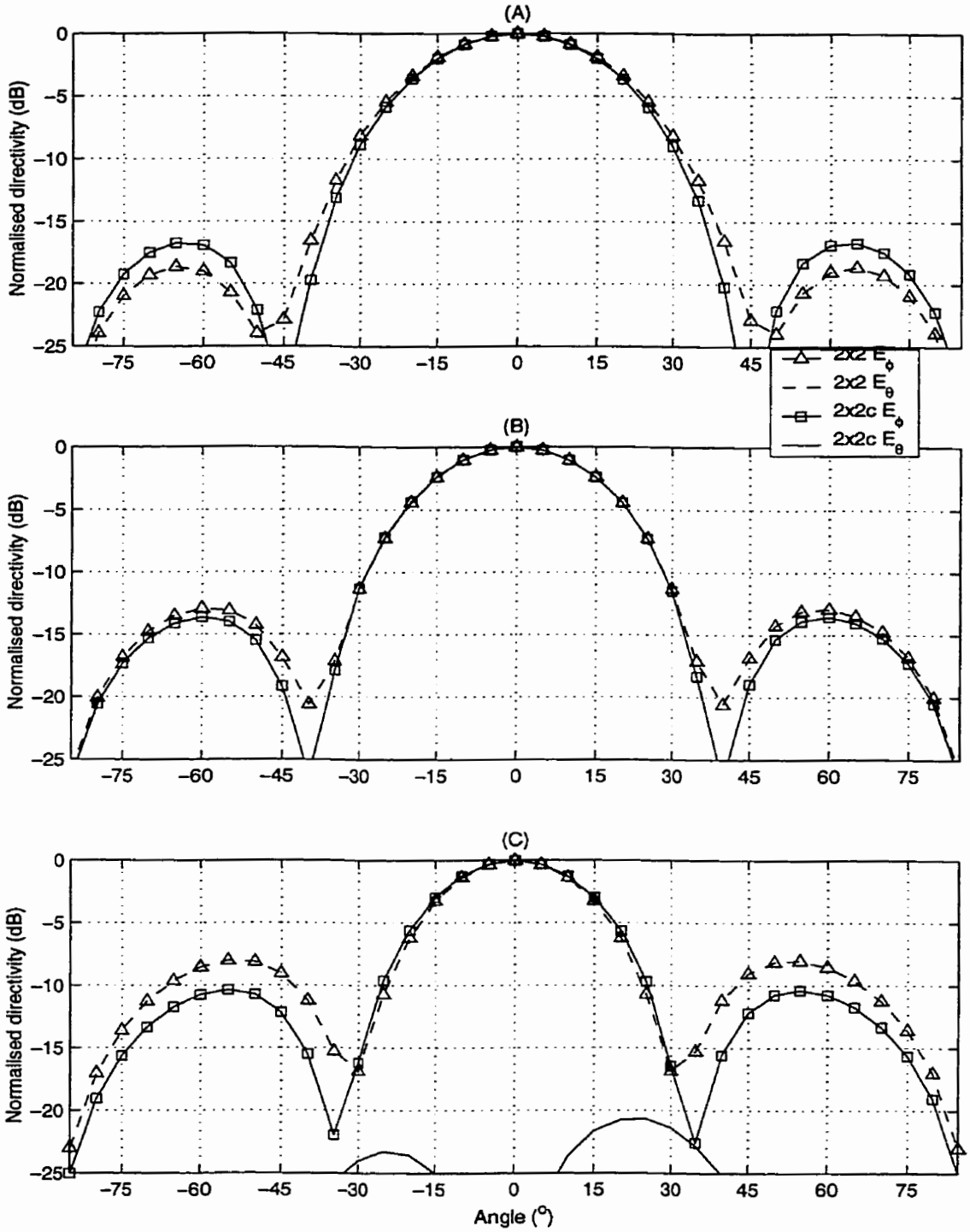

Figure 2.14: H-plane radiation patterns of 180° fed 2x2 subarray using IE3D.

(A) 27.8GHz, (B) 29.3GHz, (C) 30.8GHz.
"2x2" 2 of 1x2 subarrays, with individual sources
"2x2c" full 2x2 with central feedline, to which source was attached
patch dimensions and spacing taken from Table 2.4

Figure 2.10A. The feedline running between the two patches either affected the mutual coupling between those patches and/or enabled coupling between the line and the patches. The E-plane radiation patterns of the in-phase fed 2x2 above 29.3GHz were nearly symmetrical about boresight, although the nulls filled in with increasing frequency, Figure 2.11.

The central feedline in the 180° fed 2x2 array had two functions; not only to deliver equally split power to each 1x2 subarray but to also introduce the required 180° phase delay, Figure 2.10B. However, a microstrip delay line can only introduce a 180° phase delay at one frequency (28GHz here), and for all others there was a phase error. In the E-plane, the phase error scanned the mainlobe off boresight, made the sidelobes asymmetric and moved the nulls. Each E-plane null was scanned a different amount by the phase error at each of the three frequencies studied, Figure 2.13. Where the phase error on the microstrip delay line of the 180° fed 2x2 array was detrimental for the E-plane pattern performance compared to the ideal case, in contrast it caused a lowering of the H-plane sidelobes above 27.8GHz, and a deepening of the H-plane nulls across the entire band studied. Thus, the phase error on the 180° microstrip delay line away from its design frequency had beneficial affects upon the H-plane radiation patterns.

2.2.4 Summary of NRE patches and small arrays

Three slightly different NRE patches were evaluated as single elements and as small array elements using the commercially available MOM software Zeland IE3D™. This initial numerical study showed the effect of NRE patch side length aspect ratio on minimum peak cross-polarised component noted by prior investigators held for the thicker dielectric substrate used here. The optimal aspect ratio was about 1.5, as found by Ohberhart [72].

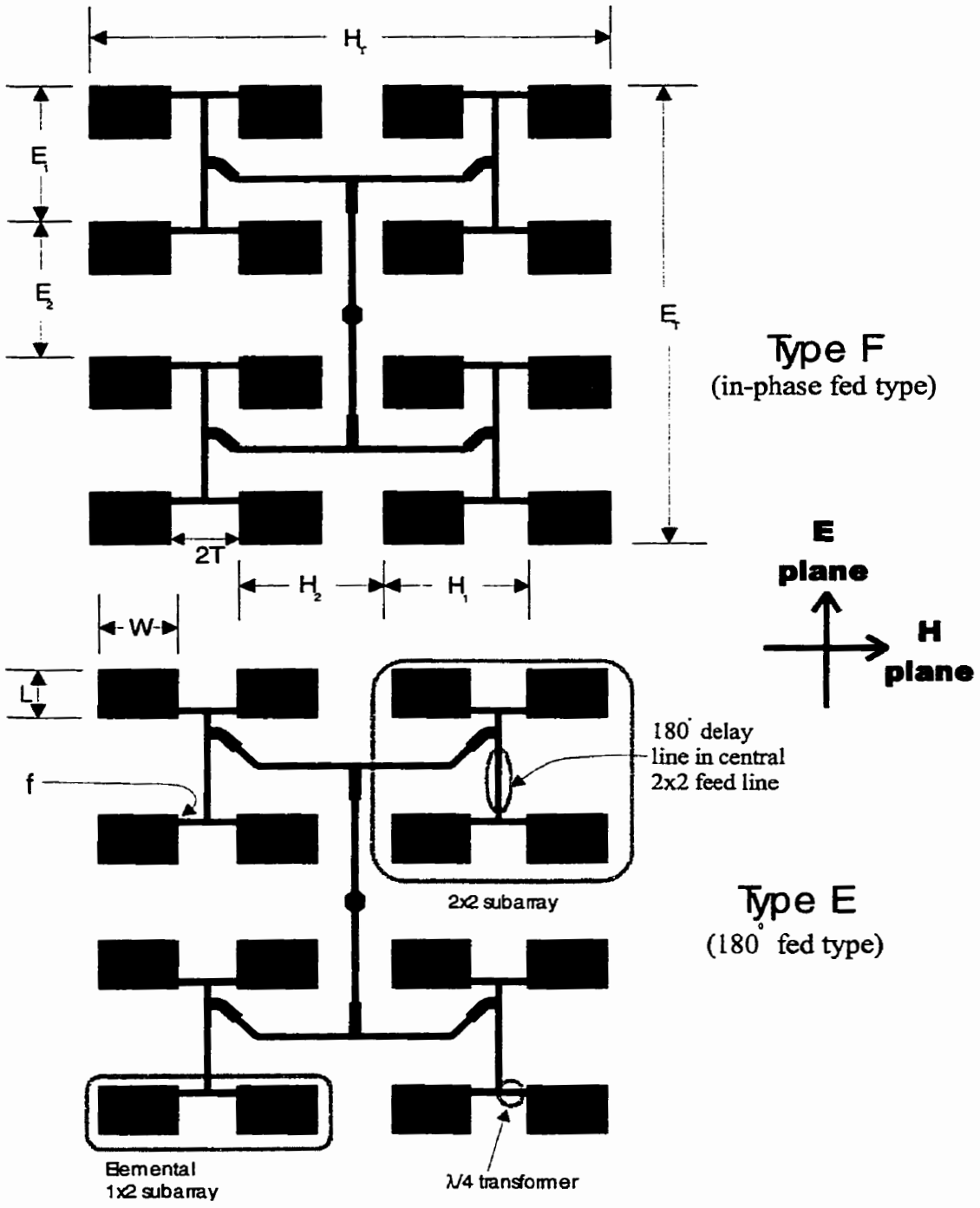

Figure 2.15: NRE 4x4 patch array topologies and dimensioning regime

key for dimensions given in Table 2.5

Two cross-polarised radiation suppression techniques were trialed in the small arrays. These were to use the patches in 1x2 array opposing pairs and 180° feeding between pairs of 1x2 subarrays. These techniques proved successful in simulation, but phase errors on the 180° delay line away from its design frequency caused the E-plane radiation pattern nulls to scan and fill compared to the ideal case.

2.3 LMCS band 4x4 subarrays

A total of six 4x4 NRE patch arrays were made from the four 1x2 subarray designs discussed in the previous section, Table 2.5. All six were an appropriate size for use as waveguide fed subarrays at LMCS band [15]. The comparison was made by examining the directivity (or scaled directivity in the case of the experimental results), input impedance and radiation pattern shapes across 10% bandwidth. The 1x2 subarray type (A, D, H or M) and 2x2 feeding technique (in-phase or 180°) were all found to affect 4x4 subarray performance. The influence of these various structural differences upon the input impedance of the 4x4 arrays was also commented upon. Reasonable agreement was found between the numerical and experimental 4x4 array results.

Table 2.5: Critical dimensions of LMCS band 4x4 patch arrays

Array	Feed type	L (mm)	W (mm)	f (mm)	E1 (mm)	E2 (mm)	H1 (mm)	H2 (mm)	2T (mm)	ET (mm)	HT (mm)
F28A	0°	3.100	4.478	0.363	8.116	8.116	8.294	7.938	3.816	27.45	29.00
E28A	180°	3.100	4.478	0.363	8.730	7.502	8.294	7.938	3.816	27.45	29.00
E28D	180°	2.988	4.478	0.307	8.730	7.502	8.294	7.938	3.816	27.95	29.00
E28H	180°	2.988	4.478	0.307	8.730	7.502	7.294	8.938	2.816	27.95	28.00
F28M	0°	2.888	4.378	0.257	8.116	8.116	7.694	8.538	3.316	27.24	28.30
E28M	180°	2.888	4.378	0.257	8.730	7.502	7.694	8.538	3.316	27.85	28.30

all arrays except F28M tested experimentally
dimensions illustrated Figure 2.15

2.3.1 Array descriptions

Both A and M 1x2 subarrays, from subsection 2.2.2, were used in in-phase fed 2x2 subarrays of 4x4 subarrays (type F prefix), Table 2.5 & Figure 2.15. The two type F 4x4 subarrays had constant patch spacing in the E-plane (E1=E2), but spacing E_1 had to be increased (and E_2 decreased) to accommodate the 180° delay line in the type E 2x2 subarrays, Table 2.5. All four 1x2 subarrays (A, D, H and M) were used in the 180° fed type E configuration, Table 2.5. The major structural differences between these subarrays were those of the different 1x2 subarrays as discussed in subsection 2.2.2.

2.3.2 Directivity and input impedance behaviour with frequency

All six 4x4 subarrays were simulated using IE3D. Comparing the three 180° fed (E prefix) arrays using normal $\lambda/4$ transformers (E28A, E28D & E28M), the peak directivity moved to progressively higher frequencies with a shortening of the patch resonant length L, Table 2.5 & Figure 2.16. The peak directivity and 1dB directivity bandwidth also tended to increase, although the shape of the characteristic remained more or less constant, Figure 2.16. The 0.1mm shorter patch length L of patch D compared to patch A moved the characteristic of E28D 0.4GHz higher in frequency than that of the otherwise identical E28A, Table 2.5 & Figure 2.16. A similar relationship existed between E28D and E28M, although the H-plane dimensions were not identical, the differences in directivity with frequency were the result of differences in the 1x2 subarrays, Figures 2.7 & 2.9.

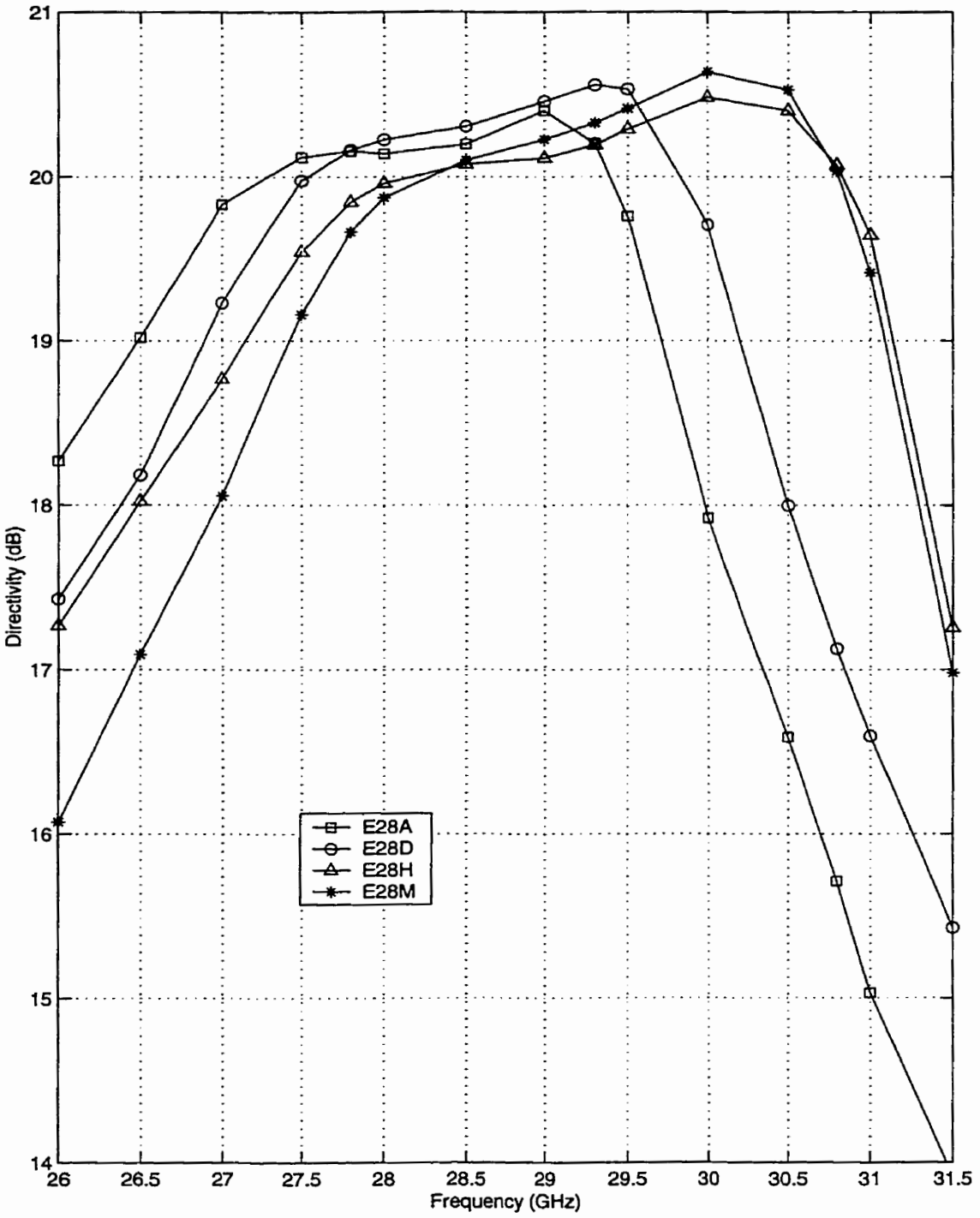

Figure 2.16: Directivity characteristics of 180° fed (type E) 4x4 arrays using IE3D.

patch dimensions and spacing taken from Table 2.5

Table 2.6: 1dB directivity bandwidths of 4x4 arrays using IE3D.

Array type	Frequency of peak (GHz)	Peak directivity (dB)	1dB bandwidth (%)
F28A	28.25	20.11	4.09
E28A	29	20.40	5.06
E28D	29.3	20.56	4.89
E28H	30	20.48	6.15
F28M	29.5	20.48	5.52
E28M	30	20.63	5.53

complementary to Figures 2.16 and 2.17; structures described in Table 2.5 & Figure 2.15

Shortening the λ/4 1x2 subarray impedance transformer length 2T (and H1) by 26% gave E28H 1.2% additional 1dB directivity bandwidth compared to E28D, Figure 2.16 & Table 2.6. The upper limit of the 1dB directivity bandwidth of E28H was about 1GHz above that of E28D, Figure 2.16. Thus a widening of the directivity performance was obtained from using the type H 1x2 subarray in a 4x4 array. The improvement was the consequence of lowering the sidelobes and widening the null placement of the 1x2 type D subarray H-plane radiation pattern from shortening the transformers, Figures 2.7 & 2.8.

Feeding the two 1x2 subarrays in each 2x2 subarray in-phase (F prefix) as opposed to 180° out of phase (E prefix), caused the directivity to rise to and fall away from its peak value less rapidly irrespective of the patch type used, Figure 2.17. The directivity characteristics of F28A and F28M were much gentler than those of E28A and E28M, respectively. Also, the in-phase fed 4x4 arrays (F28A & F28M) gave slightly lower peak directivities, and at lower frequencies, than the 180° fed designs, Figure 2.17 & Table 2.6.

This discussion of the directivity behaviour of the six 4x4 subarrays at LMCS band has so far neglected the effects of input impedance and radiation efficiency. To investigate these other operational quantities, in addition to confirming that these subarrays would work experimentally, all of the subarrays, except F28M, were built and tested. The radiation pattern measurements

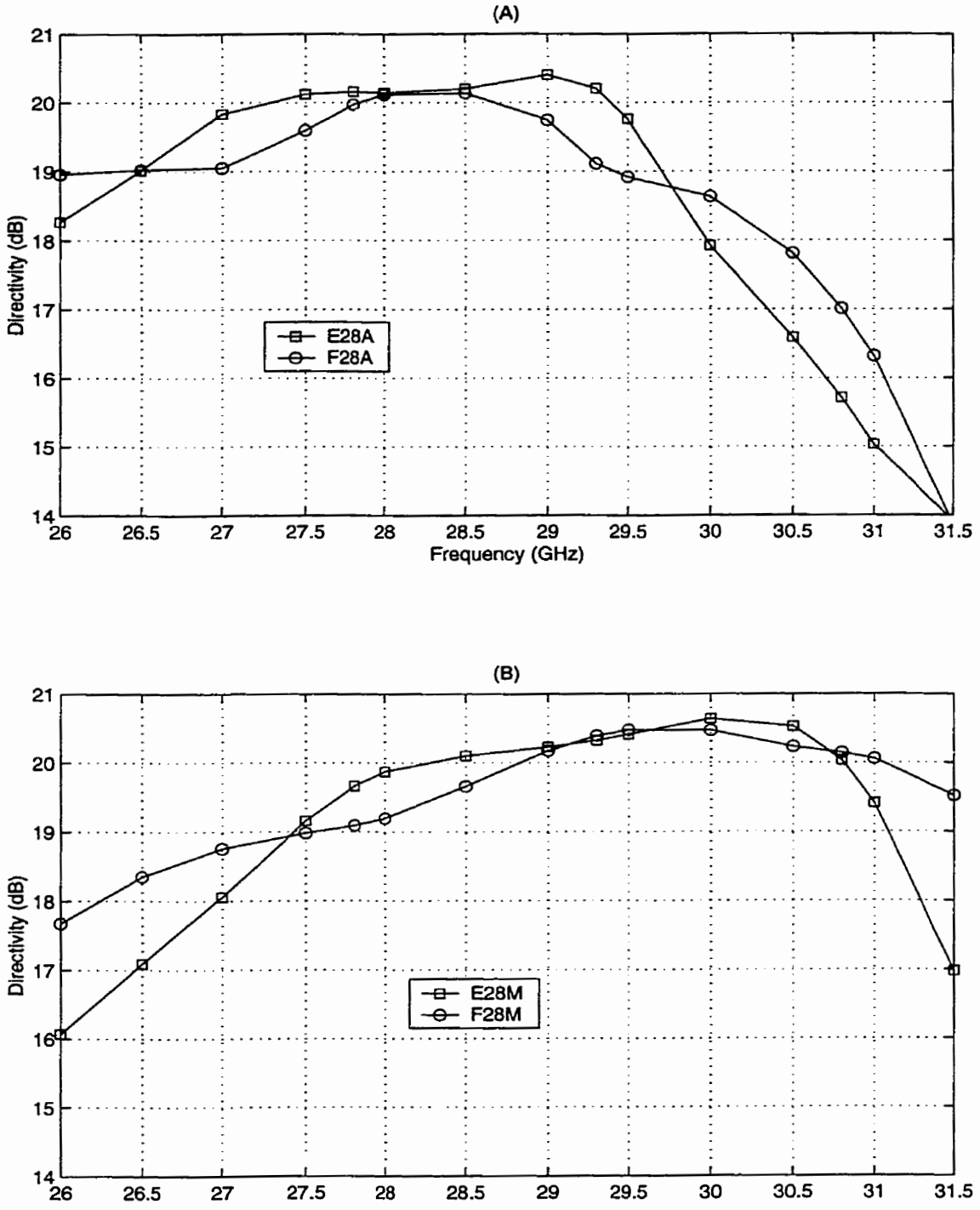

Figure 2.17: Comparison of directivity characteristics of 180° fed (type E) and in-phase fed (type F) 4x4 arrays using IE3D.

(A) Arrays using patch design A, (B) Arrays using patch design M patch dimensions and spacing taken from Table 2.5.

were done in the compact range, anechoic chamber at the University of Manitoba, over the range of 26.5-31.5GHz. A EMC 31608 horn was used as the standard gain horn for the measurements, with a 10dB attenuation included in the calibration.

Before a full discussion of the experimental results, the experimental and numerical results of two 4x4 arrays were compared. The purpose of such a comparison was to check against serious manufacturing errors and to validate the accuracy of the meshing used in the IE3D numerical models.

Both of the available commercial Method of Moments (MOM) and Finite Element Method (FEM) numerical simulation software tools were capable of modeling the 4x4 microstrip patch arrays. The MOM software was Zeland IE3D™, which was well suited to the simulation of such arrays in a speedy and efficient manner, even with fine edge cells ("edge elements") required to model the current distribution across a microstrip line accurately. The FEM software was Ansoft HFSS™, which was not well suited for this type of antenna, as it requires the discretisation of the entire dielectric and a radiation space resulting in very large numbers of unknowns. To compare the two, IE3D took some 15 minutes for a single frequency step while HFSS took approximately 20 hours for identical 4x4 patch arrays and having been run on identical personal computers. IE3D was used to match the input impedance of the 4x4 arrays at 28GHz.

The experimental results from the two 4x4 patch arrays were compared to the numerical simulation results as a check against manufacturing defects, and to confirm that the simulation tools were accurate with the meshing used in the models. The directivity calculated by either IE3D or HFSS for each frequency point was multiplied by the radiation efficiency, then directly comparable to the experimentally measured gain added to the mismatch loss derived from the experimentally measured input impedance. For the in-phase fed F28A array, the IE3D results

were very close to the experimental results in shape but were shifted up 1GHz (3.5%), Figure 2.18A. The results from HFSS were close at the scaled directivity peak, rolloff and upper frequency end point. In contrast, for the 180° fed E28A array the IE3D scaled directivity was 0.5-1dB lower than the experimental results, and the rollup was shifted up in frequency about 3.5%, Figure 2.18B. The rolloff of the scaled directivity was slightly shifted up in frequency compared to the experimental results. The scaled directivity results from HFSS fit as a line of best fit through the experimental results across the plateau and down the rolloff (above 28.5GHz). In summary, the experimental results have been compared to the boresight scaled directivity predicted by integral (MOM) and a differential (FEM) method full wave numerical simulations. Several differences between the MOM and FEM were caused by differences in segmentation schemes. The segmentation of the patches and microstrip lines was considerably coarser in the FEM models, and could not be refined due to the RAM limitations of the personal computer used. Despite this, both available commercial software packages gave results close to those measured experimentally for large and complex structures which could not have been modeled in full a few years ago. This has shown the value of the software, and the applicability of these to future work.

The general features of the experimentally measured scaled directivity of the five 4x4 subarrays generally match those of the IE3D directivity characteristics, Figures 2.16, 2.17 and 2.19. The scaled directivity rolloff order was as predicted for the 180° fed arrays: E28A, E28D, E28H, E28M, Figure 2.19A. As F28M was not built, only F28A could be compared to E28A for a contrast of in-phase to 180° feeding within the 2x2 subarrays. As predicted by IE3D, the 180° fed subarray gave broader range of higher scaled directivity values, Figure 2.19B. The only prominent features in the scaled directivity characteristics not predicted by IE3D was the 1.5dB artifact at 27.8GHz from E28A and the 2dB discontinuity at 28.5GHz from E28H, Figure 2.19A. These anomalies did not appear in the IE3D directivity characteristic, Figure 2.16. These scaled directivity artifacts were due to the main lobe scanning in the E-plane. Despite these artifacts the

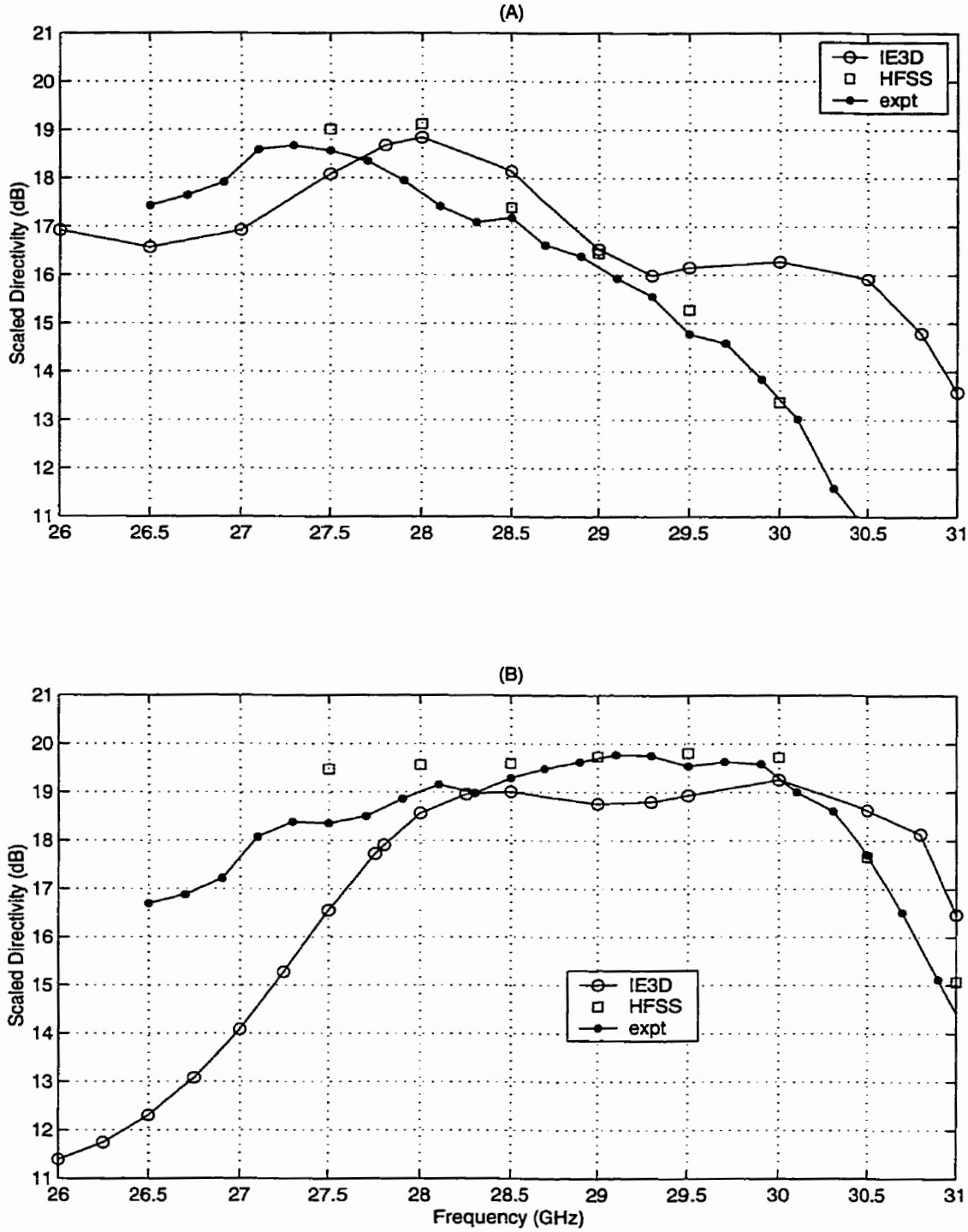

Figure 2.18: Comparison of experimental and numerical scaled directivity characteristics of two 4x4 arrays.

(A) F28A array, (B) E28M array
patch dimensions and spacing taken from Table 2.5

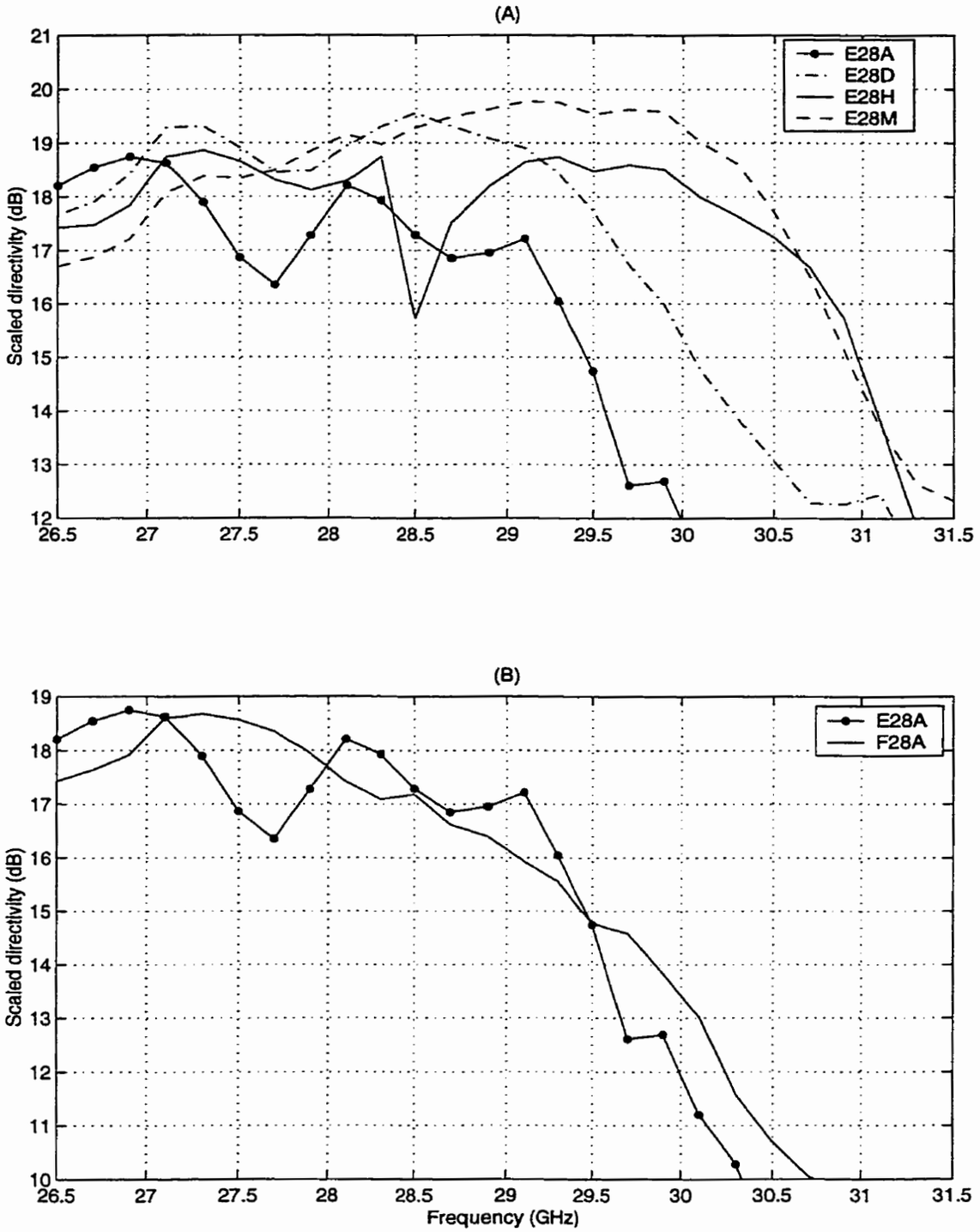

Figure 2.19: Experimental scaled directivity characteristics of five 4x4 arrays.

(A) 180° fed (E prefix) arrays, (B) comparison of E28A & F28A arrays
"E28A" identical in both (A) and (B)
patch dimensions and spacing taken from Table 2.5

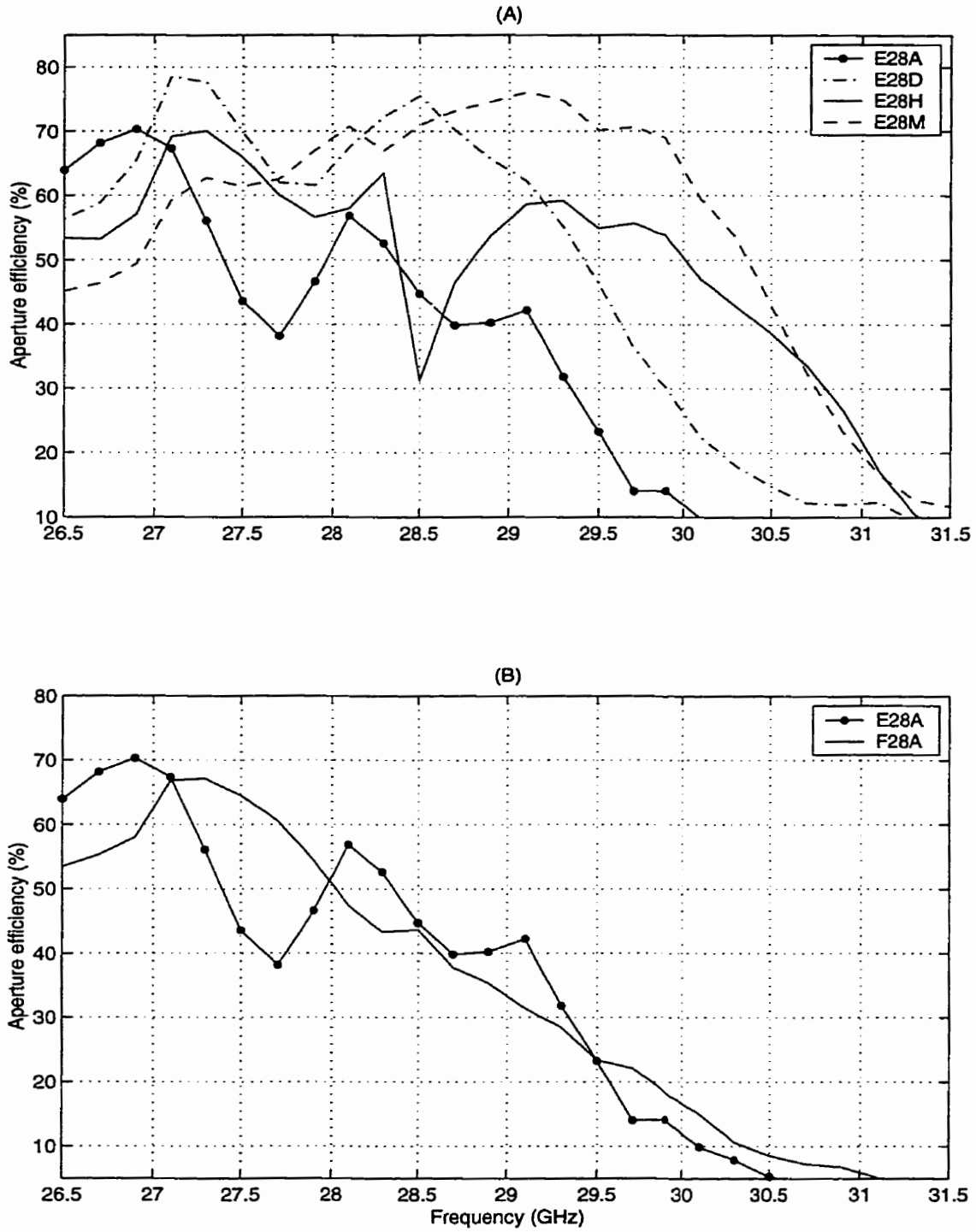

Figure 2.20: Experimental aperture efficiency characteristics of five 4x4 arrays.

(A) 180° fed (E prefix) arrays, (B) comparison of E28A & F28A arrays
"E28A" identical in both (A) and (B)
patch dimensions and spacing taken from Table 2.5

experimentally measured results from the five 4x4 subarrays were in reasonable agreement with the IE3D results and were thus adjudged to be sound.

The experimentally measured scaled directivity of each subarray was used to calculate its aperture efficiency, Figure 2.20. The subarray area used for the aperture efficiency calculations was (2E1+2E2)x(2H1+2H2), Table 2.5. The area of each 4x4 subarray was thus identical at (2x16.232mm)x(2x16.232mm)=1054mm^2, so the relative relationships in scaled directivity were preserved in the aperture efficiency. Aperture efficiencies of about 70% were expected, as this is typical for microstrip arrays of this size where the microstrip feed network is not yet long enough to become a significant loss mechanism [58]. So, given that all five subarrays achieved aperture efficiencies of the order of 70%, the performance of those was adjudged to be satisfactory [187]. That both E28D and E28M achieved aperture efficiencies of the order of 75%, and that the latter did it across 1GHz, was better than expected performance. The high aperture efficiency results from E28M across the LMCS band show its suitability as a waveguide fed array element, as a replacement for and improvement over the RE 4x4 patch subarray previously used by Weiss [15]. These results also show the advantages of the 180° feeding technique within NRE patch arrays.

The input impedance characteristics of the five 4x4 subarrays reveal the effects of the various 1x2 subarray designs and feeding techniques, whether in-phase or 180°. All of the E type (180° fed) subarrays showed two distinct resonances in input impedance, Figure 2.21A. This feature was peculiar to the LMCS band subarrays, as there was only one resonance in the input impedance of the 12GHz 180° fed 4x4 subarrays (types E, G and H) [181]. The double resonance was thus an advantage of the approximately 10% greater electrical thickness of the dielectric substrate used for the LMCS band arrays. The relative positioning of the resonances was indicative of several geometrical features of the 1x2 subarrays. The lower resonance of E28D and E28H were coincident, Figure 2.21A. As both patch size (W & L) and feeding position (f) were identical for

1x2 subarrays D and H, this was the determining factor for the lower resonance, Table 2.5. The 26% difference in transformer length (2T) did not affect the lower resonance at 27.5GHz, Figure 2.21A. As the lower resonance of E28A was at a lesser frequency to that of E28D, patch resonant length (L) was the determining factor, as the two arrays were otherwise identical. In contrast, the second resonance was a function of the transformer length (2T) and patch width (W). The second resonance of E28A and E28D were coincident, and the only common geometrical parameters were W and 2T, Figure 2.21A. The second resonance of E28M, and possible second resonance of E28H at 30GHz, appearing at frequencies higher than that of E28A and E28D was further indicative of the importance of W and 2T. The transformer length was shorter in the H 1x2 subarray, while both transformer and patch widths were shorter for the M 1x2 subarray, Table 2.5. A shorter resonant structure would be expected to have a shorter resonant wavelength and consequently a higher resonant frequency. Thus, certain salient geometrical parameters of the four 1x2 subarrays were found to be critical in determining the resonant frequencies shown by the input impedance of probe fed, type E 4x4 subarrays.

The feeding method employed in the 2x2 subarrays, whether in-phase or 180°, also affected the input impedance of the 4x4 subarrays. Comparing E28A and F28A, both feeding techniques produced two resonances, Figure 2.21B. As a relative shift from the lower resonance of E28A (26.75GHz), the lower resonance of F28A (27.65GHz) was 3.36% higher in frequency, Figure 2.21B. This was not a result of the difference in E-plane spacing within the 2x2 subarrays (E_I) which was 7.0% or the feed line length between the 1x2 subarrays (6.67mm for E28A as opposed to 7.81mm for F28A), Figure 2.15 & Table 2.5. Thus it was found that the feeding technique used between the 1x2 subarrays affected the input impedance, although the cause was not immediately obvious from the geometrical dimensions.

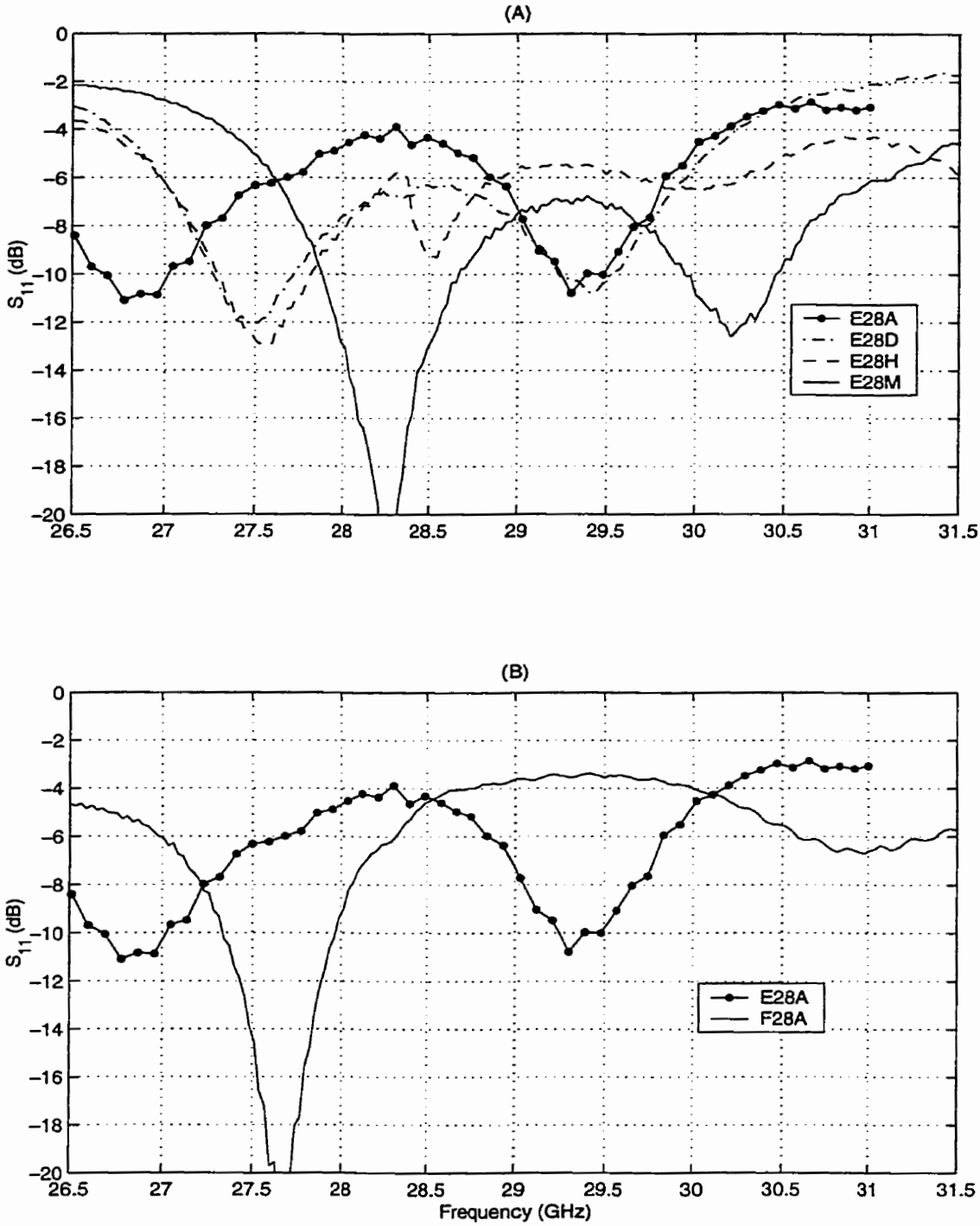

Figure 2.21: Experimental input impedance characteristics of five 4x4 arrays.

(A) 180° fed (E prefix) arrays, (B) comparison of E28A & F28A arrays
"E28A" identical in both (A) and (B)
patch dimensions and spacing taken from Table 2.5

In summary, the four 1x2 subarrays (A, D, H and M) were used in 180° fed 2x2 subarrays which were in turn used in 4x4 subarrays. Both numerical directivity and experimental scaled directivity results were in reasonable agreement. The E28M 4x4 subarray gave close to 75% aperture efficiency across a reasonable segment of the LMCS band, showing the advantages of the smaller type M patches, also as discussed in the previous section. The salient dimensions of the 1x2 subarrays were found to determine the relative positions of the resonances in the input characteristics of the four type E 4x4 subarrays. Using the in-phase feeding technique gave narrower directivity characteristics. Both in-phase and 180° feeding within the 2x2 subarrays were found to produce a double resonance in the input impedance characteristics of the 4x4 arrays, which did not occur in the equivalent 12GHz arrays of reference [181].

2.3.3 Radiation pattern behaviour with frequency

The experimental and numerical directivities were found to be in reasonable agreement in the previous subsection for the two 4x4 subarrays. The purpose of this subsection was to compare the experimental and numerical radiation pattern shapes, as a further check on major experimental errors. Null positioning and the 2^n grating lobes are also commented upon.

Comparing the experimentally measured radiation patterns of the F28A and E28M 4x4 subarrays to those from the equivalent models in IE3D showed that the agreement was much better for E28M. For F28A, the general features of the 27.8GHz E-plane radiation pattern from IE3D resemble those measured experimentally, with the E-plane main lobe scanned 2.5° off boresight, Figure 2.22. For both 29.3 and 30.8GHz, IE3D predicted lower sidelobes and grating lobes than those in the experimental patterns. From the examination of the 2x2 subarrays in subsection 2.2.3, it was found that the central feedline in an in-phase fed 2x2 subarray scanned the E-plane main

lobe away from boresight, and that if the main lobe was scanned then the nulls would be shifted as well. The IE3D 29.3 and 30.8GHz patterns showed the 2^n grating lobes as being suppressed where in the experimental patterns these were at –8dB and –4dB, respectively, Figure 2.22 & Table 2.7. As a consequence, IE3D predicted the scaled directivity at 27.8GHz reasonably well but gave higher values than the experimental for the higher frequencies, due to the failure to predict the drop in directivity caused by the 2^n grating lobes, Figure 2.18. IE3D gave considerably lower E-plane cross-polarisation than the measured levels of –25 to –30dB.

As with the E-plane, IE3D was off in its prediction of the 2x2 subarray null (second order null in 4x4 subarray) in the H-plane of F28A. This also meant that the prediction of the level of the 2^n grating lobe level was considerably below that measured experimentally although the direction was more or less accurate, Figure 2.23 & Table 2.5. This was a serious failing in the IE3D model, especially at 30.8GHz where the experimentally measured grating lobe level was –2.5dB, 10dB higher than predicted by IE3D. The prediction of the H-plane cross-polarised component was also off by a considerable margin and worsened with increasing frequency, Figure 2.23. The peak experimental cross-polarised component at 27.8GHz was –14.5dB at 37° off boresight, and was about 5dB higher than in the equivalent IE3D pattern, Figure 2.23. The cross-polarised component had risen to –5dB by 30.8GHz. Such a high cross-polarised component would be a serious disadvantage to this array type. However, it should be noted that the cross-polarised component was reasonably symmetrical about boresight, as were the co-pol sidelobes. As the 4x4 subarray designs were symmetrical in the H-plane, reasonable symmetry in both co and cross-polarisation patterns show that F28A was free from any major manufacturing defects. Thus, it has been found that IE3D consistently under predicted both 2^n grating lobe levels and cross-polarisation in both planes of an in-phase fed array of NRE patches. The former problem in the E-plane stems from an inability to model patch to feedline coupling in the 2x2 subarrays. Further

refinement of the meshing of the models may correct this problem, but at the expense of greater computational burden. The experimental array was also free of major manufacturing defects. The numerical and experimental radiation patterns of a 180° fed 4x4 subarray were examined next.

In stark contrast to the in-phase fed 4x4 subarray, there was a high level of agreement between the IE3D and experimental radiation patterns from E28M in both planes, Figures 2.24 and 2.25. The only noticeable disparity in the co-polarised radiation patterns was that the 2^n grating lobes in the experimental E-plane at 30.8GHz were about 5dB higher than predicted by IE3D. These E-plane 2^n grating lobes appeared at 36.85° off boresight at 30.8GHz, and were not suppressed because the nulls in the 2x2 subarray E-plane pattern had been scanned to about 25° and −50° by the phase error on the 180° delay line, Table 2.7 & Figure 2.24. The rise of these grating lobes caused the rapid rolloff in directivity in the E type arrays as noted above, Figures 2.16 and 2.19. These 2^n grating lobes were successfully suppressed at the lower frequencies in the E-plane and across the entire band in the H-plane by careful placement of the 2x2 nulls, Tables 2.4 & 2.5 & Figures 2.24 & 2.25. As with F28A, IE3D was generally off in its prediction of the cross-polar levels for E28M, although the IE3D and measured cross-polarised component shape and level agreed reasonably well at 27.8 and 29.3GHz in the H-plane, Figure 2.25. The inner pair of sidelobes and the outer pair of 2^n grating lobes at 30.8GHz in the H-plane of E28M were 12dB below the main lobe peak in contrast to 2.5dB for F28A showing the advantages of the type M 1x2 subarray over the type A in terms of 2^n grating lobe mitigation, Figures 2.23 & 2.25. The H-plane sidelobe suppression from the phase error on the 180° delay line, discussed in subsection 2.2.3, also helped keep the sidelobe level lower in E28M. Comparing the experimentally measured cross-polarisation levels of F28A and E28M, the latter had H-plane cross-polarisation levels 5-10dB lower that the former, and comparable levels in the E-plane, Figures 2.22-2.25. The cross-polarised component performance of either 4x4 subarrays relate well to the cross-polarisation of the individual patch designs chosen from the patch aspect ratio study, Figures 2.5 and 2.7. The

180° delay line in the 2x2 subarrays of E28M further served to lower the H-plane cross-polarised component.

The co- and cross-polarised radiation patterns of the experimentally tested 4x4 subarrays have been compared directly to equivalent radiation patterns from IE3D, in addition to indirect comparisons to the 2x2 subarray patterns from IE3D in terms of the null positioning. There was a reasonable level of agreement, although IE3D was found to be inaccurate in its prediction of the 2x2 subarray nulls at higher frequencies and thus gave lower levels for the 2^n grating lobes than were measured experimentally. This inaccuracy was small for the 180° fed type E28M 4x4 subarray, but was significant for the in-phase fed type F28A. From the IE3D study of the effect of the central feedline in the in-phase fed 2x2 subarrays, it was surmised that there was much greater coupling between that feedline and the pair of patches that it passed between in the experimental F28A than was accounted for in the IE3D model.

Table 2.7: Subarray E-plane null positioning and expected 2^n grating lobe positioning

Array type	Frequency (GHz)	2x2 null (°) [IE3D]	4x4 2nd order null (°) [experimental]	first order expected 2^n grating lobe (°)
F28A	27.8	42 -40	42.5 -47.5	41.63
	29.3	42.5 -40	50 -47.5	39.08
	30.8	55 -38	n/a -50	36.85
E28M	27.8	32.5 -44	38.5 -42	41.63
	29.3	32.5 -40	37 -40	39.08
	30.8	25 50	22.5 -55	36.85

two values indicate asymmetric null positioning with respect to boresight
first order 2^n grating lobes calculated using equation 6-86b of [179] for 2x2 - 2x2 spacing (E1+E2) from Table 2.5
complementary to Figures 2.13, 2.22 & 2.24

Table 2.8: Subarray H-plane null positioning and expected 2^n grating lobe positioning

Array type	Frequency (GHz)	2x2 null (°) [IE3D]	4x4 2nd order null (°) [experimental]	first order 2^n grating lobe (°)
F28A	27.8	38	35	41.63
	29.3	30	30	39.08
	30.8	25	20	36.85
E28M	27.8	45	43	41.63
	29.3	40	40	39.08
	30.8	35	32.5	36.85

first order 2^n grating lobes calculated using equation 6-86b of [179] for 2x2 - 2x2 spacing (H1+H2) from Table 2.5
complementary to Figures 2.6, 2.9, 2.14, 2.23 & 2.25

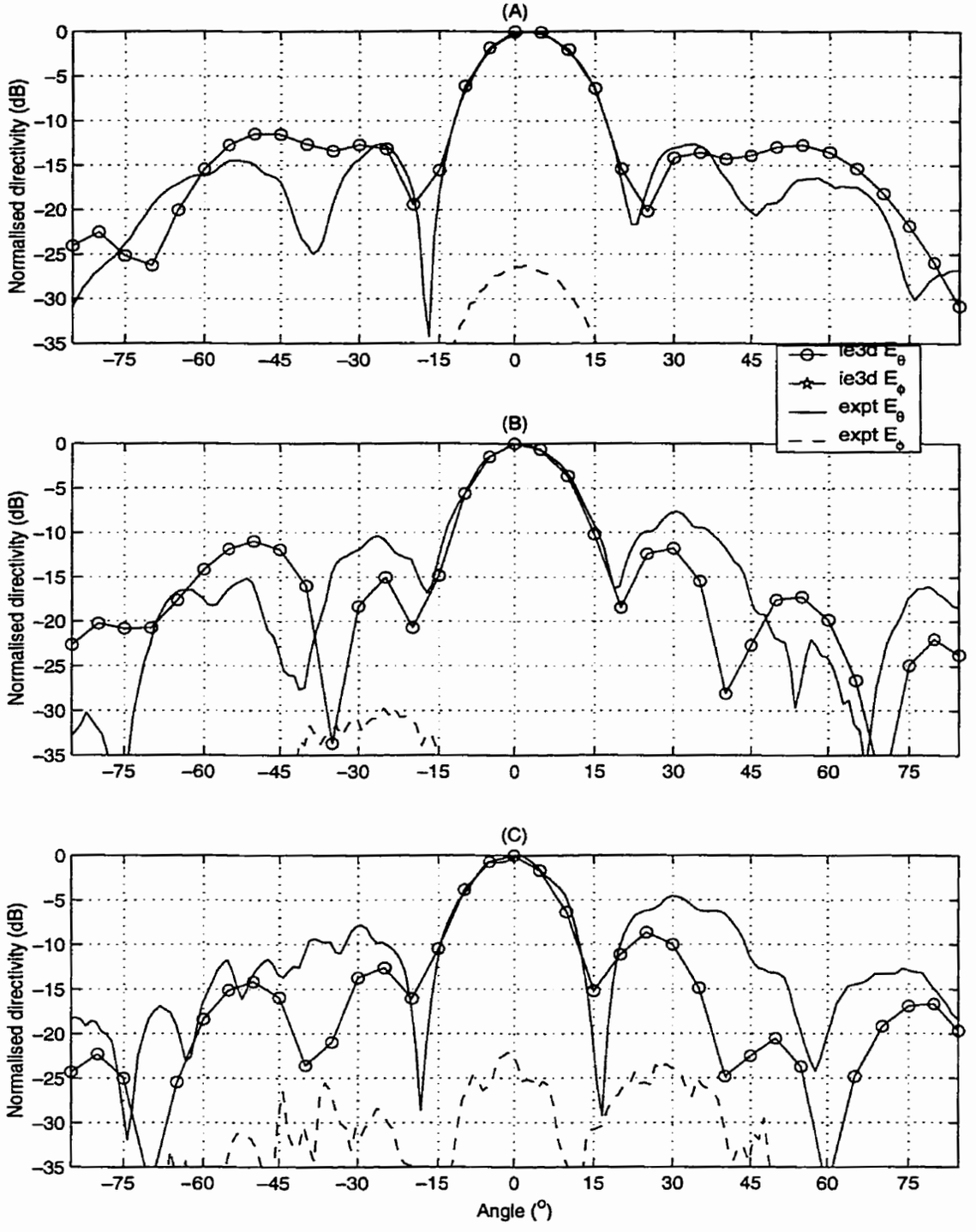

Figure 2.22: Comparison of experimental and numerical E-plane radiation patterns of in-phase fed F28A array.

(A) 27.8GHz, (B) 29.3GHz, (C) 30.8GHz.
patch dimensions and spacing taken from Table 2.5

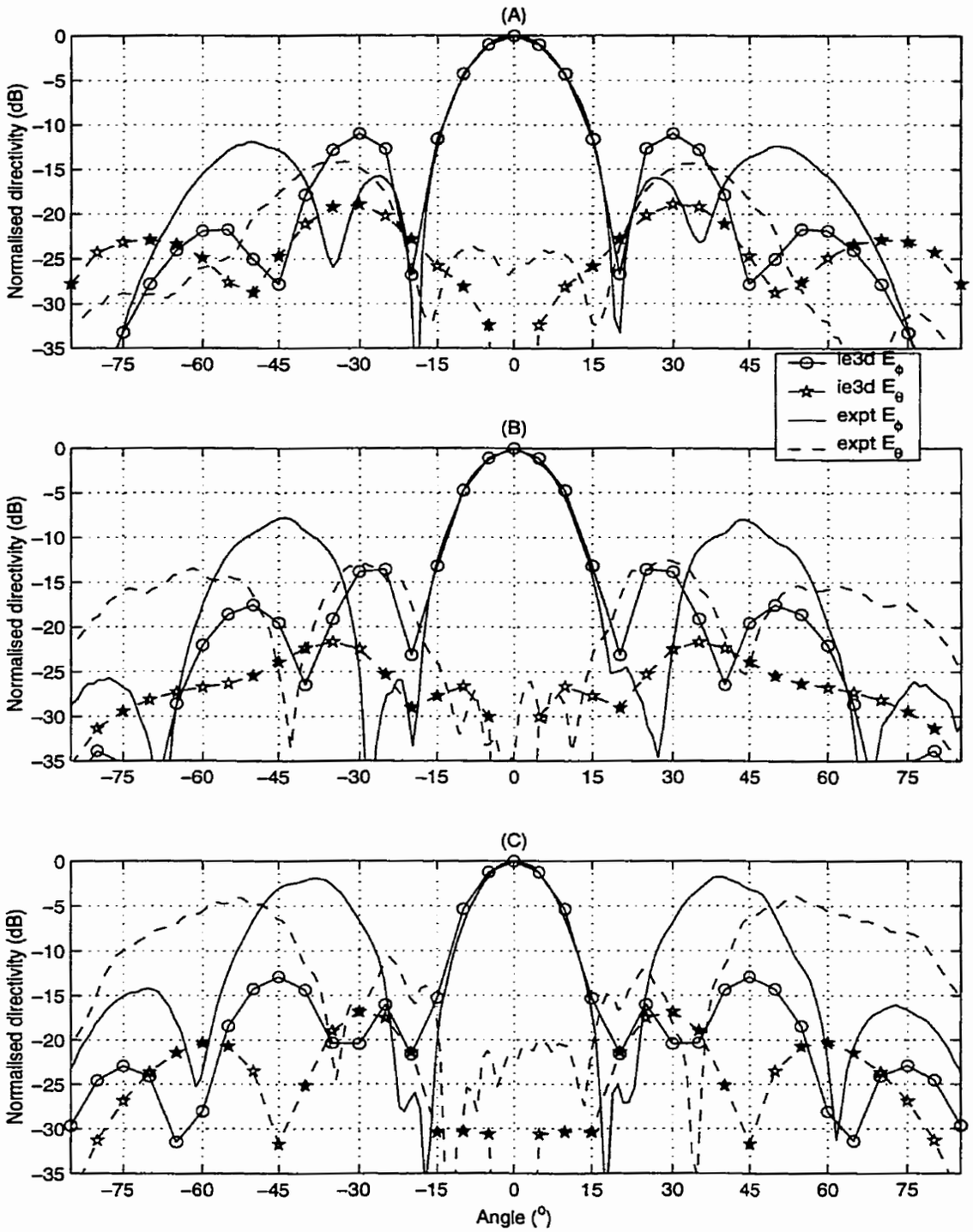

Figure 2.23: Comparison of experimental and numerical H-plane radiation patterns of in-phase fed F28A array.

(A) 27.8GHz, (B) 29.3GHz, (C) 30.8GHz.
patch dimensions and spacing taken from Table 2.5

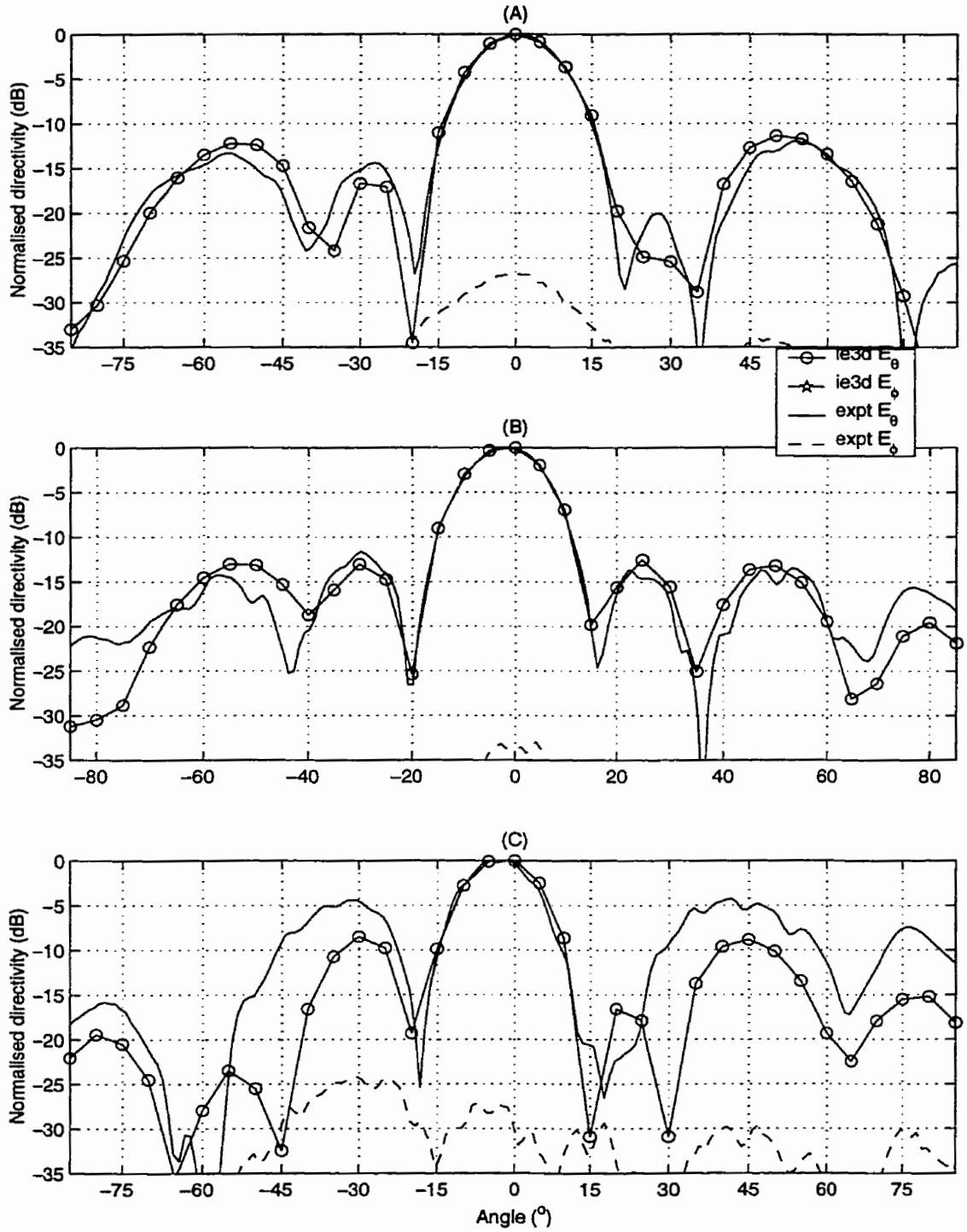

Figure 2.24: Comparison of experimental and numerical E-plane radiation patterns of 180° fed E28M array.

(A) 27.8GHz, (B) 29.3GHz, (C) 30.8GHz.
patch dimensions and spacing taken from Table 2.5

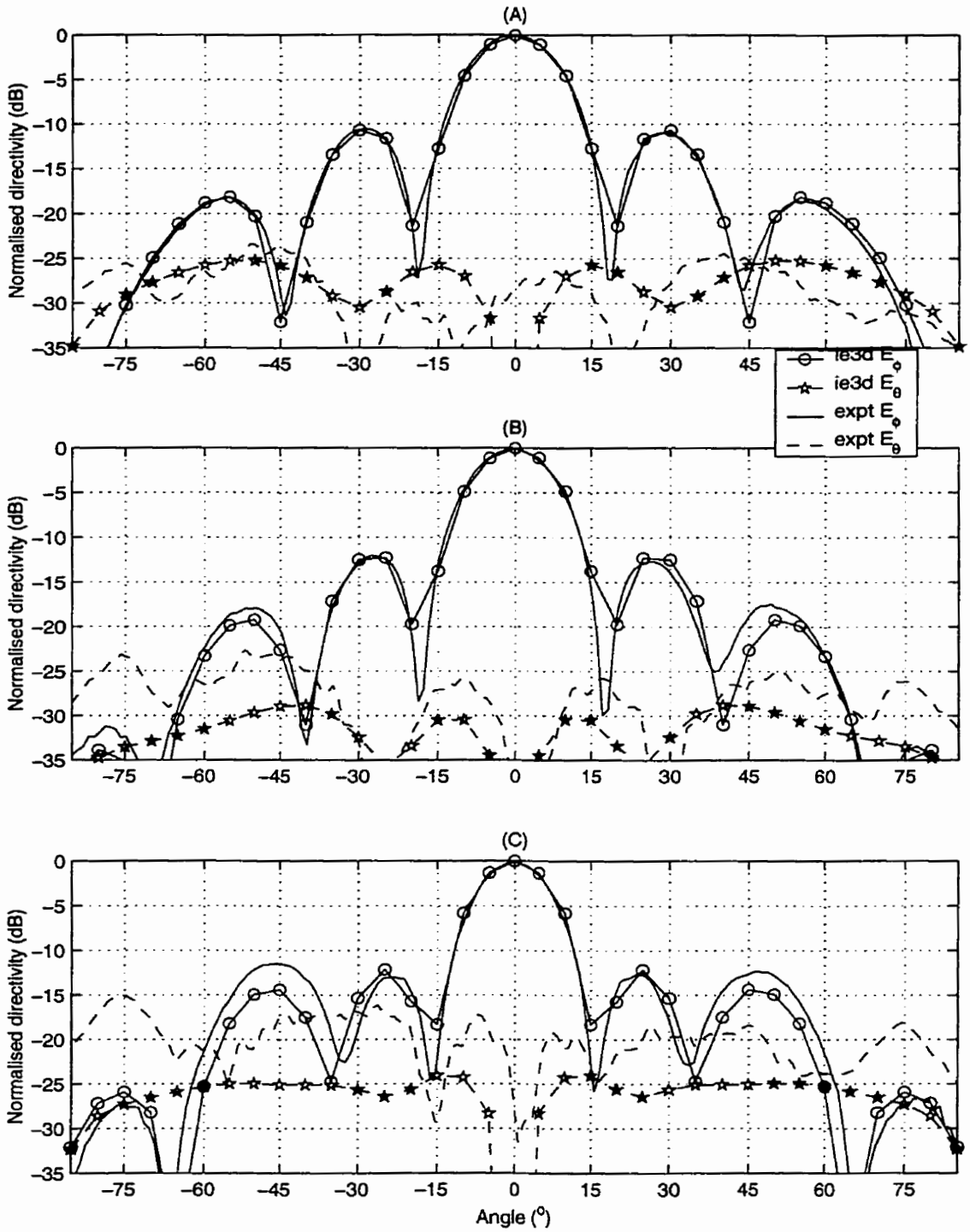

Figure 2.25: Comparison of experimental and numerical H-plane radiation patterns of 180° fed E28M array.

(A) 27.8GHz, (B) 29.3GHz, (C) 30.8GHz.
patch dimensions and spacing taken from Table 2.5

2.3.4 Summary of 4x4 microstrip subarray study

A fundamental difference was found between the directivity behaviour of the 4x4 arrays using in-phase fed 2x2 subarrays from those using the 180° type across the 10% bandwidth studied. The in-phase fed types gave a single frequency directivity peak while, in contrast, the directivity of the 180° fed types plateaued across a reasonable bandwidth of frequencies, and then rolled off very rapidly at the point where the 180° delay line phase error caused the 2x2 subarray nulls to scan away from the E-plane 2^n grating lobe directions. The type of patch and 1x2 subarray (A, D, H or M) was found to affect the maximum achievable scaled directivity, bandwidth and frequency positioning of the directivity characteristic of both in-phase and 180° array types. The two cross-polar radiation mitigation techniques tried in the 2x2 subarrays both worked in the 4x4 subarrays. However, both opposed 1x2 subarray feeding and 180° feeding were found to generate 2^n grating lobes, which were the cause of severe directivity loss in the experimental results of the 4x4 subarrays towards the upper end of the band studied. The generation of the 2^n grating lobes by 2x2 subarrays had been well documented by prior investigators investigating cross-polarised component reduction techniques in probe fed RE patch arrays, and is a disadvantage of using cross-polarised component reduction techniques on single feed point patches [65]. Null positioning in the 2x2 subarray patterns was the only method to mitigate the 2^n grating lobes available in the single layer microstrip arrays investigated here. Examples in which the 2^n grating lobes were successfully and not so successfully mitigated with nulls in the 2x2 subarray patterns were discussed. The most successful case produced about 75% aperture efficiency across 1GHz, which was better performance than the 4x4 RE patch arrays used previously as rectangular waveguide fed subarrays at LMCS band [15].

2.4 16x16 microstrip patch arrays

The F28A and E28M 4x4 subarrays for LMCS band were used as subarrays in 16x16 arrays, to gain an appreciation of the mutual coupling effects between the subarrays, to further elucidate the 2^n grating lobes which caused the loss in boresight scaled directivity, and to gain an appreciation of the losses within the long lengths of high impedance microstrip line interconnecting the subarrays, which could be used as a comparison for any future work with much lower loss rectangular waveguide feeding networks.

The 4x4 arrays, F28A and E28M, were used as subarrays to build up 16x16 arrays, simply by copying the layouts of either 4x4 array 16 times in a rectangular grid. A microstrip line corporate feed network interconnecting the centre feed points of each 4x4 subarray was then added, Figure 2.26 & 2.27. A characteristic impedance of 100Ω was used for the additional microstrip line, been identical to that used within the 4x4 subarrays. Single quarter wave transformers were used at the T junctions within the corporate feed network. Producing a 16x16 array with microstrip line interconnecting the 4x4 subarrays was much cheaper and quicker than doing an array with a rectangular waveguide corporate feeding system. Manufacture was a three step process: etch array, install SMA connector and tape to a rigid aluminium plate. Also obtained first hand experience of losses in feednetwork, and manufacturing errors seen in the results of prior investigators, as discussed in Chapter 1.

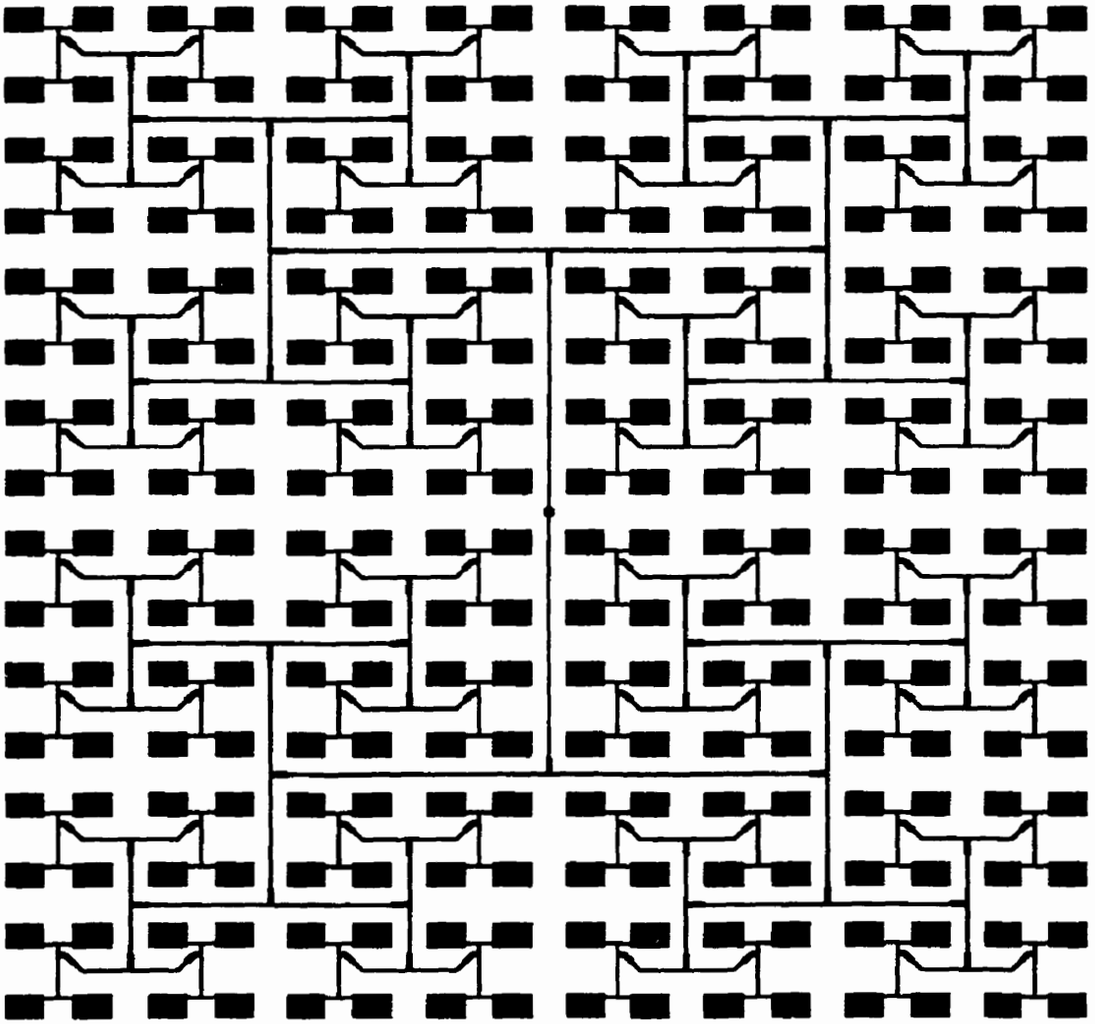

Figure 2.26: Silhouette of 16x16 E28M array.

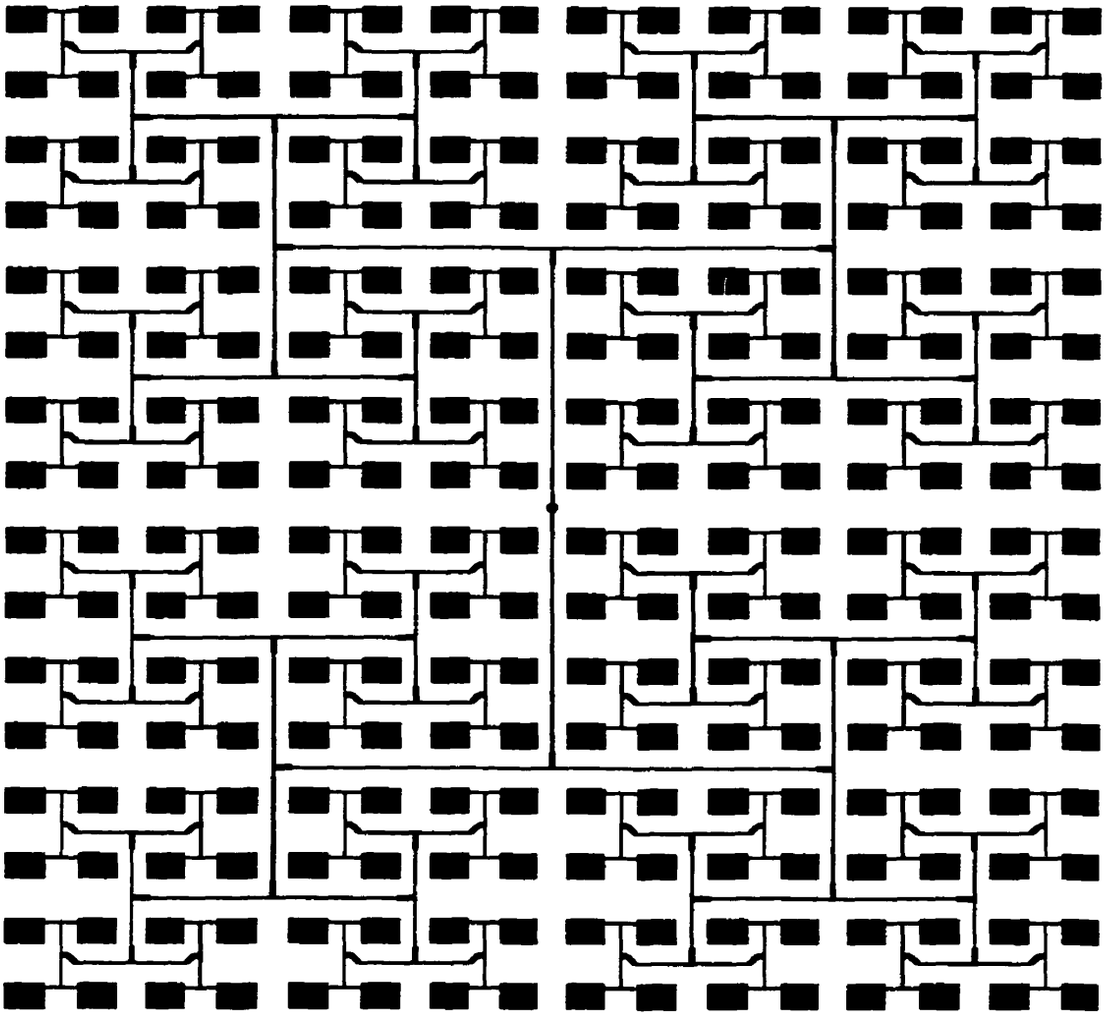

Figure 2.27: Silhouette of 16x16 F28A array.

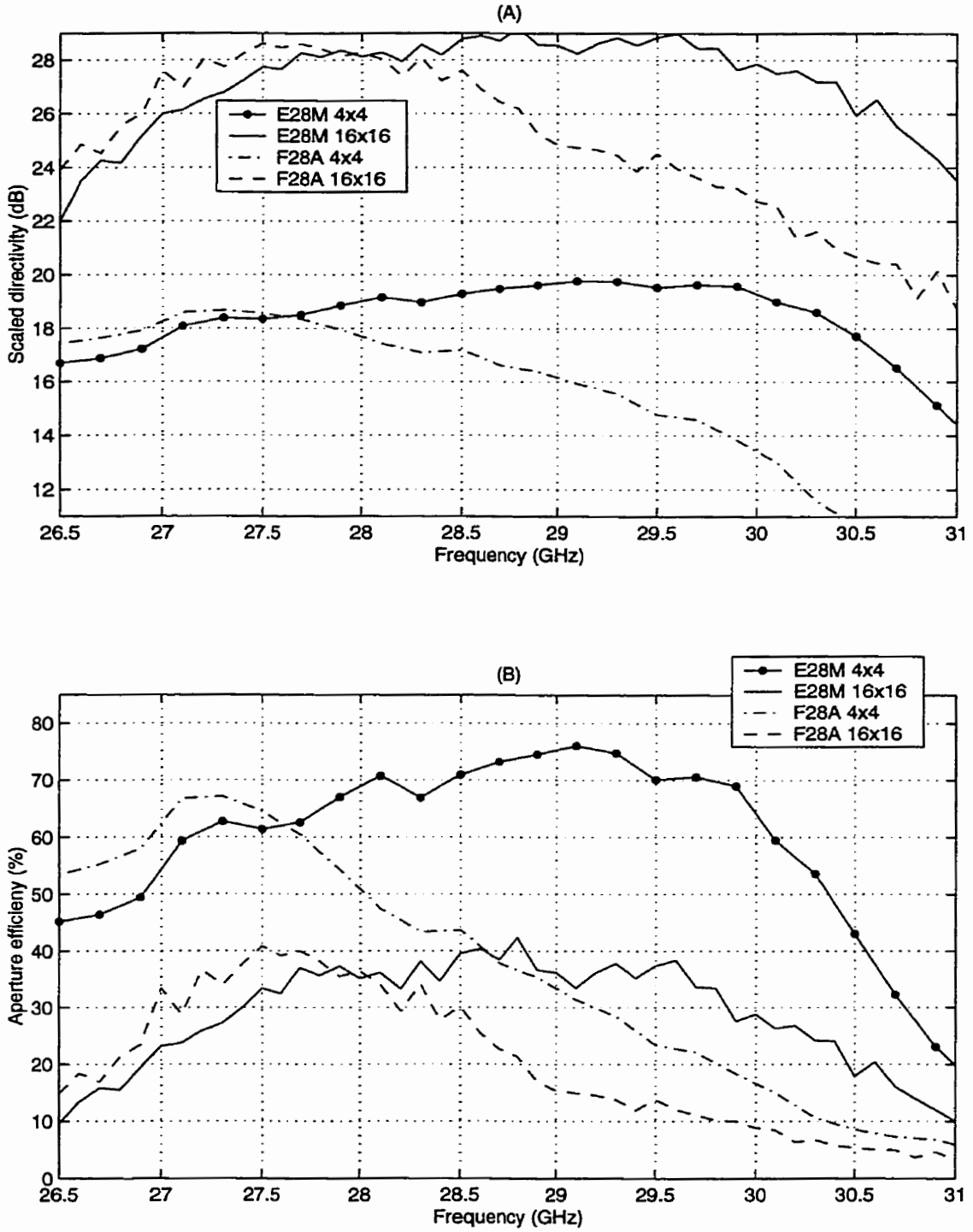

Figure 2.28: Comparison of experimental scaled directivity and aperture efficiency characteristics of E28M and F28A 4x4 and 16x16 arrays.

(A) scaled directivity, (B) aperture efficiency
patch dimensions and spacing taken from Table 2.5

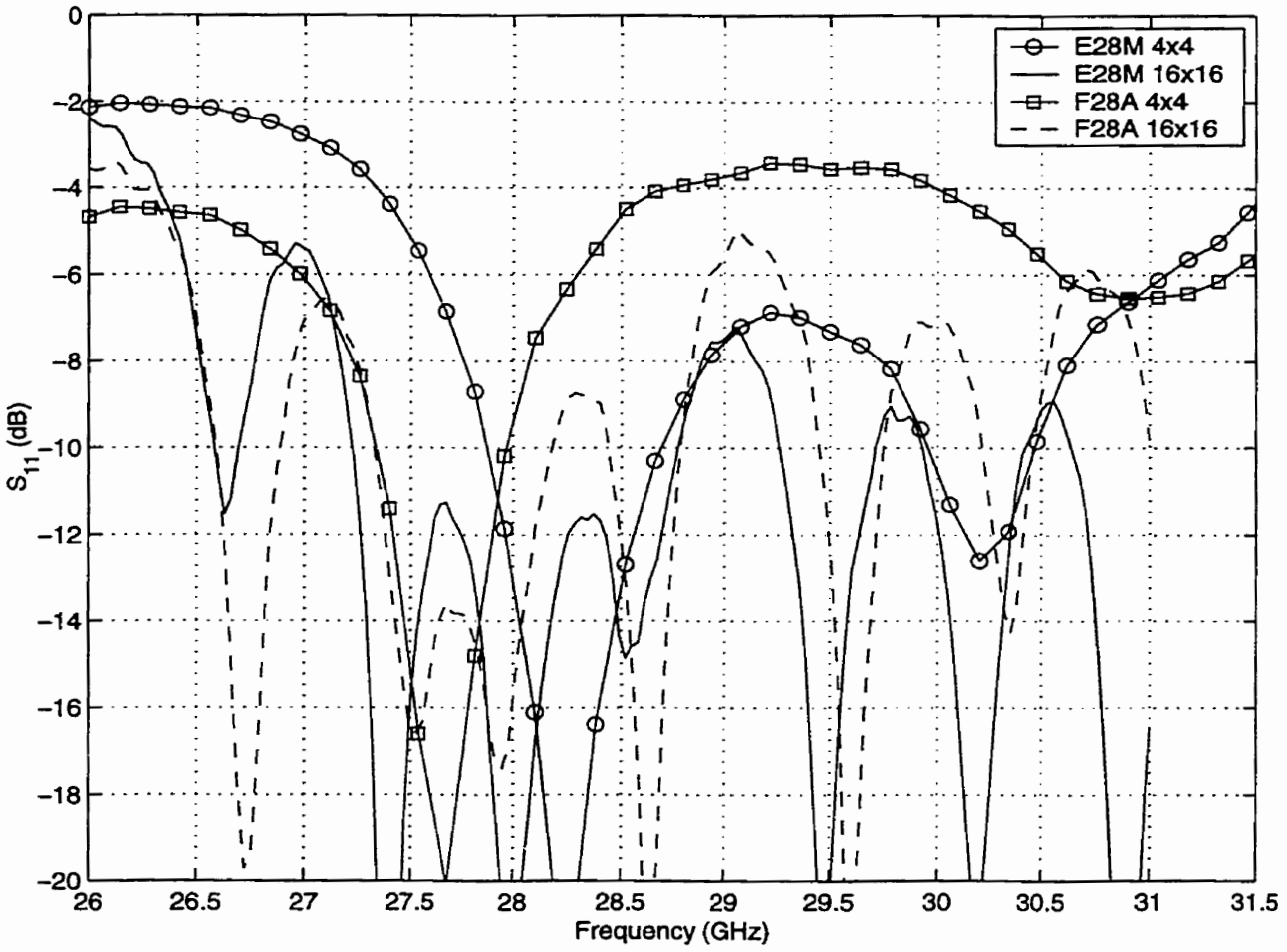

Figure 2.29: Comparison of experimental input impedance characteristics of E28M and F28A 4x4 and 16x16 arrays.

patch dimensions and spacing taken from Table 2.5

2.4.1 Directivity behaviour with frequency

Similar to the 4x4 subarrays, the 16x16 type E28M array gave a higher peak scaled directivity than the type F28A array, Figure 2.28A. The scaled directivity behaviour with frequency was consistent with that of the 4x4 arrays in that F28A gave a single frequency peak while E28M gave a plateaued characteristic, Figure 2.28A. The aperture efficiency characteristics have the same form as the directivity characteristics as the areas were identical, Figure 2.28B. Another difference between the 4x4 and 16x16 arrays of either type was the widening of the $S_{11} \leq$-10dB bandwidth and the introduction of multiple resonances, Figure 2.29.

2.4.2 Radiation pattern behaviour with frequency

The initial step in examining the performance of the 16x16 arrays was to check for major experimental errors. The 4x4 arrays had symmetrical H-plane patterns showing a lack of major manufacturing defects, Figures 2.23 & 2.25. This was not the case for both 16x16 arrays where the H-plane sidelobes were not symmetrical, showing the effects of manufacturing defects, Figures 2.31 & 2.33. Reasonable measures were taken to ensure flatness when testing the 16x16 arrays by taping the arrays onto a heavy aluminium sheet. Thus manufacturing defects were the main cause of the lack of symmetry in the H-plane radiation patterns, as noted in Chapter 1 in relation to the large microstrip arrays built by prior investigators. Uneven etching was indicated by the various circle/square etch quality indicators (similar to print alignment markers) placed around the edge of the 16x16 arrays.

The main difference in performance between the type E28M and F28A arrays was that the 2^n grating lobes remained low across the range of frequencies studied in the type E28M array. In

the H-plane of both array types the 2x2 subarray repetition distance was $\approx 1.60\lambda_o$ at 27.8GHz, so expect 2^n grating lobes at 42° at 27.8GHz and 37° at 30.8GHz, Table 2.8. These are seen clearly in the H-plane pattern of the type F28A array, and became more prominent as frequency increased and the 2x2 - 2x2 spacing increased as a multiple of λ_o, Figure 2.31. The H-plane 2^n grating lobes at 30.8GHz were 2.5dB below the level of the main lobe in the 4x4 array and 4dB down in the 16x16 array, Figure 2.23 & 2.31. This was a major source of directivity loss, as the radiated power was split almost equally between the main lobe and the two grating lobes, in the H-plane. The 2^n grating lobes were not overly apparent in the H-plane radiation patterns of the type E28M arrays. In both the type E28M 4x4 and 16x16 arrays, the H-plane 2^n grating lobes were suppressed by a well placed null in the 2x2 subarray, as discussed in subsection 2.2.3, Table 2.8. So more radiated power was available for the main lobe, explaining the higher scaled directivity of the type E28M 4x4 array than that of the type F28A 4x4 array across the range of frequencies studied. This effect resulted in the broader bandwidth scaled directivity performance of the type E28M 16x16 array compared to the type F28A array, Figure 2.28A. It should also be noted that the H-plane cross-polar component of the type E28M array was generally about 5-10dB lower than that of the type F28A array, showing the benefit of the 180° delay line within the 2x2 subarrays of the E28M array. Both 2^n grating lobe suppression and reduced cross-polarised component led to improved boresight scaled directivity performance of the E28M 16x16 array across a wider segment of the LMCS band.

Examining the E-plane radiation patterns, the 2^n grating lobes of the type F28A array were not as prominent (-10dB) at 30.8GHz as in the H-plane, Figure 2.30. The two possible causes were that the E-plane 2^n grating lobes were lower because of better 2x2 subarray null placement, or that the excitation of the 1x2 subarrays was more alike in the E-plane, making the 2^n grating lobe effect less prominent. Ideally, the 1x2 subarrays in the F28A 16x16 array were excited

identically but, as shown in subsection 2.2.3, the central feedline within each 2x2 subarray coupled to the upper 1x2 pair of patches causing the radiation pattern to scan. Examining the radiation patterns, the 16x16 2^n grating lobes were at least 10dB lower than predicted by the array factor across the entire band, suggesting that the lower grating lobes were due to a mutual coupling effect as this was not accounted for in the array factor, Figure 2.30. The 2^n grating lobe suppression in the F28A 16x16 E-plane was consistent with that predicted by the positioning of the 2x2 subarray nulls in the IE3D models, Table 2.7. According to the IE3D models, all the 2x2 nulls should have been very close to the 2^n grating lobe directions, except one at 30.8GHz where the null scanned to 50°. That the positive angle 2^n grating lobe (at 37°) was 2dB higher than the negative one conforms to the prediction based purely on 2x2 null placement. However, the agreement between the IE3D 2x2 subarray E-plane null placement and the experimental second order null was not good, Table 2.7. Thus, mutual coupling between the 4x4 subarrays caused the 16x16 arrays to behave more in accord with the IE3D 2x2 than the experimental 4x4 did.

The H-plane sidelobes and cross-polarised component of F28A were reasonably symmetrical to about 25° off boresight, Figure 2.31. For wider angles, there was some asymmetry and the grating lobes had a 3dB difference in level across the entire bandwidth. In contrast, the first sidelobes of the E28M 16x16 had a 3-5dB difference across the entire bandwidth studied, Figure 2.37. Thus the H-plane radiation patterns of the E28M array were more asymmetric than those of F28A. This indicated that E28M had more manufacturing errors than F28A. The 2^n grating lobes in the E-plane of the E28M 16x16 array were 5dB higher than those of F28A at 30.8GHz, Figures 2.30 & 2.32. This was due to the E28M 2x2 nulls been further removed from the 2^n grating lobe position, Table 2.4. At 27.8 and 29.3GHz, the grating lobes were suppressed to about –20dB, Figure 2.32. This behaviour was more consistent with the experimental 4x4 array null positioning, Table 2.7. Thus phase errors on the 180° delay line in the 2x2 subarrays, as discussed in subsection 2.2.3, caused high E-plane 2^n grating lobes at 30.8GHz which brought

about the rapid rolloff of the scaled directivity as noted above, whilst conversely improving the H-plane pattern in terms of cross-polarised component and grating lobes over that of the F28A array. Thus, the causes of the difference in scaled directivity bandwidth between the two array types have been identified, and the cause of that difference has likewise been found within the geometrical structures of the arrays.

In terms of 2^n grating lobe control, different phasing (180° phase shift) between the 1x2 subarrays was shown to lower the sidelobes and cross-polarised component in the 2x2 subarrays but the patch and 1x2 subarray design are of the greatest importance, as were responsible for the co-polarised null placement and majority of cross-polarised component generation. The 2^n grating lobes were created by the non-identical feeding to the patches in each 2x2 subarray, and were a negative consequence of the cross-polarised component reduction techniques which involved feeding the patches in a manner that the cross-polarised modes on the patches (TM_{01} and TM_{02}) were in phase opposition in the array principal planes. The E28M array gave reasonable boresight scaled directivity coverage of the LMCS frequency bands and was a very low profile antenna array. Performance could be further improved by feeding with a low loss rectangular waveguide feed network, at least to the 4x4 subarray level, as this will reduce the ohmic losses that occurred in the long lengths of microstripline in the 16x16 arrays and remove the long lengths of microstripline as a source of manufacturing error.

Multiplication of the co-polar radiation patterns of the 4x4 subarrays by appropriate array factor yielded patterns equivalent to those of a full 16x16 arrays. However, the effects of mutual coupling and manufacturing defects were not accounted for by this array factor multiplication method. Excluding the manufacturing defects seen as asymmetries in the H-plane radiation patterns, the remainder of the differences between the experimentally measured 16x16 arrays and

the array factor multiplication of the patterns of the 4x4 subarrays would be due to mutual coupling.

Examining the sidelobes of both 16x16 arrays across both E and H-planes and all frequencies studied, there was an almost random agreement between the array factor and experimental results. For certain sidelobes, the array factor produced exactly the same sidelobe level, shape and angular position as that measured experimentally. For others, only the angular position was correct, and for the remainder there was no resemblance. The sidelobes and 2^n grating lobes for which the array factor and experimental 16x16 had good agreement were not greatly influenced either by mutual coupling or manufacturing defects. The remaining sidelobes and grating lobes were affected by mutual coupling. However, exact demarcation of the effects of mutual coupling between adjacent 4x4 subarrays and the effects of manufacturing defects was only possible for the H-plane radiation patterns, where reasonable symmetry indicated an absence of manufacturing defects. Generally, the H-plane sidelobe levels were lower in the experimental results, Figures 2.31 & 2.33. For example, the array factor generally predicted that the first sidelobe levels at about –8dB below the mainlobe, but experimentally the levels were about –13dB. Thus the first sidelobes were lower than predicted by the array factor due to mutual coupling.

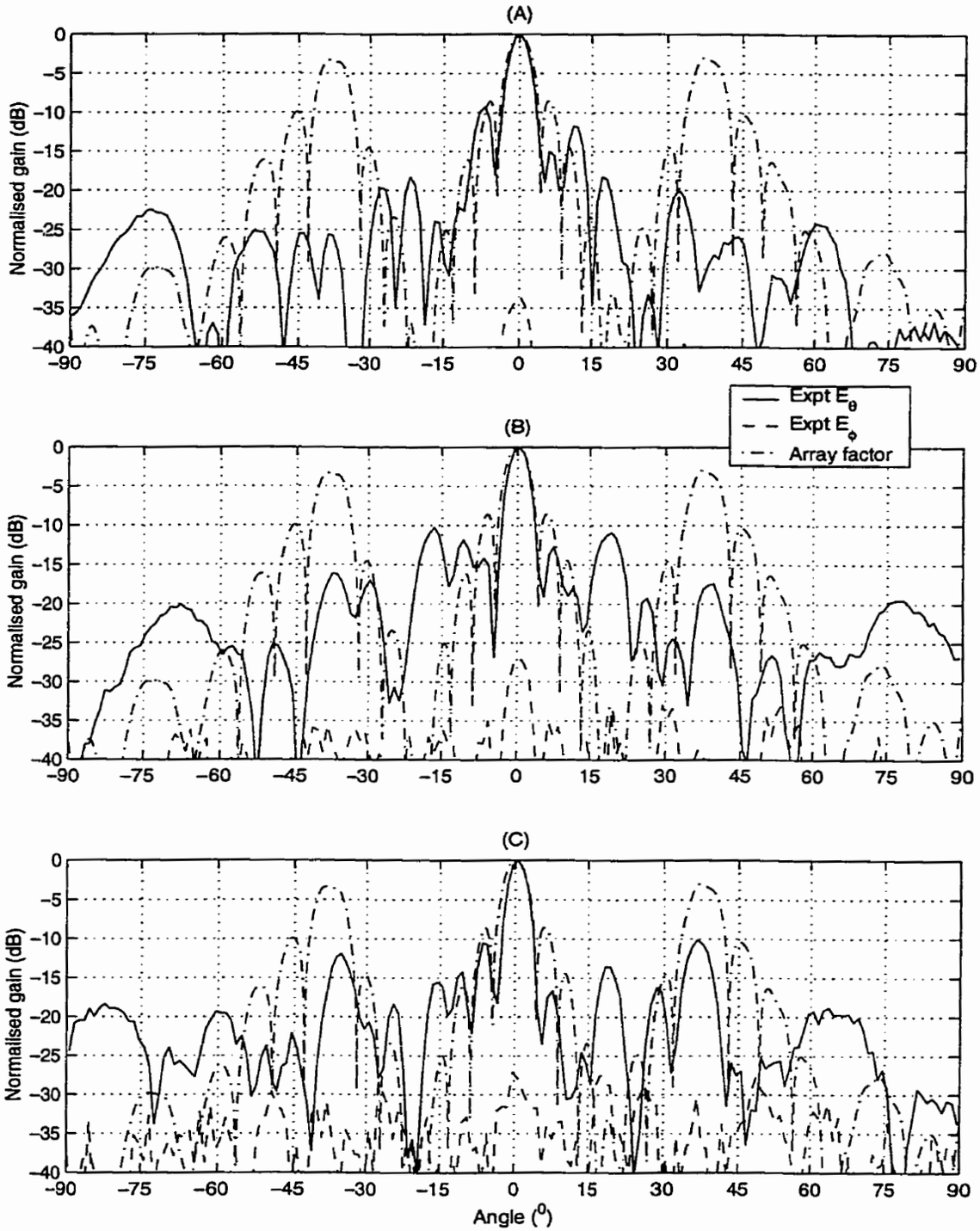

Figure 2.30: Experimental E-plane radiation patterns of in-phase fed F28A 16x16 array.

(A) 27.8GHz, (B) 29.3GHz, (C) 30.8GHz.
"expt" was 16x16 array, "array factor" was 4x4 co-polarised component multiplied by appropriate array factor
patch dimensions and spacing taken from Table 2.5

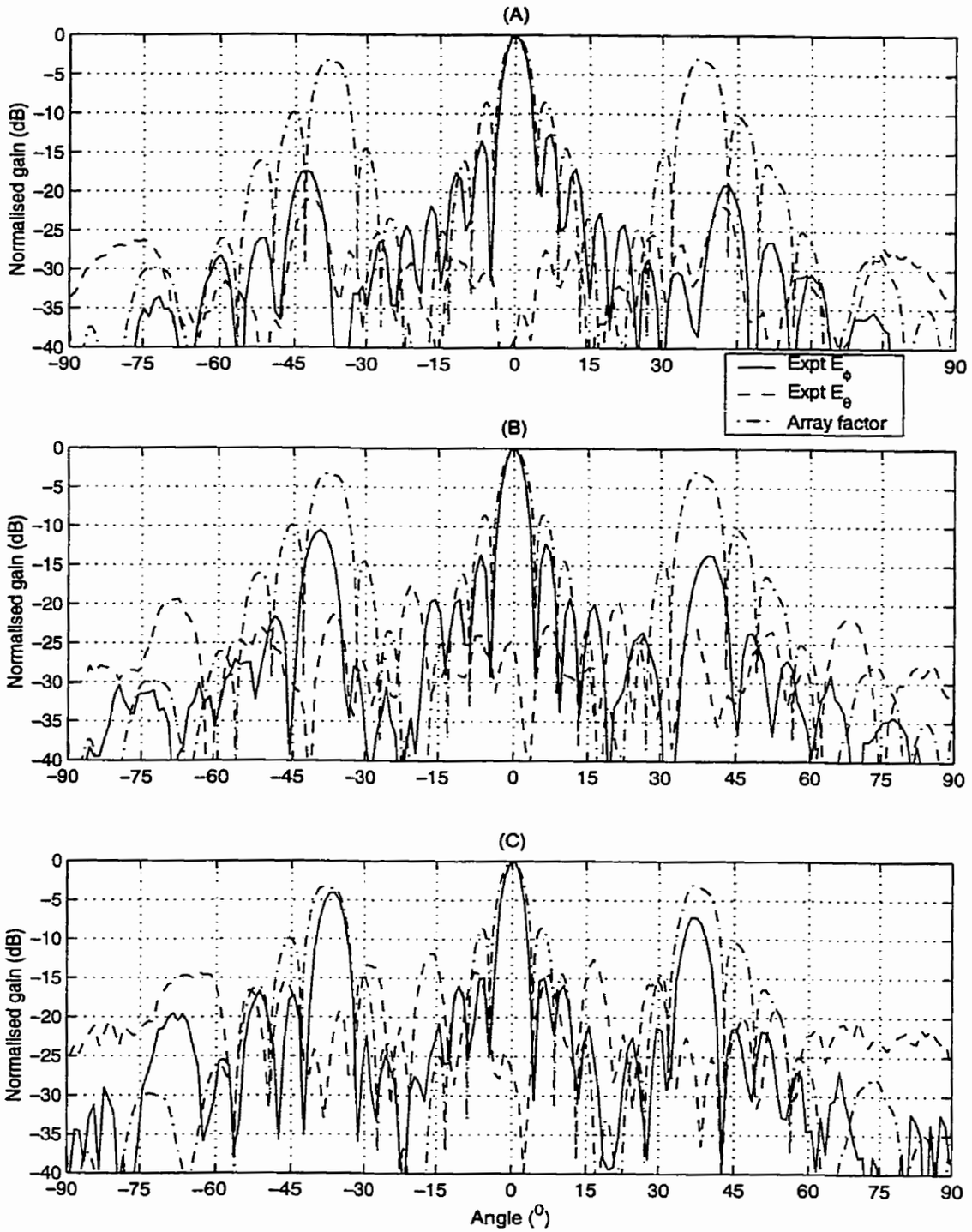

Figure 2.31: Experimental H-plane radiation patterns of in-phase fed F28A 16x16 array.

(A) 27.8GHz, (B) 29.3GHz, (C) 30.8GHz.
"expt" was 16x16 array, "array factor" was 4x4 co-polarised component multiplied by appropriate array factor
patch dimensions and spacing taken from Table 2.5

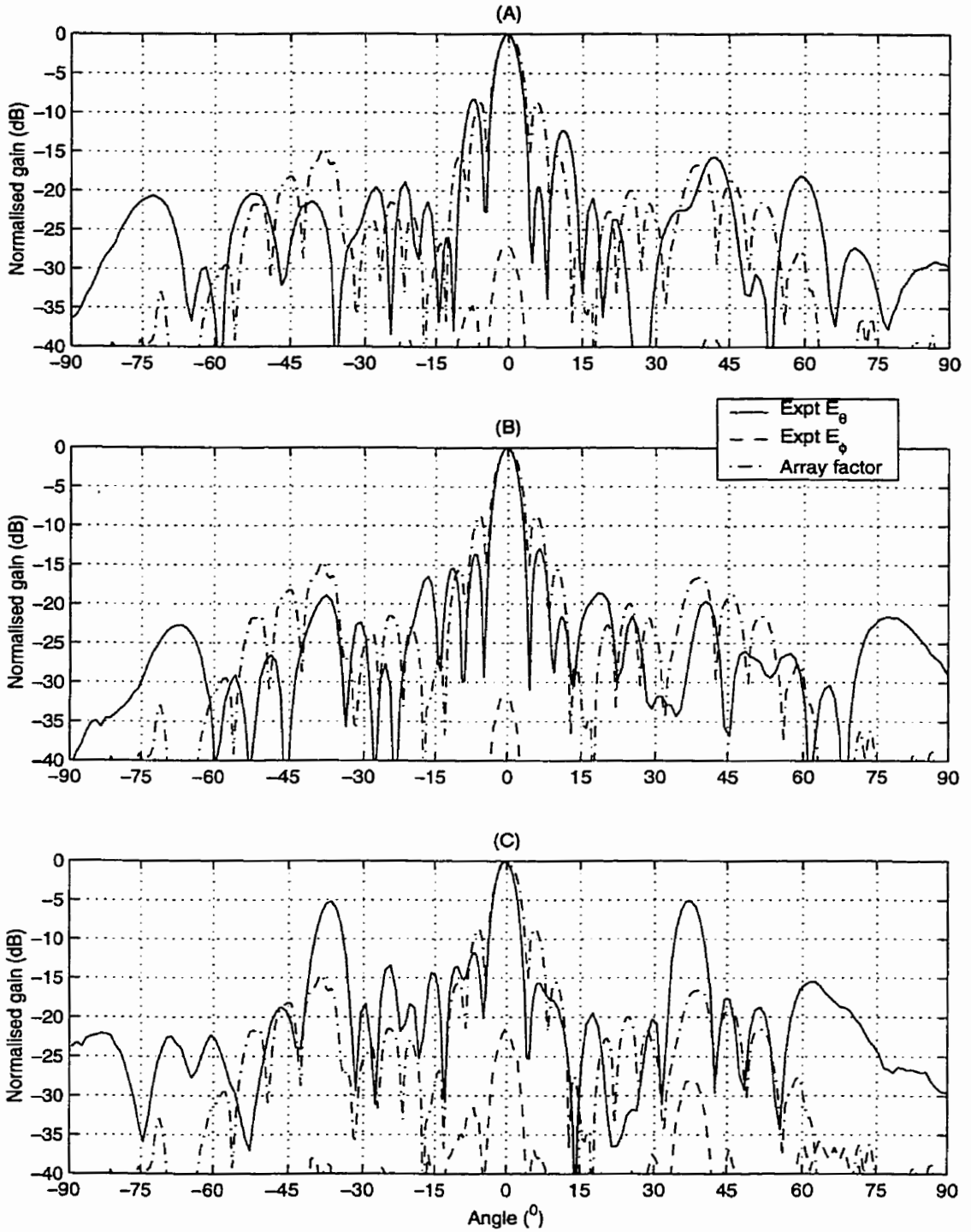

Figure 2.32: Experimental E-plane radiation patterns of in-phase fed E28M 16x16 array.

(A) 27.8GHz, (B) 29.3GHz, (C) 30.8GHz.
"expt" was 16x16 array, "array factor" was 4x4 co-polarised component multiplied by appropriate array factor
patch dimensions and spacing taken from Table 2.5

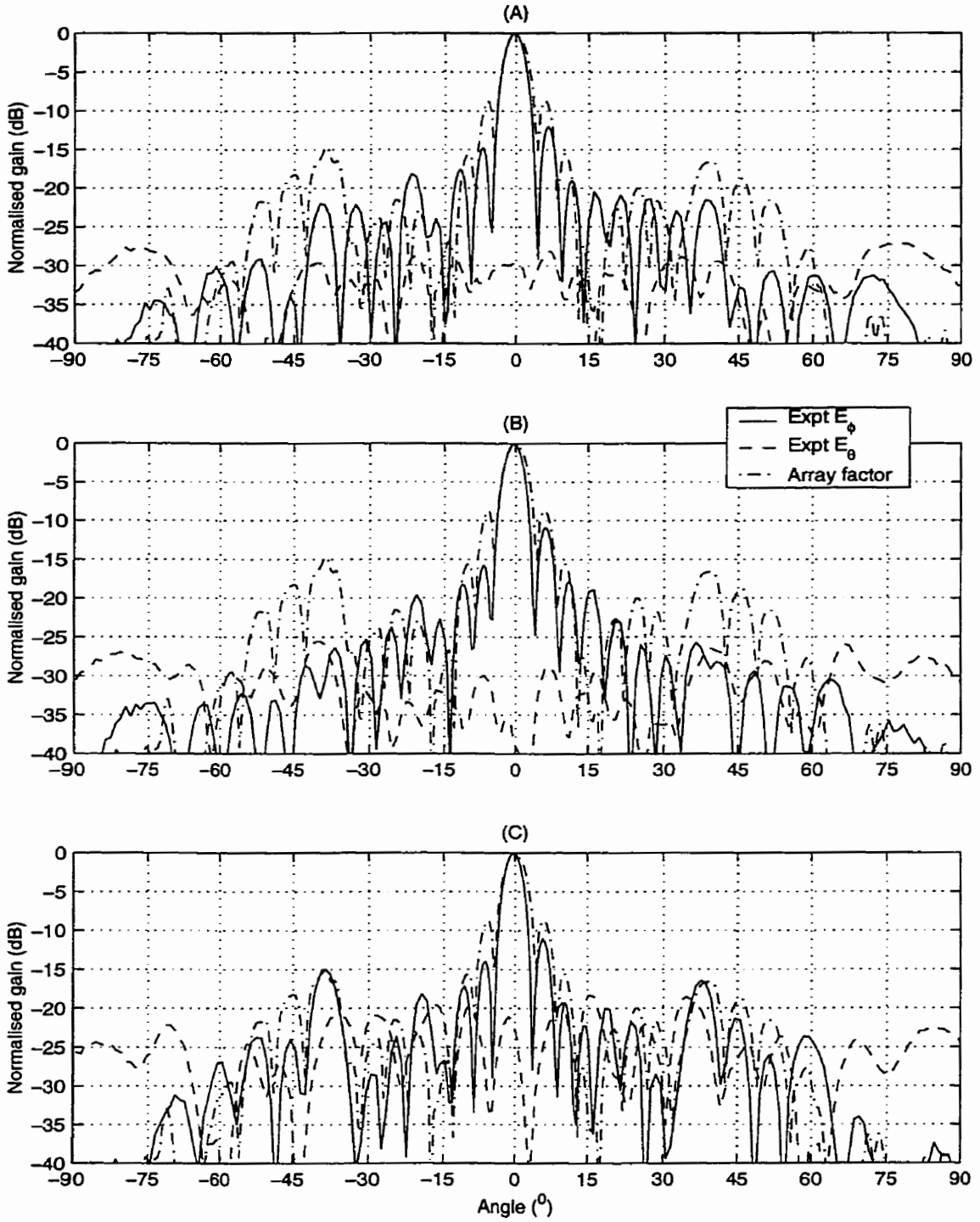

Figure 2.33: Experimental H-plane radiation patterns of in-phase fed E28M 16x16 array.

(A) 27.8GHz, (B) 29.3GHz, (C) 30.8GHz.
"expt" was 16x16 array, "array factor" was 4x4 co-polarised component multiplied by appropriate array factor
patch dimensions and spacing taken from Table 2.5

2.4.3 Summary of 16x16 microstrip array study

It was found that the input impedance bandwidth of the 16x16 arrays was improved over that of the 4x4 subarrays, Figure 2.29. The sidelobe levels of the 16x16 arrays were generally lower than that predicted by multiplying the 4x4 array radiation patterns by an appropriate array factor. The array factor was employed in an examination of the 2^n grating lobes, which were shown to be a major factor in loss of directivity for both F28A and E28M array types, as frequency was increased across the band of interest. The cause of the 2^n grating lobes was shown to be the repetition spacing of like radiators within the 16x16 arrays being above $1\lambda_o$ (about $1.60\lambda_o$). It was found that both 16x16 arrays suffered from experimental (over etching) errors as sidelobe levels and cross-polarised components were not perfectly symmetrical in the H-plane. The directivity behaviour of each 16x16 arrays was consistent with that of the 4x4 array used as a subarray.

2.5 G/T performance of arrays

Noise interferes with signal reception, and has sources both external to an array (from its environment) and internal [190]. The minimum detectable signal level is limited by the noise in the system. External noise sources, such as thermal radiation from the ground and atmospheric noise, can be detected by sidelobes, manifesting as the overall antenna temperature, T_A. Ohmic losses in the feed network and elemental antennas of an array are a source of internal noise. The G/T performance of a 16x16 microstrip array with and without feed network losses are compared in this subsection, to further elucidate the impact of the high feed network losses. The estimated gain figure of 29.26dBi for a E28M 16x16 array and feed network loss of 2dB were used here [193]. As the loss figure was derived from the measured performance of the 4x4 and 16x16 F28A microstrip arrays, it includes not only the ohmic losses but also the radiation losses (including the emissivity of the microstrip transmission line).

The antenna temperature, T_A, is not determined by the structure of the antenna, but arises from the sensitivity of the antenna (through its directional radiation pattern) to external sources [191]. The antenna temperature is a weighted average of the temperature from all external sources, where the weighting is dependant upon the radiation pattern of the antenna. For a ground based, point to multi-point architecture such as LMCS, the antennas will usually be aimed at the horizon. So, the lower half of an antenna's radiation pattern will see the ground (290°K), while the upper half will see the sky (3°K).

$$T_A = 0.5 \times 290°K + 0.5 \times 3°K = 146.5°K$$

Giving a weighting of 0.5 to either source, T_A=146.5°K. This figure applies to all antennas with symmetrical radiation patterns, aimed at the horizon.

When a lossy transmission line connects the antenna array elements to the receiver, the lossy transmission line reduces the effects of the antenna noise (T_A), but also contributes thermal noise proportional to its temperature [192]. The temperature of the antenna/lossy feed network system (T_{Ae}) {assuming no impedance mismatch between source/transmission line and antenna/transmission line} is given by a combination of equations (5-71b) and (5-72) of [192] {not given a designation in the text}.

$$T_{Ae} = \left(\frac{T_A + (L-1)T}{L} \right)$$

where T is the temperature of the lossy transmission line (25°C = 298°K)

L is the loss in the lossy transmission line (2dB from measurement in F28A arrays, which converted from dB gives L=1.5849)

using T_A=146.5°K, T_{Ae}=202.41°K

The temperature of the antenna/lossy feed network system (T_{Ae}) for the E28M 16x16 array was 202.41°K, roughly a 30% increase over that of the antenna temperature (T_A). If the lossy feed network was replaced with a lossless, or near lossless, feed network, the noise temperature of the combined antenna/transmission line system is the antenna temperature without modification. This would be the case if the microstrip corporate feed network was swapped for a rectangular waveguide feed network. The G/T for both cases will be assessed.

For the case with the lossy transmission line, the gain is known from the experimental results [193]:

$$G = 29.262\text{dBi} = 843.72$$

$$T = T_{Ae} = 202.41°K$$

$$(G/T)_{Lossy} = 843.72/202.41 = 4.17 = 6.2\text{dB}$$

For the case with the lossless transmission line, the gain is the transmission line losses added to the gain of the lossy case (this is a 4x4 array of 4x4 E28M subarrays {16x16 patches} fed by a lossless feed network, but including the transition loss from coaxial probe to microstrip line, the effects of which was included in the measured gain of the 4x4 E28M subarray: ie. this is a 16x16 patch array with 75% aperture efficiency):

$$G = 29.262\text{dBi} + L = 29.262\text{dBi} + 2\text{dB} = 31.262\text{dBi} = 1337.21$$

$$T = T_A = 146.5^{\circ}\text{K}$$

$$(G/T)_{\text{No losses}} = 1337.21/146.5 = 9.13 = 9.6\text{dB}$$

So, the G/T difference between the 16x16 microstrip array with and without a lossy feed network was 3.4dB, assuming that the transition loss from the lossless transmission line to 4x4 microstrip E28M subarrays was the same as that from coaxial probe to microstrip. This shows the consequence of 2dB losses in the feed network upon the G/T of the array used for an application such as LMCS, where it is aimed at the horizon. It should be noted that the feed network losses impacted the G/T in two ways. Firstly, the gain of the array was reduced by the feed network losses. Secondly, the feed network losses raised the array/feed network system temperature. This double impact upon the G/T by the feed network losses causes a change in G/T greater than the loss itself. These calculations also showed the advantages of feeding the 4x4 subarrays within a 16x16 array with a rectangular waveguide feed network instead of microstrip line.

2.6 Conclusions

The purpose of this chapter was to investigate NRE patch arrays as candidates for waveguide fed subarrays, to be used in a similar fashion to the RE patch subarrays considered by a prior investigator [15]. The study followed a design process starting with a NRE patch design through to a large array, and found a high degree of continuity with null placement. The process of large array design could possibly be automated at some time in the future. The importance of careful NRE patch design and 1x2 subarray design to the behaviour of large arrays was demonstrated.

The design reduced cross-polarised component to a limiting value with NRE patch design. The limiting value was higher for thick substrate used here (-17dB) compared to that for thin substrates used by prior investigators (-22dB) [72]. The cross-polarised component was further reduced in the principal planes by opposed but in-phase feeding in 1x2 subarrays and 180° electrical and physical feeding between 1x2 subarrays in the 2x2 subarrays. These methods were successful in reducing cross-polarised component but produced 2^n grating lobes, which caused directivity loss in the larger arrays. Null placement in 2x2 subarray patterns was used with varying degrees of success to mitigate 2^n grating lobes.

The experimental results of 4x4 NRE subarrays (the size used for rectangular waveguide fed subarray by Wiess [15]) comparable to, or better, than previously reported for single RE patch arrays. The best design employed 180° delay line and achieved 75% aperture efficiency. The highest aperture efficiency in 16x16 arrays was 40%, due to high feed network ohmic losses.

Effects of phase error on the 180° delay line in the 180° fed 2x2 subarrays were noted, as was the patch to line coupling in the in-phase fed 2x2 subarrays. In the former case, phase error

caused the rapid directivity loss seen at higher frequencies, as the 2x2 E-plane nulls were scanned and thus no longer mitigated the 2^n grating lobes.

CHAPTER 3: Numerical study of short backfire antennas

3.1 Introduction

The aim of the studies detailed in this chapter was to develop a low profile, 2.0-3.0λ_o diameter waveguide fed array element which intrinsically mitigates grating lobes either by high directivity, null placement, or a combination of both. Short backfire antennas (SBAs) offer a low profile alternative to horn antennas, while having similar radiation characteristics. An array of short backfire antennas (SBAs) could be die cast in two metal blocks, Figure 3.1. The subreflectors would be suspended from an overlaying radome (not shown), and matching pins or irises could be inset as a thin metal sheet between the upper antenna block and lower waveguide block, Figure 3.1. Such an array will be thermally stable and thus offer that advantage over microstrip technology, but at the cost of greater height and weight.

As noted in the introductory chapter, there was scant literature surveying different cavity shapes of SBAs. Thus, before investigating SBAs as possible array elements, a study of seven different cavity shapes was undertaken using the commercially available finite element method (FEM) software HFSS 6.0™. Cavity depth and waveguide inset depth were also briefly considered. A theoretical analysis technique could not be used as it does not exist, as noted in Chapter 1 and Rayner [175]. The advantage of conducting numerical as opposed to experimental trials is that studies can be undertaken more quickly and at less cost. In total, some 205 trials were run on HFSS for this chapter. As with the previous microstrip work, the antennas were primarily assessed in terms of directivity, aperture efficiency and input impedance, but at 15 GHz. This is half of the desired design frequency, at which manufacturing tolerances were less stringent and

any antennas found suitable to be used as array elements merely needed to be halved in all dimensions to operate at 30GHz.

The SBA geometry chosen for these experiments was unusual because the subreflector was at the same height as the cavity rim, Figure 3.2. The intention being to suspend the subreflector on a thin dielectric film attached to the top of the cavity wall. This avoided using thick machinable plastic support structures for the subreflector, as used by some prior investigators [150,157,158]. This approach was taken as such supports can alter the cavity fields. However, it has been shown that having the subreflector at the same height as the top of the cavity wall is not optimal in terms of cross polarisation level [175].

Finally, a SBA cavity optimised for a high aperture efficiency is presented. This novel design has a curved juncture between cavity rim and floor. A comparison is made to the typical cylindrical cavity type by examination of the aperture fields, and the cause of the directivity difference identified.

3.2 Numerical model definition

All trials were conducted using the commercially available FEM software HFSS 6.0. A simplified model was used for the diameter studies and other trials undertaken for this chapter. This simplified model consisted of solids representing the SBA cavity and waveguide feed set against a rectangular prism radiation space, Figure 3.3. All faces of the prism were radiation boundary conditions, except that to which the cavity was connected. Between the cavity and prism, all field quantities were continuous. The remaining part of that connecting face of the prism was assigned to perfect E conductor boundary condition, making it appear that the cavity

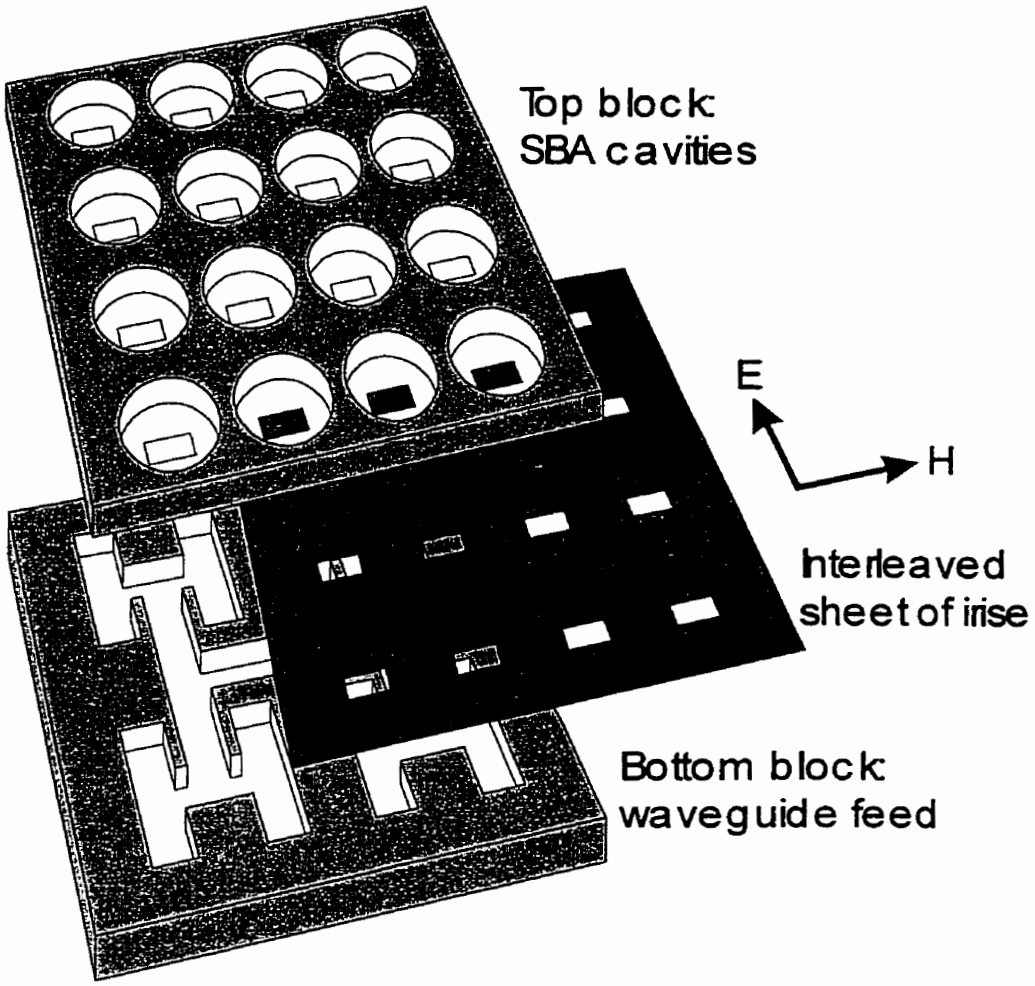

Figure 3.1: **Array of SBAs showing cast blocks & thin metal sheet for impedance matching**

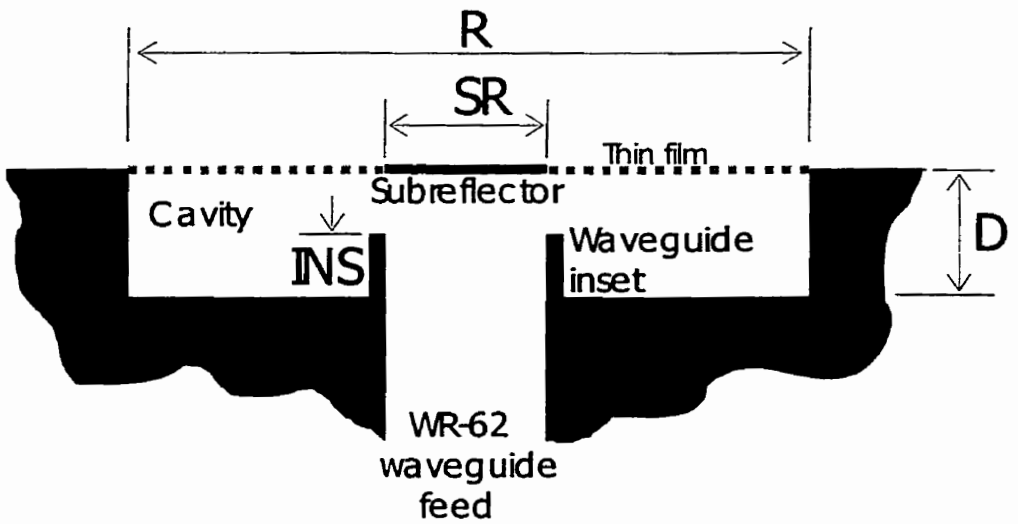

Figure 3.2: **Cross section of the SBA geometry investigated**

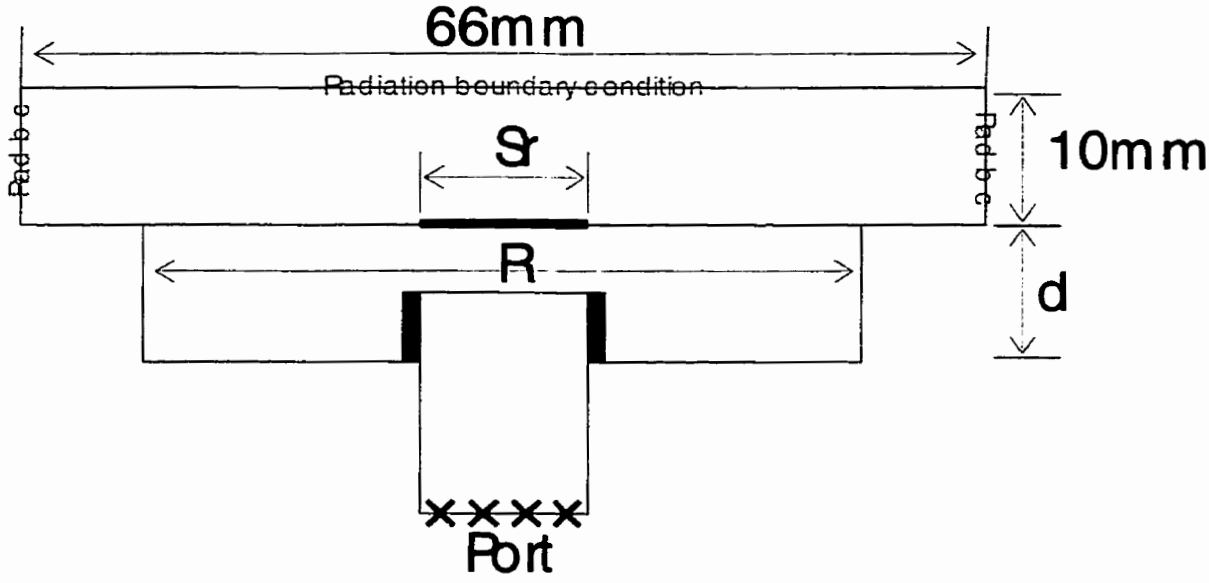

Figure 3.3: Geometry of infinite ground plane numerical model of SBA

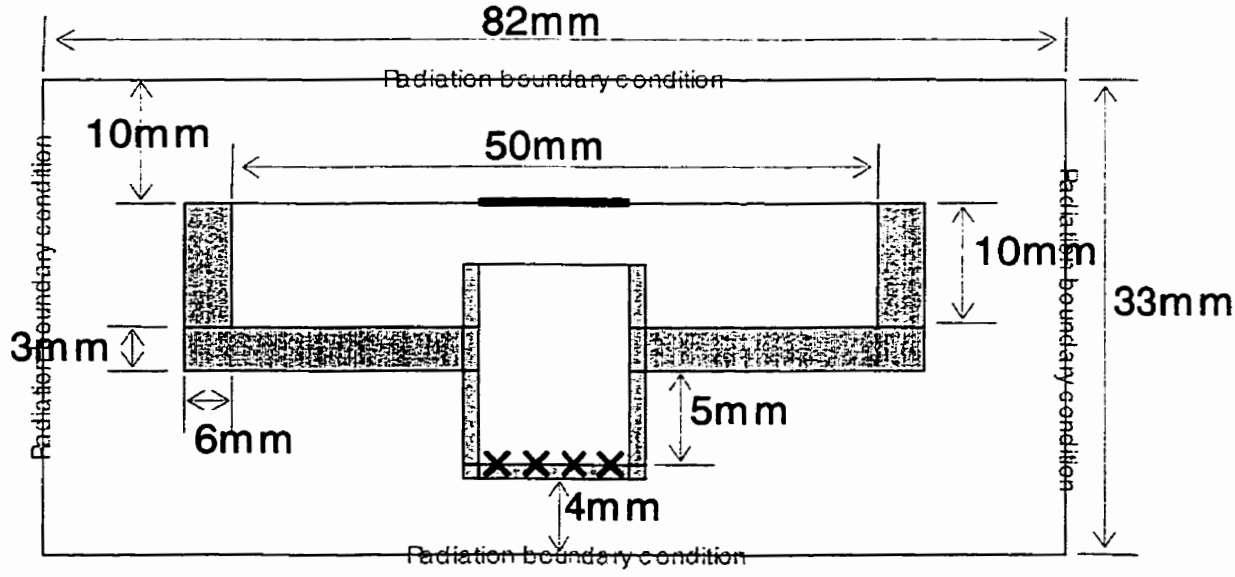

Figure 3.4: Geometry of finite ground plane numerical model of SBA

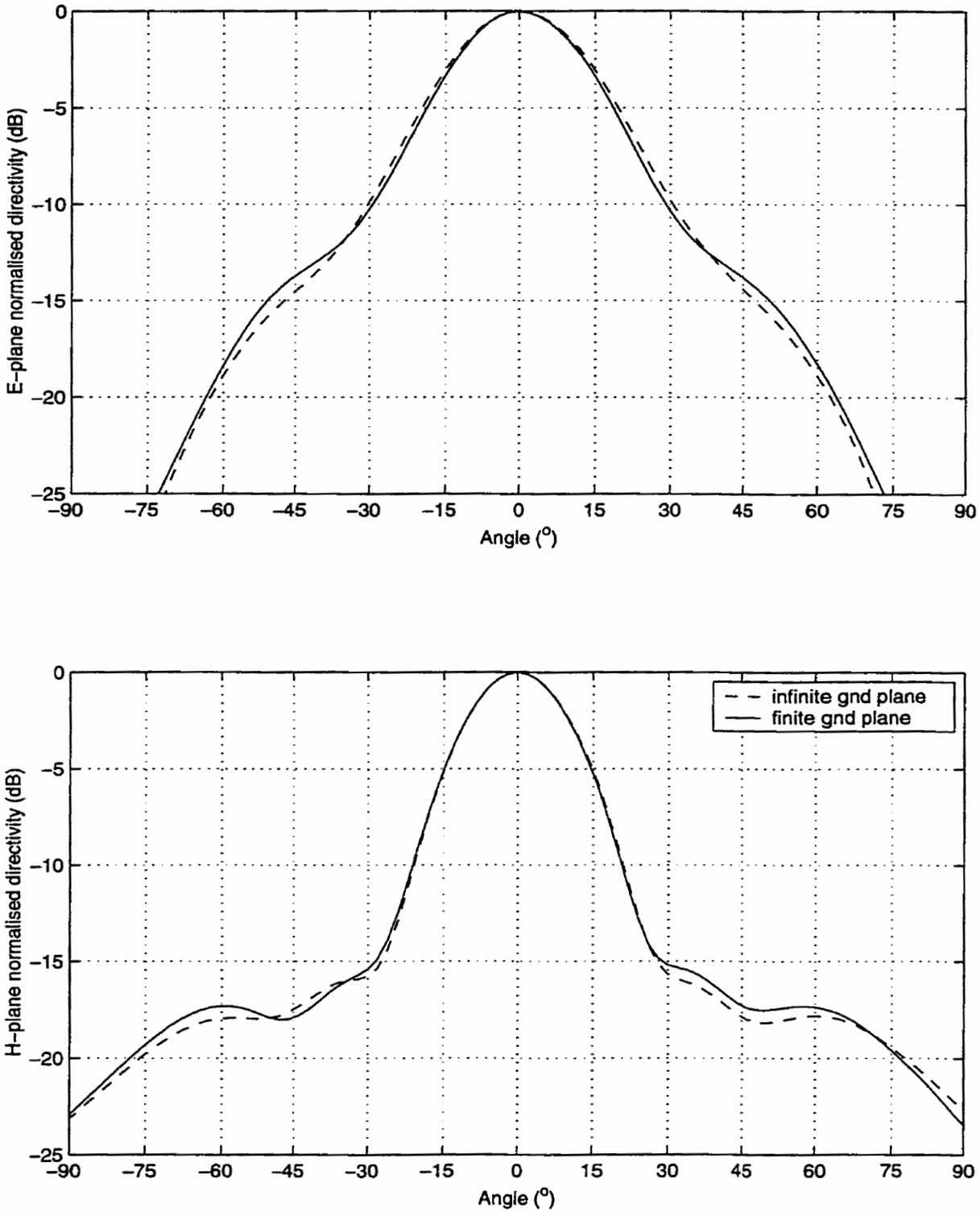

Figure 3.5: Comparison of radiation patterns from finite and infinite ground plane models

D=0.5λ_o, SR=0.5λ_o, subreflector was circular, f=15GHz, cavity profile was Fig. 3.8A

was set into an infinite ground plane. This infinite ground plane model was structurally simple and relatively small in computational requirements. However, many features such as the thickness of the cavity walls (which may cause some diffraction effects) are wholly lacking, and a comparison to a full model was necessary for model validation. Such a full and finite ground plane model represents all features that would be found in an experimental antenna, Figure 3.4. A comparison of equivalent infinite and finite ground plane antennas is made, being followed by a more complete description of the infinite ground plane model that was used later in this chapter.

A comparison of the far field radiation patterns in the principal (E and H) planes of the infinite and finite ground plane SBA models shows that the pattern shapes are indistinguishable to about 15dB below the peak of the main-lobe, Figure 3.5. For lower levels and angles greater than 20°, the patterns are very similar. The angles at which various features occurred were identical, leaving only slight differences in level. The cross polar component of the radiation patterns in both planes were below –45dB from the peak of the main-lobe. The levels of the cross polarised component were roughly equal, but the features were different. This is sufficient agreement, as the values of the cross polar components are so small in comparison to the co polar components. Therefore, the infinite ground plane model has been shown to yield near identical radiation pattern characteristics to a model that fully represented all characteristics of a SBA. Further, this additionally suggests that the neglected features are of little importance to the operation of a SBA. Confidence in the accuracy of numerical tool HFSS is a consequence of obtaining similar results from two quite different, but electrically equivalent, models. The reasonable agreement between experimental and numerical results for a similar type of antenna provides further confidence in HFSS for modeling this type of antenna. A more complete description of the infinite ground plane model follows.

A radiation space is required for radiating structures modeled in HFSS; a prism of $3.3x3.3x0.5\lambda_o$ (66x66x10mm) filled with vacuum was used for this purpose, Figure 3.3. This is in contrast to the finite ground plane model which was enclosed by a cylindrical radiating space, Figure 3.4. For all trials, the boundaries of the radiation space were seeded with triangles of side no greater than $0.1\lambda_o$ (2mm) so that the radiation boundaries of all models would be comparable, irrespective of how many iterations were taken by the solver to reach the solution criteria of max. $\delta S=0.02$. The typical number of tetrahedra for an infinite ground plane model was 28,000. All circles and circular solids were segmented at 16 segments per 360°. An inset waveguide feed depth of $0.25\lambda_o$ was usually used. A thickness of 1mm was used for the WR-62 rectangular waveguide. The design frequency was 15GHz, having a free space wavelength (λ_o) of 20mm. All trials were conducted using HFSS 6.0 running on either Pentium II or Pentium III IBM compatible personal computers. Either computer had 500MBytes of RAM, which although large placed an upper limit on the fineness of meshing possible and solvable problem size.

The simplified SBA model used throughout this chapter was introduced in this section. It was compared to an equivalent model that accounted for all features of an experimental SBA. The high level of agreement between the results from the two very structurally different models, validated not only the software but also the simplified model. Use of the simplified model required the solution of a much lower number of unknowns, and was more convenient as the cavity was not buried within a radiating space and a metal cup, as in the finite ground model. The equivalence of the infinite and finite ground plane model also suggested that the neglected features in the former were relatively unimportant to the operation of this type of antenna. As a result, the fields within the cavity are much more important than any on the surrounding ground plane or outside of cavity walls.

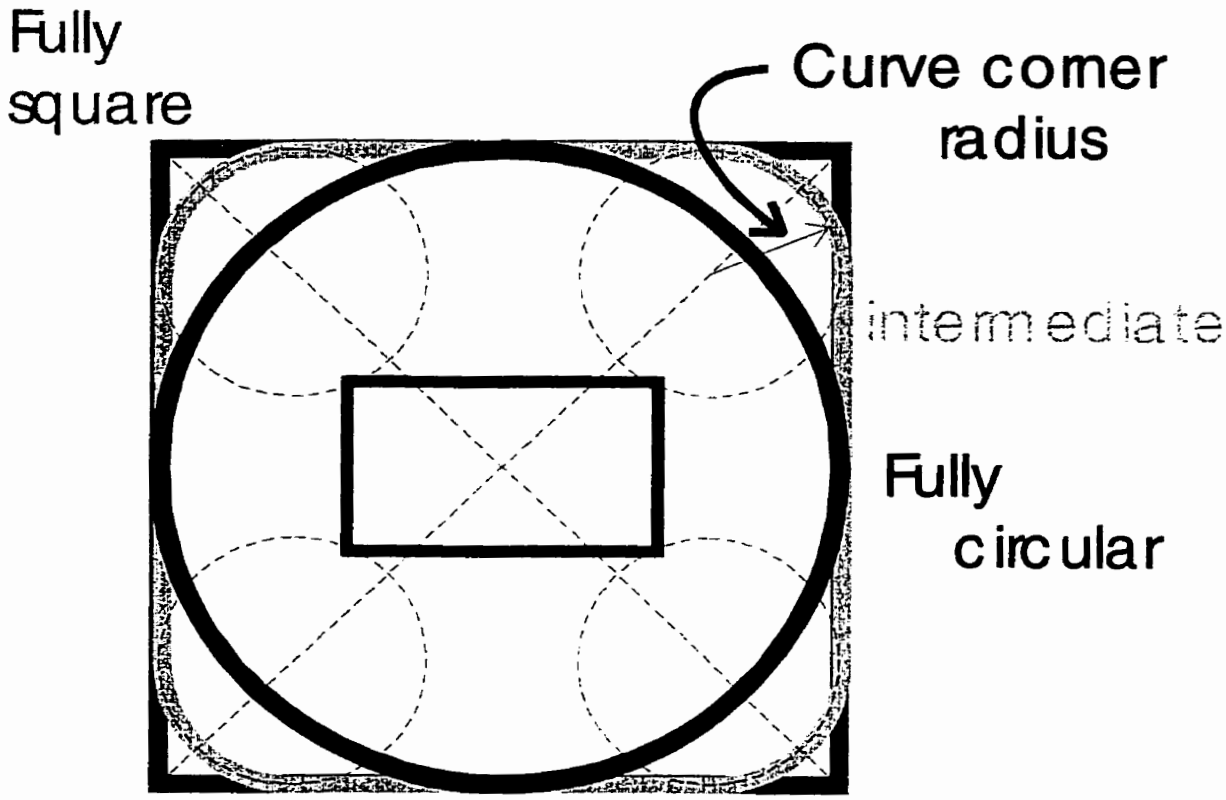

Figure 3.6: Representative diagram of metamorphosis from square to circular SBA

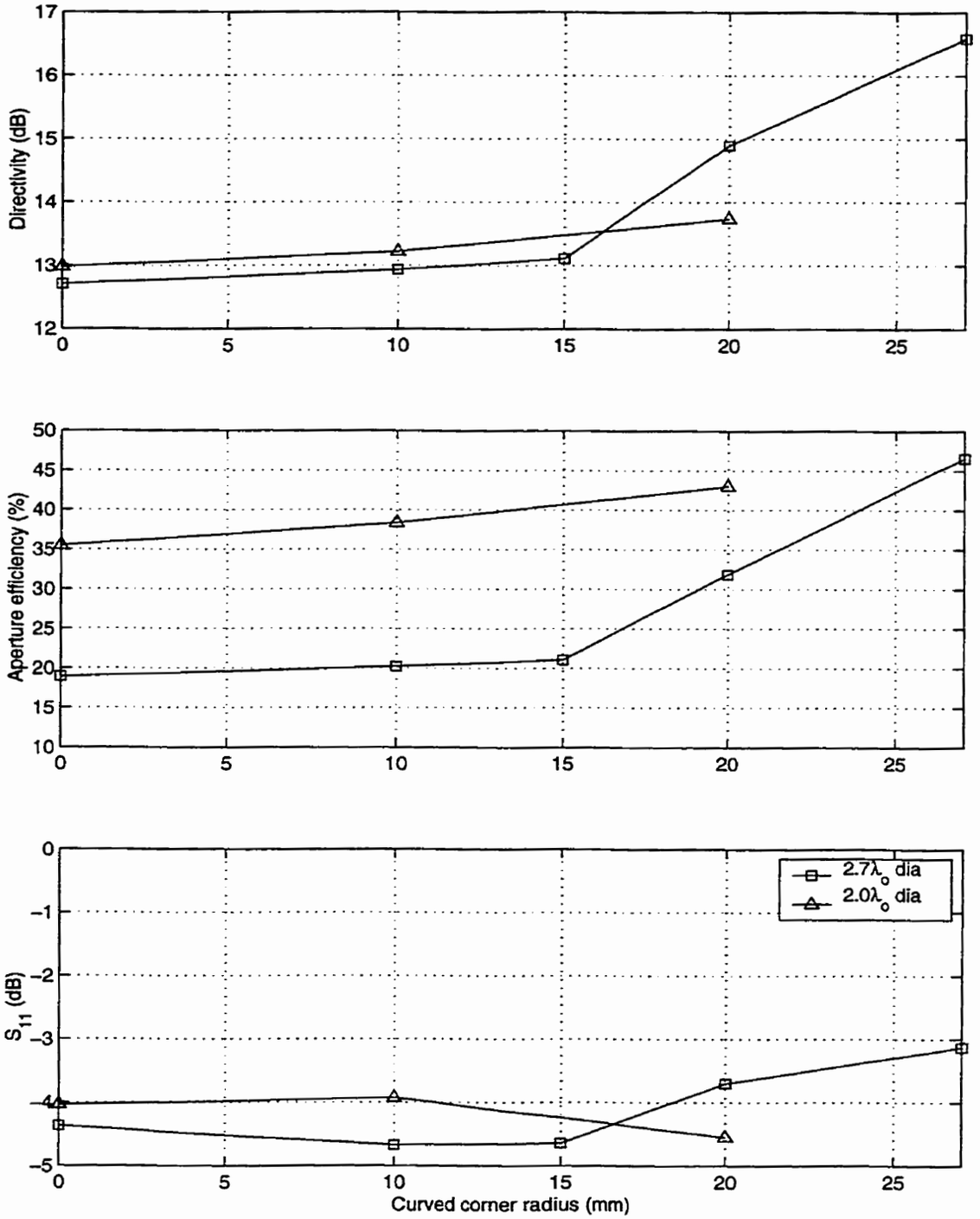

Figure 3.7: Boresight radiation and input impedance variation in metamorphosing from fully square to fully circular circumference shape

illustrated in Figure 3.6
D=0.5λ_o, SR=0.5λ_o, subreflector was circular, f=15GHz, cavity profile was Fig. 3.8A

3.3 Effect of cavity circumference shape

The existing literature suggests that there is little performance difference between square and circular reflectors [26, 27, 156, 167]. Two reflector diameters were investigated; $2.0\lambda_o$ and $2.7\lambda_o$. All models had a flush rectangular waveguide feed (no inset into the cavity), a $0.5\lambda_o$ diameter circular subreflector in the mouth of the reflector cavity, which was $0.5\lambda_o$ in depth. The trials involved a stepped metamorphosis from square to circular reflectors, done by replacing each of the square corners with a cylindrical section, Figure 3.6. This was done in 3 steps for the $2.0\lambda_o$ diameter antenna, and in 5 for the $2.7\lambda_o$ diameter antenna. The centre points of the sides of the square cavities were common to the circular cavities.

Comparison of the directivity and derived aperture efficiencies for the cavity diameters studied shows that there is a much greater difference between the square and circular versions for the larger cavity diameter, Figure 3.7. The directivity increased most rapidly for curved sections of just over half the diameter to full circular cavity. For the $2.0\lambda_o$ diameter antenna, the directivity difference between square and circular was 0.7dB, while it was 4dB for the $2.7\lambda_o$ diameter antenna, Figure 3.7. This observation of the $2.0\lambda_o$ design is in agreement with the literature where it was stated that there was little difference between square and circular cavities, and it is likely that approximately $2.0\lambda_o$ diameter antennas were used [26,27,156,167].

The difference was significant for the $2.7\lambda_o$ diameter antenna. For the square cavity case, the $2.0\lambda_o$ reflector had a higher directivity and radiation efficiency than the larger diameter. This, perhaps, explains the aversion to large diameter cavities by previous investigators, as the smaller antennas make better use of lateral space in terms of the achievable directivity and aperture efficiency. However, the circular $2.7\lambda_o$ diameter antenna gave about a 4% higher efficiency than

the circular $2.0\lambda_o$ diameter antenna. So, unintentionally, a case has been found for which a larger diameter cavity produced a higher aperture efficiency than a $2.0\lambda_o$ diameter cavity, which has been much favoured in the past [142,144]. This has shown that a larger antenna can make better use of its aperture area than a smaller one, and suggests that the undertaking of a careful parametric study of cavity diameter influence upon directivity would be of value.

In summary, for both diameters studied, a circular cavity circumference shape gave the higher directivity, and thus circular cavities are recommended if high directivity is sought. Additionally, for larger reflector diameters it is more important to use a circular cavity. The need for a careful study of the effects of cavity diameter upon directivity was identified.

3.4 Effect of cavity profile

A number of unique cavity profiles have been shown to improve the directivity of single antennas for the particular diameters studied [150-152, 157, 158], and it has been noted that insetting the rectangular waveguide feed into the cavity formed by the cavity floor and rim has likewise produced some improvement in the limited number of diameters studied [142]. There is thus a need to qualify these effects, and that of cavity diameter, as an initial step in the investigation of short backfire antennas as array elements.

A parametric study of cavity diameter using HFSS was undertaken on seven different reflector profiles, Figure 3.8. All profiles were circularly symmetric about the centre of the waveguide feed. For most of these, both inset and flush rectangular waveguide feeds were tried.

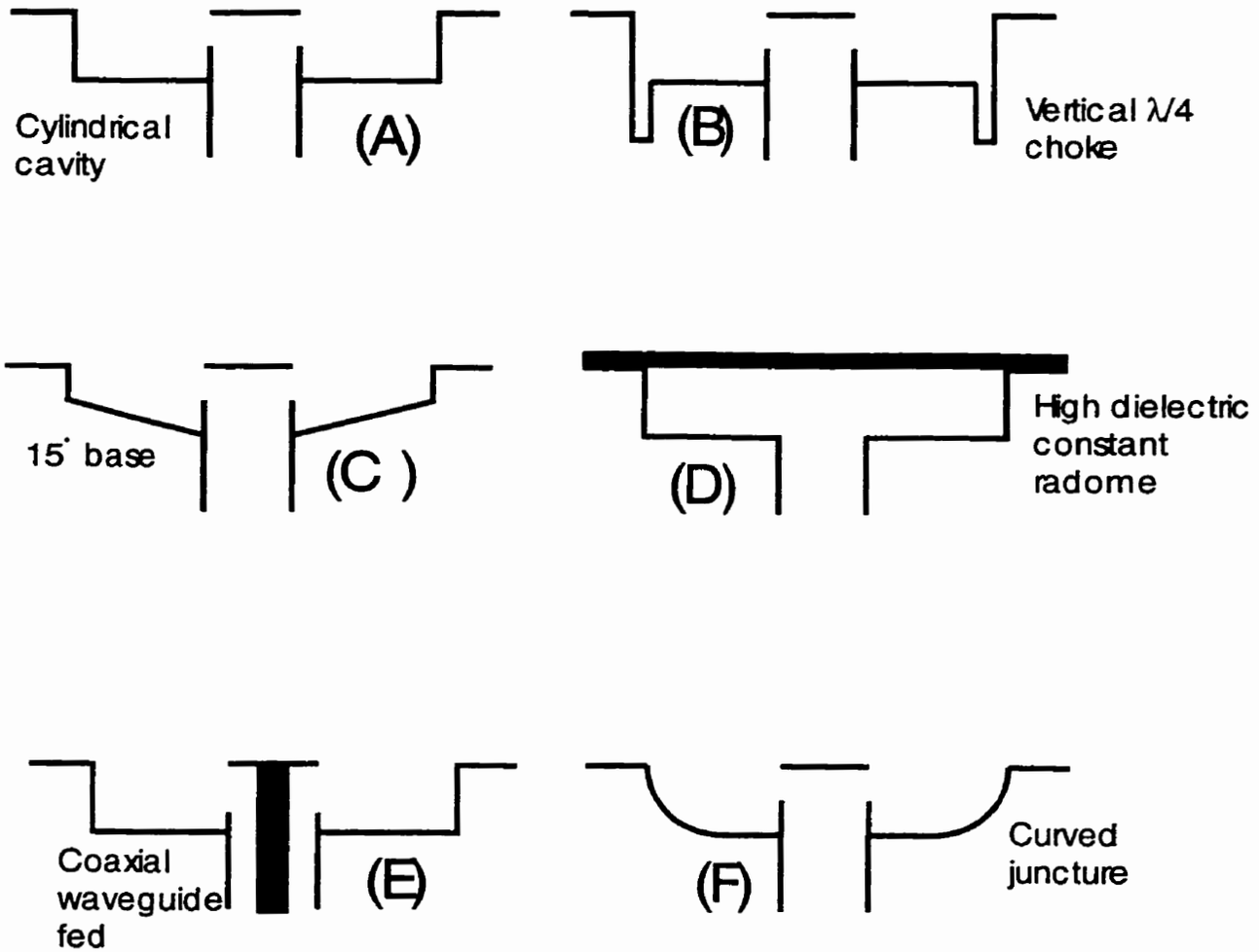

Figure 3.8: Representative diagrams of SBAs profiles for parametric study

the cylindrical cavity profile (A) was also used for a square cavity antenna

Diameters from 1.8-3.2λ_o were investigated. The same cavity depth (rim height) of 0.5λ_o, 0.5λ_o diameter circular subreflector (0.5λ_o square for the square reflector) and radiation space were used as above in model validation and study of cavity circumference shape. For inset feed cases, the waveguide mouth was positioned half way between the cavity floor and subreflector; 0.25λ_o above the cavity floor. Once again, the directivity at boresight and resultant aperture efficiency were studied. In all presented data sets, the flat cylindrical base with flush feed was used as a reference for ease of comparison, as was done by [149, 150] with an inset fed antenna.

3.4.1 Flat based cylindrical cavity

Over the range of diameters, the directivity of the flat based cylindrical cavity ranges from 10.5-16.5dB (9-47% aperture efficiency) with flush feed, and from 8.5-16db (10-50% aperture efficiency) with inset feed, Figure 3.9. Higher directivity can be achieved with flush feeding, slightly higher aperture efficiency can be achieved with inset feeding. Across the range of diameters the flush and inset both had a lesser and greater peak in directivity, with a null inbetween, Figure 3.9. The lesser directivity peak for both flush and inset feeding occurred at 2.1λ_o. In contrast, the greater peaks occurred at different diameters, showing the effect of insetting the rectangular waveguide feed 0.25λ_o. Insetting the feed pulled the peak directivity from a diameter of 2.65λ_o to 2.45λ_o, and reduced its level by 0.5dB. It is interesting to note that the flush fed design gave higher directivities, by about 0.5dB, for diameters below 2.2λ_o. This contradicts the consensus from the literature that using an inset feed will produce better performance in an approximately 2.0λ_o diameter antenna [142-145]. This contradiction to the existing literature is due to the directivity being studied here as opposed to the gain which was

measured in previous investigators experimental studies. The mismatch loss of the flush fed antennas was thus probably higher than that of the inset fed, giving the latter a higher gain.

Examination of the S_{11} results for the flush and inset antennas across the range of diameters confirms this observation, Figure 3.9. For diameters of about $2.0\lambda_o$, the inset feed gave return loss values better than -10dB, while the flush feed gave rather poor input impedance matching of about -3.5 dB, Figure 3.9. The inset feed design happens to give good input impedance matching at diameters of about $2.0\lambda_o$ coincident with the lesser peak in directivity. This has led to the widespread use of this particular design. The inset feed also gave reasonable matching at diameters around $3.05\lambda_o$, explaining the occasional appearance of the $3.05\lambda_o$ design in the literature [150], despite its low directivity. The flush fed design had good matching at a diameter of $2.4\lambda_o$. However, this is a point of very poor aperture efficiency, again explaining its absence from the literature. Examination of both flush and inset feed designs shows that there may be a correlation between high directivity and poor input impedance matching, with the popular $2.0\lambda_o$ inset fed design been an obvious exception. Given the influence that insetting the rectangular waveguide has been shown to have upon directivity, aperture efficiency and input impedance, further investigation of its effects is warranted.

For increasing diameter, both the E and H plane far field radiation patterns of the inset fed cylindrical cavity SBAs show several common features. Comparing the radiation patterns for $2.2\lambda_o$, $2.6\lambda_o$ and $3.0\lambda_o$, it is seen for increasing cavity diameter that the main lobe beamwidth becomes narrower, the distinct nulls around 30° off boresight change and high side-lobes appear around 50°, Figures 3.10 and 3.11. The E and H radiation patterns for a diameter of $2.2\lambda_o$ most closely resemble those of a uniform aperture distribution, having side lobe levels of about -13.2dB. The radiation patterns of the larger diameters in both planes differ markedly from those

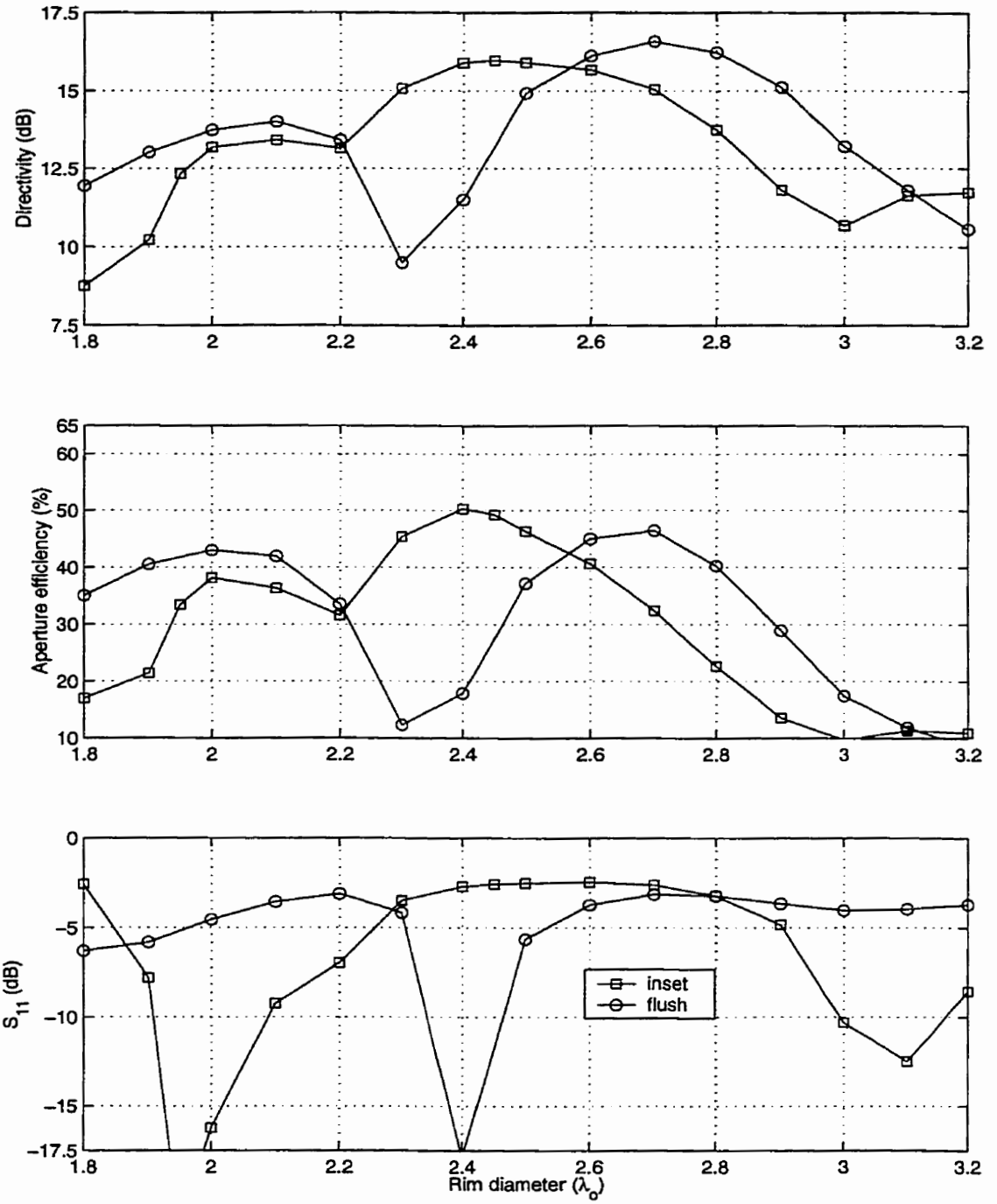

Figure 3.9: Boresight radiation and input impedance variation with increasing diameter for inset and flush fed cylindrical base SBAs

D=0.5λ_o, SR=0.5λ_o, subreflector was circular, f=15GHz, cavity profile was Fig. 3.8A

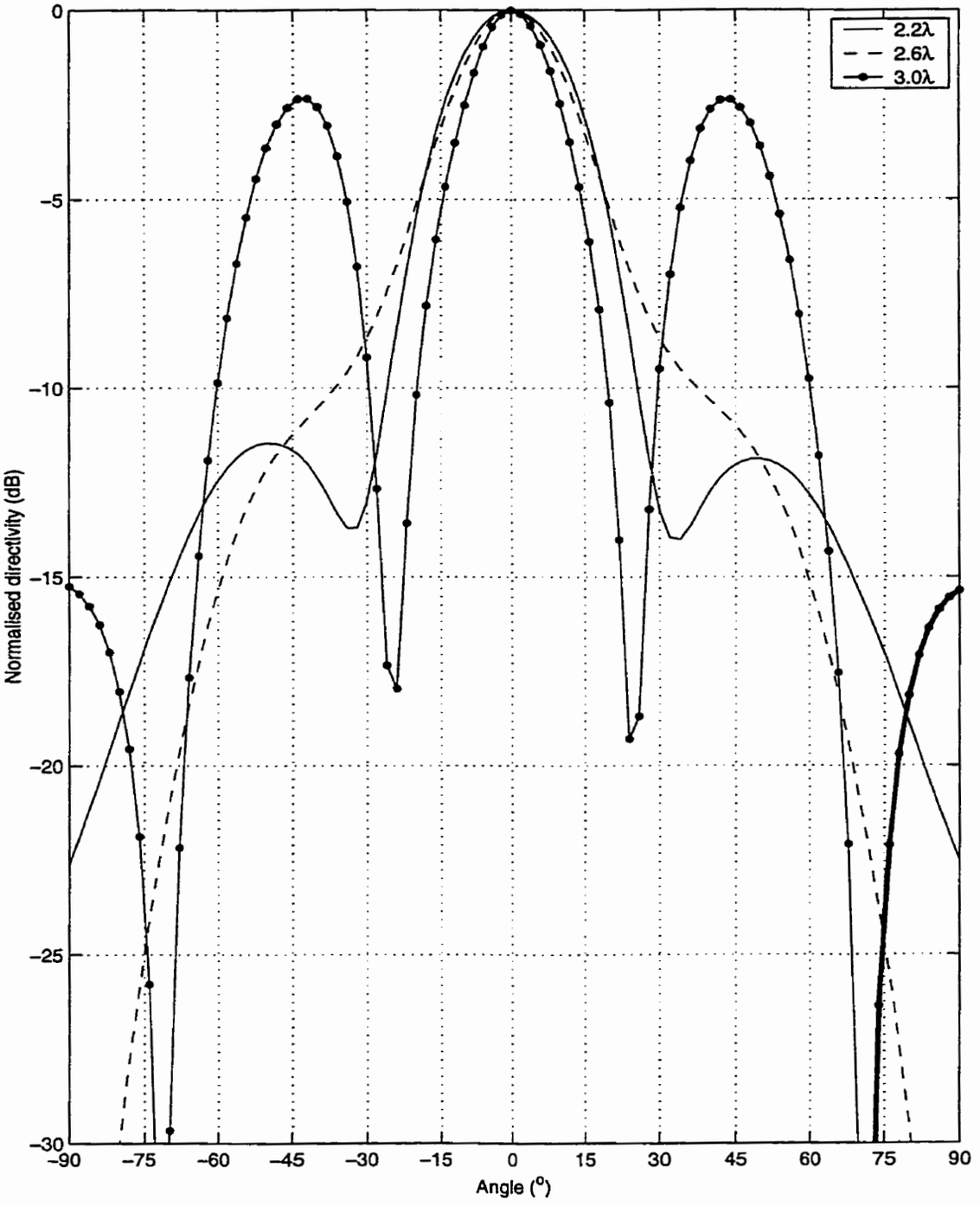

Figure 3.10: Selected E plane radiation patterns of flat based cylindrical SBAs

complementary to Figure 3.9
D=0.5λ_o, SR=0.5λ_o, subreflector was circular, f=15GHz, cavity profile was Fig. 3.8A

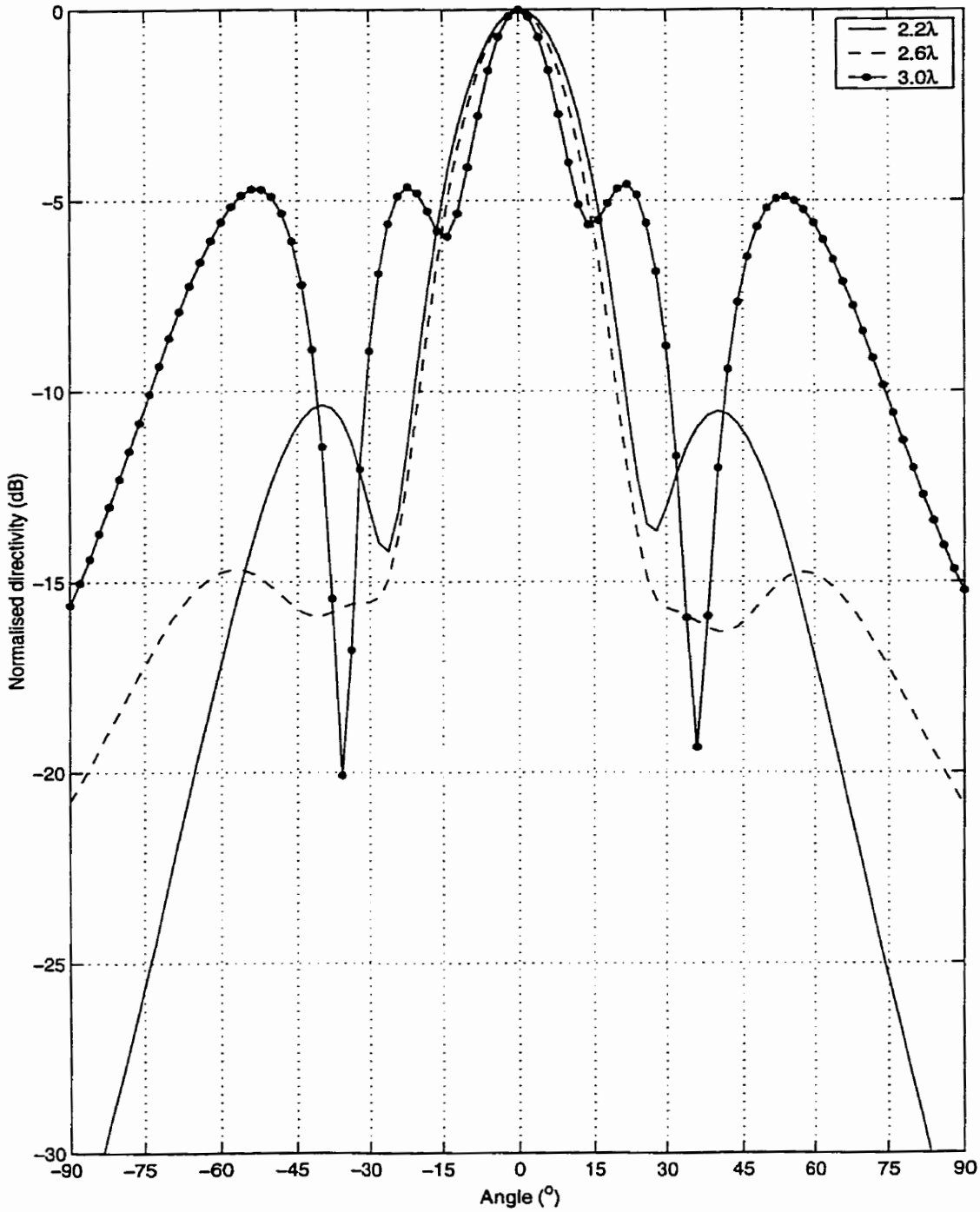

Figure 3.11: Selected H plane radiation patterns of flat based cylindrical SBAs

complementary to Figure 3.9
D=0.5λ_o, SR=0.5λ_o, subreflector circular, f=15GHz, cavity profile was Fig. 3.8A

of the $2.2\lambda_o$ antenna. This suggests that the aperture distribution produced by these SBAs changes with increasing diameter. These changes are responsible for variations in directivity noted in the diameter study above, Figure 3.9. The narrowing of the main-lobe in both planes, and the decrease in the H plane side-lobe level explains the 2.5dB increase in directivity going from $2.2\lambda_o$ to $2.6\lambda_o$, Figures 3.9-3.11. Whereas the rise of the 50° side-lobes to –2.5dB in the E plane and –5dB in the H plane consumed a large amount of power and caused the low directivity of the $3.0\lambda_o$ antenna.

With respect to null placement for grating lobe suppression, the radiation pattern of the $2.2\lambda_o$ diameter is the only one with nulls at the required angle. For an array with an interelement spacing of $2.3\lambda_o$ ($0.1\lambda_o$ given to cavity wall thickness) the first order grating lobe is expected at 26°. The H plane pattern has a null at 27°, which would suppress the first order grating lobe. In the E plane, however, the equivalent null is at 33°, and is thus not coincident with the grating lobe. Therefore this SBA would be suitable as an element in a one dimensional H plane array, but not for a two dimensional array as power will be lost into the E plane grating lobe. The radiation pattern changes that occurred with increasing diameter have been shown to have caused the directivity variation noted in the diameter study. Also, one of the antennas was assessed as an array element.

From the presented diameter study and radiation patterns, it has been found that the diameter of the cavity of a flat based cylindrical SBA affects the antenna's radiation pattern, directivity, aperture efficiency and return loss. The cavity diameter is thus a design parameter for SBAs. In the following sections, similar diameter studies are conducted for various other cavity profiles.

3.4.2 Flat based rectangular cavity

The behaviour of the square cavity antennas with square subreflectors differs markedly from those having the circular cavities, Figure 3.12. The variation of directivity with reflector side length did not show the lesser peak-null-greater peak relation as with the cylindrical cavities, and, generally, the inset feed gave higher directivity, Figure 3.12. The inset feed gave about 47% aperture efficiency for side lengths of 1.9-2.2λ_o (indicating broad bandwidth behaviour), above which it rapidly decayed to around 10%. The flush fed antenna over the same range of side length was characterised by much lower aperture efficiencies and violent variation of directivity with cavity side length. So, the introduction of an inset feed had a beneficial effect upon the radiation characteristics of a square sided cavity short backfire antenna. Also, comparison of the 2.0λ_o and 2.7λ_o flush fed antennas to those studied as part of the cavity shape change study shows a decrease in directivity of 0.7dB and 2dB, respectively, Figures 3.7 & 3.12. The only structural difference was that square, as opposed to circular, subreflectors were used for the diameter study in this work. It can thus be concluded that as with the cavity circumference shape, a circular subreflector will give a higher directivity for flush feeding. The input impedance behaviour with square cavity side length differed between flush and inset fed cases, as with the cylindrical cavity antennas discussed above, Figure 3.12. The input impedance of the flush fed version was relatively stable about —5dB across the range of diameters studied. In contrast, the S_{11} of the inset fed design was much more variable, and had a well matched point at a side length of 1.8λ_o. As with the cylindrical cavity, the cavity size has been shown to effect the directivity and input impedance matching.

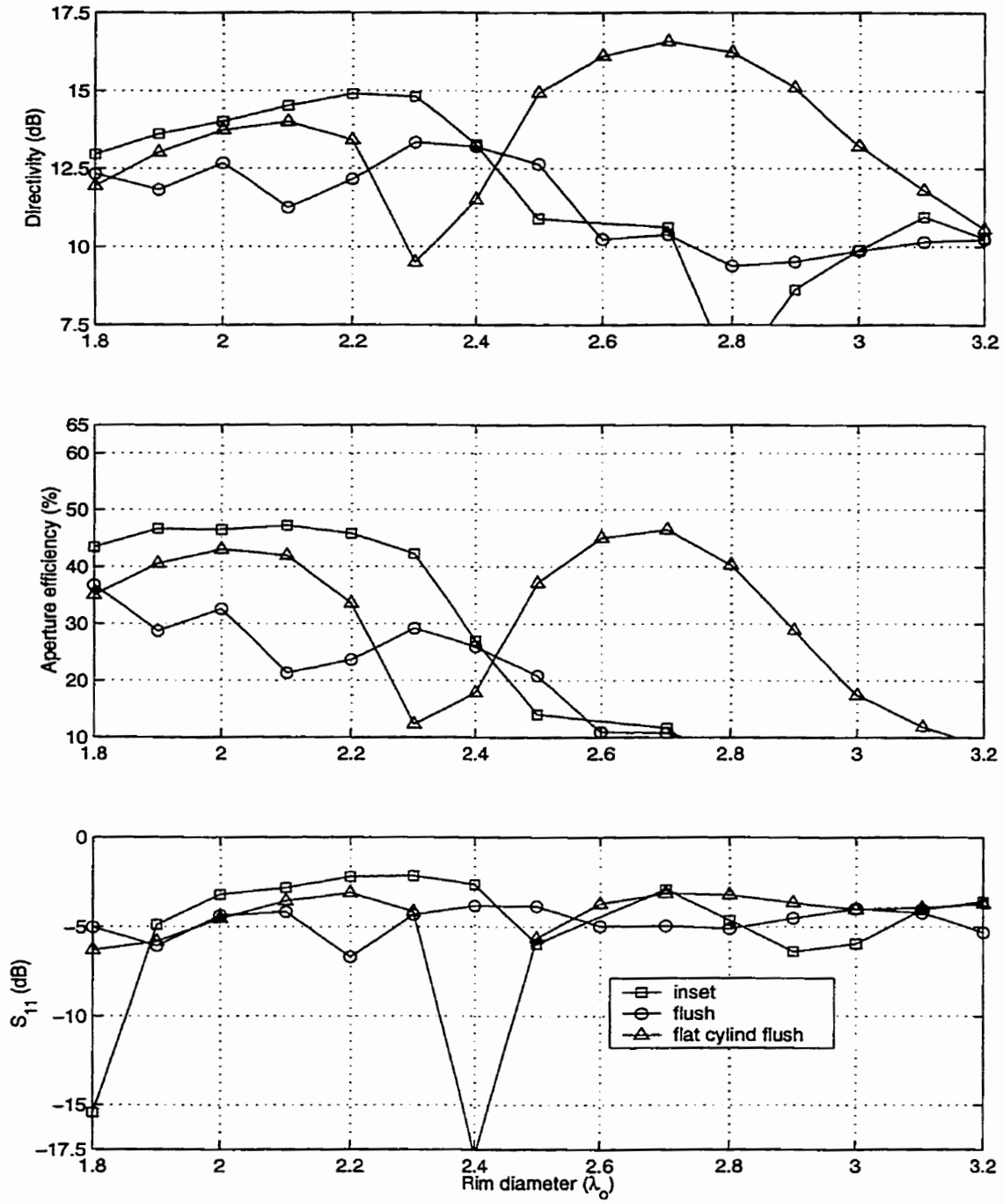

Figure 3.12: Boresight radiation and input impedance variation with increasing diameter for inset and flush fed rectangular cavity SBAs

the "flat cylind flush" trace is from Figure 3.9, for comparison
D=0.5λ_o, SR=0.5λ_o, subreflector square, f=15GHz, cavity profile was Fig. 3.8A (square)

3.4.3 Choked flat based cylindrical cavity

Addition of a pair of quarter wavelength ($\lambda_g/4$) chokes to the rim of a large diameter cylindrical cavity short back fire antenna has been shown to be a successful method for increasing the directivity [149-151]. A quarter wavelength choke transforms its terminating short circuit into a open circuit at its mouth. However electrically beneficial, the chokes were placed as to spread outward from the cavity rim. This adds at least another $\lambda_o/2$ to the antenna diameter and increases the minimum possible interelement spacing within an array by the same amount, bringing the grating lobes closer to the main lobe. In contrast, a single vertical choke coincident with the rim would not increase the lateral dimensions of the antenna, Figure 3.8B, while possibly giving the same electrical benefits. This appears to be the case as directivity improvements of the order of 1dB were obtained over the normal cylindrical cavity designs, by the addition of a 1.5x5mm ($0.075x0.25\lambda_o$) slot at the edge of the reflector, Figure 3.13. Comparison of the flush fed cylindrical cavity results to those with the choke added shows some similarity in the diameters at which the lesser peak-null-greater peak pattern occurred. The main consequences of the addition of the choke has been to decrease the level of the lesser directivity peak and to raise the greater peak. The directivity of the flush fed $2.7\lambda_o$ diameter antenna was increased by about 1dB, and the aperture efficiency by about 12%, Figure 3.13. The addition of the inset feed improved the directivity and aperture efficiency for reflector diameters less than $2.7\lambda_o$. A peak aperture efficiency of 60% was obtained for a diameter of $2.55\lambda_o$, being about 16% higher than that obtained for the non-choked inset fed antenna of identical reflector diameter, Figure 3.13. For a diameter of $3.0\lambda_o$, the aperture efficiency of the unmodified cylindrical cavity was 10% and 27% after addition of the chokes, an improvement of about 4.5dB in directivity. This is a fair comparison of the performance improvement brought about by the addition of a choke, unlike the dubious comparison of an unmodified $3.0\lambda_o$ diameter cavity to a choked $2.5\lambda_o$ diameter cavity

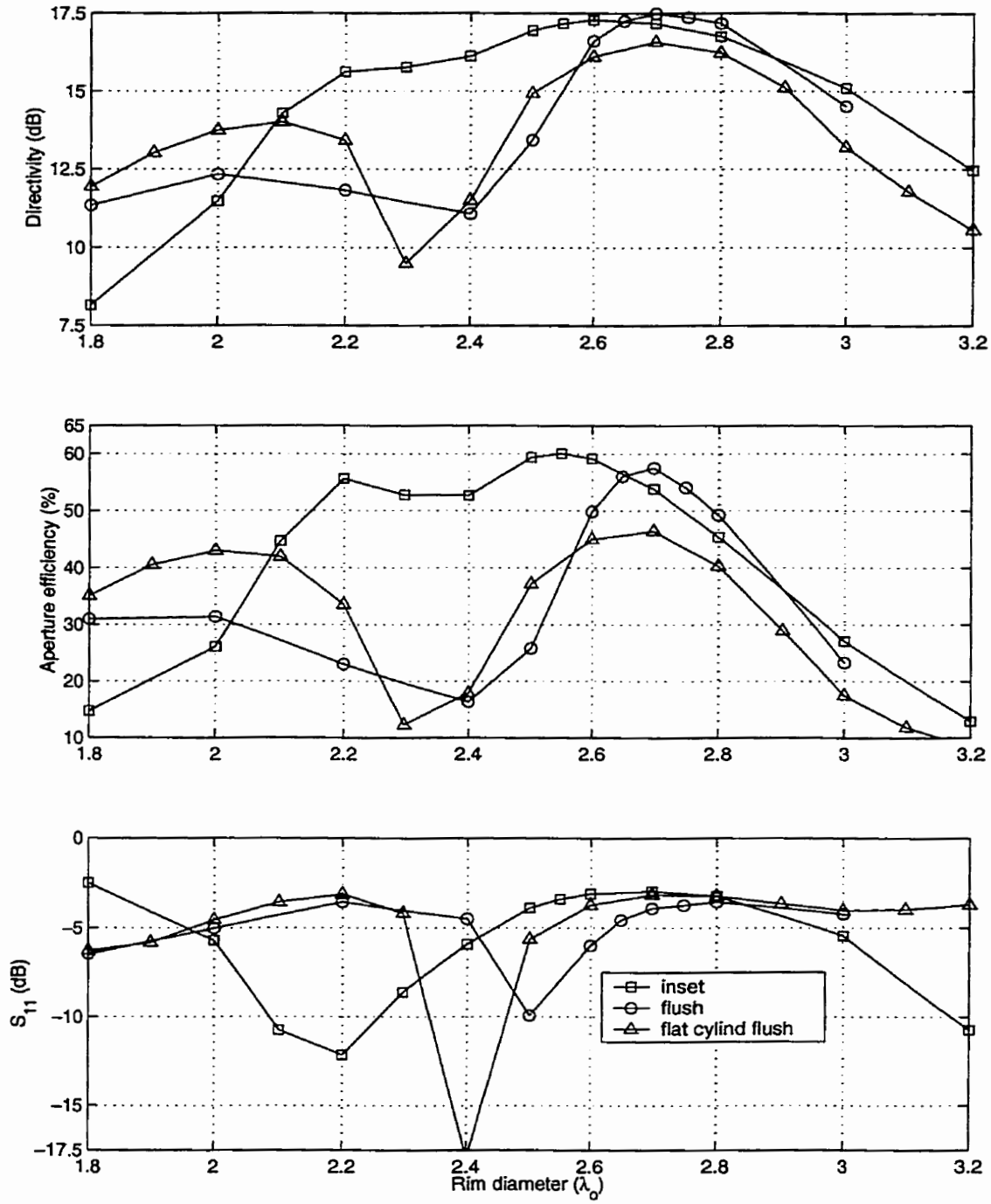

Figure 3.13: Boresight radiation and input impedance variation with increasing diameter for inset and flush fed vertical choked SBAs

the "flat cylind flush" trace is from Figure 3.9, for comparison
choke dimensions: 0.075 x 0.25λ_o (1.5 x 5mm)
D=0.5λ_o, SR=0.5λ_o, subreflector circular, f=15GHz, cavity profile was Fig. 3.8B

[149,150], where the unmodified $2.5\lambda_o$ cavity almost certainly had a higher directivity than the $3.0\lambda_o$ cavity even without the pair of chokes. The directivity improvement brought about by the addition of the chokes is presumed to be the result of changes to the aperture distribution across the cavity mouth brought about by placing an electrical open circuit at the juncture of cavity floor and rim. The second choke half way up the rim used in the literature may well have been superfluous [149,150]. The input impedance of both the flush and inset fed designs with the addition of the choke bore the same general characteristics as the unmodified antennas, Figure 3.13. The principle difference was that the well matched points from the unmodified antennas moved up in diameter upon addition of the chokes ; $0.2\lambda_o$ for the inset fed and $0.1\lambda_o$ for the flush fed. This shows the effects of the chokes, through modification of the modes within the cavities and the consequent effects upon the input impedance. It should be noted that the $2.2\lambda_o$ diameter antenna is practical in terms of both high aperture efficiency and good input impedance matching.

In summary, a means to increase the directivity for certain diameters of flat based cylindrical cavity antennas using a quarter wavelength choke, arranged so as not to consume additional lateral space, has been identified. This means of directivity improvement is laterally space efficient, but maybe troublesome to manufacture as the choke is thin in comparison to its depth. No work has been done to qualify the sensitivity of choke length, and choke lengths other than a quarter wavelength may have beneficial effects for other cavity diameters.

3.4.4 15° inclined base cylindrical cavity

Inclining the base of a cylindrical or square cavity antenna, by about 15°, in combination with an additional subreflector has been shown to increase the input impedance bandwidth without

adversely affecting the directivity [155, 156]. A cylindrical cavity with base inclined at 15°, with only a $0.5\lambda_o$ circular subreflector, was the next profile investigated, being similar to [150]. The cavity floor about the feed was flat to a radius of about $0.75\lambda_o$ (15mm), and at a depth of $0.5\lambda_o$, Figure 3.8C. Both the flush and inset fed 15° inclined base designs show the same general behaviour with increasing reflector diameter as shown by the normal flat based cylindrical cavity antennas. There is a high degree of correlation between the behaviour of the corresponding flat and inclined base antennas, as the peaks and nulls of directivity and diameters of best input impedance matching are more or less coincident, Figures 3.9 & 3.14. The main differences in directivity brought about by inclination of the base were decrease in level of the lesser peak of the flush fed design, and a raise in levels of all other peaks. The improvement for the greater peak in directivity at $2.7\lambda_o$ for the flush design was minor, about 0.1dB. While for greater diameters the difference was much more pronounced, about 4.5dB at $3.2\lambda_o$. Both peaks of the directivity characteristic of the inset fed type were raised by about 1dB (10% aperture efficiency) by inclination of the base. This means that the inset fed inclined base designs make better use of the lateral space as radiating elements than the flat based designs, Figure 3.14. Inclination of the base of a cylindrical cavity by 15° has been shown to change the levels of the directivity peaks as cavity diameter was increased, but not to change the positions of those peaks. Also, there was little change in the return loss. The greatest change was to raise the directivity peaks of the inset feed types; the best aperture efficiency been 60% at a reflector diameter of $2.45\lambda_o$.

3.4.5 High dielectric constant radome and coaxial waveguide fed cylindrical cavities

Two other previously investigated profiles were considered. The first employs a high dielectric constant radome over a flush fed $0.5\lambda_o$ deep cylindrical cavity [164]. The high dielectric

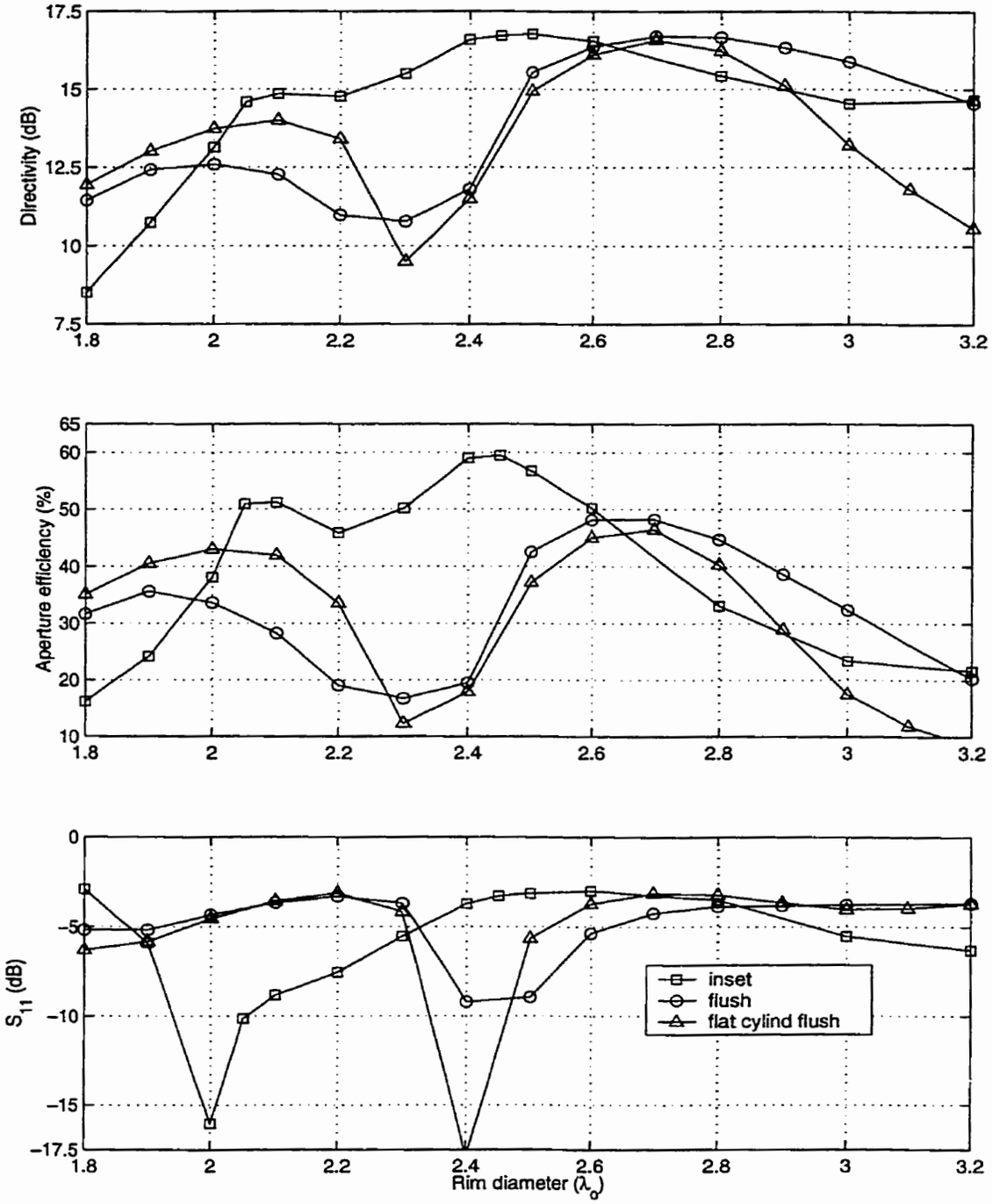

Figure 3.14: Boresight radiation and input impedance variation with increasing diameter for inset and flush fed 15° base SBAs

the "flat cylind flush" trace is from Figure 3.9, for comparison
D=0.5λ_o, SR=0.5λ_o, subreflector circular, f=15GHz, cavity profile was Fig. 3.8C

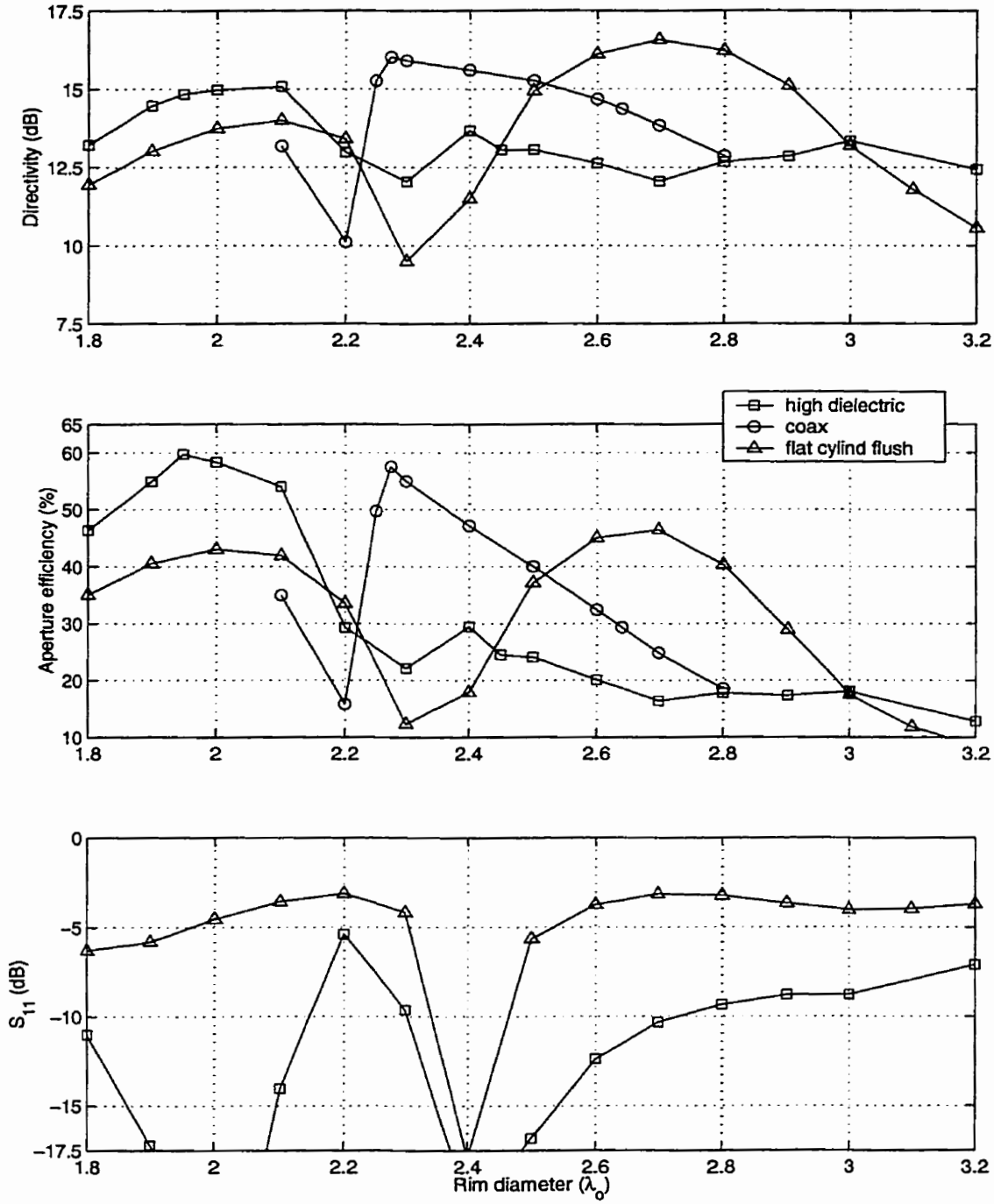

Figure 3.15: Boresight radiation and input impedance variation with increasing diameter for coaxial waveguide fed and flush fed dielectric radome SBAs

the "flat cylind flush" trace is from Figure 3.9, for comparison
D=0.5λ_o, SR=0.5λ_o, subreflector circular, f=15GHz, cavity profile was Fig. 3.8D & E

constant radome/subreflector was 1.44mm thick, having a relative permittivity of 10.2, Figure 3.8D. In the HFSS model, a virtual prism was inserted within the radome to ensure that 3 tetrahedral finite elements spanned the radome, and a convergent mesh was used. If this was not done, HFSS when subdividing the radome would only place one tetrahedral across the radome, giving approximately 4 finite elements per wavelength, which was insufficient for a convergent solution. The introduction of the virtual object, however, greatly increased the number of tetrahedra, in turn leading to very large numbers of unknowns and increased computation time compared to the other types of antenna investigated. Despite these modeling difficulties, the $1.95\lambda_o$ diameter antenna had an aperture efficiency of 60%, the second highest achieved by any of the structures studied, and some 15% (0.6dB in directivity) higher than that achieved by the same sized cylindrical cavity with a $0.5\lambda_o$ diameter subreflector, Figure 3.15. For greater diameters, the aperture efficiency dropped to about 20%. It should be pointed out that the aperture efficiency falls away rapidly on either side of the peak at $1.95\lambda_o$, which suggests that the directivity bandwidth of this antenna will be narrow. The input impedance was better than −10dB for diameters of 1.75-$2.15\lambda_o$, covering the high directivity peak, Figure 3.15. Thus, this unusual style of short back fire antenna should give a high gain for an element of its size. The input impedance matching was similarly good for diameters of 2.3-$2.7\lambda_o$, but the aperture efficiency was quiet low across the larger diameters as noted previously.

The second previously investigated type has a flat based cylindrical cavity with a circular subreflector, but was excited by a coaxial waveguide [148]. The centre conductor extends out of the waveguide mouth to contact the subreflector, and presumably has some effect upon the excitation of the cavity, Figure 3.8E. This type was only studied over the range of 2.1-$2.8\lambda_o$. The reported peak gain was at $2.65\lambda_o$ [148], although it has been found here that the peak directivity and aperture efficiency occurred at a cavity diameter of $2.275\lambda_o$, Figure 3.15. The aperture

efficiency fell away either side of the peak even more rapidly than for the high dielectric constant radome design discussed above. The directivity bandwidth of this antenna would be quiet narrow. It was not possible to excite the desired mode within a coaxial waveguide in the HFSS model, so a transition section of circular waveguide was used to excite the coaxial waveguide, leading to inaccurate return loss values, hence its absence from Figure 3.15.

Two atypical short backfire antenna designs have been investigated for the influence of rim diameter upon the achievable directivity, both gave peak aperture efficiencies of around 60%, but these characteristics are surmised to be very narrow bandwidth, which with the problems associated with production of these particular styles, excludes their applicability as array elements.

3.4.6 Cylindrical cavity with curved juncture

Cavity designs with smooth instead of sharp corners are preferable for casting, as smooth surfaces mold more readily. To this end, the juncture of the cavity floor and rim was modified with a curve of $0.5\lambda_o$ (10mm) radius, Figure 3.8F. As with the other cylindrical cavity short backfire antennas, this profile was investigated for both flush and inset feeding, but only over the range of $2.2\text{-}3.2\lambda_o$ diameters as the curve impacted upon the feed for smaller diameters. In contrast to the normal cylindrical cavity, the characteristics of the flush and inset have only one peak, Figure 3.16. Peak aperture efficiencies were achieved by the inset feed, away from which the aperture efficiency decreased steadily, suggesting a wider directivity bandwidth than any of the other profiles studied. The peak aperture efficiency was 62% for a diameter of $2.6\lambda_o$, incidentally being almost coincident with the greater peak of the flush fed normal cylindrical cavity, Figure 3.16. The flush fed antenna with the 10mm radius juncture gave a peak aperture efficiency of 52%

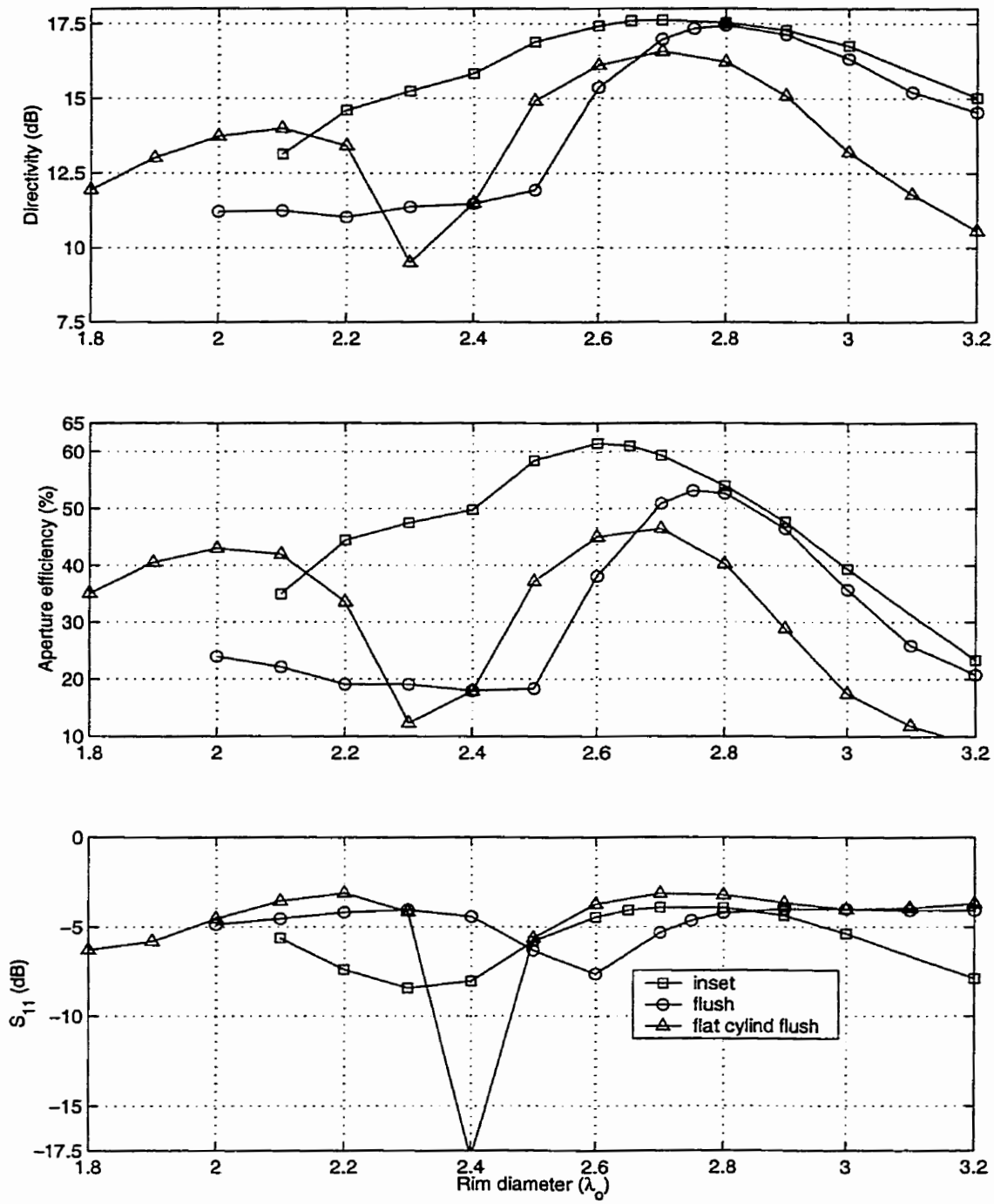

Figure 3.16: Boresight radiation and input impedance variation with increasing diameter for inset and flush fed curved juncture SBAs

the "flat cylind flush" trace is from Figure 3.9, for comparison
curved juncture radius: $0.5\lambda_o$ (10mm)
D=$0.5\lambda_o$, SR=$0.5\lambda_o$, subreflector circular, f=15GHz, cavity profile was Fig. 3.8F

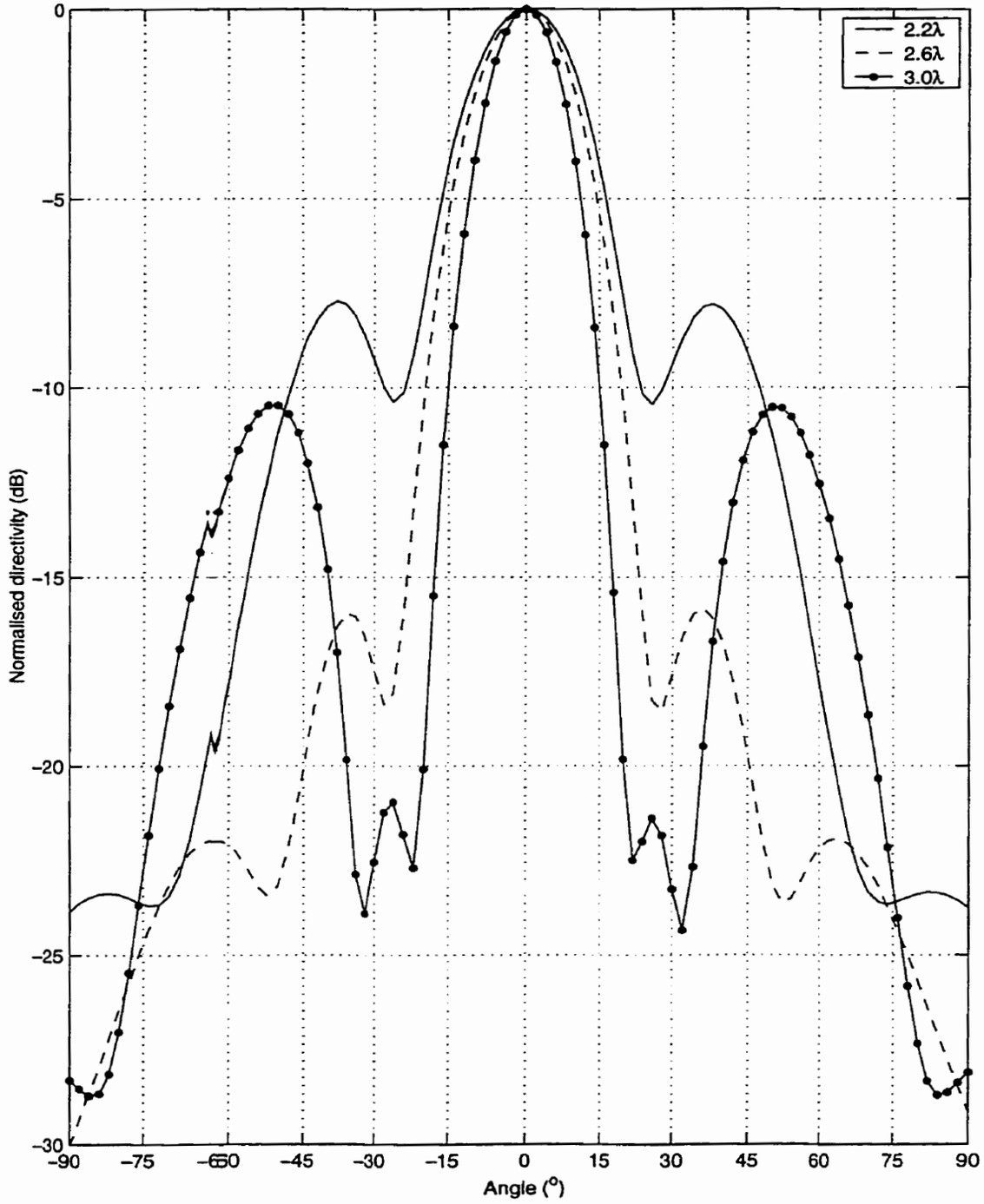

Figure 3.17: Selected E plane radiation patterns of curved juncture SBAs

D=0.5λ_o, SR=0.5λ_o, subreflector circular, f=15GHz, cavity profile was Fig. 3.8F complementary to Figure 3.16

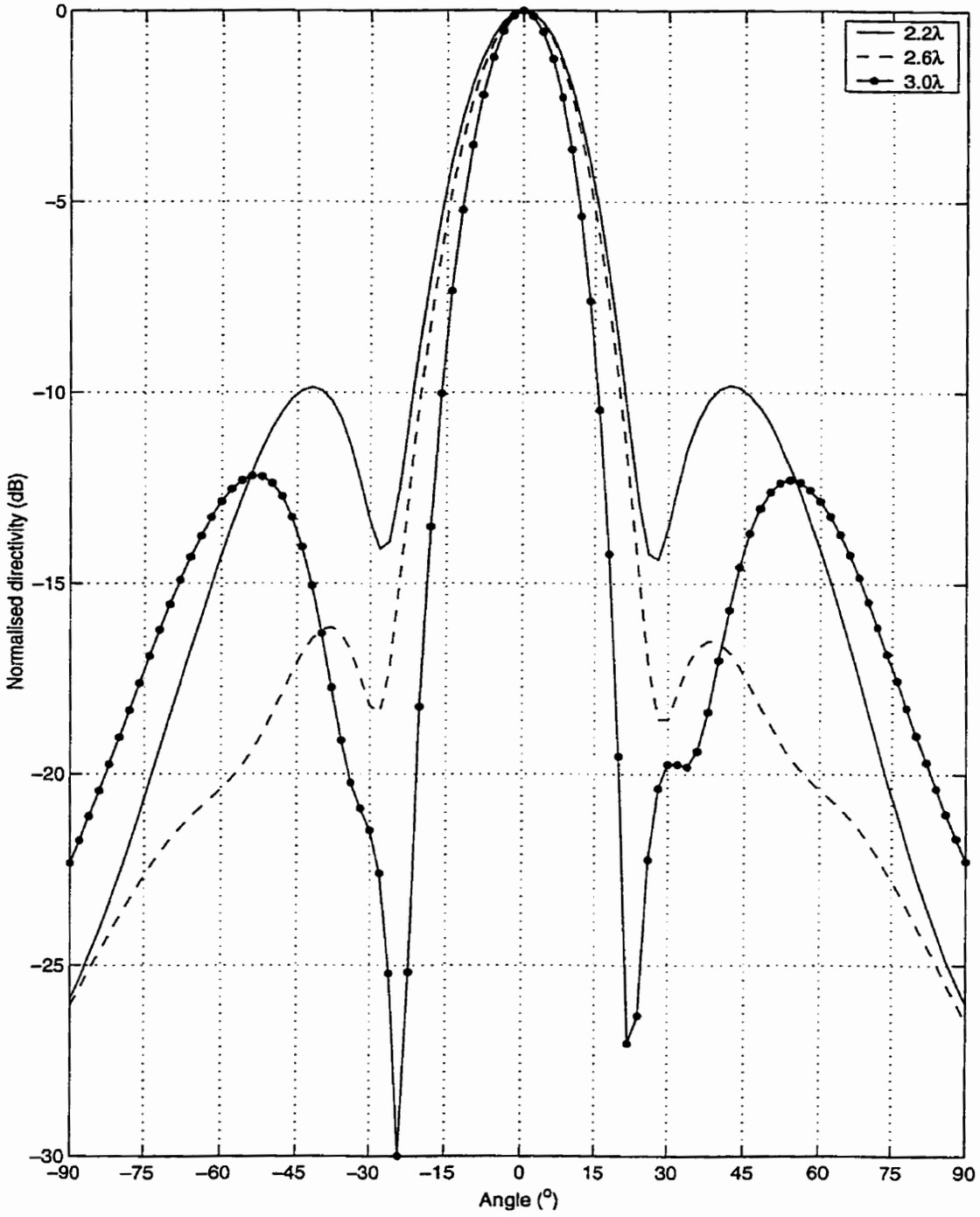

Figure 3.18: Selected H plane radiation patterns of curved juncture SBAs

D=0.5λ_o, SR=0.5λ_o, subreflector circular, f=15GHz, cavity profile was Fig. 3.8F complementary to Figure 3.16

for a diameter of $2.75\lambda_o$, and had a rapid rolloff for smaller diameters. Interestingly, the rolloff for larger diameters is almost identical to that of the inset antenna. Thus, introduction of the inset waveguide both increased the aperture efficiency for lesser diameters and smoothed the characteristic. Above a diameter of $2.8\lambda_o$ there was little effect from the inset feed, other than increasing the aperture efficiency by a couple of percent. Addition of the curved juncture appears to have moved the points of best input impedance matching up in diameter by about $0.2\lambda_o$, Figures 3.9 & 3.16. The inset design had matching better than –8dB at $2.3\lambda_o$. The beneficial effects of a curved juncture between the cavity floor and rim has been demonstrated for larger diameter antennas. The effects of the radius of the curved juncture upon alterations to the modes within the cavity along with the exact nature of those alterations merits further study.

The E and H plane radiation patterns of the curved juncture cavity SBAs share some similar features with those of the flat based cylindrical cavity discussed above, Figures 3.10 and 3.11. The beamwidth narrowed as the diameter increased from $2.2\text{-}3.0\lambda_o$, Figures 3.17 and 3.18. In common with the flat based cylindrical cavities, although more overtly here, the first null moved toward boresight and a second side-lobe around 50° arose. In contrast to the flat based SBAs, the E and H plane are much more alike here. The first side-lobe in the H plane of the curved juncture moves from 40° in the pattern of the $2.2\lambda_o$ diameter antenna to 37.5° for a diameter of $2.6\lambda_o$, and then to 30° for a diameter of $3.0\lambda_o$. Over this span, the level of the first side-lobe reduced from –10 dB to –20dB, Figure 3.18. The behaviour of the first side-lobe in the E plane is similar, Figure 3.17. The second side-lobe is more prominent in the E plane. For a diameter of $2.2\lambda_o$, the second side-lobe was at 82.5°, then at 65° for a diameter of $2.6\lambda_o$ and finally at 50° for a diameter of $3.0\lambda_o$, Figure 3.17. The level of the second side-lobe increased from –23.5dB to –11dB over this range, and as with the flat based cylindrical cavity designs was the cause of loss

of directivity for a diameter of $3.0\lambda_o$. However, the second side-lobes in both planes were about 6dB lower than those of the flat based cylindrical cavity design, Figures 3.10 and 3.11.

The nulls in both E and H radiation patterns of the $2.2\lambda_o$ design are at about 26°, which would be coincident with the grating lobes if used as an array element. However, the high first side-lobes are unattractive, Figures 3.17 and 3.18. In this respect the $2.6\lambda_o$ and $3.0\lambda_o$ diameter SBAs are more suitable, although the nulls do not fall exactly at the grating lobe positions of 22° and 19°, respectively, Figures 3.17 and 3.18. The nulls are off by about 4° in both cases. Although not exactly coincident with the grating lobe directions, the well-defined nulls in the radiation patterns of the $2.6\lambda_o$ and $3.0\lambda_o$ diameter SBAs may be close enough to partially mitigate the grating lobes that arise from having such large array elements.

In summary, introduction of the $0.5\lambda_o$ radius curved juncture between the cavity floor and wall maintained the shape of the main-lobe, modified the behaviour of the first side-lobe and suppressed the level of the second side-lobe. On the basis of these numerical results, the large cavity diameter, curved juncture SBAs are more suitable as waveguide fed array elements than the flat based cylindrical cavity SBAs, in terms of high directivity, side-lobe management and possibly null placement.

3.4.7 Summary of cavity diameter study

Seven different SBA cavity profiles have been investigated for the influence of cavity diameter, and inset or flush rectangular waveguide feeding. Cavity profile and cavity diameter have been shown to affect the directivity, aperture efficiency, and return loss of a SBA. The specifications of the seven most practical designs and the eight peak aperture efficiency designs are summarised in Tables 3.1 and 3.2, respectively. A design was judged practical if it had an aperture efficiency of better than 40% and $S_{11} \leq$-10dB. It is interesting to note that the "practical" have an average diameter of $2.13\lambda_o$, Table 3.1. In contrast, the average high aperture efficiency designs is $2.44\lambda_o$, Table 3.2. In general, this suggests that the highest aperture efficiency will occur at frequencies above that at which a SBA has low return loss. The $1.95\lambda_o$ diameter hidielectric constant radome SBA is an exception, as it has both 60% aperture efficiency and excellent input impedance matching. All of choked, 15° inclined base and curved juncture cavity profiles gave SBA designs having aperture efficiencies about 60%, Table 3.2. Three of these four were inset fed. All five 60% aperture efficiency designs are candidates for array elements. The curved juncture and 15° base are preferable as these do not require expensive dielectric substrates or drilling of chokes.

Table 3.1: Summary of practical SBA designs

antenna profile	diameter study (figure)	feed type	diameter (λ_o)	directivity (dB)	aperture efficiency (%)	S_{11} (dB)
cylindrical Fig. 3.8A	3.9	inset	2.0	13.18	38.18	-16.224
square Fig. 3.8A	3.12	inset	1.8	12.96	43.46	-15.430
choked cylindrical Fig. 3.8B	3.13	inset	2.2	15.62	55.66	-12.148
15° base Fig. 3.8C	3.14	inset	2.05	14.60	50.93	-10.132
15° base Fig. 3.8C	3.14	flush	2.5	15.53	42.52	-8.930
hi dielectric Fig. 3.8D	3.15	flush	1.95	14.84	59.73	-19.895
curved juncture Fig. 3.8F	3.16	inset	2.4	15.94	50.78	-8.162

$D=0.5\lambda_o$, $SR=0.5\lambda_o$, f=15GHz
complementary to Figures 3.9-3.16

Table 3.2: Summary of high aperture efficiency SBA designs

antenna profile	diameter study (figure)	feed type	diameter (λ_o)	directivity (dB)	aperture efficiency (%)	S_{11} (dB)
cylindrical Fig. 3.8A	3.9	inset	2.4	15.89	50.31	-2.700
square Fig. 3.8A	3.12	inset	2.1	14.52	47.21	-2.833
choked cylindrical Fig. 3.8B	3.13	inset	2.55	17.17	60.06	-3.390
choked cylindrical Fig. 3.8B	3.13	flush	2.7	17.50	57.52	-3.902
15° base Fig. 3.8C	3.14	inset	2.45	16.78	59.47	-3.278
hi dielectric Fig. 3.8D	3.15	flush	1.95	14.84	59.73	-19.895
curved juncture Fig. 3.8F	3.16	inset	2.6	17.42	61.48	-4.453
curved juncture Fig. 3.8F	3.16	flush	2.75	17.34	53.16	-4.647

$D=0.5\lambda_o$, $SR=0.5\lambda_o$, f=15GHz
complementary to Figures 3.9-3.16

3.5 Effect of cavity depth

A cavity floor-subreflector separation of $0.5\lambda_o$ has been most popular for rectangular waveguide excited antennas [150-152, 157, 158], although it has been shown that higher directivity can be achieved with $0.6\lambda_o$ spacing [142]. By the envisioned method of manufacture, the rim height and cavity floor-subreflector separation are identical as the subreflector will be suspended from a thin dielectric sheet supported by the rim or upper surface of the upper metal block, Figure 3.2. Thus, for a survey of the effects of cavity depth upon directivity, the reflector-subreflector separation was varied likewise. As a further simplification, the inset waveguide was always positioned half way between the cavity floor and subreflector. So in total, a variation of cavity depth caused a variation in 3 geometrical parameters. This study was only done for a diameter of $2.5\lambda_o$, and, as the diameter was fixed, there was a direct relationship between aperture efficiency and directivity.

Three designs were trialed for the effects of cavity depth upon directivity. Two were flat based cylindrical cavities, one having the standard $0.5\lambda_o$ (10mm) diameter subreflector and the other a smaller $0.4\lambda_o$ (8mm) diameter subreflector. The third design used the $0.5\lambda_o$ curved juncture described above, and had a $0.5\lambda_o$ diameter subreflector. All three data sets superfically show the same behaviour with cavity depth. For the shallow and deep extents of the range studied, $0.4\lambda_o$ and $0.8\lambda_o$ respectively, the directivity, and consequently the aperture efficiency, are low, Figure 3.19. The directivity rose to a peak at $0.55\lambda_o$ in the variation from swallow to deep. On careful examination, all three data sets have a unique shape with cavity depth, and peak at different depths, Figure 3.19. The peak of the curved juncture was at about $0.56\lambda_o$ deep, $0.53\lambda_o$ deep for the cylindrical cavity with $0.5\lambda_o$ subreflector, and at $0.575\lambda_o$ with $0.4\lambda_o$ subreflector. The peak levels in amplitude speak of considerable differences in the modes within the cavities of the

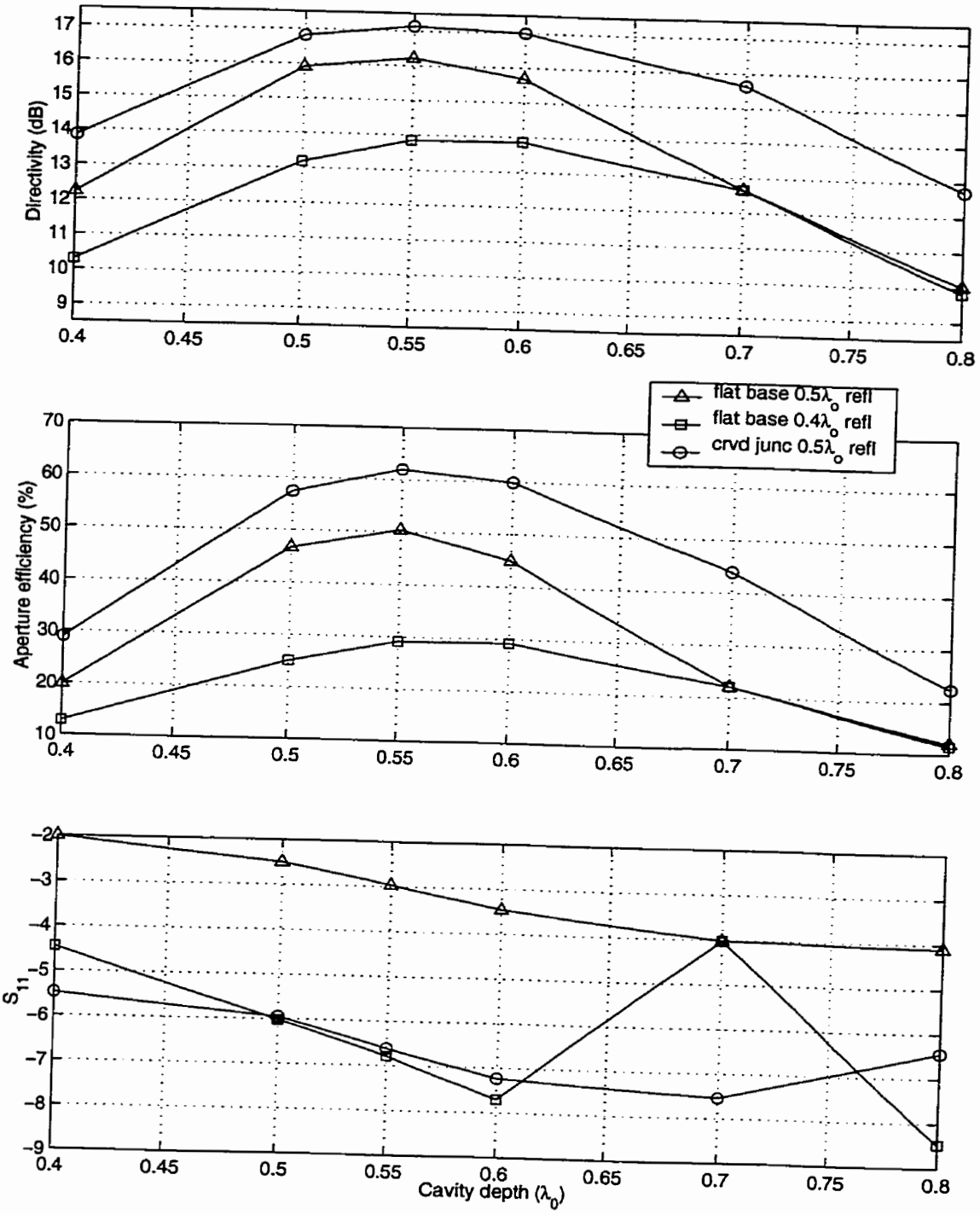

Figure 3.19: Boresight radiation and input impedance variation with depth of SBA cavity

f=15GHz, "flat base" was profile Figure 3.8A, "crvd junc" was profile Figure 3.8F

respective antennas at a cavity depth of about $0.55\lambda_o$. Merely increasing the diameter of the subreflector from $0.4\lambda_o$ to $0.5\lambda_o$ increased the directivity by 2.3dB and improved the aperture efficiency by 21%, Figure 3.19. Whereas for depths greater than $0.7\lambda_o$ the characteristics are identical, suggesting that the differences in subreflector diameter are immaterial as some other factor is dominant in determining the modes within the cavities for the greater depths. The input impedance matching of the two different subreflector sizes also differs. The $0.4\lambda_o$ subreflector gave about –4dB better S_{11} than the $0.5\lambda_o$ subreflector design across the range of cavity depths studied, Figure 3.19. The behaviour with cavity depth is similar in that the input impedance matching gradually improves with cavity depth. As to whether this was the result of increased inset of the waveguide feed, increased cavity height, increased separation of the subreflector from the waveguide feed mouth, or some combination of these is not important as all three variables were linked in this study. However, the subreflector reradiates power induced upon it by the feed back into the feed mouth, so that the power travelling down the feed is a superposition of reflection from impedance mismatch and misdirected power from the subreflector and cavity modes [175]. Based on this premise, for any particular cavity design, there should be subreflector positions and designs which either reradiate a little back into the feed mouth or do so as to cancel the mismatch reflection. Following this line of speculation, the $0.5\lambda_o$ subreflector was more suitable for the cavity with the $0.5\lambda_o$ curved juncture. This was because the input impedance was some –4dB improved over that of the normal, flat based, cylindrical cavity for all depths studied, Figure 3.19.

The characteristic was a little different with the curved juncture in that the S_{11} began to raise again at a depth of $0.8\lambda_o$. As the only structural difference was the curved juncture, it was considered to be the sole cause of all differences between the results. In addition to the effects upon the S_{11}, the curved juncture gave at least 1dB higher directivity than the flat base cylindrical

cavity, with identical $0.5\lambda_o$ subreflector, across the entire range of depths studied. The difference is greatest at $0.7\lambda_o$, suggesting that the curved juncture significantly modified the modes within the cavity in a manner which greatly improves the directivity. Thus, some further insight into the effects of curvature of the juncture between the cavity floor and rim has been gleaned from a study of cavity depth for a specific reflector radius. For inset fed antennas it was noted that, an optimal cavity depth was about $0.55\lambda_o$ and that the optimal depth was dependant upon cavity profile and subreflector size. It is speculated that the optimal depth also depends on cavity diameter. Conducting further similar cavity depth studies for other reflector diameters and flush feeding should yield interesting results. Further work might also be undertaken upon qualifying the effects of the subreflector, as it has been shown for a cylindrical cavity of $2.5\lambda_o$ diameter that a smaller subreflector improves input impedance matching while lessening the directivity.

3.6 Effect of cavity profile upon aperture distribution

As an initial step in studying the modes within the cavities of short backfire antennas, and perhaps learning to control those, the aperture distributions of several antennas are considered. The antenna designs considered here are the $2.5\lambda_o$ diameter, $0.55\lambda_o$ depth cavity designs from the trials on cavity depth above, with variants without subreflectors. The aperture distributions considered here were extracted from the HFSS models by taking a section through the $0.5\lambda_o$ high radiation space at a height of $0.25\lambda_o$ above the cavity mouth. Data sets were for $-1.25\lambda_o$ to $+1.25\lambda_o$ (-25mm to +25mm) of the antenna centres. The resulting data sets are of complex quantities representing the three components of the electric field. The values being complex allows the extraction of amplitude and phase components for separate study. The $\mathbf{E}_y$ component was found to have the greatest amplitude, as was expected as that was the copolar component direction of the

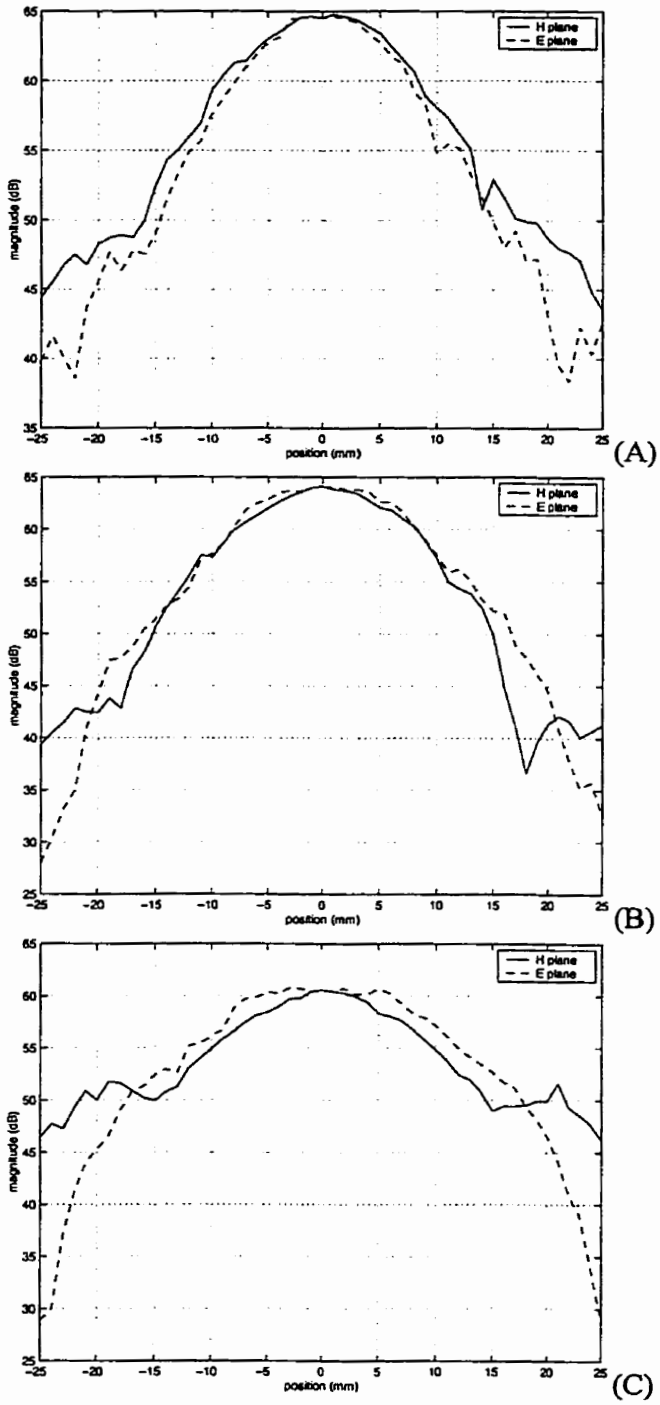

Figure 3.20: **E_y amplitude variation across aperture of $2.5\lambda_o$ diameter cylindrical cavity SBAs ($\lambda/4$ above aperture)**

(A) no subreflector, (B) SR=$0.4\lambda_o$, (C) SR=$0.5\lambda_o$
E_y amplitude as displayed here is $20\log_{10}(\text{mag}(E_y))$, f=15GHz, cavity profile was Fig. 3.8A

Table 3.3: Comparison of span of E_y across apertures of cylindrical and curved juncture SBAs

Antenna	E_y amplitude (dB)		E_y phase (°)	
	E plane	H plane	E plane	H plane
cylindrical no subreflector	26.304	21.249	270	185
cylindrical $0.4\lambda_o$ subreflector	36.066	27.501	240	85
cylindrical $0.5\lambda_o$ subreflector	31.900	14.384	165	75
curved juncture no subreflector	28.491	19.299	105	203
curved juncture $0.5\lambda_o$ subreflector	17.167	11.353	33	56

E_y amplitude as displayed here is $20\log_{10}(\text{mag}(E_y))$
$R=2.5\lambda_o$, $D=0.55\lambda_o$
complementary to Figures 3.20-3.21

Table 3.4: Comparison of centre to $\pm 0.5\lambda_o$ E_y across apertures of cylindrical and curved juncture SBAs

Antenna	E_y amplitude (dB)		E_y phase (°)	
	E plane	H plane	E plane	H plane
cylindrical no subreflector	8.312	5.828	38	31
cylindrical $0.4\lambda_o$ subreflector	6.525	6.825	22	33
cylindrical $0.5\lambda_o$ subreflector	3.974	5.700	7	17
curved juncture no subreflector	6.359	7.125	54	44
curved juncture $0.5\lambda_o$ subreflector	1.270	5.023	12	16

E_y amplitude as displayed here is $20\log_{10}(\text{mag}(E_y))$
$R=2.5\lambda_o$, $D=0.55\lambda_o$
complementary to Figures 3.20-3.21

antennas. Only the $\mathbf{E}_y$ component in the principle planes, E (x=0) and H (y=0), are considered here, as the intent is to gain some insight into the effects of subreflector and cavity profile upon the aperture distribution.

Comparison of the $\mathbf{E}_y$ amplitude distributions across the mouth of a $2.5\lambda_o$ diameter, $0.55\lambda_o$ depth, inset fed, cylindrical cavity without subreflector to variations with $0.4\lambda_o$ and $0.5\lambda_o$ subreflectors, shows that the power was more evenly distributed across the cavity mouth with the subreflectors, Figure 3.20. Without the subreflector, more power was concentrated at the centre of the cavity mouth. The difference of $\mathbf{E}_y$ amplitude between the cavity centre and edges was about –22dB for both planes, and about –7dB from centre to $\pm 0.5\lambda_o$ (±10mm), Figure 3.20 & Tables 3.3 & 3.4. Addition of a $0.4\lambda_o$ diameter subreflector gave a centre to edge difference of about –24dB for the H-plane and –32 for the E-plane. Perhaps a little more significantly, the centre to $\pm 0.5\lambda_o$ was about –6.5dB, Figure 3.20. Thus, adding a $0.4\lambda_o$ diameter subreflector reduced the amount of power at the cavity edges while broadening the power distribution at the centre a little. Adding the $0.5\lambda_o$ diameter subreflector had a more noticeable effect. The centre to edge difference was –32dB in the H-plane and –14dB in the E-plane, while the centre to $\pm 0.5\lambda_o$ difference was about –4dB in the H-plane and –6dB in the E-plane, Figure 3.20 & Tables 3.3 & 3.4. Addition of the $0.5\lambda_o$ subreflector had a different effect upon either plane, but the overall power distribution was more even across the cavity mouth. As seen above, this brought about a marked increase in directivity, Figure 3.19.

The phase of $\mathbf{E}_y$ was also affected by the addition of subreflectors to the inset fed, $2.5\lambda_o$ diameter, $0.55\lambda_o$ depth cylindrical cavity, Figure 3.21. The most striking effect was the change in phase distribution shape across the cavity mouth. Without a subreflector, the phase distribution smoothly curves from the cavity centre to the cavity edges in both planes. With the subreflectors,

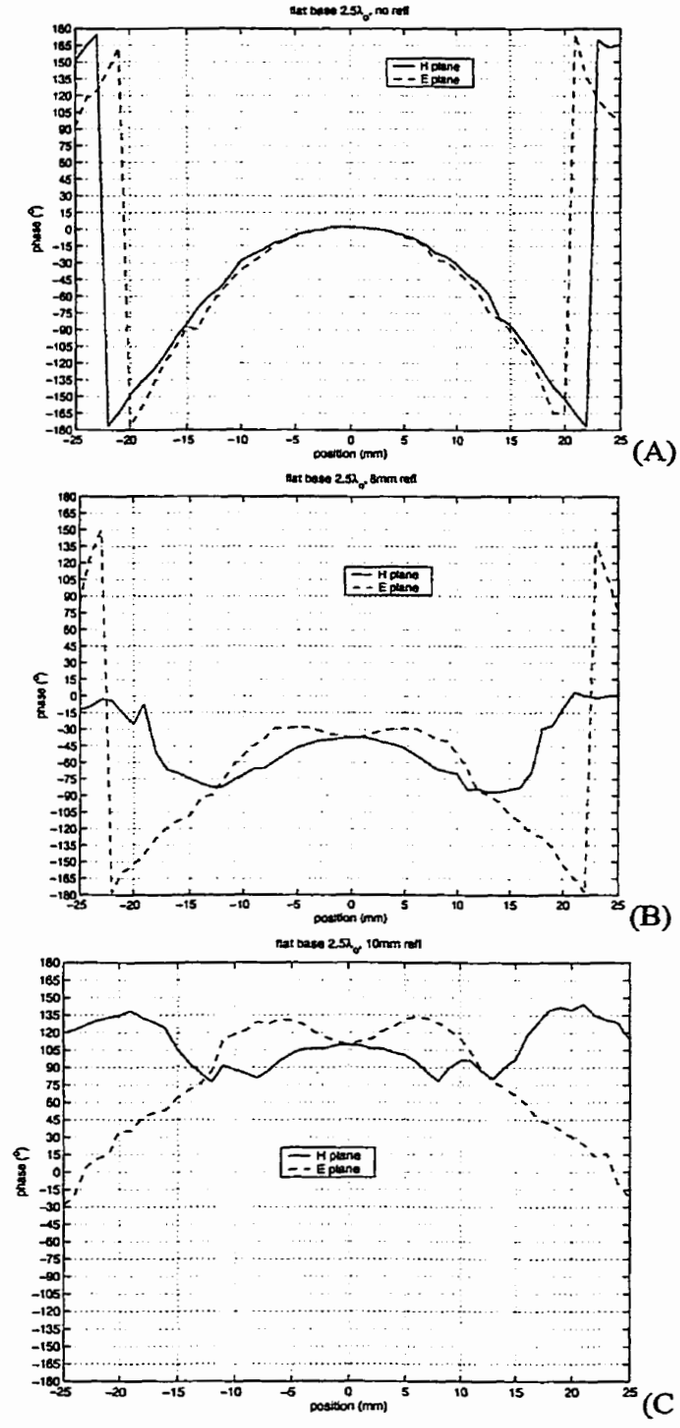

Figure 3.21: **E_y phase variation across aperture of $2.5\lambda_o$ diameter cylindrical cavity SBAs ($\lambda/4$ above aperture)**

(A) no subreflector, (B) SR=$0.4\lambda_o$, (C) SR=$0.5\lambda_o$
cavity profile was Fig. 3.8A

the E-plane phase actually increases until just before the edges of the subreflector, then does a gentle curve downward until just after the subreflector edge, and then falls away until the cavity edge, Figure 3.21. In contrast, in the H-plane the phase gently curves downward from the centre to just outside the subreflector, after which it curves upward until reaching the cavity edges. There were also large differences in the range of phase. The phase range across the cavity mouth was 270° in E-plane and 185° in the H-plane with no subreflector, Table 3.3. With the $0.4\lambda_o$ diameter subreflector, it was 240° in the E-plane and 85° in the H-plane, while being 165° in the E-plane and 75° in the H-plane with the $0.5\lambda_o$ diameter subreflector. Thus, addition of the subreflectors modified the cavity mouth phase distributions even more radically than the amplitude distribution. The aperture phase distribution affects the interaction of the radiated fields in the far field to form the radiation pattern, and with further study might be better understood and controlled.

The cavity with the $0.5\lambda_o$ radius juncture between reflector and rim was also considered, to see if some insight into the causes for it having produced higher directivities than the normal cylindrical base antennas. Even without the subreflector, the aperture distribution of the cavity with the curved juncture differs noticeably from that of the normal flat based cavity, Figures 3.20 & 3.22. From the centre to $\pm 0.85\lambda_o$ ($\pm$17mm) the E and H-plane $\mathbf{E_y}$ amplitude distributions are near identical, unlike that of the flat based cavity for which the E-plane distribution was a little narrower. The centre to $\pm 0.5\lambda_o$ difference was about -6.5dB and to the cavity edges -28dB in the E-plane and -19 dB in the H-plane, Tables 3.3 & 3.4. Thus, the $0.5\lambda_o$ radius curved juncture between the cavity floor and rim had a similar effect upon the amplitude distribution as the subreflectors described previously. Upon addition of a $0.5\lambda_o$ diameter subreflector to the curved juncture cavity, the changes to the amplitude distribution were profound. Using comparisons of various points in the distribution to the centre as done above was pointless due to the very unusual amplitude distribution. In the E-plane, progressing outward from the centre the amplitude rose

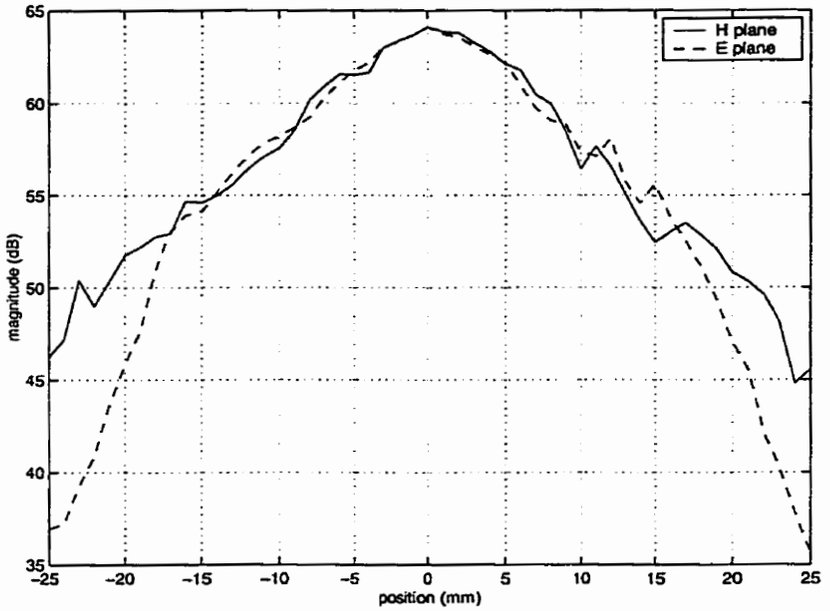

(A)

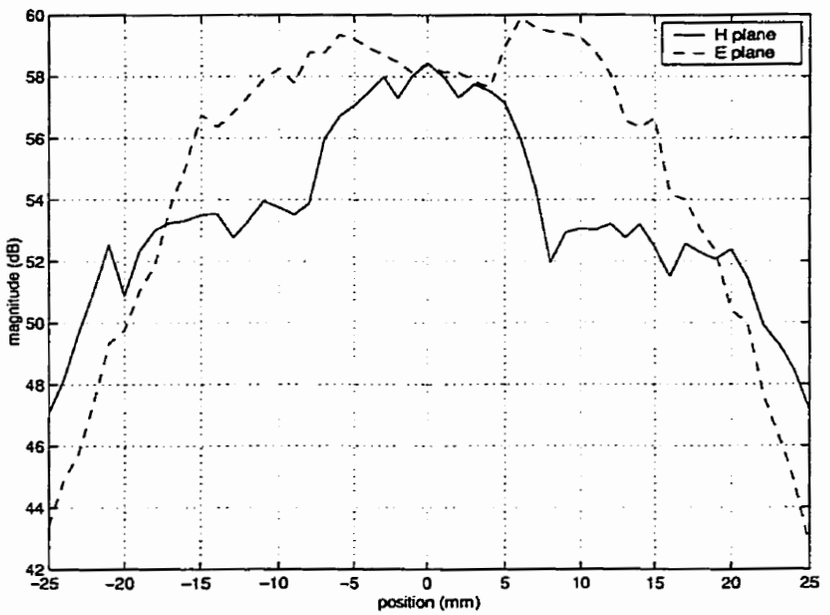

(B)

Figure 3.22: **E_y amplitude variation across aperture of $2.5\lambda_o$ diameter curved juncture SBAs ($\lambda/4$ above aperture)**

(A) no subreflector, (B) SR=$0.5\lambda_o$
profile was Fig. 3.8F
E_y amplitude as displayed here is $20\log_{10}(\text{mag}(E_y))$

until the edge of the subreflector after which it was tapered exponentially until the cavity edge. In stark contrast, the H-plane amplitude distribution fell away sharply from the centre until just before the subreflector edge, after which it was more or less flat until tapering off at the cavity edge, Figure 3.22. The amplitude distributions in both planes are thus very strange in comparison to normal cylindrical cavity, and show how cavity profile can be used alter the amplitude distribution. The overall lesser range of the amplitude distribution of the curved juncture cavity with $0.5\lambda_o$ subreflector caused the higher directivity noted above, Figures 3.16 & 3.19.

The phase distribution across the mouth of the cavity with the $0.5\lambda_o$ radius juncture between cavity floor and rim without a subreflector was similar to that of the normal cavity, in that the phase gently decreased in a curve away from the cavity centre, Figures 3.21 & 3.23. However, in the E-plane the phase starts to increase about $0.25\lambda_o$ from the cavity edge. The phase variation across the aperture was about 105° in the E-plane and about 203° in the H-plane, Figure 3.23 & Table 3.3. Upon addition of the $0.5\lambda_o$ subreflector, the phase variation was greatly decreased, having been about 33° in the E-plane and about 56° in the H-plane, Table 3.3. This was significantly different from the phase distributions of the normal cavity with a $0.5\lambda_o$ subreflector, especially in the E-plane. Thus, the addition of the $0.5\lambda_o$ radius juncture between cavity floor and rim, in combination with a $0.5\lambda_o$ diameter subreflector, has been shown to flatten the phase distribution across the entire mouth for the particular cavity diameter and depth studied.

The near field amplitude and phase distributions for a set of antennas having identical cavity diameter and depth have been examined. The addition of a subreflector has been shown to generally flatten the amplitude and phase distributions, with one particular subreflector diameter having been more effective at this than the other studied. A curved juncture between cavity floor and rim has been shown to further flatten the amplitude and phase distribution, leading to the

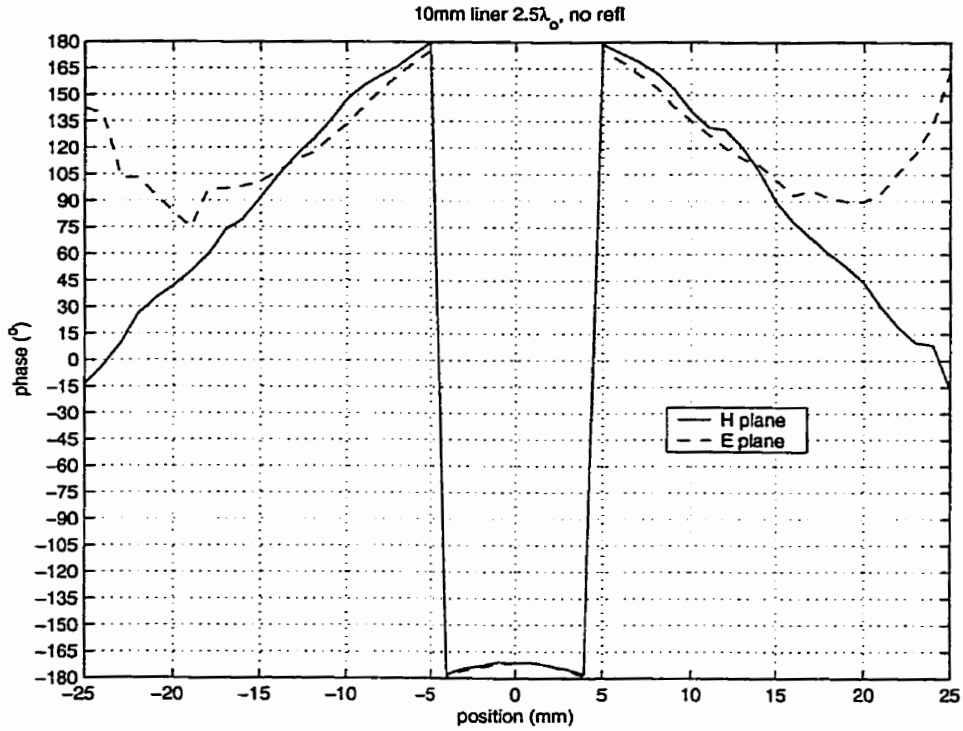

(A)

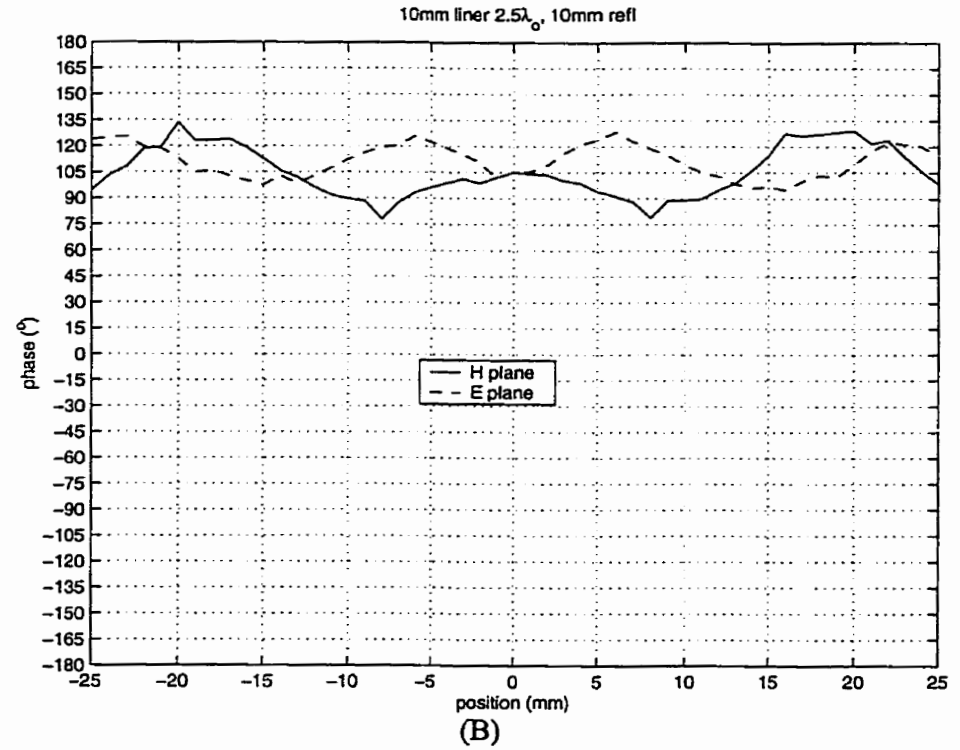

(B)

Figure 3.23: E_y phase variation across aperture of $2.5\lambda_o$ diameter curved juncture SBAs ($\lambda/4$ above aperture)

(A) no subreflector, (B) $0.5\lambda_o$ diameter subreflector
profile was Fig. 3.8F

increases in directivity noted earlier. It is speculated that for a given cavity diameter and depth, an optimal combination of subreflector diameter and juncture radius will provide optimal directivity. Further similar work is necessary on other cavity dimensions to be able to draw a generalised insight into the workings of this technique and a precise means of control.

3.7 Effect of juncture curvature

The effect of the radius of the curved juncture of SBA profile Figure 3.8F is investigated in this section. Both an inset and flush fed $2.6\lambda_o$ diameter, $0.5\lambda_o$ depth cavities were used. The juncture radius was increased from $0\text{-}0.5\lambda_o$ (0-10mm) in five steps, Figure 3.24. This was a stepped metamorphosis of profile Figure 3.8A to Figure 3.8F. The effect upon directivity was greatest for the inset fed design, where there was a 1.8dB increase, Figure 3.24. The peak directivity occurred at a radius of $0.4\lambda_o$ (8mm) for the inset design and at $0.25\lambda_o$ (5mm) for the flush fed. The optimal radius for highest directivity is thus not $0.5\lambda_o$ as used in all the preceding trials, and is dependant upon feeding method. It is interesting to note that the return loss decreased with increasing curve radius, Figure 3.24. Thus the influence of juncture radius on the modes in the cavity was shown by examination of the return loss and peak directivity here, in addition to a diameter survey and radiation pattern above.

3.8 Effect of waveguide feed inset depth

Throughout the diameter survey earlier in this chapter, the differences between inset and flush feeding were noted. Inset depth is studied in this section. Three different cavities were

considered, although all had a cavity depth of $0.55\lambda_o$ (11mm). The flat base cylindrical cavity SBA had a diameter of $2.5\lambda_o$. The other two SBAs both had $0.5\lambda_o$ radius curved junctures, and were of cavity radius $2.5\lambda_o$ and $2.6\lambda_o$. The only difference between these latter two SBAs was $0.1\lambda_o$ in diameter. The waveguide inset feed depth was varied from 0 (flush with the cavity floor) to $0.275\lambda_o$ (half way between the cavity floor and subreflector) in six steps.

The directivity and aperture efficiency of all three SBAs were affected by changes in inset depth, Figure 3.25. The changes in directivity (and aperture efficiency) were similar for the two curved juncture SBAs, having a peak around an inset depth of $0.2\lambda_o$. The $2.6\lambda_o$ diameter, curved juncture SBA had a peak aperture efficiency of 70% at this depth, being about 10% higher than any other designs in this study, Table 3.2. Although the directivity of the flat based SBA also peaked at $0.2\lambda_o$ the relationship with inset depth was not a simple curve with a peak near one extremity of the range, Figure 3.25. Also, the amount of change in directivity across the range of inset depths was not as great for the flat based SBA. The directivity of the flat based SBA is thus relatively insensitive to the inset depth of the exciting rectangular waveguide mouth. This is in accord with the findings for a similar $2.0\lambda_o$ diameter dipole excited flat based cylindrical cavity SBA [175]. The range of aperture efficiency for the flat based SBA across the range of inset depths studied here was about 5%, in contrast to 40% and 20% for the $2.5\lambda_o$ and $2.6\lambda_o$ curved juncture SBAs, respectively, Figure 3.25. Thus, the radiation characteristics of the curved juncture SBAs are more sensitive to the waveguide inset feed depth than the flat based SBAs, showing the importance of feed phase centre to this type of antenna [148].

The return loss of the curved juncture, $2.5\lambda_o$ diameter SBA changed the most with inset depth, achieving $S_{11} \leq -10$dB at a depth of $0.15\lambda_o$. The S_{11} ranged over 6dB as the inset depth was

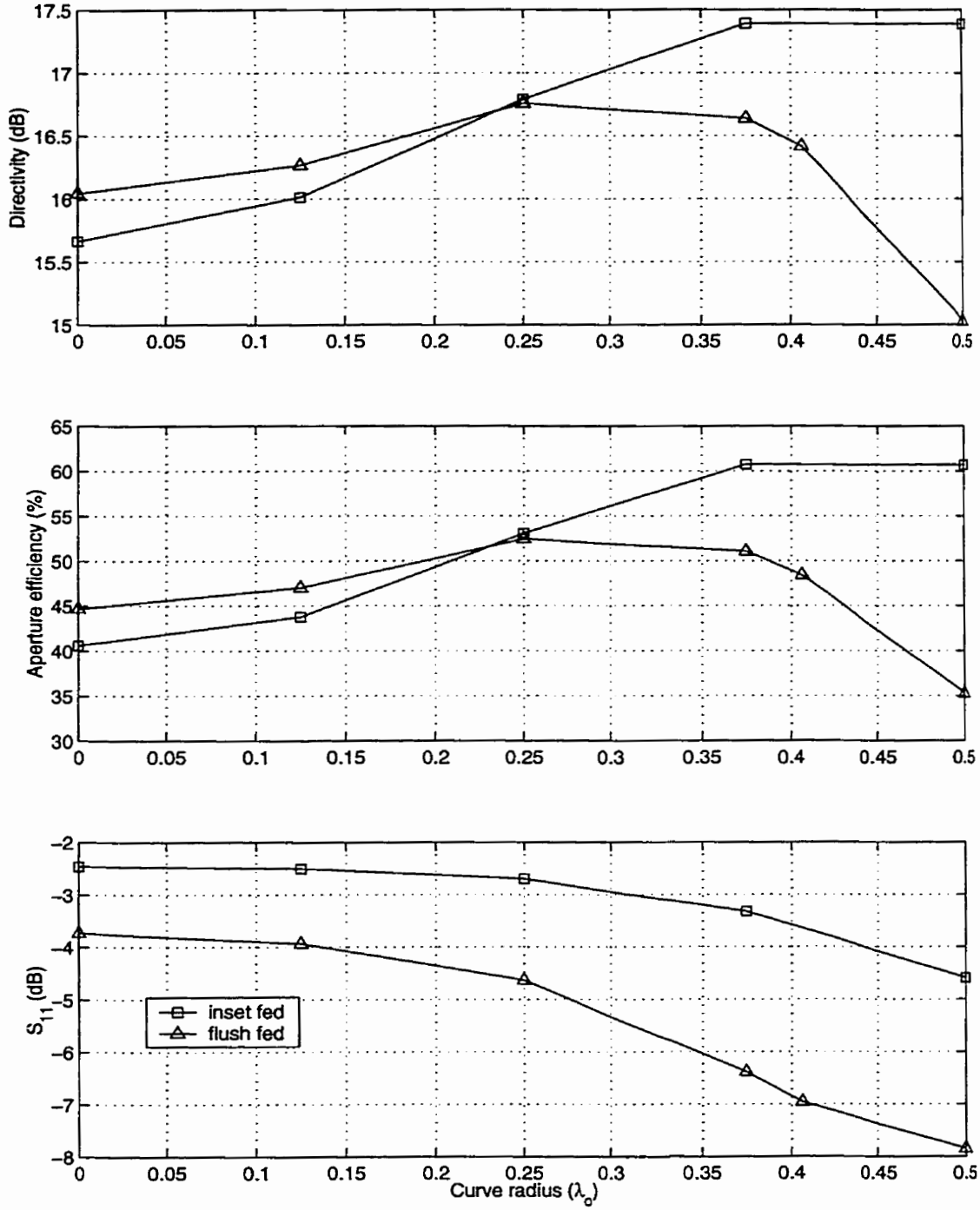

Figure 3.24: Effect of radius of curved juncture upon $2.6\lambda_o$ diameter, $0.5\lambda_o$ depth SBAs

cavity profile was Figure 3.8A at radius = $0\lambda_o$
cavity profile was Figure 3.8F at radius = $0.5\lambda_o$
f=15GHz

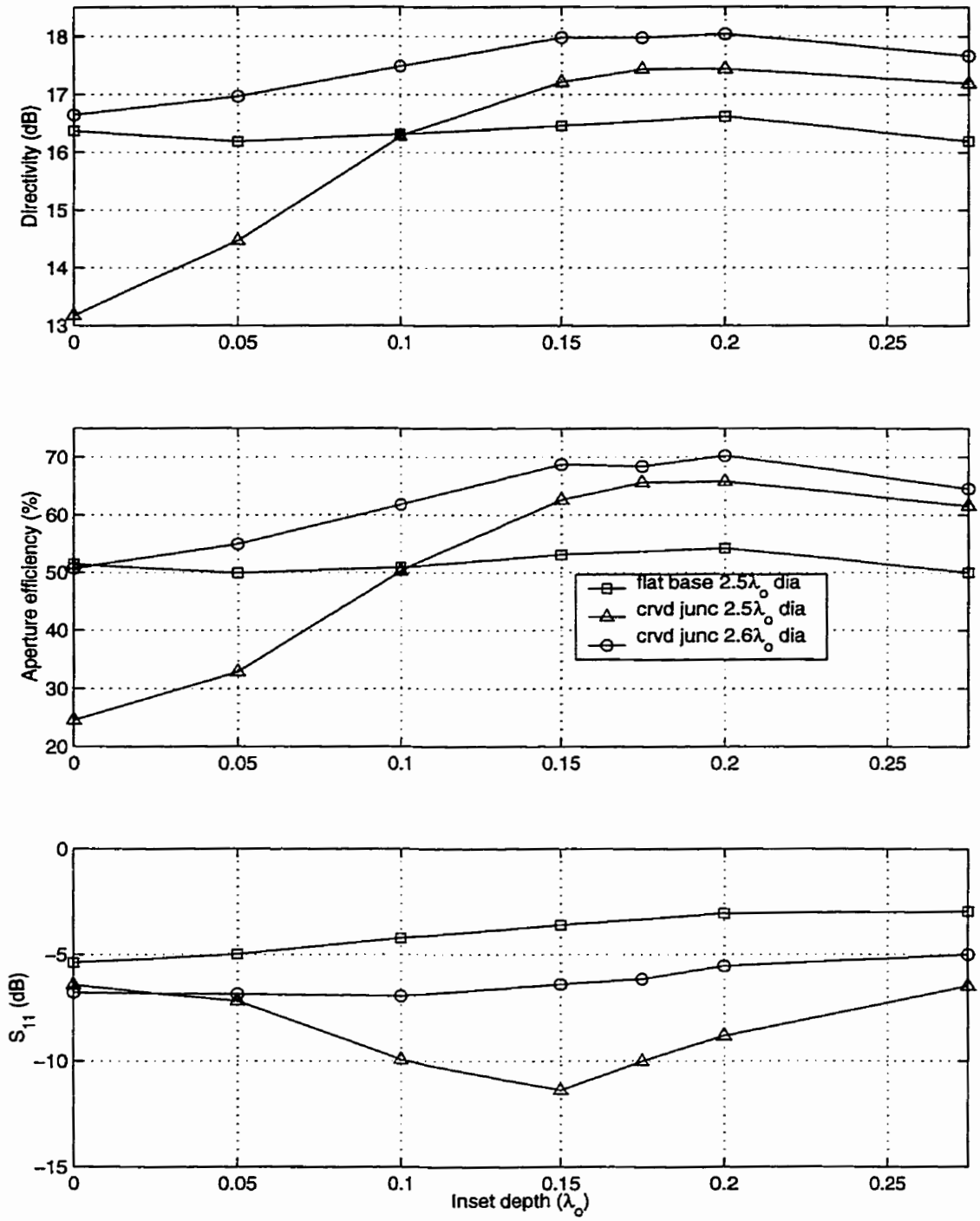

Figure 3.25: Effect of waveguide feed inset depth into the cavities of SBAs

"flat base" was cavity profile Figure 3.8A, "crvd junc" was cavity profile Figure 3.8F

f=15GHz, D=0.55λ_o, curved juncture radius=0.5λ_o

increased. The variation was only about 2dB for the other two SBAs. Thus the inset depth is a critical input impedance matching parameter for some SBAs, and not for others.

In this section, waveguide feed inset depth into the cavity was investigated briefly. This parameter was shown to affect the directivity of a SBA; therefore becoming a more critical parameter for curved juncture designs. Inset depth also proved critical to the input impedance matching of one of the three SBAs studied. In addition, a curved juncture SBA with an aperture efficiency of 70% was found, being some 10% higher than any previous design in this study.

3.9 Conclusions

In this chapter, SBAs were investigated using the commercial FEM numerical tool HFSS 6.0. The aim was to build up a resource of parametric design information which does not presently exist in the published literature. An additional aim was to gain some insight into the physical mechanisms underlying the behaviour of this type of antenna. A numerical study had the advantages of lower cost and a faster turn around than doing a similar study experimentally. The inability to conduct the necessary large number of trials quickly and cheaply has been a major impediment to the study of this type of antenna by prior investigators, for which there are no theoretical models. The work of prior investigators suggested that the directivity of SBAs could be increased by either cavity shaping or modification of the juncture of the cavity floor and rim. Thus the parametric study focused upon this, with some 205 trials having been conducted. Cavity circumference shape, diameter, profile and depth have been studied.

A simplified, infinite ground plane model of SBAs was used in HFSS for all the trials in this chapter. This model was validated by comparison with a finite ground model which accounted for all features of an experimental SBA. The features neglected in the infinite ground plane model, but included in the finite ground model, were cavity and floor thickness, and all outside aspects of these. The radiation space of the finite ground model completely enclosed it, so that any effects upon the radiation pattern from those features would be accounted for. A high level of agreement was found between the radiation patterns of the two models. This validated the use of the much simplified and much smaller infinite ground plane model. Also, this finding suggested that the features neglected in the infinite ground plane model were relatively unimportant to the operation of a SBA. So, the fields within the cavity are much more important, and contain much more of the power, than any on the surrounding ground plane or outer cavity walls. A later examination of the fields across the aperture of several SBAs showed that the majority of power was concentrated

near the cavity centre. The fields at the cavity edge were typically some 30dB below those at the centre. This was consistent with the low interelement coupling in an array environment noted by Molker [166].

The study of cavity circumference shape determined that there was little difference between square and circular shapes for a diameter of $2.0\lambda_o$. This finding is in agreement with the literature that reports an inter-changability of shape [26, 27, 156, 167]. However, for a diameter of $2.7\lambda_o$, the circular circumference had 28% higher aperture efficiency than the square circumference. Thus cavity circumference shape is more critical for larger diameter SBAs.

It was found that cavity shaping was a good method for increasing aperture efficiency. The aperture efficiency of the commonly used cylindrical cavity SBA was bettered by at least 10% using any of the choked, high dielectric constant radome, 15° inclined base or curved juncture profiles. The highest aperture efficiency of 61.5% was obtained with an inset fed, $2.6\lambda_o$ diameter curved juncture profile. The addition of a curved juncture to a cylindrical cavity SBA was shown to significantly modify the far field radiation patterns and near field aperture distributions, compared to the normal flat based cavity. This particular design was found to have a reasonably high aperture efficiency as the far field radiation pattern nulls were close to the expected array grating lobe directions suitable for mitigation. The cavity edge was considered easier to die cast because the curved juncture was in place of a shape corner. Thus, it was investigated experimentally for use as an array element in the following chapter, with some modification to the feed inset depth which further increased the aperture efficiency to about 70%.

The aperture efficiency of the larger diameter ($\approx 2.6\lambda_o$) curved juncture SBAs was found to be sensitive to the inset depth of the exciting waveguide mouth into the cavity. In contrast, a

similar diameter flat based cylindrical cavity SBA was relatively unaffected by inset depth. These findings showed the importance of exciter phase centre to the curved juncture SBA. The optimal inset depth increased the aperture efficiency of the curved juncture SBA by roughly a further 10%. The radius of the curved juncture was also found to affect the achievable directivity, although not as radically as feed inset depth. With a combination of both feed inset depth and juncture radius, it should be possible to realise a SBA with at least 70% aperture. Such an SBA would thus be comparable to a similar sized microstrip array in terms of aperture efficiency, and have the added advantage of being more readily connected to a low loss rectangular waveguide feed network. This optimised SBA design, along with several other designs, were investigated experimentally with a view to application as array elements in the next chapter.

CHAPTER 4: Experimental study of SBAs and array

4.1 Introduction

Four short backfire antennas (SBAs) were selected from the 205 designs of the previous chapter for experimental investigation. This was done to learn more about the SBAs as single antennas, to validate the results of the numerical study of the previous chapter, and to assess the four SBAs as array elements. The better of the four SBAs was then used as an element in a small array. This SBA was based upon the optimal design from the numerical study of the previous chapter. It had a diameter of $2.6\lambda_o$ and a curved juncture between the cavity floor and rim. This was the minimum sized array element that allowed use of a full sized, and thus lowest possible loss, WR-62 rectangular waveguide of type D, Figure 1.1. The four SBAs are described in more detail in the next subsection.

A numerical integration method to derive the directivity of the SBAs from the measured radiation patterns was developed, similar to that used by Rayner [174]. The method used here was based upon the $cos\phi/sin\phi$ dependence of the E_θ/E_ϕ components of the far field radiation pattern main lobe of the $2.6\lambda_o$ diameter curved juncture SBA. Such observations of the E_θ/E_ϕ azimuthal dependence had not been made before. The numerically-derived directivity characteristics of the four SBAs were each unique and showed that the highest directivity of each occurred above the band of frequencies where each had well matched input impedance.

Good agreement between the characteristics of two SBAs and the matching results from the numerical study was found. This validated the numerical study.

The experimental investigation of the four SBAs revealed several features of these medium gain antennas not previously reported in the open literature. Most importantly, when using a single $0.5\lambda_o$ diameter subreflector, the frequencies at which a large diameter SBA produced the highest directivity were above that at which the antenna had well matched input impedance. This was suggested during the numerical study of the previous chapter, and dictates the use of matching circuits if the highest possible gain is to be obtained from a SBA, or array of SBAs. Also, the lowest peak sidelobe levels and widest E-plane mainlobe beamwidths were found to coincide with the peak directivity of each antenna. The wide beamwidths prevented complete cancellation of the grating lobes when the SBAs were tested as array elements using appropriate array factors. This was caused by the first nulls of the SBA radiation patterns not being coincident with the first order grating lobes in the array factor. However, the nulls were generally close enough to partially suppress the grating lobes, and the $2.6\lambda_o$ diameter, curved juncture SBA was the best of the four tested, in this respect. However, the wide elemental beamwidth of the $2.6\lambda_o$ diameter curved juncture SBA caused high first sidelobes (about −10dB) in the 2x2 array. This would be a disadvantage comparing to parabolic reflector antennas for LMCS application.

Excellent agreement was found between the measured radiation patterns of the 2x2 array of SBAs and those predicted by HFSS. The first order grating lobes were partially suppressed by the purposely placed null in the array element radiation pattern. The increase in scaled directivity from array element to 2x2 array was 6dB as expected from HFSS. However, about 1dB was lost in the feednetwork of the experimental 2x2 array. Future work will concentrate upon identification of the source of the feed network losses, and the development of a wideband input impedance matching network. If this is successful, an array with an aperture efficiency of 60%, or better, across 11% bandwidth will be realised, as predicted by HFSS. Despite the feed network problem, the

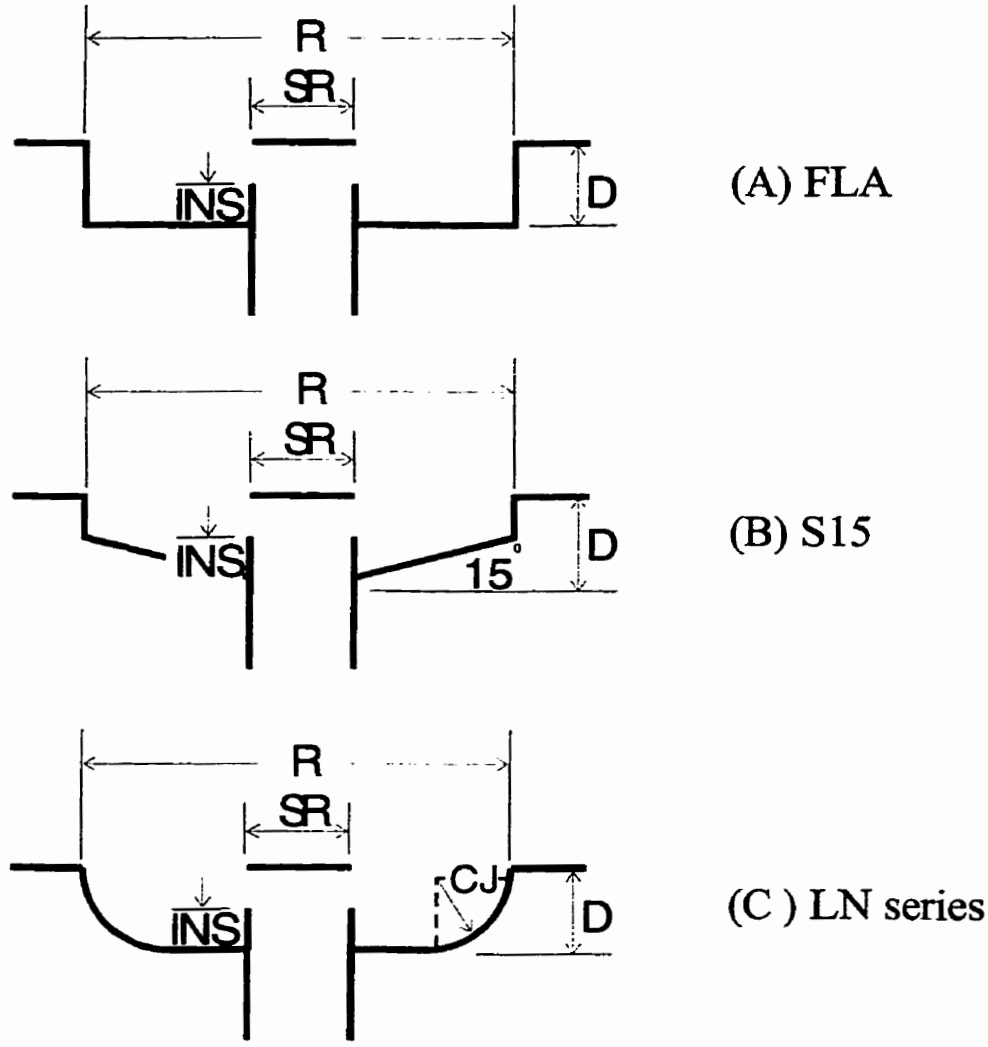

Figure 4.1: Cross sections of the four experimentally investigated SBAs

Table 4.1: Descriptions of the four experimental SBAs

antenna	description	profile	R (λ_o)	D (λ_o)	INS (λ_o)	CJ (λ_o)
FLA	flat based cylindrical	Fig. 4.1A	2.5	0.5	0.25	n/a
S15	15° base	Fig. 4.1B	2.5	0.5	0.25	n/a
LN24	curved juncture	Fig. 4.1C	2.4	0.55	0.175	0.4
LN26	curved juncture	Fig. 4.1C	2.6	0.55	0.175	0.4

radiation pattern behaviour of an optimised large diameter SBA was demonstrated in a small array environment and it was found to be satisfactory.

4.2 Antenna descriptions

The dimensions and construction method of the four tested experimentally SBAs are described in this section. The design frequency was 15GHz, half that of the desired LMCS band. This reduced the manufacturing tolerance requirements, and made the SBAs of a size that could easily be constructed by hand.

The specifications of the four SBAs are given in Table 4.1. Two of the SBAs had diameters of $2.5\lambda_o$, and one each of $2.4\lambda_o$ and $2.6\lambda_o$. The latter two antennas had cavities with identical curved junctures between cavity floor and rim, so any differences were the result of the $0.2\lambda_o$ difference in diameter. The two $2.5\lambda_o$ diameter SBAs differed only in that one had an inclined cavity base, so any operational differences between that pair of antennas were likewise the result of that sole structural difference. The selection of these four SBAs from the approximately 205 designs from the numerical study is a reasonable sample of the different types of cavity profile that were investigated. Additionally, all four designs did not require expensive high dielectric constant substrates, intricate machining such as milling out thin quarter wave chokes, nor difficult construction such as assembly of a coaxial waveguide feed.

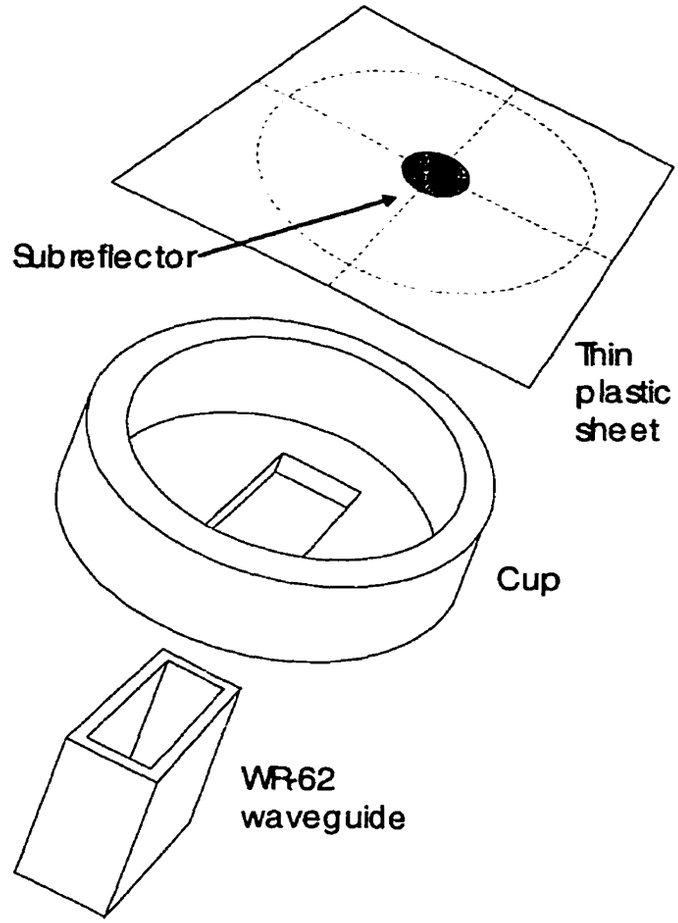

Figure 4.2: Illustrative diagram of SBA construction

4.2.1 Cavity construction

Four SBA designs were chosen for experimental investigation, selection having been based upon the numerical study detailed in the previous chapter. All cavities were cut from 62mm diameter, 13mm thick cylinders of brass on a lathe, to form a shallow cup. Turning the cavity from a solid piece of brass avoided any complications from air gaps or incomplete electrical contact between sections comprising the cavity. Such air gaps may have altered the cavity fields in the work of some prior investigators [150, 157, 158]. As the cavities were cut into solid blocks of metal here, any differences between the four SBAs were purely the result of cavity shaping and not the vagaries of ill-considered construction methods. However, all four cavities required a

considerable amount of skill to turn on a lathe by hand. A slot was cut in the centre of the floor of each brass cup to accommodate the WR-62 rectangular waveguide feed, Figure 4.2. The short length of WR-62 waveguide was soldered to the cup. A WR-62 flange was soldered onto the other end of the waveguide, for connection to waveguide-coaxial transitions, or other WR-62 waveguide circuit elements.

4.2.2 Subreflector construction and mounting

Centring lines, a circle the diameter of the SBA under test, and a circle the diameter of the subreflector were laser printed onto overhead transparency film. The subreflector was cut from sticky backed copper foil and set at the centre of the overhead film. The centring lines and cavity circumference circle provided lateral positioning guides. Further refinement of lateral position was achieved with a setsquare set off the outer edge of the cup. Accurate vertical positioning was achieved by pushing one end of a $2.0\lambda_o$ long folded paper plug into the waveguide mouth. The plug had a rectangular cross section and fit snugly into the WR-62 waveguide. The other end of the plug (projecting out of the waveguide) was made level with the top of the cavity rim with a thick and flat sheet of metal. This simple method ensured that the top of the plug was of equal height to the cavity rim. The subreflector on the overhead film was then positioned laterally and was affixed with double sided tape.

This method of subreflector positioning is thought superior to the methods used by prior investigators, as none of the support structures could have interfered with the fields within the cavity. The heavy machinable plastic support struts ($\approx 0.25\lambda_d$ thick) used by some prior investigators probably affected the operation of their SBAs [150, 157, 158]. Also, the axial rod

support used in the majority of dipole excited SBAs may modify the cavity fields [174], and is not structurally compatible with rectangular waveguide excited SBAs. Thus, a simple method for positioning the subreflector (employing simple constructions of paper and thin plastic film) was used in the experimental trials of the SBAs. This was adjudged to be preferable to the positioning methods of some prior investigators, which may have affected antenna performance.

4.3 Method employed for directivity calculation

A means of determining the directivity from measured principal plane radiation patterns would be useful when a standard gain reference is not available. Such circumstances were encountered with dipole excited SBAs by Rayner [174]. The solution to this problem involved integration of the radiation patterns in the principal planes to obtain the directivity [174]. The same method was employed here, and reasonable agreement was found between the calculated directivity and the measured scaled directivity (gain + mismatch loss) for LN24 and LN26 across 13-16GHz.

Before developing the numerical method to integrate the experimental radiation patterns of the SBAs, the angular dependence of the far field radiation pattern components had to be found. This had not been done previously in the open literature for SBAs, and no comments were made by Rayner [174]. In the main lobe (θ=0°-20°), the azimuthal dependence of E_θ^2 was $cos^2\phi$, while it was $sin^2\phi$ for E_ϕ^2, Figures 4.3A-C. For wider angles beyond the null in the co-polarised radiation pattern, the azimuthal dependence was only loosely $cos^2\phi/sin^2\phi$, Figures 4.3D-F. However, as the majority of the far field power was concentrated in the main lobe, the wider angle power levels could be ignored, Figure 4.3. Thus, the $cos^2\phi/sin^2\phi$ dependence of the components

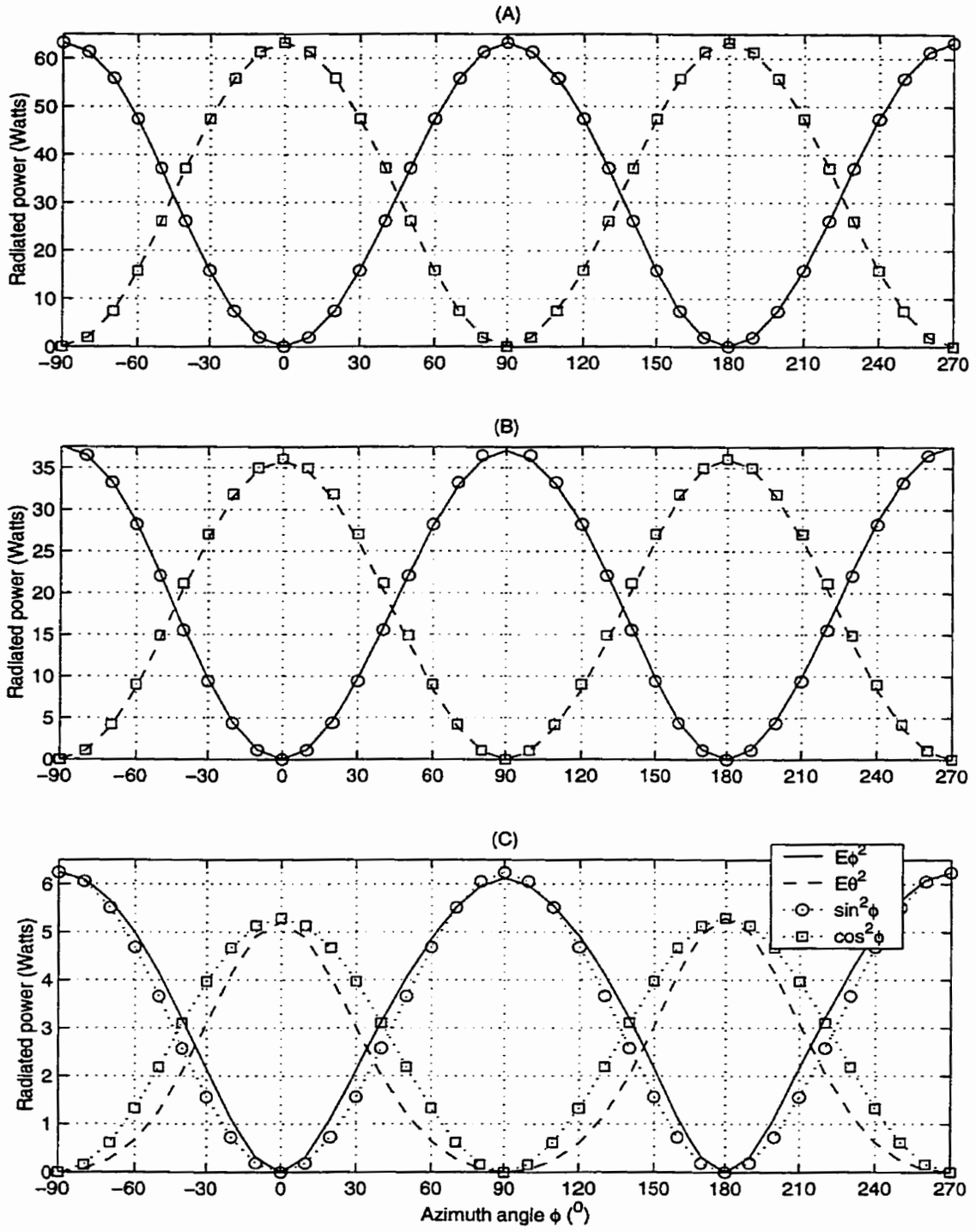

Figure 4.3a: Azimuth angle dependence of far field radiation components from LN26 at 15GHz using HFSS

"(A)" θ=0°, "(B)" θ=10° , "(C)" θ=20°
geometry given in Table 4.1

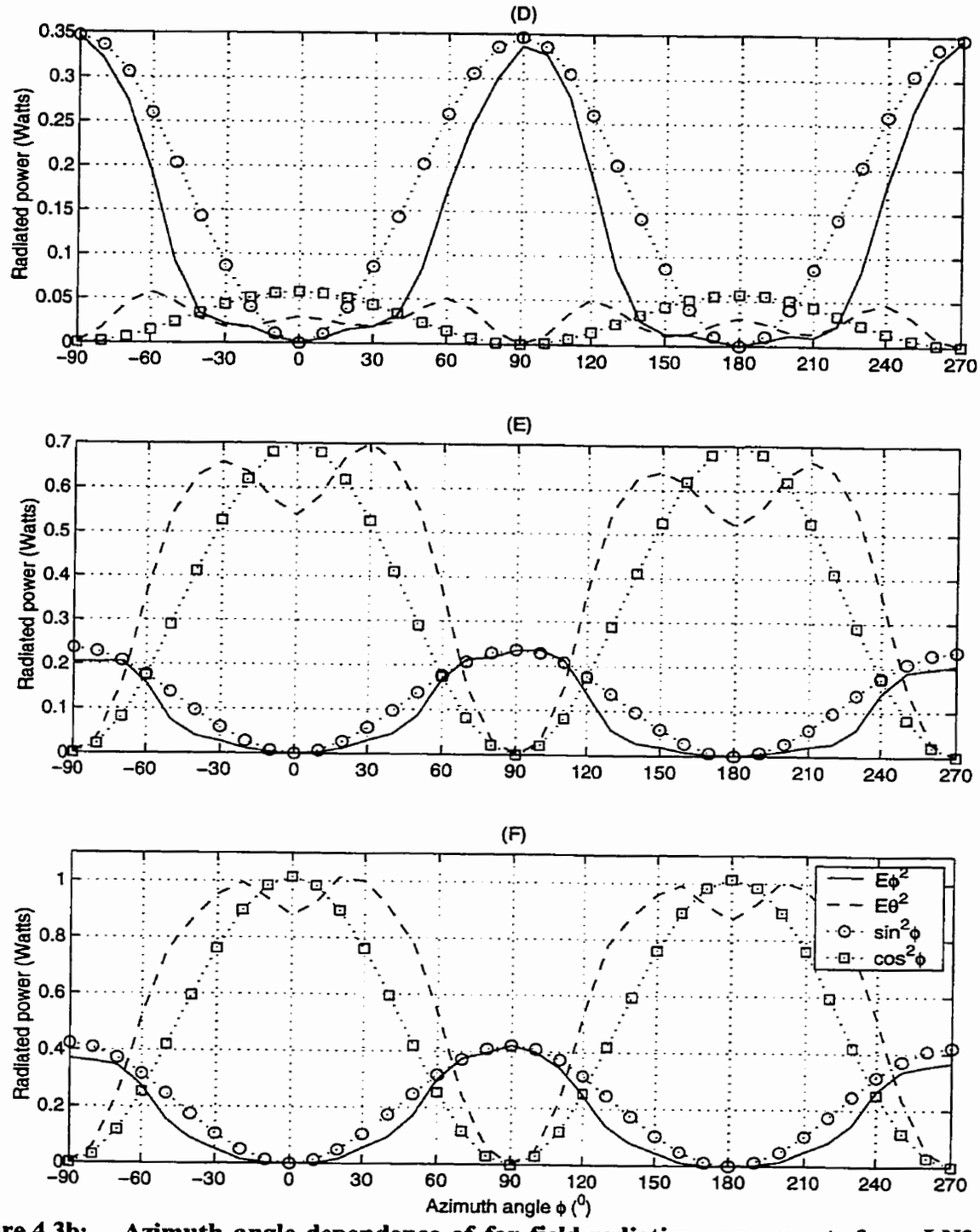

Figure 4.3b: Azimuth angle dependence of far field radiation components from LN26 at 15GHz using HFSS

"(D)" θ=40°, "(E)" θ=50°, "(F)" θ=60°
geometry given in Table 4.1

of the far field radiated power was used to develop the numerical integration procedure. This type of azimuthal dependance is typical for both circular and rectangular aperture antennas [179].

The procedure to calculate the directivity from the radiation patterns of an antenna is given in Balanis [179] (equations 2-34 to 2-43), and is presented here with modifications appropriate to the situation of the four SBAs.

The radiation intensity of a given antenna is given by

$$U = B_o F(\theta,\phi) \qquad (5\text{-}1)$$

where B_o is a constant

F is the function describing the variations of the far field radiation pattern power with θ and ϕ, and

$$F(\theta,\phi) = f(\theta)\cos^2\phi + g(\theta)\sin^2\phi \qquad (5\text{-}2)$$

where $f(\theta)$ describes the θ variation of E_θ^2 far field radiation pattern component

$g(\theta)$ describes the θ variation of E_ϕ^2 far field radiation pattern component

and the $cos^2\phi$ and $sin^2\phi$ describe the ϕ variation of the far field radiation pattern components, as found previously in this section.

The directivity of the antenna is given by equation (2-35) of [179]:

$$D_o = \frac{4\pi U_{max}}{P_{rad}} \qquad (5\text{-}3)$$

where U_{max} is the maximum value of the radiation intensity

P_{rad} is the total radiated power

$$P_{rad}=B_o\int_0^{2\pi}\left\{\int_0^{\pi}\{F(\theta,\phi)\sin\theta d\theta\}\right\}d\phi \qquad (5\text{-}4)$$

Simplifying eqaution (5-4) by substituting in equation (5-2):

$$P_{rad}=B_o\int_0^{2\pi}\left\{\int_0^{\pi}\{f(\theta)\cos^2\phi+g(\theta)\sin^2\phi\}\sin\theta d\theta\right\}d\phi \qquad (5\text{-}5)$$

and using the sum rule of integration:

$$P_{rad}=B_o\int_0^{2\pi}\left\{\int_0^{\pi}\{f(\theta)\cos^2\phi\}\sin\theta d\theta\right\}d\phi+B_o\int_0^{2\pi}\left\{\int_0^{\pi}\{g(\theta)\sin^2\phi\}\sin\theta d\theta\right\}d\phi \qquad (5\text{-}6)$$

The ϕ dependent components can be evaluated as definite integrals:

$$\int_0^{2\pi}\cos^2\phi d\phi=\int_0^{2\pi}\frac{1}{2}\{1+\cos2\phi\}d\phi=\pi \text{ and } \int_0^{2\pi}\sin^2\phi d\phi=\int_0^{2\pi}\frac{1}{2}\{1-\cos2\phi\}d\phi=\pi \qquad (5\text{-}7)$$

So, the total radiated power becomes a single integration in θ:

$$P_{rad}=\pi B_o\int_0^{\pi}\{f(\theta)+g(\theta)\}\sin\theta d\theta \qquad (5\text{-}8)$$

As the θ dependent components of the far field radiation pattern were only available in numerical form, the trapezoidal was used to evaluate the integral using summations.

In situations where $F(\theta,\phi)$ is only available as numerical data, the integrations required to solve for P_{rad} can be approximated by summations:

$$P_{rad} = \int_0^{\pi} \{f(\theta)+g(\theta)\}\sin\theta d\theta = \sum_{i=1}^{N}\left[(f(\theta)+g(\theta))\sin\theta\Delta\theta_i\right] \qquad (5\text{-}9)$$

For N uniform divisions over the π range of θ and M uniform divisions over the π range of ϕ:

$$\Delta\theta_i = \frac{\pi}{N} \qquad (5\text{-}10)$$

Combining equations (5-9) and (5-10), a digital form of the radiated power is obtained similar to equation (2-43) of [179]:

$$P_{rad} = B_o\left(\frac{\pi}{N}\right)(\pi)\sum_{i=1}^{N}\left[(f(\theta)+g(\theta))\sin\theta\right] \qquad (5\text{-}11)$$

The principal plane radiation patterns were measured at 0.5° increments across the range of θ = 0° to 90°, and zero contribution was assumed for θ = 90° to 180°, thus making N=361.

The total power radiated was:

$$P_{rad} = \left(\frac{\pi^2}{361}\right)\left[\sum_{i=1}^{181}\left[f(\theta_i)\sin\theta_i\right]+\sum_{i=1}^{181}\left[g(\theta_i)\sin\theta_i\right]\right] \qquad (5\text{-}12)$$

where $f(\theta_i) = F(\theta_i, 0^o)$ is the E-plane pattern

$g(\theta_i) = F(\theta_i, 90^o)$ is the H-plane pattern, from equation (5-2).

Equation (5-7) was encoded in a short Matlab programme and applied to the radiation patterns of LN24 and LN26. The directivity calculated characteristic from the radiation patterns of both LN24 and LN26 agree well with the measured scaled directivity (gain + mismatch loss) over the range of 13-16GHz in shape, Figure 4.4. The calculated directivity was smoother than the experimentally measured scaled directivity, but the general trend with frequency is identical, verifying the method.

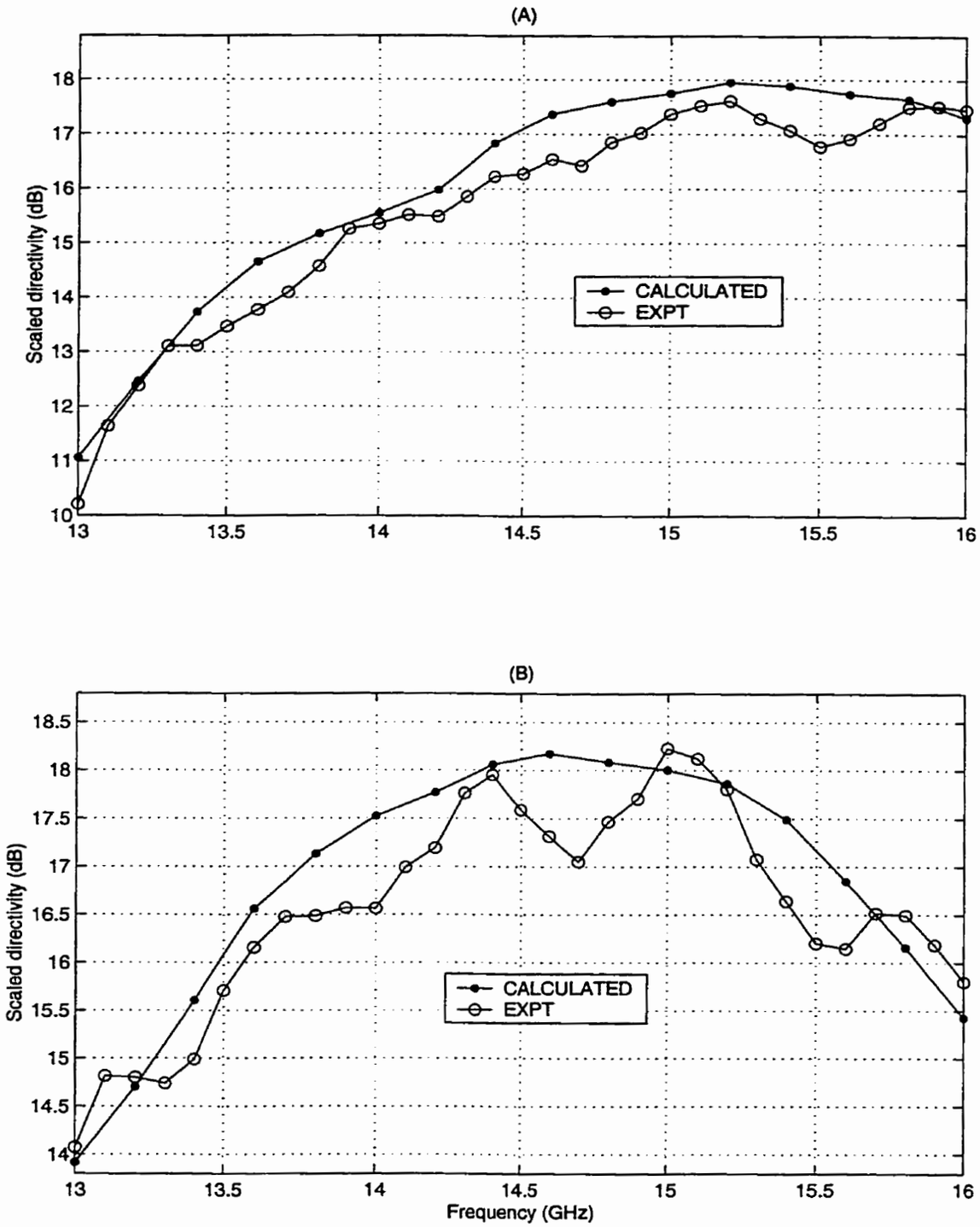

Figure 4.4: Comparison of experimental and calculated scaled directivity of LN series SBAs

(A) LN24, (B) LN26
a radiation efficiency of 90% was assumed for the calculated directivity
geometries given in Table 4.1

Thus, the directivity calculated from the measured principal plane radiation patterns of LN24 and LN26 were found to agree well with the directly measured scaled directivity across 21% bandwidth (13-16GHz). This conforms with a prior usage of the same technique on SBAs in the literature [174]. Also, the azimuthal dependence of the θ and ϕ components of the far field radiation pattern of a SBA were examined here for the first time. The azimuthal dependence was found to be $cos^2\phi/sin^2\phi$, consistent with other circular and rectangular aperture antennas.

4.4 Single SBA behaviour with frequency

The 4 SBAs were tested experimentally to gain further knowledge about the behaviour of this type of antenna. In this section, the far field radiation pattern characteristics of the four SBAs are compared and contrasted. Measurements were made across 13.4% (14-16GHz) bandwidth centred on the design frequency (15GHz), and were conducted in the compact range, anechoic chamber at the University of Manitoba, with a 10dB attenuator calibrated in place. The radiation pattern shapes, –3dB beamwidths, first null positioning, peak sidelobe levels and directivity variation across the bandwidth studied are all discussed.

4.4.1 SBA radiation pattern variation with frequency

The principal plane radiation patterns of the four SBAs investigated experimentally are presented and discussed in this subsection. The specifications of the four SBAs were given above, Table 4.1. The focus here is upon changes in cross-polarised radiation level and co-polarised radiation pattern shape across the 13.4% bandwidth (14-16GHz). Brief comments are also made

about the effects of the various cavity profiles upon the radiation patterns. This gave an overview of SBA behaviour across the bandwidth envisioned for LMCS.

Examining the far field co-polarised principal plane radiation patterns of all four SBAs, all produced boresight directed main lobes with 40-60° –10dB beamwidths, Figures 4.5-4.8. All these patterns had various nulls and side lobes, except the E-plane pattern of FLA, Figure 4.5A. The –3dB beamwidths, null positioning and side lobe level of the principal plane co-polarised radiation patterns across the 13.4% bandwidth studied are discussed in detail in the following subsections. Examining the far field cross-polarised principal plane radiation patterns of all four SBAs, the cross-polarised component peak was in the main lobe direction, at –25dB to –30dB below the main lobe peak. For all designs except LN26, the cross-polarised component was highest at 14GHz, and generally decreased with increasing frequency. The trend was reversed in LN26, Figure 4.8.

The only structural difference between SBAs FLA and S15, was that the cavity floor of the latter was inclined at 15°, Figure 4.1 & Table 4.1. Thus, any difference in far field radiation patterns of the two SBAs was a result of the one structural difference. Comparing the E-plane co-polarised patterns of S15 and FLA at the design frequency, inclination of the cavity floor to 15° narrowed the –10dB beamwidth by about 20°, introduced a null at 35° and decreased the power levels for angles wider than 35°, Figures 4.5A & 4.6A. The general features of the co-polar pattern of S15 changed little over the upper half of the bandwidth studied whereas those of FLA did. In the H-plane, the boresight cross-polar component was unchanged by inclination of the floor to 15°, Figures 4.5B & 4.6A. The H-plane co-polar pattern sidelobe level around 45° was increased by inclination of the cavity floor to 15°. The H-plane co-polarised radiation pattern shape varied less across 13.4% bandwidth than that of FLA did, Figures 4.5B & 4.6B. Thus, inclination of the

cavity floor to 15° made the co-polarised radiation patterns across 13.4% bandwidth less frequency variant.

The only structural difference between the two curved juncture SBAs was that LN26 had a $0.2\lambda_o$ greater diameter than LN24, Figure 4.1 & Table 4.1.

Comparing the E-plane co-polarised far field radiation patterns of LN24 and LN26, increasing the cavity diameter $0.2\lambda_o$, narrowed the −10dB beamwidth a few degrees, the first nulls were deepened, and the first sidelobe was suppressed about 6dB, Figures 4.5A & 4.6A. Where the well defined second null was in the E-plane pattern of LN24, at about 55° off boresight, LN26 had a peak of its second sidelobe. The H-plane radiation patterns of LN26 showed similar behaviour to LN24 in almost all aspects. The H-plane main lobe beamwidth narrowed across the 13.4% band. The H-plane first null and sidelobe moved toward boresight with increasing frequency, as for LN24, Figures 4.7B & 4.8B. The H-plane nulls in the pattern of LN26 were deep and the sidelobe level was about −18dB at the design frequency (15GHz), Figure 4.8B. However, the first null had filled in at 16GHz and the first sidelobe had risen to −11dB, distorting the main lobe, Figure 4.8B. This adversely affected the performance of LN26 as an array element at higher frequencies. The majority of the null filling and sidelobe level increase occurred between 15.5GHz and 16GHz, so these detrimental effects are outside the lower 10% of bandwidth, envisioned for LMCS. In comparison to the H-plane behaviour of LN24, increasing the cavity diameter $0.2\lambda_o$ narrowed the −10dB beamwidth by about 5° and the first null and sidelobe moved closer to boresight. The level of the first sidelobe decreased about 2dB with the $0.2\lambda_o$ diameter increase. The odd H-plane 16GHz pattern only occurred with LN26 and not LN24, thus being an effect of diameter increase. The H-plane sidelobe level was also reasonably high at about −13dB, 55° off boresight at 16GHz, Figure 4.8B.

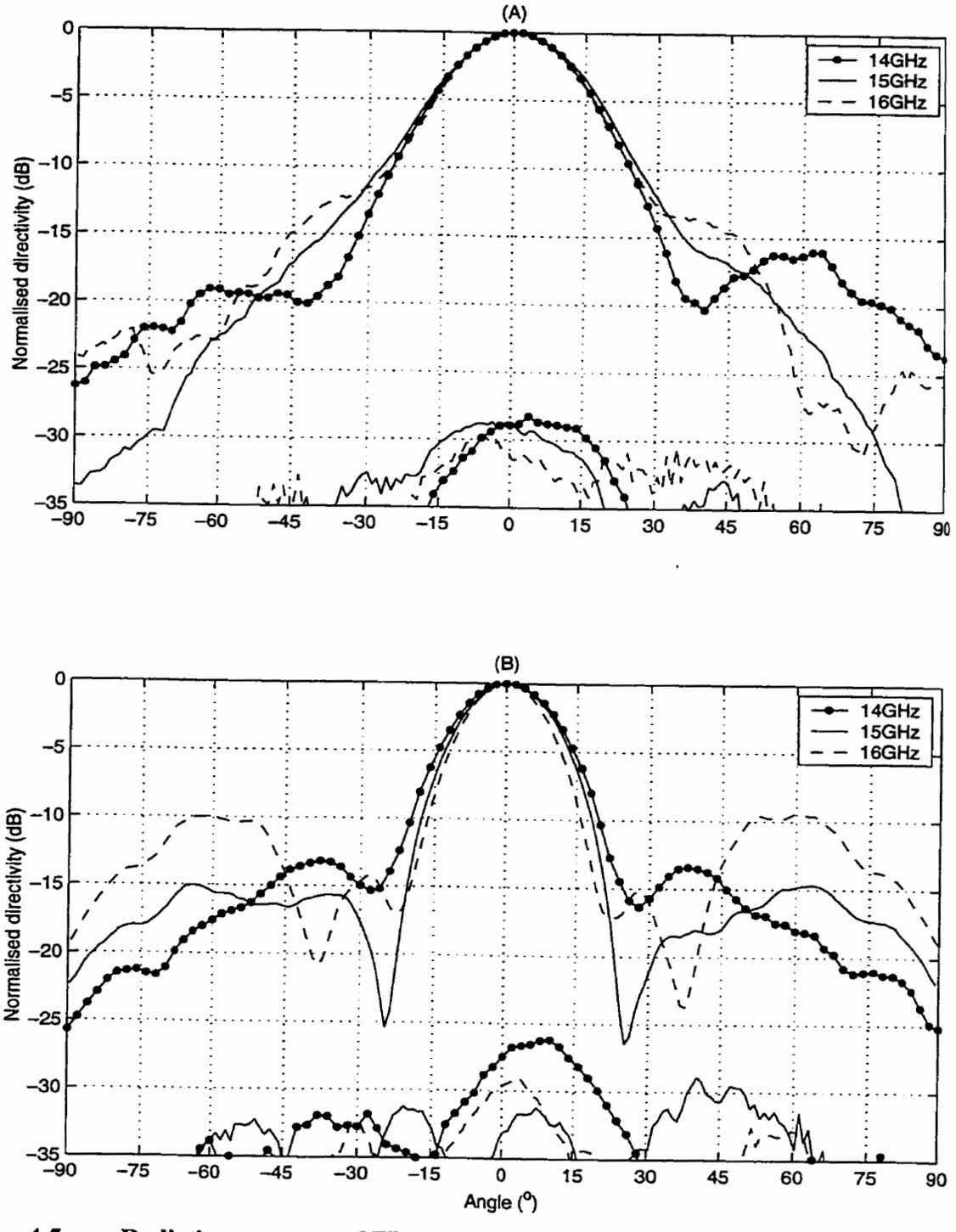

Figure 4.5: Radiation patterns of FLA across 13.4% bandwidth

(A) E-plane, (B) H-plane

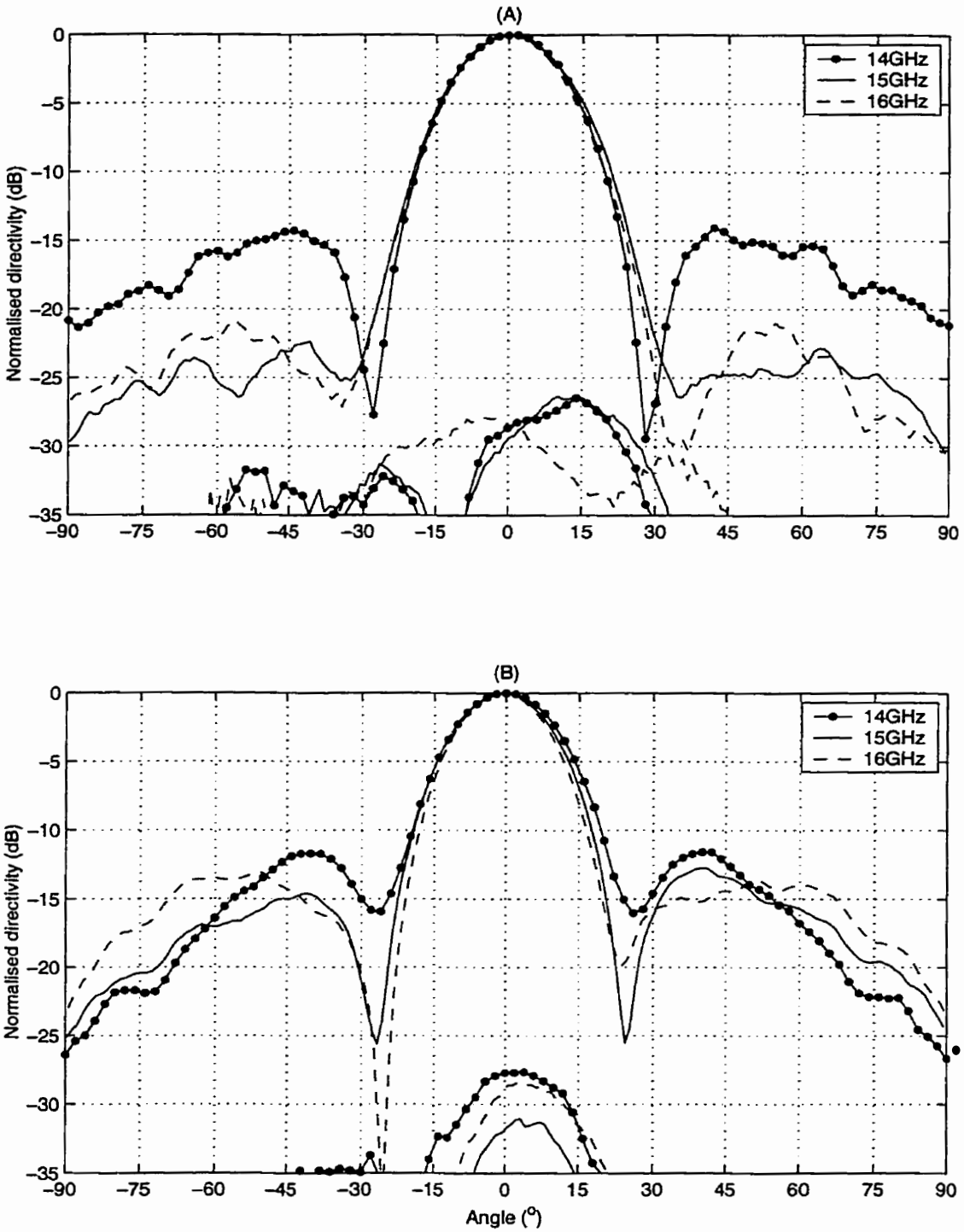

Figure 4.6: Radiation patterns of S15 across 13.4% bandwidth

(A) E-plane, (B) H-plane

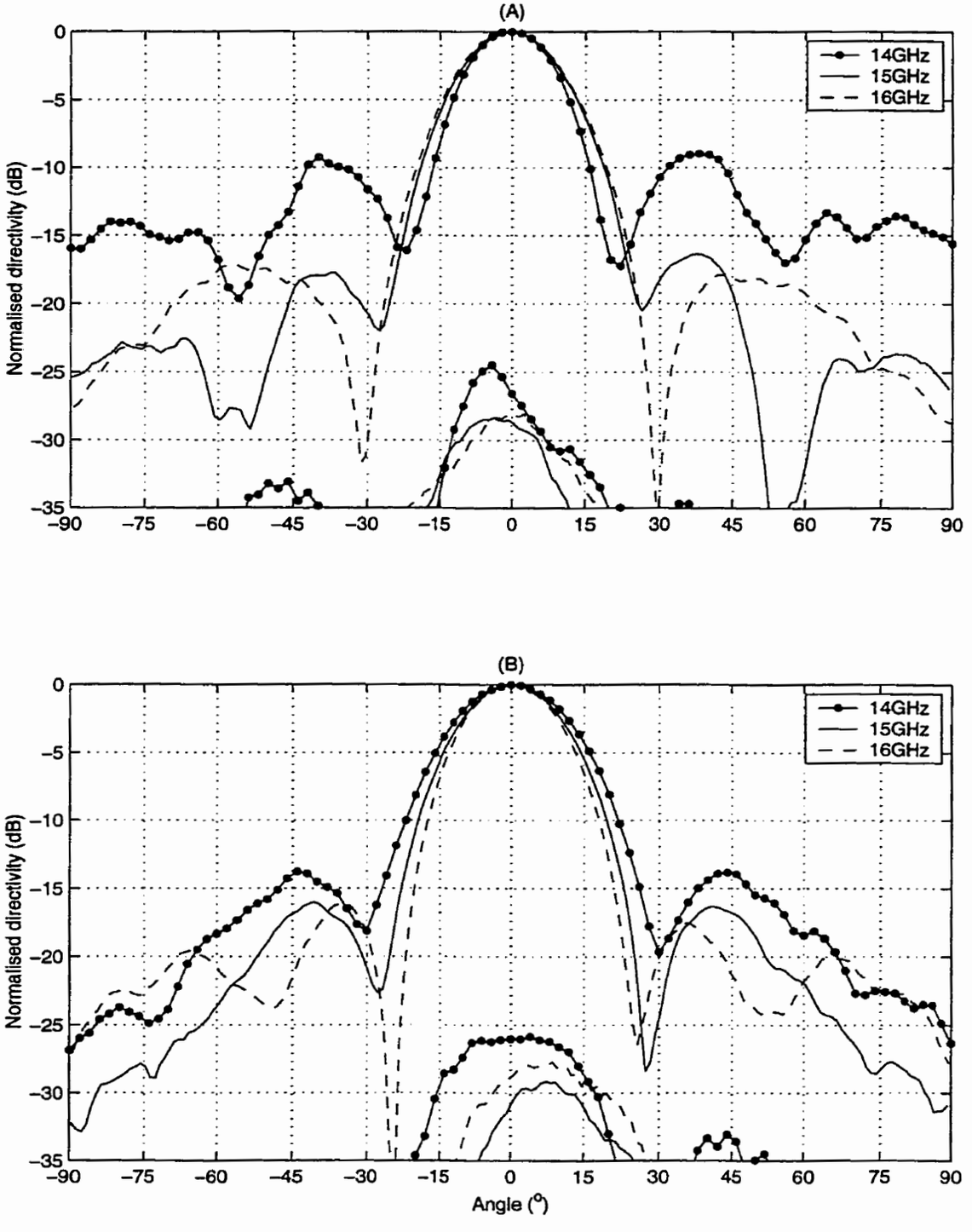

Figure 4.7: Radiation patterns of LN24 across 13.4% bandwidth

(A) E-plane, (B) H-plane

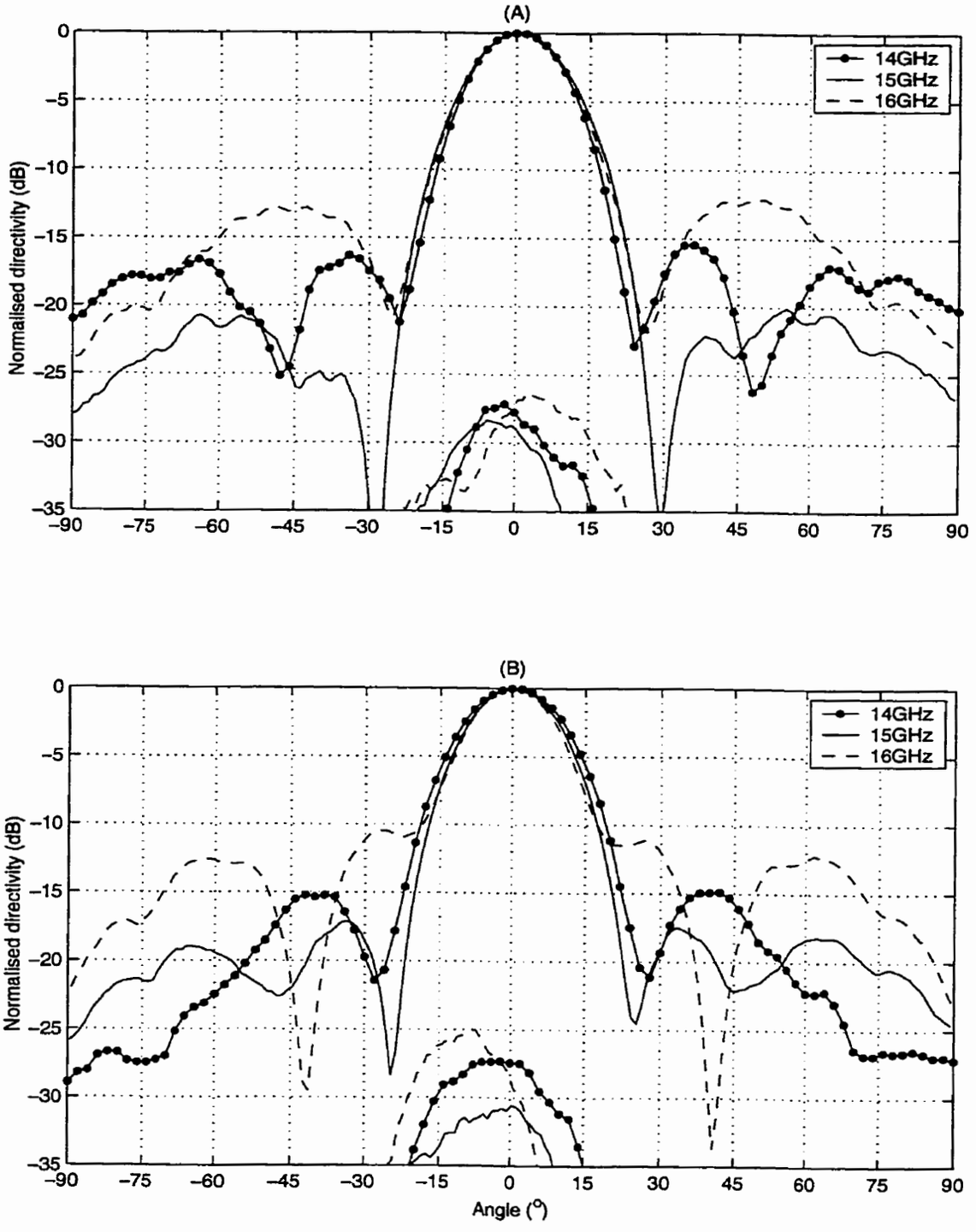

Figure 4.8: Radiation patterns of LN26 across 13.4% bandwidth

(A) E-plane, (B) H-plane

In summary, the effects of the inclination of the base of the $2.5\lambda_o$ diameter antennas, and increase in diameter for the curved juncture SBAs, upon the radiation patterns were highlighted. Inclining the base to 15° narrowed the E-plane mainlobe considerably and decreased the power levels at wider angles. So, shaping the cavity profile in this way made a $2.5\lambda_o$ diameter SBA more suitable for use as an array element. Inclination of the cavity base to 15° also made the radiation patterns less frequency variant across the bandwidth studied. A comparison of the $2.4\lambda_o$ and $2.6\lambda_o$ diameter curved juncture SBAs showed that the increase in diameter narrowed the beamwidths in both planes, moved some of the nulls and sidelobes, and introduced high sidelobes into the mainlobe at the upper extent of the bandwidth studied.

4.4.2 3dB beamwidth variation with frequency

The changes in the SBA radiation patterns with frequency are easier to comprehend if the salient quantities are extracted and plotted separately. All data was extracted using the pattern processing features of Datapro™ on the personal computer controlling the compact range. The –3dB beamwidths of the four SBAs are considered here.

The FLA SBA had the broadest E-plane –3dB beamwidth, due to the absence of nulls in that plane, Figures 4.5A & 4.9A. The –3dB beamwidths varied across 27.5° to 25.5°. Interestingly, the –3dB beamwidth in the E-plane for FLA (the simplest SBA) did not simply narrow with increasing frequency. The beamwidth was broadest at the design frequency (15GHz), having its lesser values at ±6.7% (14 & 16GHz).

Inclination of the cavity base to 15° narrowed the E-plane −3dB beamwidth of S15 by about 4° from that of FLA, by the introduction of the nulls into that plane, Figures 4.6A & 4.9A. The range of the −3dB beamwidths was reduced to about 1° across the 13.4% bandwidth studied, and the shape of the characteristic altered a little. However, the widest −3dB beamwidth occurred near the design frequency.

It was noted above that the E-plane −10dB beamwidth of the two curved juncture SBAs (LN24 & LN26) broadened with increasing frequency, in contrast to that of the other two SBAs which narrowed. The −3dB beamwidth of the $2.4\lambda_o$ diameter curved juncture SBA LN24 held to the trend of the −10dB beamwidth, by increasing about 2.5° across the bandwidth studied. In contrast the −3dB beamwidth of the $2.6\lambda_o$ diameter LN26 varied less than 1°, and thus was relatively invariant across the bandwidth.

The behaviour of the E-plane −3dB beamwidths of the 4 SBAs across 13.4% bandwidth was not simple. The curved juncture was better than the 15° base for narrowing the −3dB beamwidth, but the beamwidth of LN24 broadened with increasing frequency. This feature may be undesirable in an array setting.

In contrast to the E-plane, the H-plane −3dB beamwidth of all four SBAs narrowed with increasing frequency, Figure 4.9B. Once again the $2.6\lambda_o$ diameter curved juncture LN26 SBA had the narrowest beamwidth. The $2.4\lambda_o$ diameter LN24 was 2.5° broader, and had the broadest −3dB beamwidths. This shows the effect of cavity diameter upon the −3dB beamwidth of this type of SBA.

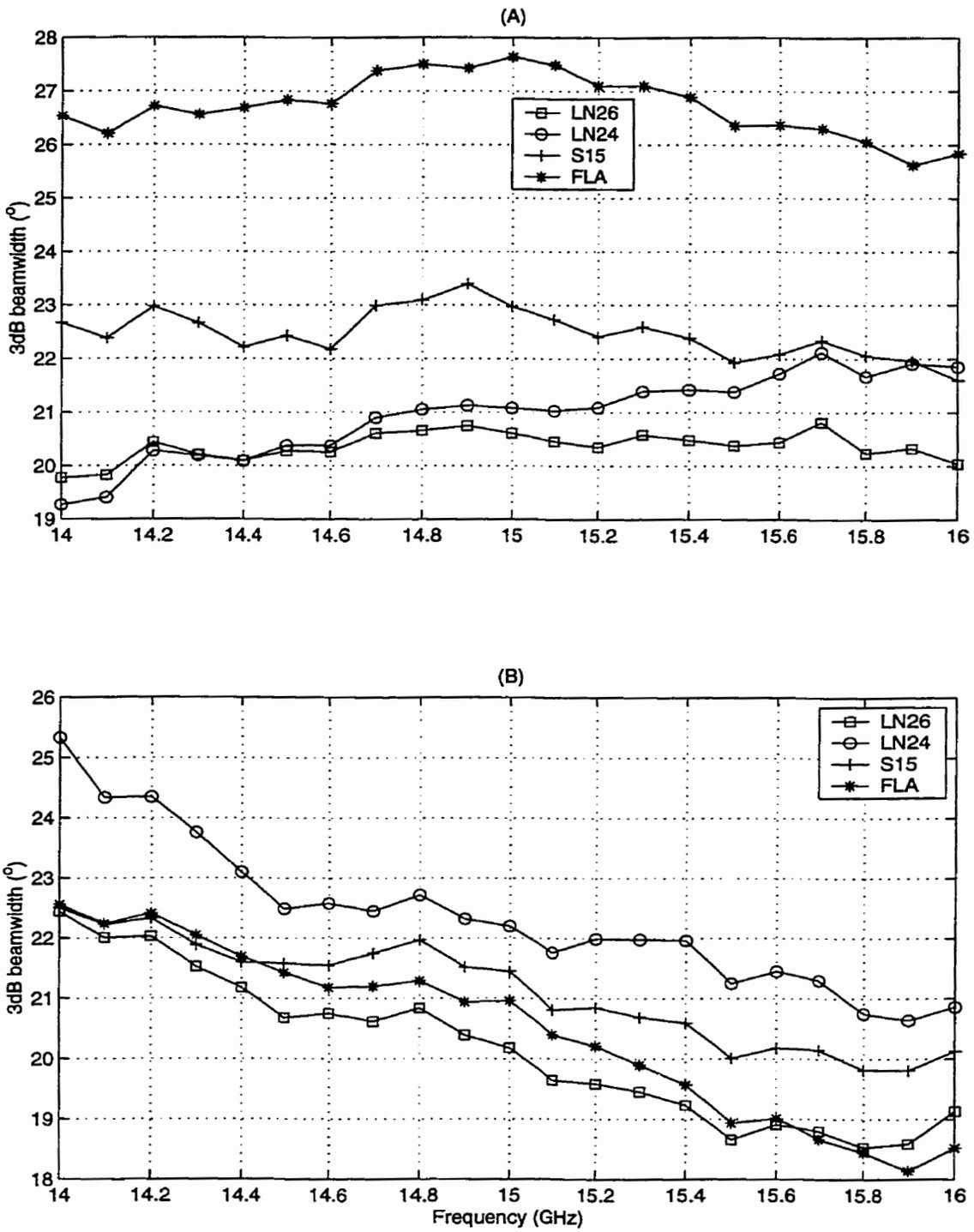

Figure 4.9: -3dB beamwidth variation across 13.4% bandwidth

(A) E-plane, (B) H-plane

Comparing the FLA and S15 SBAs, inclination of the cavity floor to 15° had the effect of broadening the H-plane –3dB beamwidth by about 1°, above the design frequency, Figure 4.9B. Inclining the cavity floor had the opposite effect to that in the E-plane, Figure 4.9A. This suggests that it would be best to only shape the cavity profile in the E-plane and to leave the H-plane flat if minimal –3dB beamwidth is desired. This is discussed further in the Future Work section of Chapter 4.

In summary, the major effects of profiles Figure 4.1B and 4.1C upon the –3dB beamwidths were in the E-plane. The unmodified profile (FLA) gave narrower –3dB beamwidths than both the $2.5\lambda_o$ diameter 15° inclined cavity base and $2.4\lambda_o$ diameter curved juncture SBAs in the H-plane. Thus, cavity profile shaping can be used to either narrow or broaden the –3dB beamwidths. As a generalisation, the SBAs displayed more complicated –3dB beamwidth behaviour in the E-plane than in the H-plane.

4.4.3 Null position variation with frequency

The changes in the SBA radiation patterns with frequency are easier to comprehend if the key quantities are extracted and plotted separately. All data was extracted using the pattern processing features of Datapro™ on the personal computer controlling the compact range. E and H-plane co-polarised pattern first null position variation is examined in this subsection. Null positioning in an array element radiation pattern is an important means of grating lobe mitigation.

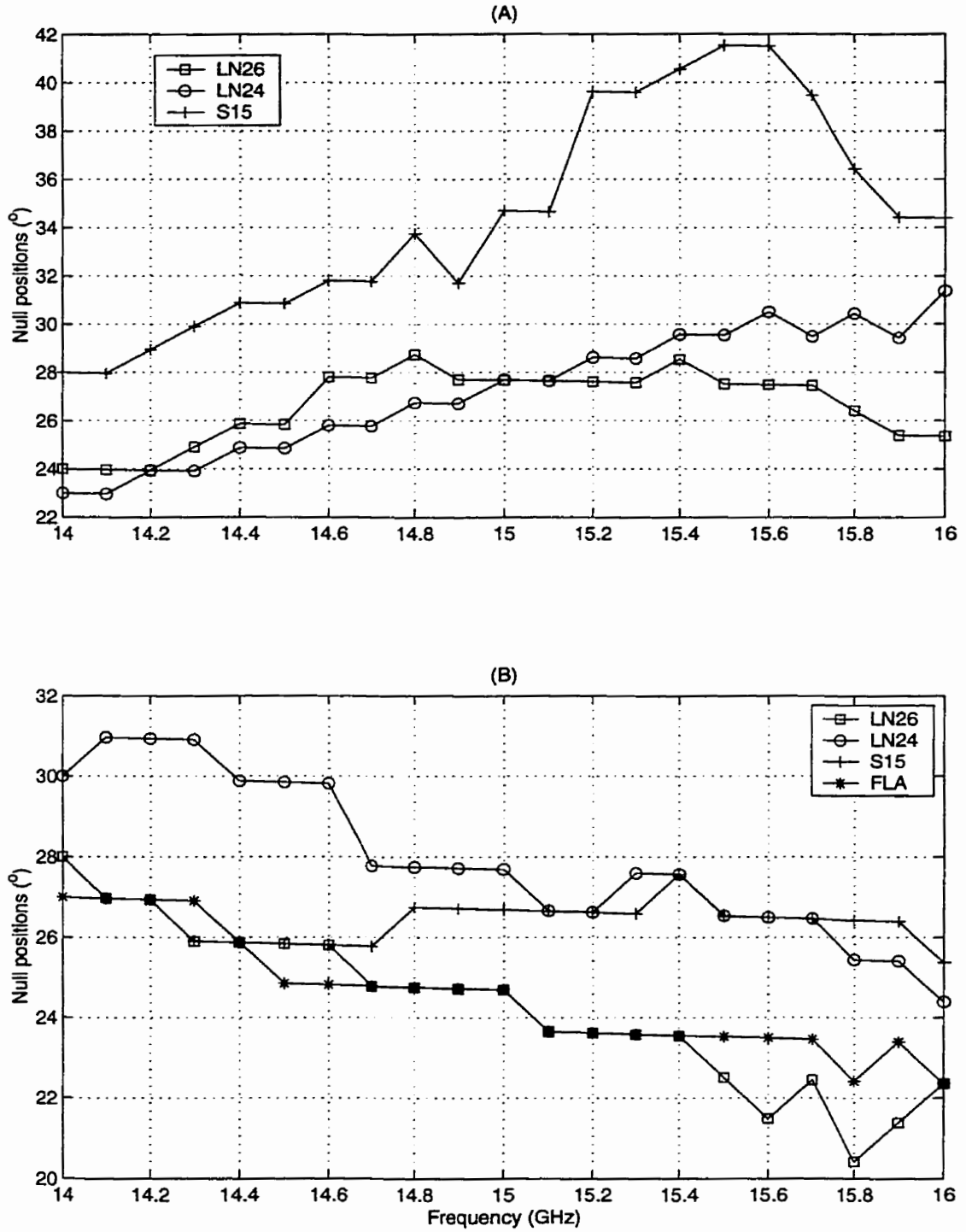

Figure 4.10: First null position variation across 13.4% bandwidth

(A) E-plane, (B) H-plane

As with the E-plane –3dB beamwidths, the E-plane first order null positions of the SBAs did not follow simple trends across the 13.4% bandwidth studied, Figure 4.10A. There is no data for FLA as it did not have nulls in the E-plane.

The E-plane nulls of S15 moved 14° away from boresight between –6.7% of the design frequency to +3.35%, Figure 4.10A. Above this point, the trend reversed and the nulls moved 6° back toward boresight. The total range was 14°. The range of movement for LN24 was 8°. In contrast to S15, the E-plane nulls of LN24 simply moved away from boresight with increasing frequency, Figure 4.10A. The range for LN26 was the smallest at 4°, with the null positions being furtherest from boresight about the design frequency. LN26 also had nulls closest to boresight of the four SBAs studied.

In keeping with the narrowing of the –3dB beamwidths in the H-plane with increasing frequency, the H-plane nulls of all four SBAs moved toward boresight, Figure 4.10B. The range of movement was about 6° for FLA, LN24 and LN26. For S15, the range was about half at 2.5°. It is interesting to note that the $2.5\lambda_o$ diameter FLA had nearly identical null positioning to the $2.6\lambda_o$ diameter LN26, Figure 4.10B. The $0.1\lambda_o$ increase in diameter and the curved juncture did not significantly alter the null positioning in the H-plane, in stark contrast to the E-plane, Figures 4.5, 4.8 & 4.10. On average, the H-plane nulls of LN24 were 4° further from boresight than those of LN26, showing the effect of the $0.2\lambda_o$ difference in diameter. The introduction of the 15° inclined base prevented the H-plane nulls from moving closer to boresight over the range of frequencies –3.35% to +6.67% of the design frequency, comparing S15 to FLA, Figure 4.10B. Thus, inclination of the base is a method for fixing the H-plane nulls across 10% bandwidth.

As with the –3dB beamwidths examined in the previous subsection, the nulls followed reasonably simple trends in the H-plane and complex trends in the E-plane. This further highlights the fundamental differences between the E and H-planes of rectangular waveguide excited SBAs.

4.4.4 Sidelobe level variation with frequency

The changes in the SBA radiation patterns with frequency are easier to comprehend if the salient quantities are extracted and plotted separately. All data was extracted using the pattern processing features of Datapro™ on the personal computer controlling the compact range. The peak sidelobe level is an important parameter for medium gain antennas such as SBAs. Sidelobes consume power, reducing the achievable directivity, in addition to increasing off boresight reception sensitivity. Examining the peak sidelobe level, whether from the first, second or higher order sidelobes, across 13.4% bandwidth will further add to an understanding of SBAs.

All three SBAs with sidelobes in the E-plane showed similar peak sidelobe level behaviour with frequency, Figure 4.11A. The peak sidelobe levels were higher at either end of the band of frequencies studied, than at the centre. The FLA SBA did not have distinct sidelobes in the E-plane, as with the nulls. The S15 antenna had the lowest sidelobe levels; its lowest being –25dB below the mainlobe peak at about +3.4% above the design frequency, Figure 4.11A. Thus, inclining the base at 15° not only narrowed the E-plane –3dB beamwidth, it also produced very low E-plane sidelobes, in contrast to the high wide angle power levels of the FLA SBA.

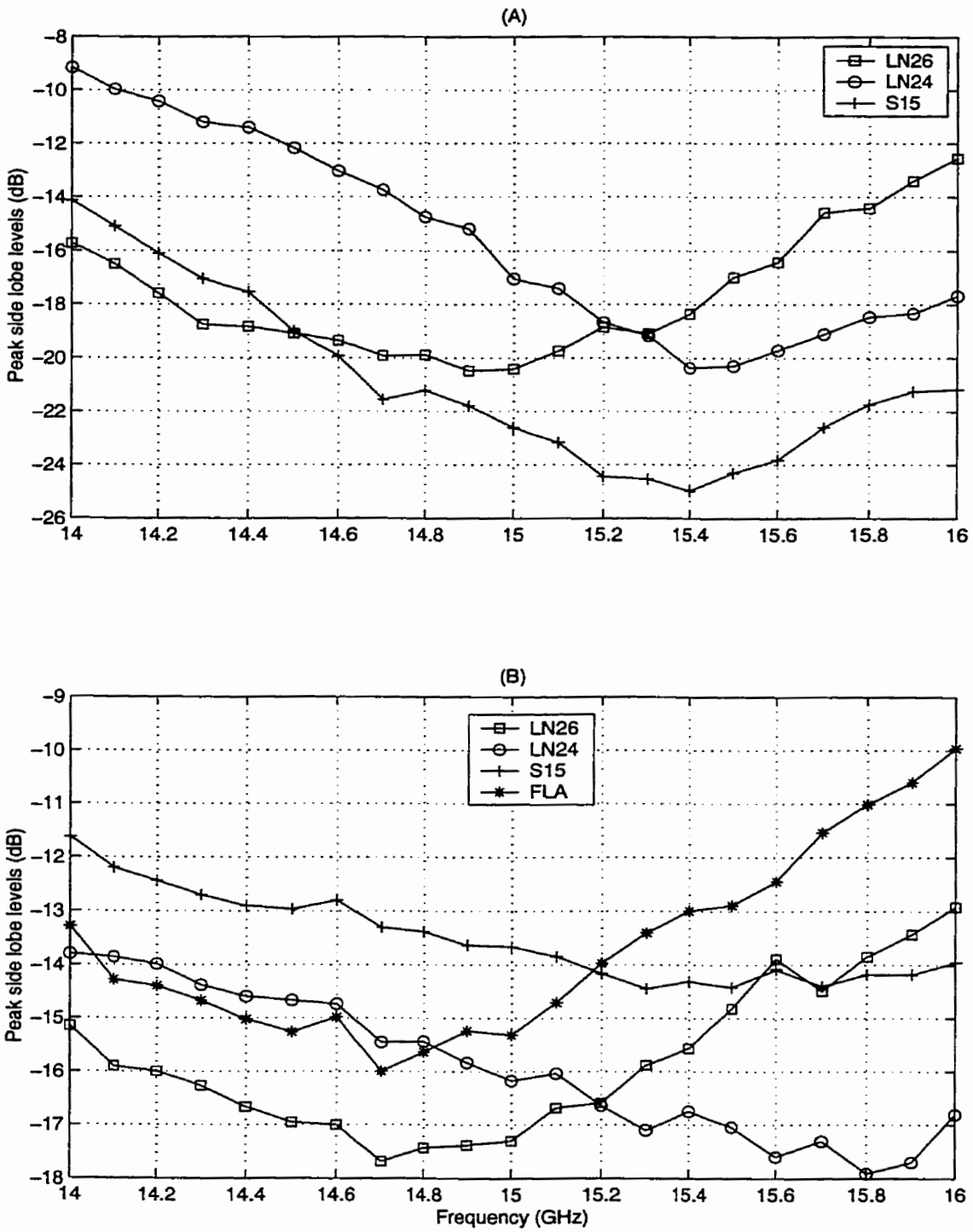

Figure 4.11: Peak sidelobe level variation of SBAs across 13.4% bandwidth

(A) E-plane, (B) H-plane

Interestingly, the minimum H-plane peak sidelobe levels of the curved juncture SBAs were identical, Figure 4.11B. The $2.6\lambda_o$ diameter LN26 had its minima at the design frequency, while that of the $2.4\lambda_o$ diameter LN24 was at +3.4% above the design frequency, Figure 4.11B. The chief effect of the $0.2\lambda_o$ decrease in diameter was to shift the minimum sidelobe level up 3.4% in frequency. The bandwidth over which the sidelobe level was within 2dB of the minimum was greater for the $2.6\lambda_o$ SBA, showing some advantage for the larger diameter.

As with the H-plane –3dB beamwidth and first order null positioning, the H-plane sidelobe level of LN26 follows a near identical trend to FLA, Figure 4.11B. The only difference was that the H-plane peak sidelobe levels of LN26 were 2dB lower than those of FLA. The minimum peak sidelobe level for both SBAs was close to the design frequency. The behaviour of the two remaining SBAs, LN24 and S15, differed in that the sidelobe level simply decreased with increasing frequency, over the bandwidth studied, Figure 4.11B. However, the H-plane sidelobe level of both LN24 and S15 show signs of increasing in level near the upper extent of the range studied. Thus addition of the 15° inclined base raised the minimum achievable sidelobe level by 2.5dB, and increased the bandwidth over which the sidelobe level remained low, Figure 4.11B. As to the differences between the $2.4\lambda_o$ and $2.6\lambda_o$ diameter curved juncture SBAs, as with the E-plane sidelobe level, decreasing the diameter $0.2\lambda_o$ moved the minimum of the characteristic upward in frequency (6.7% here).

In summary, there are a number of similarities between the peak sidelobe behaviour in the principal planes. The sidelobe levels followed similar trends to those of the –3dB beamwidths and first order null positioning. The minimum peak sidelobe level values for each individual SBA were more or less coincident at the same frequencies at which the greater values of E-plane –3dB beamwidth and null offset from boresight occurred. These frequencies, unique for each of the four

SBAs studied, were found to closely match the directivity peak in the following subsections. Knowledge of these types of radiation pattern parameter linkages is fundamental and needed for any further work on radiation pattern shaping.

4.4.5 Directivity variation with frequency

As explained in the previous subsection, the poor input impedance characteristics of the four SBAs prevented direct measurement of gain and consequently scaled directivity across the full bandwidth of interest (scalable by two to LMCS band). A method of far field pattern integration previously reported [174] was found to yield credible directivity figures in comparison to that measured across 21% bandwidth, section 4.3. The directivity calculation method having thus been found satisfactory, was applied to all four SBAs across the full 13.4% bandwidth of interest, 14-16GHz.

The directivity characteristics of each of the four SBAs is unique, in common with the –3dB beamwidth, first null and peak sidelobe levels, Figure 4.12A. There is a link between the minimum peak sidelobe level in both planes and peak directivity, Figures 4.11 & 4.12A. For each of the four SBAs the peak sidelobe level minimums and maximum directivity occurred at the same frequency. For FLA and LN26, this was close to the design frequency, while it was near the upper end of the bandwidth for S15 and LN24, Figure 4.12A. These are also about the frequencies at which the maxima of the E-plane –3dB beamwidths and greatest offsets of the first null from boresight occurred, Figures 4.9 & 4.12A. Thus, the frequency at which a rectangular waveguide fed SBA produces its peak directivity is also that at which it has its lowest peak sidelobe level, broadest –3dB E-plane beamwidth and the greatest first E-plane null offset from boresight. No

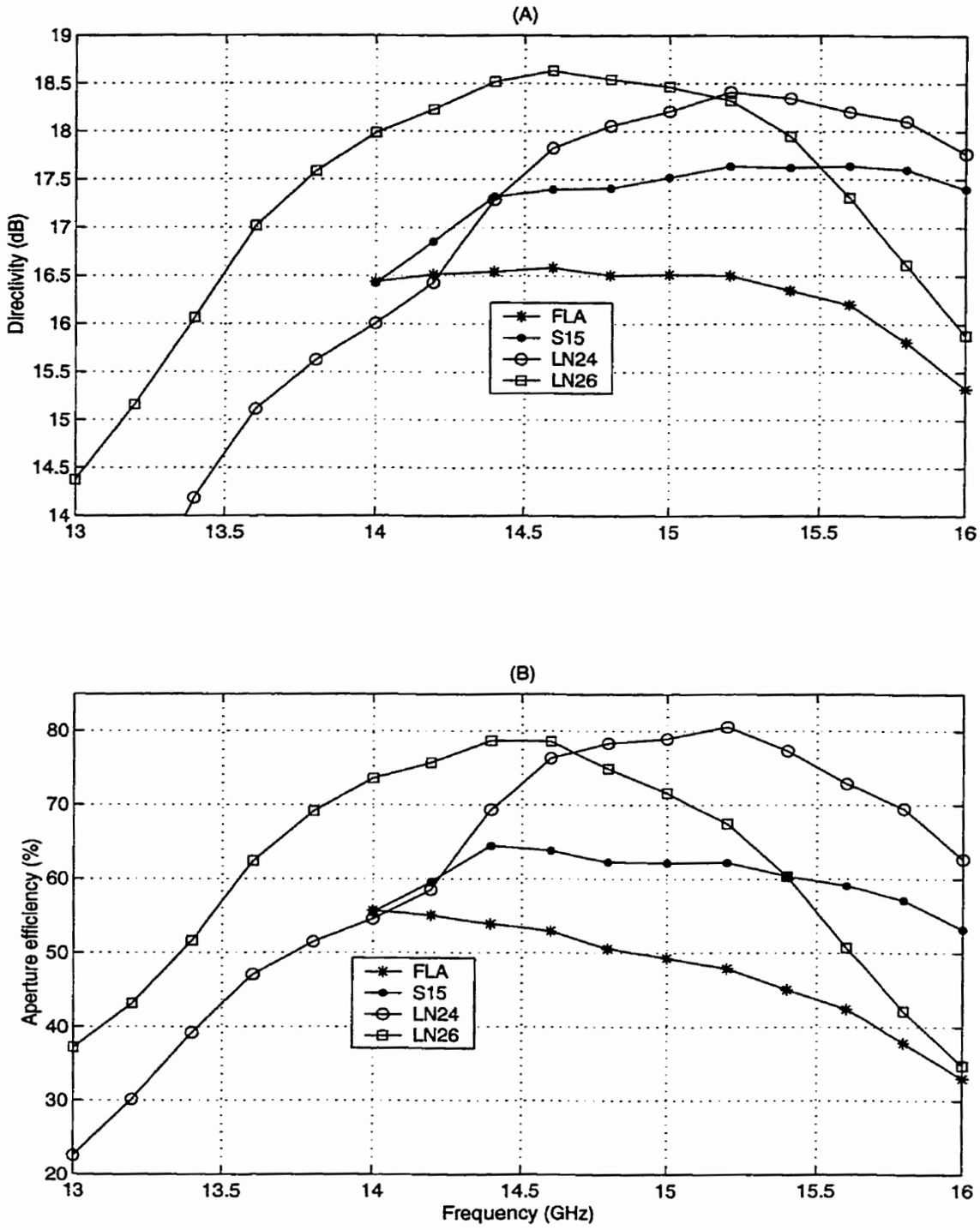

Figure 4.12: Calculated directivity and aperture efficiency of all 4 SBAs

(A) calculated directivity, (B) aperture efficiency from calculated directivity used unit cell as area for aperture efficiency calculation geometries described in Table 4.1 & Figure 4.1

such generalisations about SBA behaviour behaviour were found in the literature. These characteristics are contradictory with respect to using SBAs as large diameter array elements, where it is desirable to have a high directivity with nulls close to boresight for grating lobe mitigation. It should also be noted that the input impedance matching for all four SBAs was poor at the frequency of peak directivity. This is as predicted in the previous chapter, and could be compensated for with a matching network in an array.

The $2.6\lambda_o$ diameter curved juncture SBA LN26 gave the highest calculated directivity of the four SBAs, Figure 4.12A. This was at 14.6GHz and corresponded to an aperture efficiency of 71.5%, Figure 4.12B. Similarly high aperture efficiencies of about 70% were achieved by the $0.2\lambda_o$ smaller diameter LN24, but at the design frequency and above. Thus, both curved juncture SBAs achieved aperture efficiencies about 70% as predicted in the numerical study of SBAs, in the previous chapter. The $0.2\lambda_o$ difference in the diameter caused the bands of high aperture efficiency from either SBA to fall at different points within the bandwidth studied. The higher aperture efficiencies from LN26 were below the design frequency, while those from LN24 were above. Presumably, a $2.5\lambda_o$ diameter SBA if built would fall between these two. The $2.6\lambda_o$ diameter LN26 had a 1dB directivity bandwidth of 12%, while the $2.4\lambda_o$ diameter LN24 had 10%. Both satisfy the presumed requirement of 10% for a LMCS antenna array element. Additionally, LN26 had a wider 1dB bandwidth, showing some benefit of a larger diameter SBA.

As predicted in the numerical survey of SBAs, in the previous chapter, the flat based FLA and 15° inclined base S15 SBAs gave 20% and 10% lower aperture efficiency, respectively, than the curved juncture SBAs, Figure 4.12A. The only structural difference between the $2.5\lambda_o$ diameter FLA and S15 SBAs was the 15° inclination of the cavity base of the latter. Thus any performance difference was solely the result of the angle of the cavity base. So, inclination of the

base to 15° increased the aperture efficiency by 10% and the directivity by 0.8dB across most of the bandwidth studied. This was chiefly the result of improvements to the E-plane radiation pattern, as discussed previously. This shows the value of cavity shaping.

In summary, the directivity behaviour of the four SBAs was discussed. Peak aperture efficiencies of 75% were obtained from both curved juncture SBAs. The peak directivities were found to coincide with poor input impedance matching, low sidelobe levels but broad E-plane −3dB beamwidths and wide first null placement.

4.5 Validation of numerical study

Four rectangular waveguide excited SBAs were built and tested to further study those particular types. Experimental investigation of the SBAs was used to validate the results of the numerical study in the previous chapter. Some of the results discussed in prior sections of this chapter hinted that there was good agreement between experimental results and HFSS models. The experimental and HFSS scaled directivity and input impedance characteristics of LN24 and LN26 across 21% bandwidth are compared in this section.

Comparing the experimental and HFSS scaled directivity characteristics of LN24, there was good agreement in terms of level, Figure 4.13A. However, the HFSS response was moved about 500MHz (3.4%) higher in frequency than the experimental results. This frequency offset was also apparent in the input impedance characteristic of LN24, Figure 4.13B. A similar offset occurred between the experimental and HFSS input characteristics of LN26, Figure 4.14B. Due to the artifacts in the experimental scaled directivity characteristic of LN26, it is difficult to identify

the peak of the characteristic, and thus determine the offset between the experimental and HFSS characteristics, Figure 4.14A. However, the calculated directivity did not show the artifacts, Figure 4.4B & 4.12A. The difference between the calculated directivity peak and the HFSS scaled directivity peak was 700MHz, Figures 4.12A & 4.14A. This was close to the 3.4% frequency offset of the LN24 results.

In summary, the experimental and HFSS scaled directivity of LN24 and LN26 were compared across 21% bandwidth. The HFSS results were found to be shifted approximately 3.4% upward in frequency, although the prediction of peak values and characteristic shapes was found to be excellent. These results validate the numerical study of the previous chapter, although they recommend that the design frequency should be shifted down 3.4%, from 15GHz to 14.5GHz.

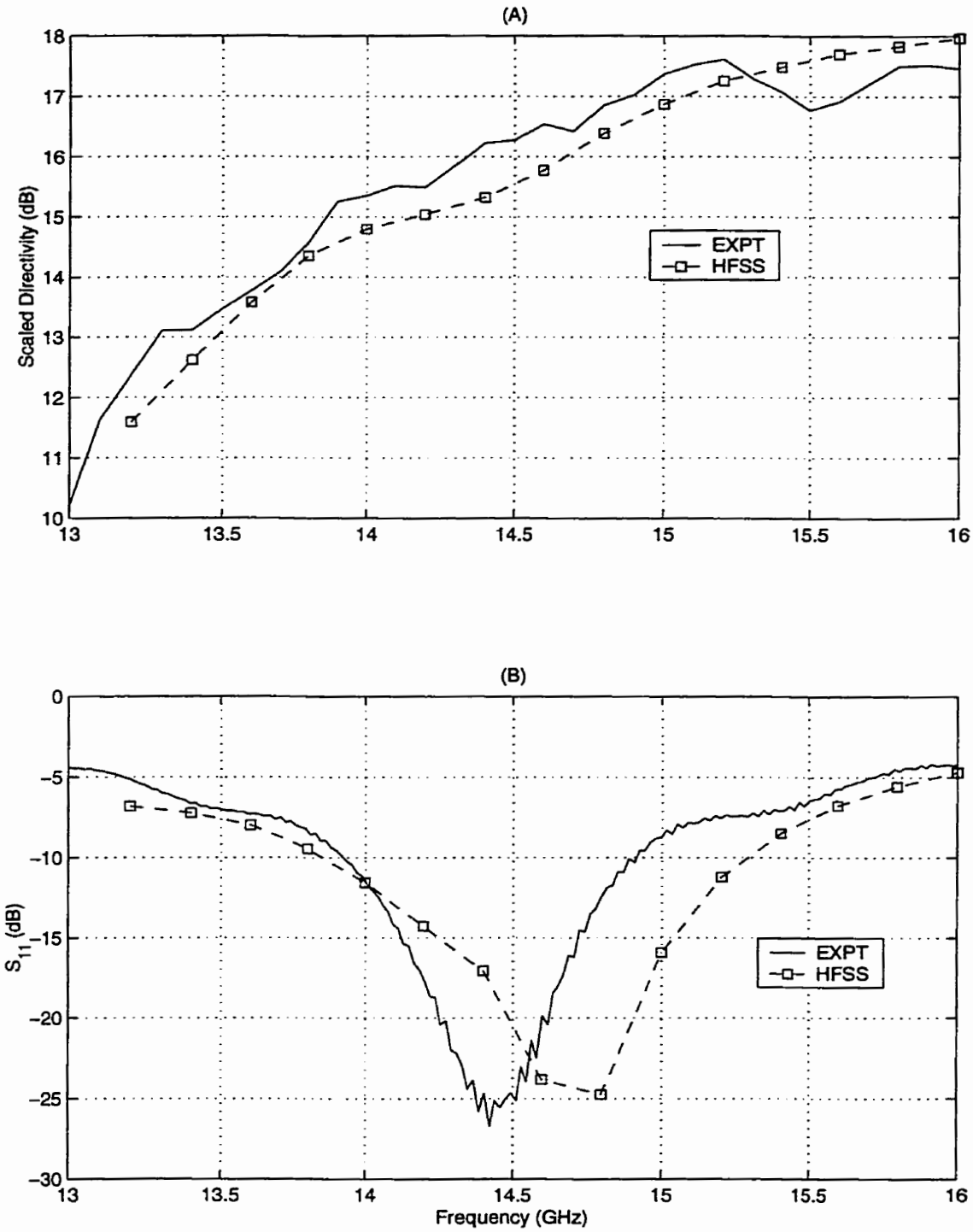

Figure 4.13: Comparison of experimental and HFSS scaled directivity and input impedance of LN24

(A) scaled directivity, (B) input impedance
"EXPT" of (A) is "EXPT" of Figure 4.4A

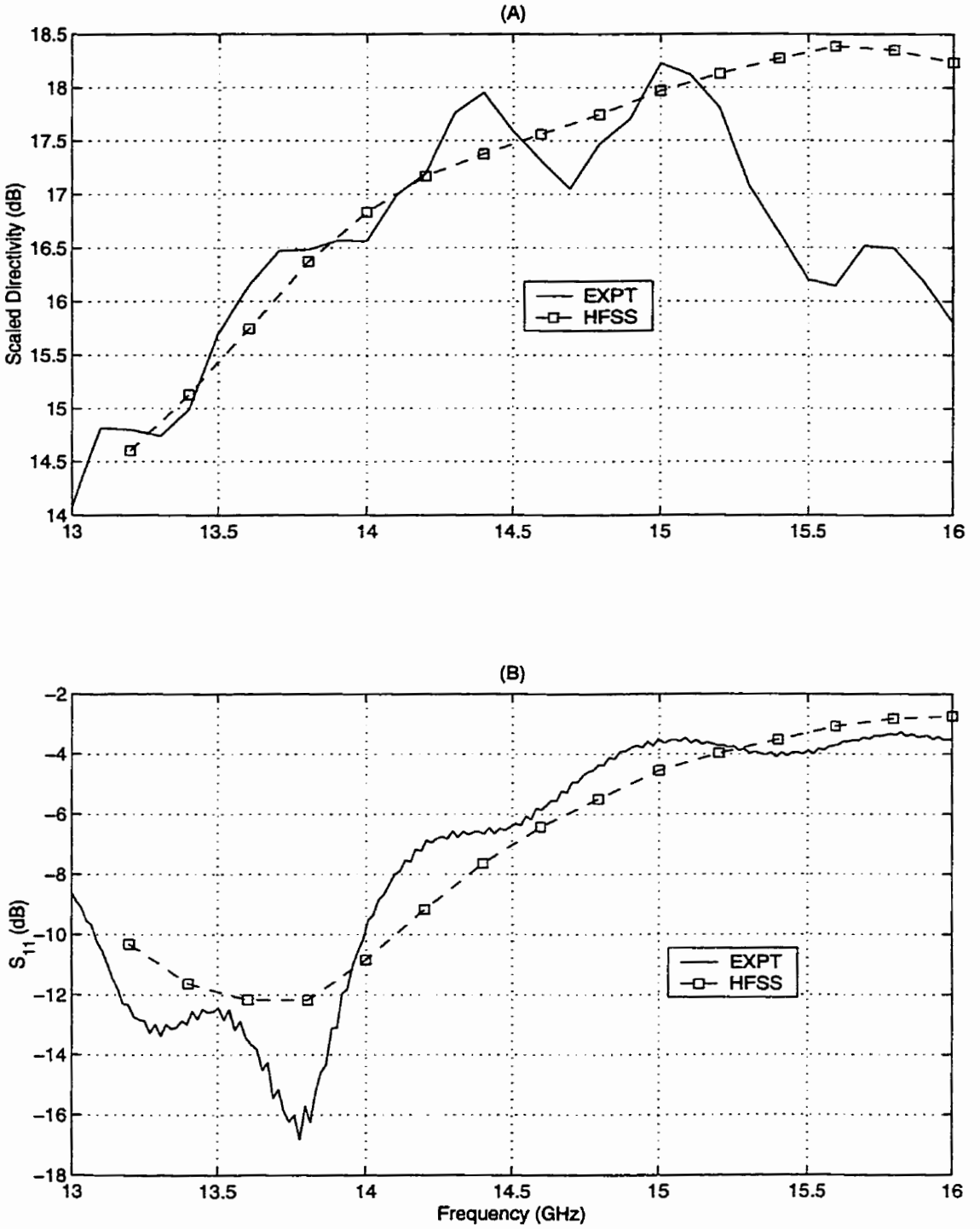

Figure 4.14: Comparison of experimental and HFSS scaled directivity and input impedance of LN26

(A) scaled directivity, (B) input impedance
"EXPT" of (A) is "EXPT" of Figure 4.4B

4.6 Array element assessment

In this section, the co-polarised radiation patterns at the design frequency are used in a theoretical assessment of the 4 SBAs as array elements. The chief concern with using large array elements such as these SBAs (having diameters in excess of $1\lambda_o$) in a boresight array is that a considerable amount of radiated power will be lost into grating lobes. This effect may greatly reduce the achievable directivity, and consequently gain, of an array, possibly making it impractical for applications such as LMCS.

The co-polar, principal plane radiation patterns of all four SBAs were multiplied by appropriate array factors (equations 6.10 of [179]) to obtain the radiation patterns that could be expected if such were built. The array factor for each SBA was obtained by the same procedure as that used for the microstrip subarrays in Chapter 2. The use of the array factor was justified as the interelement coupling was extremely low [166], due to the low field strength at the cavity edges, chapter 3. Here a 1mm thick cavity rim was assumed between each SBA. Thus, the $2.4\lambda_o$ diameter LN24 became a $2.45\lambda_o$ sided square array element unit cell, and so on. The predicted array radiation patterns were calculated for 2x2 and 8x8 arrays, Figures 4.15-4.18.

The 2x2 and 8x8 predicted radiation patterns for each of the four SBAs are each unique, Figures 4.15-4.18. The differences and similarities are much more pronounced in the 8x8 array patterns than in the 2x2 patterns. For example, the first order grating lobes at 23° and the second order grating lobes at 53° are clearly visible in all 8x8 patterns, whereas these are hard to disassociate from the sidelobes of the 2x2 array patterns, Figures 4.15-4.18. For this reason the 8x8 patterns will be given more attention.

Common to all of the predicted 8x8 array patterns was a first sidelobe level of −7dB below the mainlobe peak, Figures 4.15-4.18. This high first sidelobe was a product of the array factor and the broad beamwidth of the main lobe of each SBA. Such a high first sidelobe would be a disadvantage for this type of array in comparison to parabolic dish antennas for an application such as LMCS. Away from boresight, the low E-plane sidelobe levels of S15 served to give the best wide angle side lobe and second order grating lobe suppression of any of the four SBAs, Table 4.2 and Figure 4.16A. LN26 gave the best wide angle suppression in both planes, Table 4.2 and Figures 4.18A & 4.18B. This was largely due to low sidelobes and second order nulls between 30° and 60° off boresight in the principal planes of the measured LN26 SBA. The relatively higher sidelobe levels from LN26 at angles wider than 60° had little detrimental effect as these were suppressed by the array factor, Figures 4.18A & 4.18B.

As far as the first null of the single SBA patterns canceling the first order grating lobe, no SBA was successful in this regard, Table 4.2. Complete cancellation did not occur as the first order grating lobe was always a few degrees closer to boresight than the first order null in the elemental patterns. However, in all cases where there was a first order null, it was close enough to suppress the first order grating lobe to some degree, Table 4.2. The best case of suppression was in the H-plane of FLA. At −18dB below the main lobe peak, it is difficult to pick the first order grating lobe from the surrounding sidelobes, Figure 4.15B. In contrast, the E-plane of FLA was the worst case as there were no nulls to mitigate the grating lobes, Figure 4.15A. There the grating lobe was −8dB below the main lobe peak, rivaling the first sidelobe level. The first order grating lobes in the E-plane of FLA could thus be expected to cause a substantial loss in directivity. The best at suppressing the first order grating lobes in both planes was LN26, Table 4.2.

An assessment of the four SBAs as array elements has been conducted using the theoretical array factor. Both sidelobe and grating lobe suppression were considered. LN26 gave the best all round performance in these measures. It was thus used as an array element in the following section. However, in common with the other three SBAs, LN26 was found to give relatively high first sidelobes, at −7dB below boresight, and the elemental first order nulls did not wholly suppress the first order grating lobes. These aspects would disadvantage an array of SBAs in comparison to a parabolic dish antenna, for an application such as LMCS.

Table 4.2: Peak grating lobe levels from predicted 8x8 SBA arrays

Antenna	E-plane grating lobe level (dB)				H-plane grating lobe level (dB)			
	1st order		2nd order		1st order		2nd order	
	level (dB)	angle (°)	level (dB)	angle (°)	level (dB)	angle (°)	level (dB)	angle (°)
FLA	-8	23	-18	52	-18	23	-16	52
S15	-12.5	23	-24	52	-15.5	23	-15	52
LN24	-14	24	-23	55	-13.5	24	-18	55
LN26	-15	22	-21	49	-17.5	22	-21.5	49

Complementary to Figures 4.15-4.18

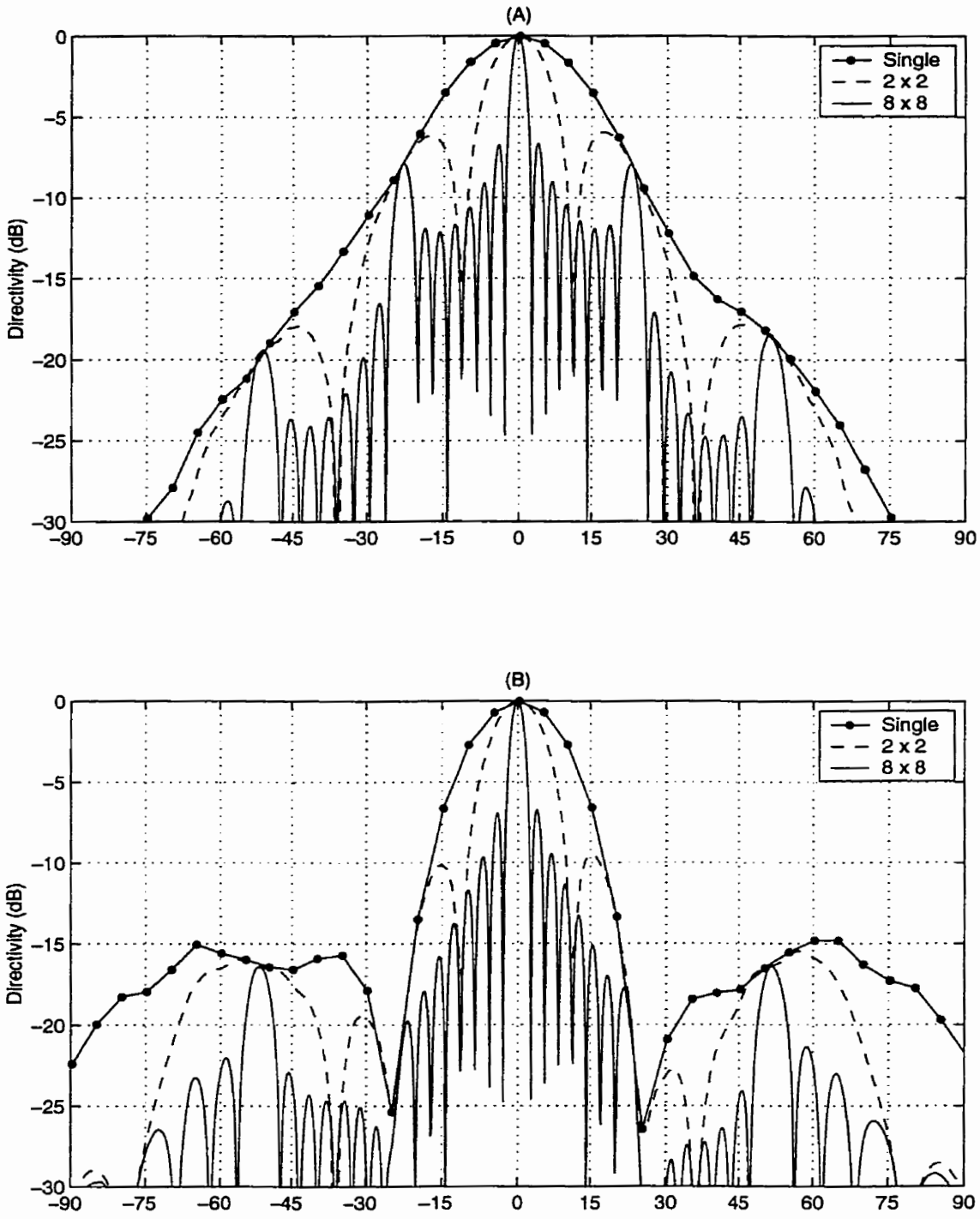

Figure 4.15: Predicted radiation patterns of 2x2 and 8x8 arrays of FLA using array factor

(A) E-plane, (B) H-plane
"single" pattern experimentally measured, from Figure 4.5, f=15GHz
"2x2" & "8x8" products of "single" & array factors

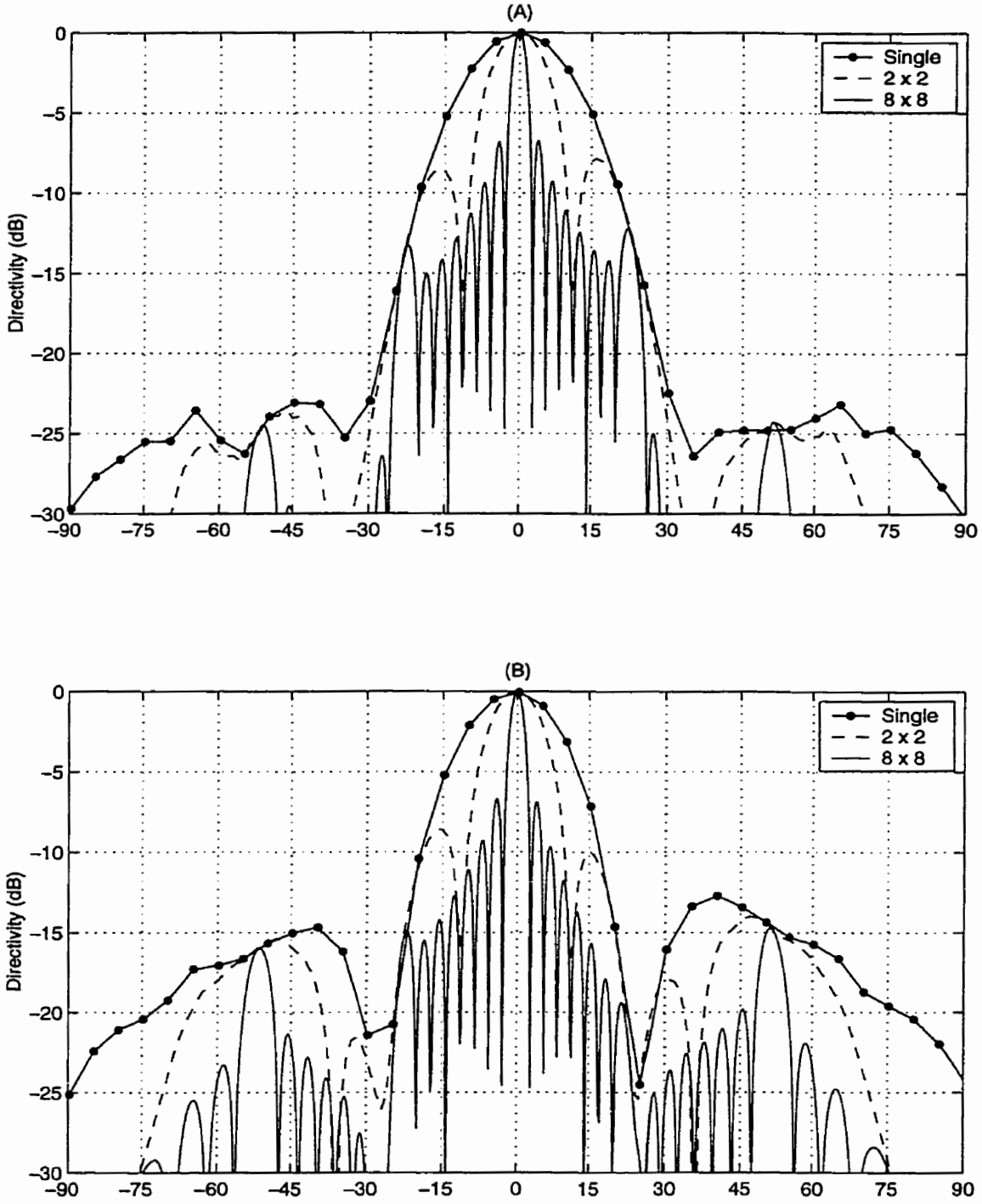

Figure 4.16: Predicted radiation patterns of 2x2 and 8x8 arrays of S15 using array factor

(A) E-plane, (B) H-plane
"single" pattern experimentally measured, from Figure 4.6, f=15GHz
"2x2" & "8x8" products of "single" & array factors

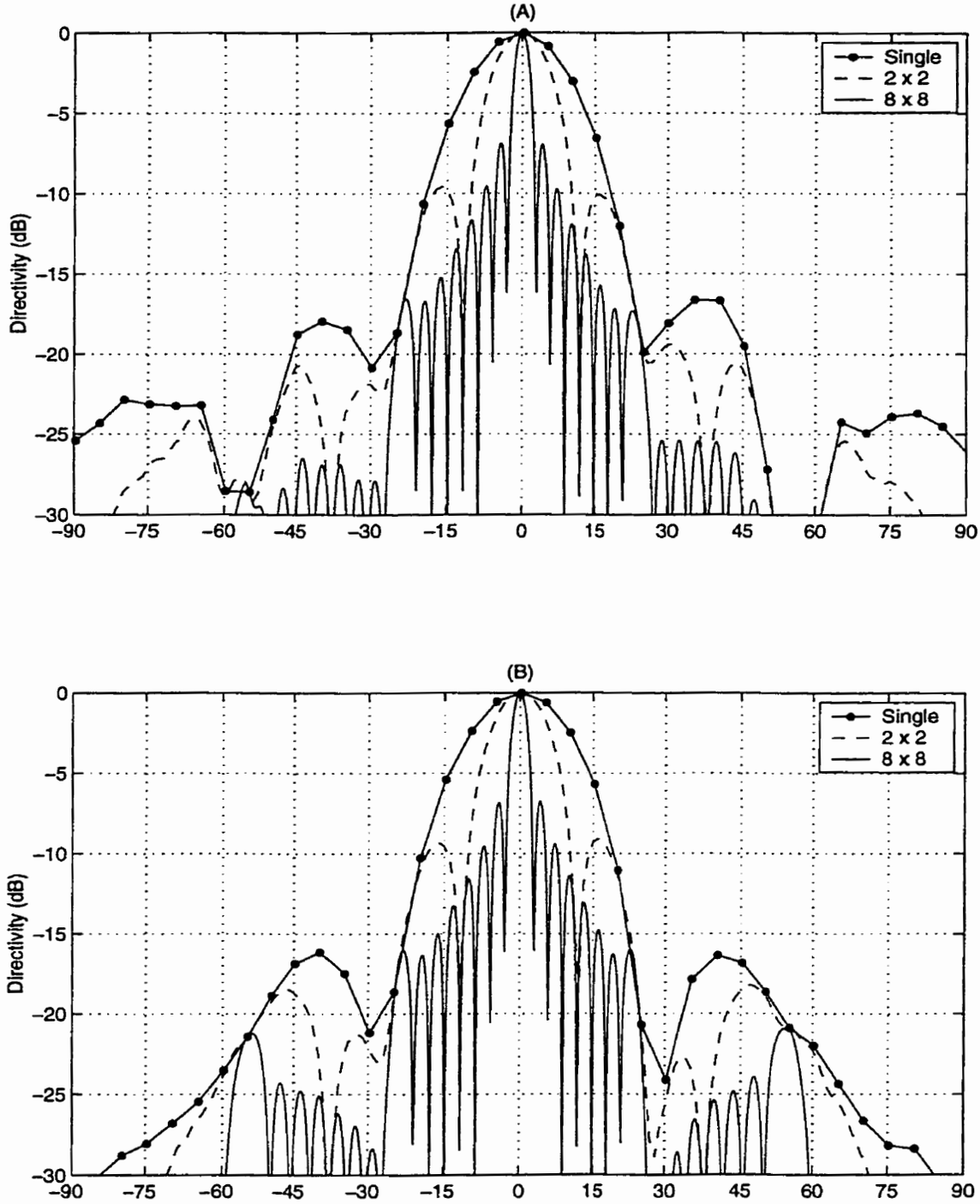

Figure 4.17: Predicted radiation patterns of 2x2 and 8x8 arrays of LN24 using array factor

(A) E-plane, (B) H-plane
"single" pattern experimentally measured, from Figure 4.7, f=15GHz
"2x2" & "8x8" products of "single" & array factors

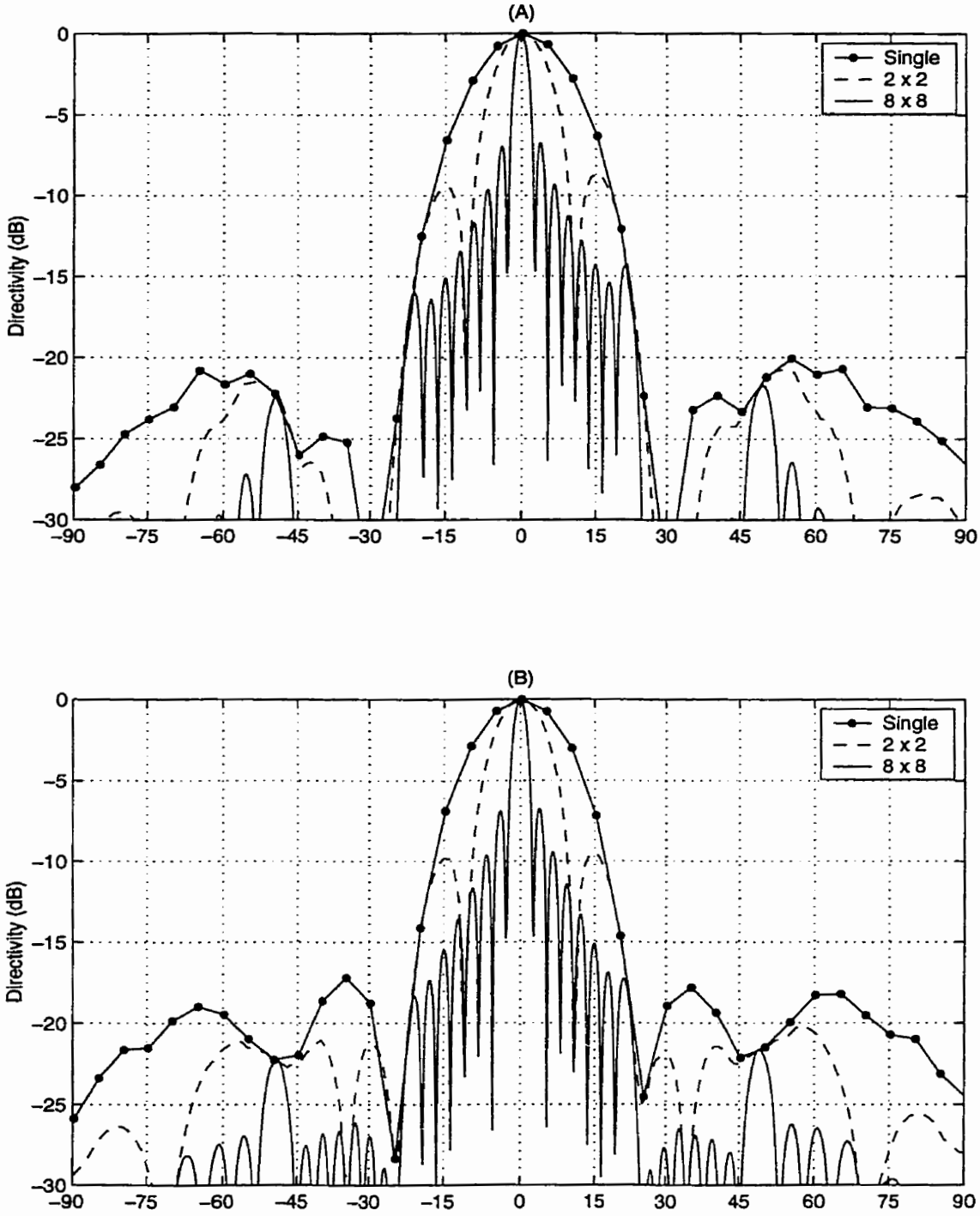

Figure 4.18: Predicted radiation patterns of 2x2 and 8x8 arrays of LN26 using array factor

(A) E-plane, (B) H-plane
"single" pattern experimentally measured, from Figure 4.8, f=15GHz
"2x2" & "8x8" products of "single" & array factors

4.7 A small array of SBAs

The LN26 SBA satisfied the requirements for a corporate WR-62 waveguide fed array element in terms of lateral size. It also gave the best far field radiation pattern null placement for suppression of the first order grating lobe, as seen in the previous section. It was used as an element in a 2x2 array, which was NC milled from two blocks of aluminium, Figure 4.19. The purpose of building this array was to confirm the accuracy of HFSS and the array factor method (used in the previous section) at predicting the radiation pattern shape, confirm that the input impedance of LN26 did not change in an array environment, and to measure the gain. The measured gain of the 2x2 array agreed well with that predicted by HFSS. However, the measured results were 2dB below that predicted by HFSS, due to losses in the feed network. Despite this feed network problem, which will be investigated as part of future work, there was excellent agreement between the 2x2 array experimental and HFSS radiation patterns. This inferred a high level of agreement for directivity.

The array element, LN26, had a cavity diameter of $2.6\lambda_o$ at 15GHz (53mm), Table 4.1. A cavity rim thickness of $\lambda_o/20$ (1mm) was used between adjacent elements in the 2x2 array, making the interelemnt spacing $2.65\lambda_o$ (53mm), Figure 4.19. This large inter-element spacing allowed the use of a full sized, corporate, WR-62 feed network, and such had to be used to illuminate the four array elements as only two WR-62 to coaxial transitions were available. The four array elements were milled into a 14mm thick block of aluminium (11mm for the cavity depth, 3mm for cavity floor thickness), with a 8mm border, Figure 4.19. The T-junction in the WR-62 network was a copy of that used by Yoshiki [14]. The intention here was to illuminate four LN26 SBAs equally in an array environment, not to design a waveguide feed network. A curved 90° H-plane bend and a stepped 90° E-plane bend connected the final T-junction to each LN26 SBA, Figure 4.19. As simulated in HFSS terminated in matched loads, the feed network gave input

impedances of the order of S_{11}=-20dB across 21% bandwidth, and should thus have had little effect upon the input impedance of the final array. The waveguide block had a thickness of 10.9mm (7.9mm for WR-62, 3mm for the waveguide channel floor thickness). In total, the 2x2 array had a thickness of about 25mm, or $1.25\lambda_o$ at 15GHz, making it a tenth to a twentith the thickness of a parabolic dish antenna.

The 2x2 array HFSS model used throughout this section fully represented all features of the experimental array described above, and was based upon the infinite ground model, Figure 3.3. The circumference of the LN26 cavities were discretised at 16 segments, as was done with the single element models in Chapter 3. The airbox for the 2x2 model was 112mm square, leaving 3.5mm between the edge of the cavities and the radiation boundary condition, as was done in the single element models in Chapter 3. The airbox had a height of 10mm ($\lambda_o/2$ at 15GHz). As the model included all features of the four LN26 SBAs and the feed network, it was both large and complex. A Pentium III personal computer with 512Mb of RAM running HFSS 7.0 computed one frequency step in approximately two hours, but crashed when the airbox was premeshed at 2mm, as had been done with the single element models. A convergence requirement of δS=0.02 was used, as had been used for the single SBA models of Chapter 3.

4.7.1 SBA array radiation pattern variation with frequency

The 2x2 LN26 array was tested in the compact range, anechoic chamber at the University of Manitoba, referenced to the EMC 08 standard gain horn with a 10dB attenuator calibrated in, for the frequency range of 13-16GHz.

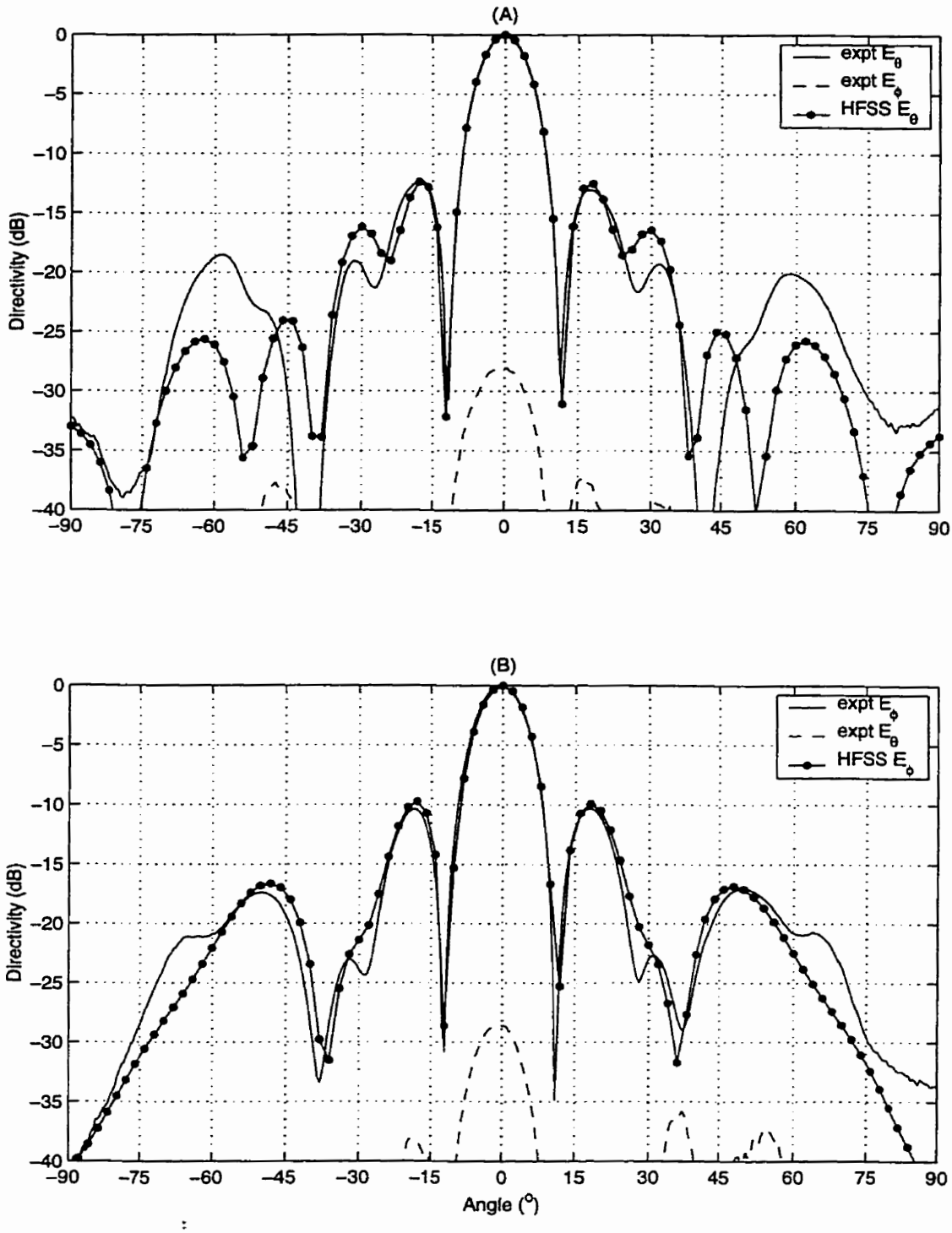

Figure 4.20: Measured and HFSS 2x2 array radiation patterns at 14GHz

"(A)" is E-plane, "(B)" is H-plane

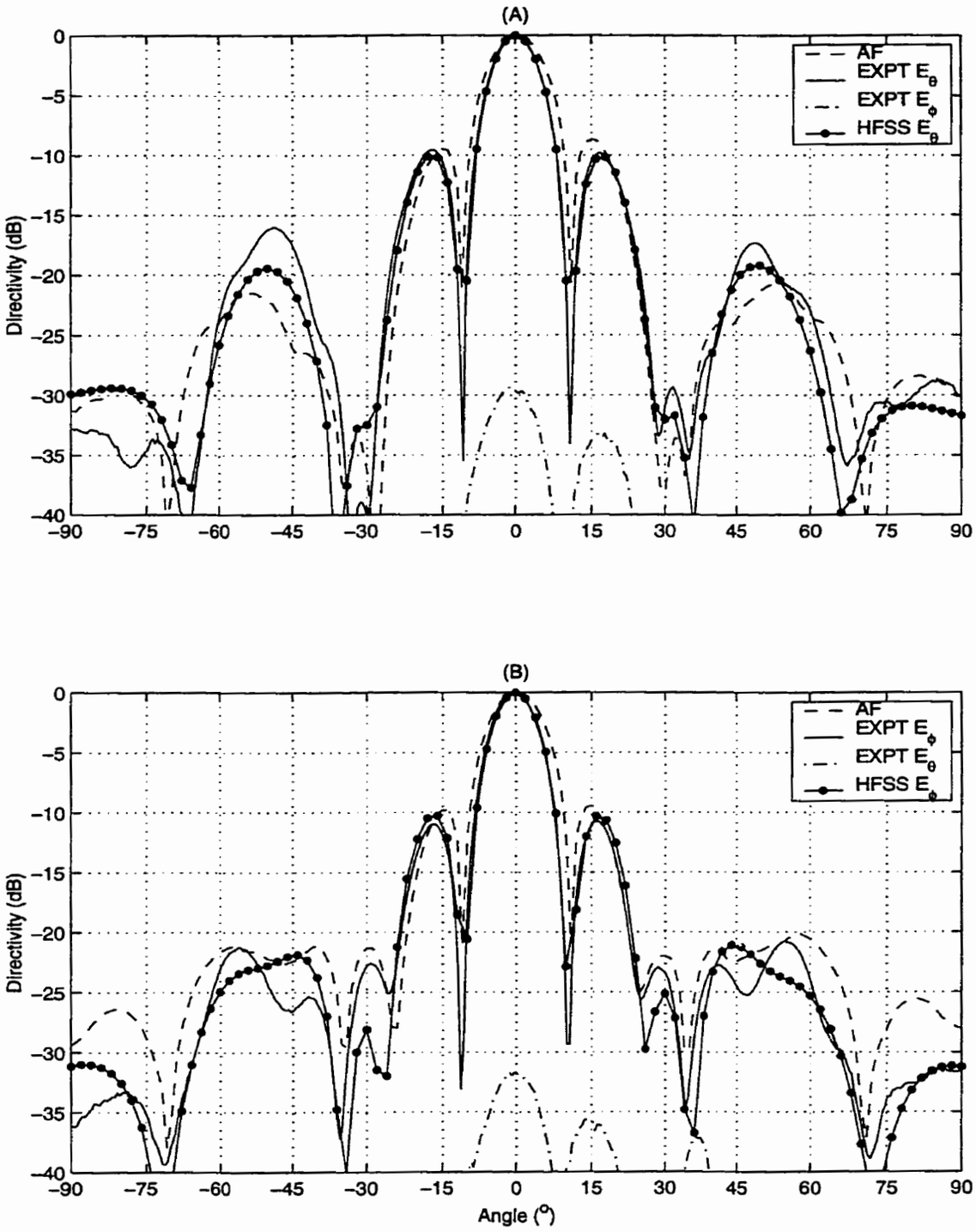

Figure 4.21: Measured and HFSS 2x2 array radiation patterns at 15GHz

"(A)" is E-plane, "(B)" is H-plane, "AF" is "2x2" traces from Figures 4.18A & 4.18B

The main lobe and first sidelobes predicted by HFSS in both principal planes compared very well with those measured at 14 and 15GHz, Figures 4.20 & 4.21. At both frequencies, the first sidelobes were −10dB below the main lobe peak at 17° off boresight in both planes. This sidelobe level was considered to be relatively high, and was the result of the relatively broad beamwidth of the single LN26. This was demonstrated in the previous section by multiplying the measured single LN26 radiation patterns at 15GHz by an appropriate array factor, to empirically predict the 2x2 array radiation patterns. The array factor predicted a broader −3dB main lobe beamwidth and higher first sidelobe level (and 2° closer to boresight) at 15GHz than was measured, Figure 4.21. Thus HFSS predicted the salient features of the 2x2 array radiation patterns more accurately than the array factor method. The disparity between experimental/HFSS and array factor radiation patterns was a result of the narrow cavity wall thickness accounted for in the latter method. This suggests that the beamwidth of a LN26 SBA in an array environment was narrower than as a single element. The accuracy of the array factor method would be improved if the radiation patterns of a LN26 SBA in an array simulator were used, instead of that of a single unit with a thick cavity wall as was done here. Interelement coupling was dismissed as a cause of beamwidth narrowing, as the coupling was below −30dB, Table 4.3. These results were in agreement with the previously reported mutual coupling between dipole excited SBAs (S_{21}≈−40dB [166]) and the observations made in the previous chapter that the power level near the SBA cavity edge was very low, at least −15dB below that at the cavity centre, Figure 3.22 and Table 3.3.

Table 4.3: Input impedance and mutual coupling of HFSS 2x2 array model

Frequency (GHz)	S_{11} (dB)	E-plane S_{21} (dB)	H-plane S_{21} (dB)
14	-10.816	-30.124	-50.028
14.5	-7.040	-34.911	-49.518
15	-4.693	-38.856	-48.182

Considering the wider angles of the 2x2 array radiation patterns, the first order grating lobe (expected at 22°, Table 4.2) was partially mitigated at 15GHz in both planes by the nulls about 30° in the single LN26 radiation patterns, Figure 4.21. At 14GHz, the first order grating lobes were expected at 24° (the interelement spacing was $2.47\lambda_o$) and were also partially mitigated in the H-plane, and suppressed to –20dB in the E-plane, Figure 4.20. Thus, the null in the single LN26 radiation pattern partially suppressed the first grating lobe across a reasonable bandwidth (14-15GHz), as desired.

The second order grating lobe was expected at 49° for 15GHz and at 54° for 14GHz. These were obvious in the measured E-plane and 14GHz H-plane radiation patterns, and had levels between –16dB to –18dB, Figures 4.20 & 4.21. Interestingly, HFSS accurately predicted the H-plane second order grating lobes, but was off in the E-plane in terms of shape and level.

The cross-polar radiation level was about –28dB in the main lobe for both planes at 14GHz, and about –30dB at 15GHz, Figures 4.20 & 4.21. This was satisfactory, and comparable to the main lobe cross-polar levels measured from microstrip arrays, Chapter 2. The wider angle cross-polar radiation levels of the 2x2 array were considerably lower than –28dB, showing a distinct advantage in this criterion over the NRE patch arrays investigated in Chapter 2.

In summary, the measured radiation patterns of the 2x2 array of LN26 SBAs were satisfactory as the first order grating lobes (caused by having such large diameter array elements) were partially mitigated across 14-15GHz, as desired. However, the first sidelobe level was high at –10dB in both planes at 15GHz and the H-plane at 14GHz. The radiation pattern shapes from the HFSS model were in excellent agreement with the measured. Differences between beamwidth and first sidelobe level and positioning of experimental and array factor method predicted radiation

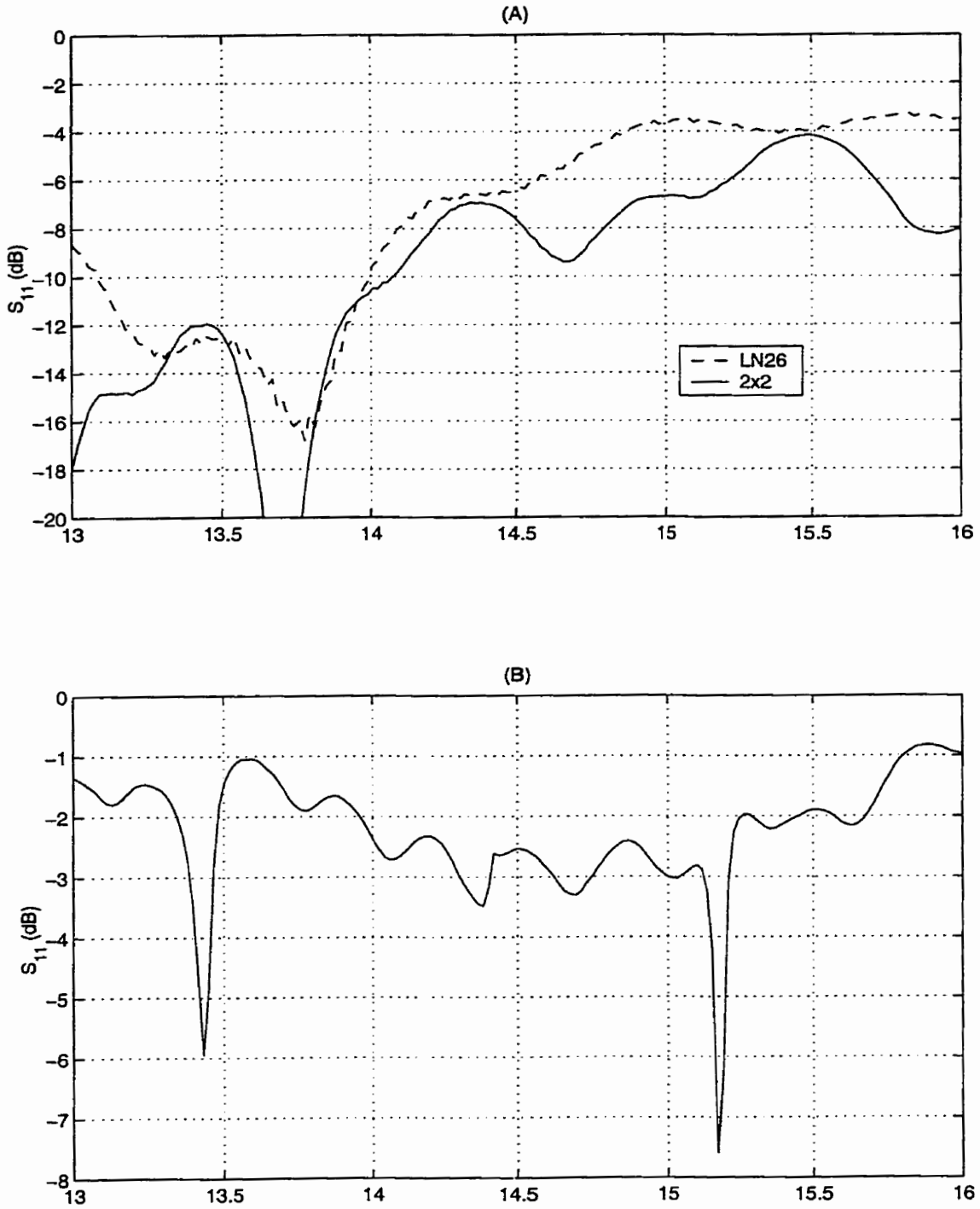

Figure 4.22: Input impedance characteristics of 2x2 array and single LN26

(A) input impedance, (B) input impedance of 2x2 array with short circuited ports

patterns suggested that there was some modification of the elemental LN26 radiation pattern in an array environment. Mutual coupling was discounted as the cause.

4.7.2 *Input impedance variation with frequency*

In this subsection, the input impedance characteristics of the 2x2 array of LN26 SBAs were compared. The input impedance of the 2x2 array very closely resembled that of the single LN26 SBA, showing that the WR-62 waveguide feed network did not greatly alter the input impedance. However, the input impedance of the WR-62 feed network with the inset feeds of the array elements terminated in short circuits was not 0dB and had many resonances. This accounts for the losses seen in the gain response of the 2x2 array.

The agreement between the experimental and HFSS input impedance characteristics for 2x2 array and single LN26 were reasonable, Figure 4.22. The input impedance of the 2x2 array was measured through a 154mm long WR-62 extension, that had to be used during radiation pattern measurements in the anechoic chamber to get the WR-62 to coaxial transition clear of the rotator head. The roughly $8\lambda_g$ extension introduced a ripple into the input impedance, Figure 4.22. Despite the ripple, there was a high degree of agreement between the array and single LN26 input impedance over 13.5-14.5GHz. Thus, the WR-62 feed network did not influence the input impedance over that range. Above and below that range, the input impedance matching of the array was better than that of the single LN26. It was not possible to clearly demarcate the influence of mutual coupling from feednetwork effects. However, HFSS predicted mutual coupling between neighbouring array elements of lower than –30dB across the bandwidth studied, so the majority of effects were from the feednetwork, Table 4.3.

The 4 output ports (inset feeds of the array elements) of the WR-62 corporate feed network were terminated in short circuits to test for any internal resonances and/or losses. Conductive glue backed copper foil was placed over the inset feeds. The resultant input impedance characteristic of the 2x2 array showed two distinct, but extremely narrow band, resonances, Figure 4.22. Due to their narrow band nature, thse were not significant. Off greater concern is the general level of the input impedance; $S_{11} \approx -2$dB where $S_{11} = 0$dB was expected, Figure 4.22. These results were confirmed by shorting the ports with firmly clamped, small aluminium sheets, and obtaining a near identical trace. When the inset feed of the single LN26 (which was fed through a straight section of WR-62) was shorted with one of the aluminium sheets, a $S_{11} = 0$dB was obtained. Thus, the result from the 2x2 array feed network with short circuited terminations was a result of the losses within the feednetwork. As the level was $S_{11} \approx -2$dB, a loss of 1dB was indicated. This feednetwork would cause the experimental scaled directivity to be offset 1dB below the scaled directivity predicted by HFSS. The source of the loss should be investigated as part of future work.

Thus, a high level of agreement between the array and single element input characteristics. A 1dB loss in the feednetwork was indicated by the input impedance characteristic of the 2x2 array when terminated in short circuits.

4.7.3 Scaled directivity and aperture efficiency variation with frequency

The radiation pattern integration routine developed in section 4.3 was used to calculate the directivity of the 2x2 array. The calculated scaled directivity closely matched the experimental results between 13 and 14GHz, Figure 4.23A. Above 14GHz, the experimental results were

affected by the high losses within the feed network due to the input impedance mismatch of each LN26 array element.

Comparing the calculated scaled directivity characteristics of the 2x2 and single LN26 across 21% bandwidth, the shapes were similar, Figure 4.4B, 4.12A & 4.23A. The difference in scaled directivity level was 4dB at 15GHz. A difference of 6dB was expected, because the aperture size was doubled twice in moving from a single LN26 to the 2x2 array. The loss of 2dB in directivity was due to losses in directivity caused by the high E-plane first sidelobe level and grating lobes. The 2x2 and single LN26 calculated directivity difference decreased to 2.5dB by 16GHz, Figure 4.23A. This further showed the influence of the high first sidelobe and increasing grating lobe levels. These in turn were the result of the frequency invariance of the E-plane –3dB beamwidth of the single LN26, subsection 4.4.2.

As the experimental and HFSS principal plane radiation patterns agreed well, there was also good agreement between the experimental and HFSS directivity for the 2x2 array, Figures 4.20 & 4.21. Thus, the unaccounted for feednetwork losses caused the low scaled directivity and aperture efficiency levels from the 2x2 array.

The aperture efficiency calculated from the scaled directivity of the 2x2 array as predicted by HFSS was about 70% from 14.5-15.4GHz, Figure 4.23B. Across the full bandwidth of interest, 14-15.5GHz (scalable by two to LMCS band: 28-31GHz), the aperture efficiency was 60% or better. Although the aperture efficiency was roughly 10% lower than that of a typical 4x4 microstrip array, the SBA array aperture efficiency would be maintained irrespective of array size due to the avoidance of high feed network losses (from which large microstrip arrays suffer greatly), Chapter 2. Similarly to the gain characteristics, the aperture efficiency characteristics of the array and single LN26 were different, Figure 4.23B. As with the scaled directivity (from

which the aperture efficiency was derived), this was due to the directivity loss to the high E-plane first sidelobe, which in turn was caused by the frequency invariance of the E-plane –3dB beamwidth of the single LN26, subsection 4.4.2.

The single LN26 and 2x2 array showed different scaled directivity and aperture efficiency behaviour with frequency. This was found to be the result of the high E-plane first sidelobe level, caused by the frequency invariance of the –3dB beamwidth of the single LN26. There was reasonable agreement between the experimental and HFSS scaled directivity and aperture efficiency for a single LN26 SBA, but this was not the case for the 2x2 array due to feednetwork losses. The aperture efficiency from HFSS was at least 60% across the bandwidth of interest, for LMCS.

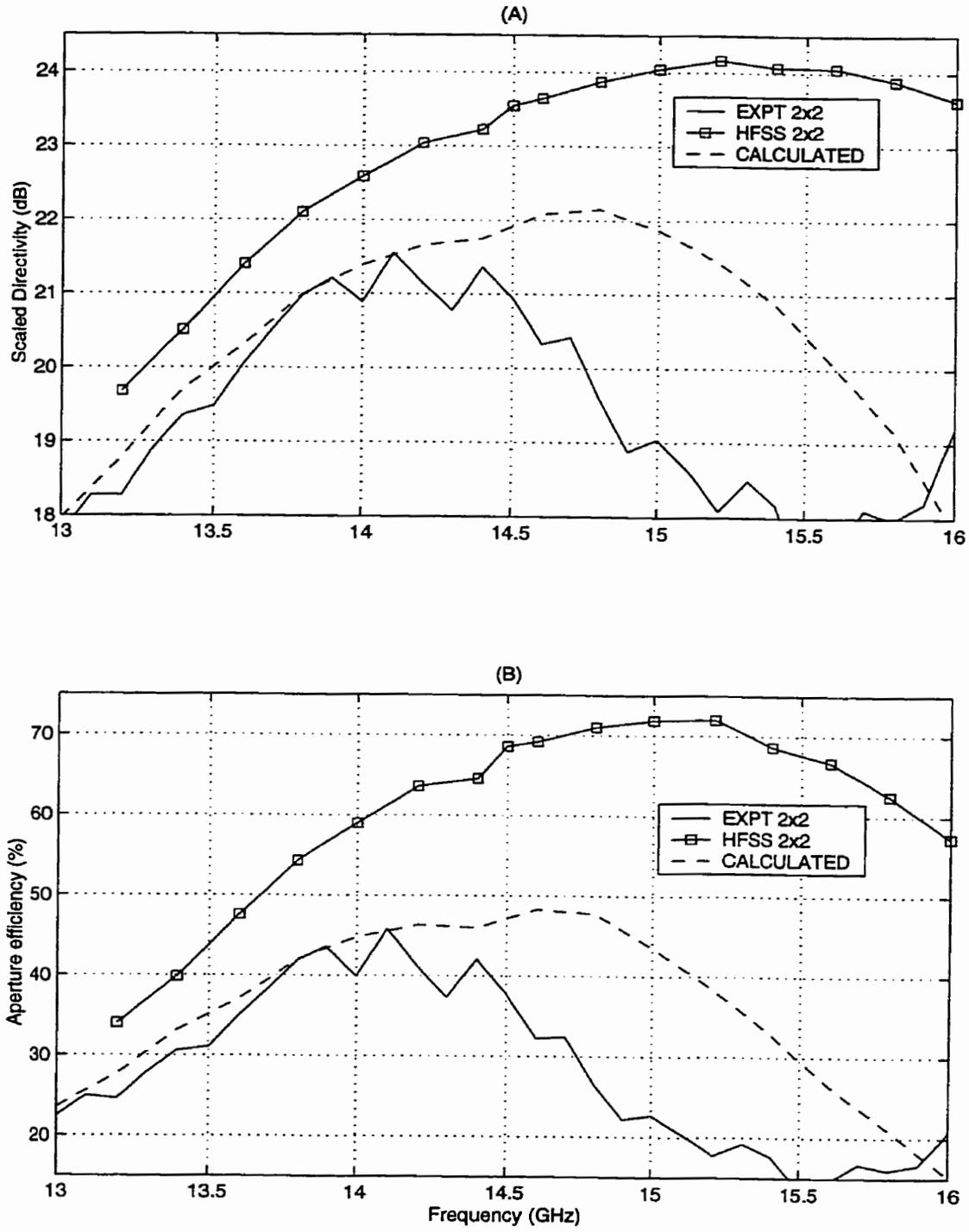

Figure 4.23: Experimental and HFSS scaled directivity and aperture efficiency of 2x2 array and single LN26

(A) scaled directivity, (B) aperture efficiency
a radiation efficiency of 90% was assumed for the calculated directivity
unit cell used for aperture efficiency calculation

4.8 Conclusions

Four short backfire antennas (SBAs) were selected from the 205 or so designs from the numerical study of SBAs for experimental investigation. This was done to learn more about the SBAs as single antennas, validate the results of the numerical study of Chapter 3, and to assess the four SBAs as array elements. The best of the four SBAs achieved an aperture efficiency of about 70%, as a square array element unit cell. This SBA was based upon the optimal design from the numerical study of Chapter 3. It had a diameter of $2.6\lambda_o$ and a curved juncture between the cavity floor and rim. This was the minimum sized array element that allowed use of a full sized, and thus lowest possible loss, WR-62 rectangular waveguide of type D, Figure 1.1. The optimised $2.6\lambda_o$ diameter SBA was used as an element in a 2x2, waveguide fed array.

Single SBAs and array were built up from cavities cut in solid blocks of brass or aluminium. This avoided any problems of current discontinuities on the cavity walls, from air gaps between sections, which may have affected the results of some prior investigators. Likewise, paper plugs and thin plastic film were used to position the subreflectors in the cavity mouths. This method of construction proved satisfactory, and avoided the use of heavy plastic mounting brackets, as used by some prior investigators, which may have affected their results.

The experimental investigation of the four SBAs revealed several features of these medium gain antennas not previously reported in the open literature. Most importantly, when using a single $0.5\lambda_o$ diameter subreflector, the frequencies at which a SBA produced the highest directivity was above that at which the antenna's input impedance was well matched. This was speculated during the numerical study of Chapter 3, and dictates the use of matching circuits if the highest possible gain is to be obtained from a SBA, or array of SBAs. Also, the lowest peak sidelobe levels and widest E-plane mainlobe beamwidths were found to coincide with the peak directivity of

each SBA. The wide beamwidths prevented complete cancellation of the grating lobes when the SBAs were tested as array elements using appropriate array factors. This was caused by the first nulls of the SBA radiation patterns not being coincident with the first order grating lobes in the array factor. However, the nulls were generally close enough to partially suppress the predicted grating lobes. The $2.6\lambda_o$ diameter, curved juncture SBA was the best of the four tested, in this respect. However, the wide elemental beamwidth of the $2.6\lambda_o$ diameter curved juncture SBA caused high first sidelobes (about -10dB) in the 2x2 array. This would be a disadvantage comparing to parabolic reflector antennas. The frequency invariance of the E-plane beamwidth was linked to the directivity roll-off of the 2x2 array.

Good agreement between the characteristics of the four SBAs and the matching results from the numerical study was found. This validated the numerical study. A numerical integration method to derive the directivity from the measured radiation patterns was developed, similar to that used by Rayner [174]. The method used here was based upon the $cos\phi/sin\phi$ dependance of the E_θ/E_ϕ components of the far field radiation pattern mainlobe of the $2.6\lambda_o$ diameter, curved juncture SBA. Such observations of the E_θ/E_ϕ azimuthal dependence had not been made before. The numerically derived directivity characteristics of the four SBAs were each unique and showed that the highest directivity of each occurred above the band of frequencies where each had well matched input impedance.

Excellent agreement was found between the measured radiation patterns of the 2x2 array of SBAs and those predicted by HFSS. The first order grating lobes were partially mitigated by the purposely placed null in the array element radiation pattern. As the measured gain of the 2x2 array suffered due to the losses in the feed network where the single LN26 SBA did not, the HFSS results were compared. The increase in scaled directivity from array element to 2x2 array was 6dB

as expected. A peak aperture efficiency of 70% was achieved by the 2x2 array. Across the 14-15.5GHz bandwidth of interest (half that of the LMCS band), the aperture efficiency predicted by HFSS was above 60%. Mutual coupling between LN26 array elements was higher than the –40dB previously reported [166] in the E-plane because the power distribution in the E-plane of the curved juncture array element was more uniform than the previously used flat based SBAs.

Future work will entail the development of a wideband input impedance matching network for the 2x2 array, and identification of the sources of the resonances and losses seen in the present corporate feed network. Also, cavity shaping only in the E-plane should be trialed in single SBAs, as the H-plane patterns were not improved by the types of circularly symmetric cavity shaping trialed to date.

CHAPTER 5: Conclusions and future work

5.1 Conclusions

Four potential technologies for low profile, medium gain, linearly polarised LMCS/LMDS/MMDS subscriber equipment antenna were identified. The two technologies most amenable to mass production, microstrip and SBA, were investigated.

NRE patch arrays were investigated as candidates for waveguide fed subarrays, to be used in a similar fashion to the RE patch subarrays considered by a prior investigator [15]. The study followed a design process starting with a NRE patch design through to a large array, and found a high degree of continuity with null placement. The process of large array design could possibly be automated at some time in the future. The importance of careful NRE patch design and 1x2 subarray design to the behaviour of large arrays was demonstrated.

The design reduced cross-polarised component to a limiting value with NRE patch design. The limiting value was higher for thick substrate used here (-17dB) compared to that for thin substrates used by prior investigators (-22dB) [72]. The cross-polarised component was further reduced in the principal planes by opposed but in-phase feeding in 1x2 subarrays and 180° electrical and physical feeding between 1x2 subarrays in the 2x2 subarrays. These methods were successful in reducing cross-polarised component but produced 2^n grating lobes, which caused directivity loss in the larger arrays. Null placement in 2x2 subarray patterns was used with varying degrees of success to mitigate 2^n grating lobes.

The experimental results of 4x4 NRE subarrays (the size used for rectangular waveguide fed subarray by Wiess [15]) comparable to, or better, than previously reported for single RE patch arrays. The best design employed 180° delay line and achieved 75% aperture efficiency. The highest aperture efficiency in 16x16 arrays was 40%, due to high feed network ohmic losses.

Effects of phase error on the 180° delay line in the 180° fed 2x2 subarrays were noted, as was the patch to line coupling in the in-phase fed 2x2 subarrays. In the former case, phase error caused the rapid directivity loss seen at higher frequencies, as the 2x2 E-plane nulls were scanned and thus no longer mitigated the 2^n grating lobes.

SBAs were investigated using the commercial FEM numerical tool HFSS 6.0. The aim was to build up a resource of parametric design information which does not presently exist in the published literature. An additional aim was to gain some insight into the physical mechanisms underlying the behaviour of this type of antenna. The work of prior investigators suggested that the directivity of SBAs could be increased by either cavity shaping or modification of the juncture of the cavity floor and rim. Thus the parametric study focused upon this, with some 205 trials having been conducted. Cavity circumference shape, diameter, profile and depth have been studied.

The study of SBA cavity circumference shape determined that there was little difference between square and circular shapes for a diameter of $2.0\lambda_o$. This finding is in agreement with the literature that reports an inter-changability of shape [26, 27, 156, 167]. However, for a diameter of $2.7\lambda_o$, the circular circumference had 28% higher aperture efficiency than the square circumference. Thus cavity circumference shape is more critical for larger diameter SBAs.

It was found that SBA cavity shaping was a good method for increasing aperture efficiency. The aperture efficiency of the commonly used cylindrical cavity SBA was bettered by at least 10% using any of the choked, high dielectric constant radome, 15° inclined base or curved juncture profiles. The highest aperture efficiency of 61.5% was obtained with an inset fed, $2.6\lambda_o$ diameter curved juncture profile. The addition of a curved juncture to a cylindrical cavity SBA was shown to significantly modify the far field radiation patterns and near field aperture distributions, compared to the normal flat based cavity. This particular design was found to have a reasonably high aperture efficiency as the far field radiation pattern nulls were close to the expected array grating lobe directions suitable for mitigation. The cavity edge was considered easier to die cast because the curved juncture was in place of a shape corner. Thus, it was investigated experimentally for use as an array element in the following chapter, with some modification to the feed inset depth which further increased the aperture efficiency to about 70%.

The aperture efficiency of the larger diameter ($\approx 2.6\lambda_o$) curved juncture SBAs was found to be sensitive to the inset depth of the exciting waveguide mouth into the cavity. In contrast, a similar diameter flat based cylindrical cavity SBA was relatively unaffected by inset depth. These findings showed the importance of exciter phase centre to the curved juncture SBA. The optimal inset depth increased the aperture efficiency of the curved juncture SBA by roughly a further 10%. The radius of the curved juncture was also found to affect the achievable directivity, although not as radically as feed inset depth. With a combination of both feed inset depth and juncture radius, it should be possible to realise a SBA with at least 70% aperture. Such an SBA would thus be comparable to a similar sized microstrip array in terms of aperture efficiency, and have the added advantage of being more readily connected to a low loss rectangular waveguide feed network. This optimised SBA design, along with several other designs, were investigated experimentally with a view to application as array elements in the next chapter.

Four short backfire antennas (SBAs) were selected from the 205 or so designs from the numerical study of SBAs for experimental investigation. This was done to learn more about the SBAs as single antennas, validate the results of the numerical study, and to assess the four SBAs as array elements. The best of the four SBAs achieved an aperture efficiency of about 70%, as a square array element unit cell. This SBA was based upon the optimal design from the numerical study of Chapter 3. It had a diameter of $2.6\lambda_o$ and a curved juncture between the cavity floor and rim. This was the minimum sized array element that allowed use of a full sized, and thus lowest possible loss, WR-62 rectangular waveguide of type D, Figure 1.1. The optimised $2.6\lambda_o$ diameter SBA was used as an element in a 2x2, waveguide fed array.

The experimental investigation of the four SBAs revealed several features of these medium gain antennas not previously reported in the open literature. Most importantly, when using a single $0.5\lambda_o$ diameter subreflector, the frequencies at which a SBA produced the highest directivity was above that at which the antenna's input impedance was well matched. This was speculated during the numerical study, and dictates the use of matching circuits if the highest possible gain is to be obtained from a SBA, or array of SBAs. Also, the lowest peak sidelobe levels and widest E-plane mainlobe beamwidths were found to coincide with the peak directivity of each SBA. The wide beamwidths prevented complete cancellation of the grating lobes when the SBAs were tested as array elements using appropriate array factors. This was caused by the first nulls of the SBA radiation patterns not being coincident with the first order grating lobes in the array factor. However, the nulls were generally close enough to partially suppress the predicted grating lobes. The $2.6\lambda_o$ diameter, curved juncture SBA was the best of the four tested, in this respect. However, the wide elemental beamwidth of the $2.6\lambda_o$ diameter curved juncture SBA caused high first sidelobes (about -10dB) in the 2x2 array. This would be a disadvantage comparing to

parabolic reflector antennas. The frequency invariance of the E-plane beamwidth was linked to the directivity roll-off of the 2x2 array.

Good agreement between the characteristics of the four SBAs and the matching results from the numerical study was found. This validated the numerical study. A numerical integration method to derive the directivity from the measured radiation patterns was developed, similar to that used by Rayner [174]. The method used here was based upon the $cos\phi/sin\phi$ dependance of the E_θ/E_ϕ components of the far field radiation pattern mainlobe of the $2.6\lambda_o$ diameter, curved juncture SBA. Such observations of the E_θ/E_ϕ azimuthal dependence had not been made before. The numerically derived directivity characteristics of the four SBAs were each unique and showed that the highest directivity of each occurred above the band of frequencies where each had well matched input impedance.

Excellent agreement was found between the measured radiation patterns of the 2x2 array of SBAs and those predicted by HFSS. The first order grating lobes were partially mitigated by the purposely placed null in the array element radiation pattern. As the measured gain of the 2x2 array suffered due to the losses in the feed network where the single LN26 SBA did not, the HFSS results were compared. The increase in scaled directivity from array element to 2x2 array was 6dB as expected. A peak aperture efficiency of 70% was achieved by the 2x2 array. Across the 14-15.5GHz bandwidth of interest (half that of the LMCS band), the aperture efficiency predicted by HFSS was above 60%. Mutual coupling between LN26 array elements was higher than the –40dB previously reported [166] in the E-plane because the power distribution in the E-plane of the curved juncture array element was more uniform than the previously used flat based SBAs.

Thus, it was found that the aperture distribution of a SBA meeting the minimum dimensions for a waveguide fed array element could be controlled. It follows that, as a waveguide fed array element, the optimised 2.6l_o diameter curved juncture SBA was comparable to the 4x4 microstrip patch arrays (whether RE [15] or NRE, as investigated here). A distinct manufacturing advantage of SBA over the microstrip arrays is that it has a direct feed to the waveguide feed network. A large scale array of SBAs, although not built here due to monetary constraints, does not require the placement of a yield lowering probe transition as the microstrip arrays do. Furthermore, SBA array manufacture does not require photolithographic etching nor the handling of flexible microstrip substrates. A large array of SBAs is thus a more viable candidate for the replacement of the present day EHF parabolic dish antennas.

5.2 Future work

5.1.1 Future work for NRE patch arrays

Slot excitation of 4x4 subarrays from waveguide, as more suitable for mass production as does not require pin which was source of failures (low yield) in a corporate waveguide feed network fed array [15].

5.1.2 Future work for short backfire antennas

A low loss feeding and matching network to feed SBA array should be developed.

Triangular grid of SBA arrays, as less vacant space between array elements, and thus higher aperture efficiency should be investigated. The vacant space will be reduced by 14%.

SBAs with cavity shaping only in E-plane should be investigated.

REFERENCES

[1] K. Miyauchi, "Millimetre-wave communications", Chapter 1 in *"Infrared and Millimetre Waves volume 9 Millimetre Components and Techniques Part I"*, K.J. Button, ed., Academic Press, 1983.

[2] S.Y. Seidel, "Radio propagation and planning at 28GHz for local multipoint distribution service (LMDS)", IEEE Antennas and Prop. Symposia, Atlanta, 1998, pp 622-625.

[3] G.M. Stamatelos & D.D. Falconer, "Millimetre radio access to multimedia services via LMDS", IEEE Globecom 1996, 1996, pp 1603-1607.

[4] R.J. Douville, "Antenna solutions for Ka band systems", Wireless 98, TRLabs, Calgary, Canada, July 1998, paper D-1, pp 171-180.

[5] M. Gagnaire, "An overview of broad-band access technologies", Proceedings of the IEEE, vol. 85, no. 12, Dec 1997, pp 1958-1972.

[6] D.A. Gray, "A broadband wireless access system at 28GHz", Proceedings of the 1997 Annual Wireless Communications Conference, Boulder, CA, Aug 11-13 1997, pp 1-7.

[7] O. Andrisano, V. Tralli & R. Verdone, "Millimetre waves for short-range multimedia communication systems", Proceedings of the IEEE, vol. 86, no. 7, July 1998, pp 1383-1401.

[8] M. Gimersky, L. Shafai, D.J. Roscoe & A. Ittipiboon, "Signal-distribution technologies for antenna arrays on millimetre waves: A report on the state of the art", Dept. of Elec. & Compt. Eng., University of Manitoba, Winnipeg, Manitoba, Canada, 1996.

[9] R.V. Lowman, "Transmission lines and waveguides", chapter 42 in *"Antenna Engineering Handbook"*, R.C. Johnson, 3rd edition, McGraw-Hill, 1993.

[10] T. Itoh & J. Rivera, "A comparative study of millimetre-wave transmission lines", Chapter 2 in *"Infrared and Millimetre Waves volume 9 Millimetre Components and Techniques Part I"*, K.J. Button, ed., Academic Press, 1983.

[11] Y. Chatani, M. Funada & M. Ohtsuka, "Planar array receiving antenna for satellite communications", Proceedings of ISAP'92, Sapporo, 1992, pp 1129-1132.

[12] E. Rammos & B.M. Bizery, "Four-horn radiating modules with integral power divider/supply network", U.S. patent 4,743,915, May 10 1988.

[13] E. Rammos & B.M. Byzery, "Unit modules for a high-frequency antenna and high-frequency antenna comprising such modules", U.S. patent 4,783,663, Nov 8 1988.

[14] K. Yoshiki, Y. Fujii & S. Egashira, "Design of waveguide parallel fed planar antenna comprised of sub-arrays with four apertures", Journal of Electromagnetic Waves and Applications, vol 11, 1997, pp 853-865.

[15] M.A. Weiss, "Microstrip antennas for millimetre waves", IEEE Trans. Antennas and Prop., vol ap-29, no 1, Jan 1981, pp 171-174.

[16] M. Haneishi, Y. Hakura, S. Saito & T. Hasegawa, "A low-profile antenna for DBS reception", IEEE Antennas and Prop. Symposia, 1987, pp 914-917.

[17] R.E. Munson & M.W. Schnetzer, "Annular slot antenna", U.S. patent 4,994,817, Feb 19 1991.

[18] M.W. Schnetzer & S.C. Olsen, "Dual polarised slotted antenna", U.S. patent 5,194,876, Mar 16 1993.

[19] T. Sehm, A. Lehto & A.V. Raisanen, "A large planar 39-GHz antenna array of waveguide-fed horns", IEEE Trans. Antennas and Prop., vol. 46, no. 8, Aug 1998, pp 1189-1193.

[20] T. Sehm, A. Lehto & A.V. Raisanen, "Planar 64 element millimetre wave antenna", Electronics Letters, vol. 35, no. 4, Feb 18 1999, pp 253-255.

[21] T. Sehm, A. Lehto & A.V. Raisanen, "A 64-element array antenna for 58GHz", IEEE Antennas and Propagation symposia, Orlando, July 1999, pp 2744-2747.

[22] E. Rammos & B.M. Bizery, "Four-horn radiating modules with integral power divider/supply network", U.S. patent 4,743,915, May 10 1988.

[23] E. Rammos & B.M. Byzery, "Unit modules for a high-frequency antenna and high-frequency antenna comprising such modules", U.S. patent 4,783,663, Nov 8 1988.

[24] J.L.F.C. Collins, "Planar horn array microwave antenna", U.S. patent 5,568,160, Oct 22 1996.

[25] T. Abiko, K. Tsukatmoto, H. Inoue & Y. Fujii, "Horn array antenna", Japanese patent H02-214,307A, Aug 27 1990.

[26] H. Koike, T. Abiko, Y. Fujii, H. Inoue & K. Tsukatmoto, "Waveguide array antenna", Japanese patent H02-223,206A, Sept 5 1990.

[27] H. Koike, T. Abiko, Y. Fujii, H. Inoue & K. Tsukatmoto, "Waveguide feeding array antenna", U.S. patent 5,243,357, Sept 7 1993.

[28] M. Ando, J. Hirokawa, T. Yamamoto, A. Akiyama, Y. Kimura & N. Goto, "Novel single-layer waveguides for high-efficiency millimetre-wave arrays", IEEE Trans. Antennas and Prop., vol. 46, no. 6, June 1998, pp 792-798.

[29] M. Ando & J. Hirokawa, "High-gain and high-efficiency single-layer slotted waveguide arrays in 60GHz band", 10th International Conference on Antennas and Prop., April 14 1997, pp 1.464-1.1.468.

[30] J.R. James & A. Henderson, "Planar millimetre-wave antenna arrays", Chapter 3 in Infrared and Millimetre Waves volume 14 Millimetre Components and Techniques Part V, K.J. Button, ed., Academic Press, 1985.

[31] C.R. Seashore, "Millimetre-wave integrated-circuit transducers", Chapter 1 in Infrared and Millimetre Waves volume 14 Millimetre Components and Techniques Part V, K.J. Button, ed., Academic Press, 1985.

[32] C.R. Seashore, J.E. Miley & B.A. Kearns, "mm-wave radar and radiometer sensors for guidance systems", Microwave Journal, Aug 1979, pp 47-58.

[33] M. Takahashi, J. Takada, M. Ando & N. Goto, "Characteristics of small-aperture, single-layered, slot antennas", IEE Proceedings Part H, vol. 139, no. 1, Feb 1992, pp 79-83.

[34] M. Ando, K. Sakurai & N. Goto, "Characteristics of a radial line slot antenna for 12GHz band satellite tv reception", IEEE Trans. Antennas and Prop., vol. 34, no. 10, June 1986, pp 1269-1272.

[35] J. Takada & N. Goto, "Planar antenna", Japanese patent H06-090,115A, Mar 29 1994.

[36] O. Shibata, S. Saito & M. Haneishi, "Radiation properties of microstrip array antennas fed by radial line", Electronics and Communications in Japan, part 1, vol 76, no 12, 1993.

[37] H. Miyashita & T. Katagi, "Radial line planar monopulse antenna", IEEE Trans. Antennas and Prop., vol. 44, no. 8, Aug 1996, pp 1158-1165.

[38] K. Nishikawa, T. Harada, T. Watanabe & M. Ogawa, "Planar antenna", Japanese patent H10-322,107A, Sep 5 1998.

[39] K. Sakakibara, J. Hirokawa, M. Ando & N. Goto, "High-gain and high-efficiency single-layer slotted waveguide array for use in 22GHz band", Electronics Letters, vol. 32, no. 4, Feb 15 1996, pp 283-284.

[40] Y. Kimura, A. Akiyama, K. Sakurai, J. Hirokawa, M. Ando & N. Goto, "Alternating-phase fed single-layer slotted waveguide arrays without electrical contact between the slot plate and the narrow walls", IEICE Autum Conference 1997, paper B-1-136, p 136.

[41] J. Hirokawa & M. Ando, "Model antenna of 76GHz post-wall waveguide-fed parallel plate slot array", IEICE Autum Conference 1999, paper B-1-99, p 99.

[42] N. Goto, "Slotted waveguide antenna", U.S. patent 4,916,458, Apr 10 1990.

[43] M. Uematsu, T. Ojima, N. Takahashi, N. Goto, J. Hirokawa & M. Ando, "Slotted leaky waveguide array antenna", U.S. patent 5,579,019, Nov 26 1996.

[44] K. Arimura, A. Tsukada, F. Takenaga & H. Kasaga, "Flat slot array antenna for te mode wave", U.S. patent 5,177,496, Jan 5 1993.

[45] M. Sato & Y. Konishi, "Antenna device", Japanese patent H10-327,014A, Dec 8 1998.

[46] K.C. Kelly, "Tab coupled slots for waveguide fed slot array antennas", U.S. patent 5,289,200, Feb 22 1994.

[47] Y. Wagatsuma & T. Yoneyama, "Performance improvement of broadside traveling wave antenna", IEICE Autum Conference 1997, paper B-1-130, p 130.

[48] K.C. Kelly, "Dual polarisation flat plate antenna", U.S. patent 4,716,415, Dec 6 1984.

[49] B. Rembold & K. Solbach, "Microwave directional antenna employing surface wave mode", U.S. patent 4,536,767, Aug 20 1985.

[50] J.P. Ladds, "Centre-fed leaky wave antenna", U.S. patent 5,231,414, Jul 27 1993.

[51] A. Yamamoto, T. Teshirogi & T. Hidai, "A feeding method for image-guide leaky-wave antenna arrays", IEICE Spring Conference 1999, paper B-1-95, p 95.

[52] J.F. Huang, K. Wu, F. Kuroki and T. Yoneyama, "Computer-aided design and optimisation of NRD-guide mode suppressors", IEEE Trans. Microwave Theory and Tech., vol. 44, no. 6, June 1996, pp 905-910.

[53] A. Takahashi, A. Kaise, T. Yoneyama and Y. Wagatsuma, "Electromagnetic radiator using a leaky NRD waveguide", U.S. patent 5,416,492, May 16 1995.

[54] J.P. Daniel, E. Penard & C. Terret, "Design and technology of low-cost printed antennas", chapter 11 in J.R. James and P.S. Hall (eds), Handbook of Microstrip Antennas, Peter Peregrinius, 1989.

[55] J. Ashkenazy, P. Perlmutter & D. Treves, "A modular approacch for the design of microstrip array antennas", IEEE Trans. Antennas and Prop., vol ap-31, no 1, Jan 1983, pp 190-193.

[56] R.E. Munson, "Microstrip Antennas", chapter 7 in "*Antenna Engineering Handbook*", R.C. Johnson and H. Jasik, eds., 3rd edition, McGraw-Hill, 1993.

[57] F. Lalezari & C.D. Massey, "mm-wave microstrip antennas", Microwave Journal, Apr 1987, pp 87-96.

[58] P.S. Hall & C.J. Prior, "Radiation control in corporately fed microstrip patch arrays", JINA'86, 1986, pp 271-275.

[59] P.S. Hall & C.M. Hall, "Coplanar corporate feed effects in microstrip patch array design", IEE Proceedings Pt. H, vol. 135, no. 3, June 1988, pp 180-186.

[60] E. Levine, G. Malamud, S. Shtrikman & D. Treves, "A study of microstrip array antennas with the feed network", IEEE Trans. Antennas and Prop., vol 37, no 4, Apr 1989, pp 426-433.

[61] L.R. Murphy, "SEASAT and SIR-A microstrip antennas", Proc. workshop on printed antenna technology, New Mexico State University, U.S.A., pp 18-1 to 18-20.

[62] N.I. Herscovici & D.M. Pozar, "Modular design of multilayer planar arrays", IEEE Antennas and Prop. Symposia, 1992, pp 309-312.

[63] M.H. Ho, K.A. Michalski & K. Chang, "Waveguide excited microstrip patch antenna - theory and experiment", IEEE Trans. Antennas and Prop., vol. 42, no. 8, Aug 1994, pp 1114-1125.

[64] B.N. Das, K.V.S.V.R. Prasad & K.V. Seshagiri Rao, "Excitation of Waveguide by stripline and microstrip-line-fed slots", IEEE Trans. on Microwave Theory and Techniques, vol. mtt-34, no. 3, March 1986, pp 321-327.

[65] K. Woelders & J. Granholm, "Cross-polarisation and sidelobe suppression in dual linear polarisation antenna arrays", IEEE Trans. Antennas and Prop., vol ap-45, no 12, Dec 1997, pp 1727-1740.

[66] J. Huang, "Low cross-pol linearly polarised microstrip array", IEEE Antennas and Prop. Symposia Digest, 1990, pp 1750-1753.

[67] Y.Y. Lu & L. Shafai, "Study of micromachined lines using FDTD", IEEE Antennas and Prop. Symposia, 1999, pp 1066-1069.

[68] R.E. Munson, "Microstrip Antenna Structures and Arrays", U.S. patent 3,921,177, Nov 18 1975.

[69] R.E. Munson, "Conformal microstrip antennas and microstrip phased arrays", IEEE Trans. Antennas and Prop., vol ap-22, no 1, Jan 1974, pp 74-78.

[70] M. Boguais, "Planar high-frequency aerial for circular polarisation", U.S. patent 5,233,361, Aug 3 1993.

[71] A. Saban, "Ka band microstrip antenna arrays with high efficiency", IEEE Antennas and Prop. Symposia, July 1999, pp 2740-2743.

[72] M.I. Oberhart & Y.T. Lo, "New simple feed network for an array module of four microstrip elements", Electronics Letters, vol. 23, no. 9, Apr 23 1987, pp 436-437.

[73] K.F. Lee, R. Acosta & R.Q. Lee, "Microstrip antenna array with parasitic elements", IEEE Antennas and Prop. Symposia, 1992, pp 794-797.

[74] H. Entschladen & U. Nagel, "Microstrip patch array antenna", Electronics Letters, vol. 20, no. 22, Oct 25 1984, pp 931-932.

[75] P.A. Miller & M.R. Staker, "A wide bandwidth high efficiency low crosspolar microstrip array antenna for communication applications", IEEE Antennas and Prop. Symposia, 1991, pp 596-599.

[76] J.F. Zurcher, J.R. Sanford, K. Wettstein & R.C. Hall, "Enhanced performance aperture-coupled planar antenna array", U.S. patent 5,355,143, Oct 11 1994.

[77] F. Carrez & J. Vindevoghel, "Study and design of compact wideband microstrip antennas", 10th International Conference on Antennas and Propagation, 1997, pp 1.423-1.426.

[78] H. Legay & L. Shafai, "Radiation characteristics of slotted oversize patch antennas", Electronics Letters, vol. 30, no. 8, Apr 14 1994, pp 749-751.

[79] T. Kawano & H. Nakano, "Numerical analysis of grid array antenna XII", IEICE Autumn Conference, 1997, paper B-1-87, p 87.

[80] D.A. Walcher, R.Q. Lee & K.F. Lee, "Microstrip patch antenna receiving array operating in the Ku band", IEEE Antennas and Prop. Symposia Digest, 1996, pp 1904-1907.

[81] R.Q. Lee, K.F. Lee & A.J. Zaman, "An experimental investigation of a 16 x 16 microstrip array with stacked parasitic elements", IEEE Antennas and Prop. Symposia Digest, 1990, pp 1766-1769.

[82] H. Legay & L. Shafai, "A self-matching wideband feed network for microstrip arrays", IEEE Trans. Antennas and Prop., vol ap-45, no 4, Apr 1997, pp 715-722.

[83] H. Legay & L. Shafai, "New stacked microstrip antenna with large bandwidth and high gain", IEE Proceedings Pt. H, vol. 141, no. 3, June 1994, pp 199-204.

[84] A.M. Jassim & H.D. Hristov, "Stepped cavity-fed microstrip array antenna", IEEE Antennas and Prop. Symposia Digest, 1993, pp 1228-1231.

[85] A.M. Jassim & H.D. Hristov, "Cavity feed technique for slot-coupled microstrip patch array antenna", IEE Proceedings Pt. H, vol. 142, no. 6, Dec 1995, pp 452-456.

[86] P.S. Hall, A. Henderson & J.R. James, "Extensions and variations to the microstrip antenna concept", chapter 23 in *"Handbook of Microstrip Antennas"*, J.R. James and P.S. Hall (eds), Peter Peregrinius, 1989.

[87] J.R. James, C.M. Hall & G. Anrasic, "Microstrip elements and arrays with spherical dielectric overlays", IEE Proceedings Pt. H, vol. 133, no. 6, Dec 1986, pp 474-482.

[88] G.W. Chantry, "The use of Fabry-Perot interferometers, etalons and resonators at infrared and longer wavelengths - an overview", J. Phys. E: Sci. Instrum., vol. 15, 1982, pp 3-8.

[89] R.N. Clarke & C.B. Rosenberg, "Fabry-Perot and open resonators at microwave and millimetre wave frequencies, 2-300GHz", J. Phys. E: Sci. Instrum., vol. 15, 1982, pp 9-24.

[90] E.A.M. Baker & B. Walker, "Fabry-Perot interferometers for use at submillimetre wavelengths", J. Phys. E: Sci. Instrum., vol. 15, 1982, pp 25-32.

[91] C.M. Kaloi, D. Hatfield & P. Simon, "Microstrip backfire antenna", IEEE Antennas and propagation symposia, 1981, pp 343-346.

[92] C.M. Kaloi, "Microstrip backfire antenna", U.S. patent 4,347,517, Aug 31 1982.

[93] G. Vandenbosch & A. Van de Capelle, "Analysis of the microstrip backfire antenna", Proc. of 5th Int. Conf. on Antennas and Propagation, ICAP 87, Mar 1987, pp 292-295.

[94] M. Ohta, K. Kaneko, H. Iyama, S. Kado, M. Hirao, H. Ishizaka, K. Ohmaru & T. Murata, "Stripline patch antenna with slot plate", U.S. patent 5,187,490, Feb 16 1993

[95] T. Matsui & M. Kiyokawa, "Gaussian-beam antenna", U.S. patent 5,581,267, Dec 3 1996.

[96] R. Sauleau, Ph. Coquet, J.P. Daniel, T. Matsui & N. Hirose, "Analysis of millimetre-wave Fabry-Perot cavities using the fdtd technique", IEEE Microwave and Guided Wave Letters, vol. 9, no. 5, May 1999, pp 189-191.

[97] K. Nakayama, "Study of curved and plane array antenna", PhD thesis, Hosei University, March 1999.

[98] A. Matsui, S. Kitao, M. Haneishi & S. Okamura, "A consideration on parallel plate mode suppression of triplate-type planar antenna", IEEE Antennas and Propagation Symposia, 1994, pp 1218-1221.

[99] M. Ohta, H. Ishizaka, R. Kose, T. Saito, N. Okubo & M. Haneishi, "Radiation properties of circularly polarised triplate-feed-type patch antennas at 60GHz band", IEICE Autum Conference, 1994, paper B-115, p 115.

[100] M. Haneishi, M. Ohta & H. Ishizaka, "Triplate plane array antenna", Japanese patent H06-002,790, 1994.

[101] H. Ohmine, T. Ishida, T. Suzuki & S. Makino, "A triplate-line feed slot-coupled microstrip antenna with a via-hole cavity", IEICE Autum Conference 1999, paper B-1-137, p 137.

[102] K. Fukuzawa, T. Otsuka, S. Tsurumaru, J. Kajikari & F. Ito, "Microwave antenna structure with integral radome and rear cover", U.S. patent 4,914,449, Apr 3, 1990.

[103] H. Nakano, M. Sugama, K. Nakayama & J. Yamauchi, "A circular aperture antenna backed by a cavity", IEICE Spring Conference, 1999, paper B-1-130, p 130.

[104] H. Nakano, T. Unno, K. Nakayama & J. Yamauchi, "FDTD analysis and measurement of aperture antennas based on the triplate transmission-line structure", IEEE Trans. Antennas and Prop., vol. 47, no. 6, June 1999, pp 986-992.

[105] K. Nakayama & H. Nakano, "Dual-polarised slot antennas with stacked and coplanar feed systems", IEEE Antennas and Propagation Symposia, 1995, pp 990-993.

[106] K. Nakayama & H. Nakano, "Dual polarised slot array antennas fed by triplate transmission lines", IEEE Antennas and Propagation Symposia, 1996, pp 1548-1551.

[107] K. Nakayama & H. Nakano, "A triplate-type aperture antenna backed by a cavity", Trans. IEICE B, vol. J82-B, no. 3, Mar 1999, pp 410-419.

[108] H. Nakano, M. Iwatsuki, K. Nakayama & J. Yamauchi, "An aperture antenna with an island for a CP wave", IEICE Spring Conference, 1999, paper B-1-80, p 80.

[109] C.G. Wildey & D.J. Iredale, "Planar microwave antenna slot array with common resonant back cavity", U.S. patent 5,119,107, June 2, 1992.

[110] E. Rammos, "A low tolerance dual slot radiator for space and ground applications", IEEE Antennas and Propagation Symposia, 1991, pp 1599-1602.

[111] E. Rammos, "Planar array antenna, comprising coplanar waveguide printed feed lines cooperating with apertures in a ground plane", U.S. patent 5,061,943, Oct 29, 1991.

[112] E. Rammos, "Planar microwave receiving and/or transmit array antenna and application thereof to reception from geostationary television satellites", U.S. patent 5,872,545, Feb 16, 1999.

[113] T. Dusseux, M. Gomez-Henry, M. Lairle & G. Raguenel, "Planar array antenna, comprising coplanar waveguide printed feed lines cooperating with apertures in a ground plane", U.S. patent 5,061,943, Oct 29, 1991.

[114] G. Dubost & C. Vinatier, "Large bandwidth and high gain array of flat folded dipoles acting at 12GHz", 3rd International Conference on Antennas and Propagation ICAP 83, 1983, pp 145-149.

[115] M. Ohta, H. Ishizaka, S. Wakushima & M. Haneishi, "A stripline feed type planar antenna for 12GHz satellite broadcasting reception", IEEE Antennas and Propagation Symposia, 1992, pp 143-146.

[116] H. Ishizaka, S. Wakushima, H. Mizugaki & M. Ohta, "Dual-polarisation planar antenna", U.S. patent 5,510,803, Apr 23, 1996.

[117] H. Ishizaka, M. Ohta, S. Wakushima & M. Haneishi, "Radiation properties of triplate feed type patch antennas with parasitic elements", IEICE Spring Conference, 1992, paper B-1-61, p 61.

[118] M. Ohta, H. Ishizaka & H. Mizugaki, "Plane antenna with high gain and antenna efficiency", U.S. patent 5,061,943, Oct 29, 1991.

[119] K. Tsukamoto, "Study of triplate plane antenna: systemisation of triplate array with periodic structure", PhD thesis, Yokohama National University, Nov 1996.

[120] T. Abiko, K. Tsukamoto, H. Inoue, Y. Fujii, M. Kanda & N. Miyachi, "Planar antenna with patch elements", U.S. patent 4,816,835, Mar 28, 1989.

[121] K. Tsukamoto, Y. Fujii, Y. Ogawa, S. Kondo, K. Masamoto, M. Niwa, M. Matsuo, Y. Kitsuda, H. Takeda, S. Miyanari, H. Yokota & S. Taniguchi, "Planar antenna", U.S. patent 4,829,309, May 9, 1989.

[122] K. Tsukamoto, K. Masamoto, Y. Fujii & Y. Kitsuda, "Planar antenna", U.S. patent 4,851,855, Jul 25, 1989.

[123] K. Tsukamoto, Y. Fujii & T. Abiko, "Planar antenna", U.S. patent 4,857,938, Aug 15, 1989.

[124] K. Tsukamoto & T. Abiko, "Planar antenna", U.S. patent 4,977,406, Dec 11, 1990.

[125] K. Tsukamoto, T. Abiko, H. Inoue & K. Okuno, "Planar antenna", U.S. patent 5,270,721, Dec 14, 1993.

[126] K. Tsukamoto & H. Arai, "Characteristic of linear polarised aperture array antenna", Trans. IEICE B-II, vol. J78-B-II, no. 3, March 1995, pp 160-166.

[127] K. Tsukamoto & H. Arai, "Dual-polarised flat antenna", IEEE Antennas and Propagation Symposia, 1995, pp 986-989.

[128] K. Tsukamoto, I. Ujiyama & K. Okuno, "Wide-band, dual polarised planar antenna", U.S. patent 5,453,751, Sep 26, 1995.

[129] K. Tsukamoto & H. Arai, "Characteristic of linearly polarised aperture array antenna", Electronics and Communications in Japan, part 1, vol 79, no. 2, 1996, pp 46-54

[130] K. Tsukamoto & H. Arai, "Input characteristic of tri-plate aperture array antenna", Trans. IEICE B-II, vol. J79-B-II, no. 1, Jan 1996, pp 26-32.

[131] K. Tsukamoto & T. Saito, "Planar antenna having polariser for converting linear polarised waves into circular polarised waves", U.S. patent 5,502,453, May 26, 1996.

[132] K. Tsukamoto & H. Arai, "Characteristics of dual polarised flat antenna", IEEE Antennas and Propagation Symposia, 1996, pp 1552-1555.

[133] K. Tsukamoto & H. Arai, "Characteristics of dual polarised flat antenna", Trans. IEICE B-II, vol. J79-B-II, no. 8, Aug 1996, pp 476-485.

[134] K. Tsukamoto & H. Arai, "Input characteristic of tri-plate aperture array antenna", Trans. IEICE B-II, vol. J79-B-II, no. 1, Apr 1997, pp 26-32.

[135] G. Dubost & R. Frin, "Plate antenna with double crossed polarisations", U.S. patent 4,922,263, May 1, 1990.

[136] A.J. Zaghloul & R.M. Sorbello, "High-gain single- and dual-polarised antennas employing gridded printed-circuit elements", U.S. patent 4,926,189, May 15, 1990.

[137] R.M. Sorbello, J.E. Effland & A.J. Zaghloul, "Dual-polarised printed circuit antenna having its elements capacitively coupled to feedlines", U.S. patent 4,929,959, May 29, 1990.

[138] E. Rammos, "New wideband high-gain stripline planar array for 12GHz satellite tv", Electronics Letters, vol. 18, no. 6, Mar 18 1982, pp 252-253.

[139] R. Simmons, "A millimetre-wave cavity backed suspended substrate stripline antenna", IEEE Antennas and Prop. Symposia, July 1999, pp 2110-2113.

[140] M. Clenet & L. Shafai, "Characteristics of conical horns loaded with internal metallic discs", ANTEM'98 proceedings, 1998, pp 345-348.

[141] G.N. Tsandoulas & W.D. Fitzgerald, "Aperture efficiency enhancement in dielectrically loaded horns", IEEE Trans. Antennas and Prop., Jan 1972, pp 69-74.

[142] A.C. Large, "Short backfire antennas with waveguide and linear fields", Microwave Journal, 1976, pp 49-52.

[143] H.D. Hristov & J.R. Urumov, "X-band backfire antenna arrays", 5th European Microwave Conference, Hamburg, Sept 1975, pp 112-115.

[144] H.W. Ehrenspeck, "The short-backfire antenna", Proceedings of the IEEE, Aug 1965, pp 1138-1140.

[145] H.W. Ehrenspeck & J.A. Strom, "High-frequency waveguide feed in with a short-backfire antenna", U.S. patent 3,774,223, Nov 1973.

[146] H. Koike, T. Abiko, Y. Fujii, H. Inoue & K. Tsukatmoto, "Waveguide array antenna", Japanese patent H02-223,206A, Sep 5 1990.

[147] H. Koike, T. Abiko, Y. Fujii, H. Inoue & K. Tsukatmoto, "Waveguide feeding array antenna", U.S. patent 5,243,357, Sep 7 1993.

[148] A.A. Kishk & L. Shafai, "Performance of short-backfire antenna with different excitation sources", Int. J. Electronics, vol. 63, no. 6, 1987, pp 825-832.

[149] P.S. Kooi, M.S. Leong & T.S. Yeo, "Dipole-excited short backfire antenna with corrugated rim", Electronics Letters, vol. 15, no. 14, July 5 1979, pp 421-423.

[150] P.S. Kooi & M.S. Leong, "Rectangular-waveguide-excited short backfire antenna with corrugated rim", Electronics Letters, vol. 15, no. 17, Aug 16 1979, pp 533-535.

[151] P.S. Kooi & M.S. Leong, "Q-band short backfire antenna arrays", Proceedings of the 10th European Microwave Conference, Poland, Sept 1980, pp 162-166.

[152] P.S. Kooi & M.S. Leong, "Q-band dielectric-loaded short backfire antenna arrays", 2nd Int. Conf. on Antennas and Propagation, IEE Conf. Pub. no. 195, IEE, London, April 1981, pp 69-73.

[153] A. Kumar & H.D. Hristov, "Microwave cavity antennas", Artech House, 1989.

[154] T. Satoh, "Dielectric-loaded horn antenna", IEEE Trans. Antennas and Prop., Mar 1972, pp 199-201.

[155] S. Ohmori, S. Miura, K. Kameyama & H. Yoshimura, "An improvement in electrical characteristics of a short backfire antenna", IEEE Trans. Antennas and Prop., July 1983, pp 644-646.

[156] H. Yoshimura, "Short backfire array antenna", Japanese patent S57-020,002A, Feb 2 1982.

[157] P.S. Kooi & M.S. Leong, "Performance of a rectangular-waveguide-excited short backfire antenna employing a conical main reflector", Electronics Letters, vol. 20, no. 18, Aug 30 1984, pp 749-751.

[158] P.S. Kooi, M.S. Leong & K.N. Wong, "Radiation characteristics of q-band short backfire antenna using a conical main reflector", ISAE'85, paper 18-7, Beijing, 1985, pp 718-723.

[159] R.M. Christmann, "Multiple frequency microwave antenna", U.S. patent 4,306,235, Dec 15 1981.

[160] S.N. Sinha & R.P. Agrawal, "Reactance-controlled short-backfire array", Electronics Letters, vol. 16, no. 7, March 27 1980, pp 253-254.

[161] O.M. Woodward, "Short backfire antenna with sum and error patterns", U.S. patent 4,240,080, Dec 16 1980.

[162] G.K. Hartmann & W. Engelhart, "Dispersion measurements of one-element short backfire (SBF) antennas", IEEE Trans Antennas and Prop, Mar 1975, pp 289-293.

[163] H.W. Ehrenspeck, "A new class of medium-size high efficiency reflector antennas", IEEE Trans Antennas and Prop, March 1974, pp 329-332.

[164] L. Shafai, D.J. Roscoe & M. Barakat, "Simulation and experimental study of microstrip fed cavity antennas", ANTEM'96 proceedings, 1996, pp 549-554.

[165] H.W. Ehrenspeck & J.A. Strom, "Short-backfire antenna-a highly efficienct array element", Microwave Journal, May 1977, pp 47-49.

[166] A. Molker, "High-efficient phased array antenna for advanced multibeam, multiservice mobile communication satellite", Third Int. Conf. on Satellite Systems for Mobile Communications and Navigation, IEE, London, June 1988, pp 75-77.

[167] T. Kataki, S. Mano & T. Numazaki, "Short backfire array antenna", Japanese patent S58-134,510A, Aug 10 1983.

[168] H.T. Killackey & J.N. Martin, "Image plate/short backfire antenna", U.S. patent 4,897,664, Jan 30 1990.

[169] T. Numazaki, T. Kataki & S. Mano, "Short backfire antenna", Japanese patent S57-065,009A, Apr 20 1982.

[170] K.M. Chen, D.P. Nyquist & J.L. Lin, "Radiation fields of the short-backfire antenna", IEEE Trans Antennas and Prop, Sept 1968, pp 596-597.

[171] M.H. Hong, D.P. Nyquist & K.M. Chen, "Radiation fields of open-cavity radiators and a backfire antenna", IEEE Trans Antennas and Prop, Nov 1970, pp 813-815.

[172] C.L. Lin & X. Song, "Short backfire antenna research", IEEE Antennas and Propagation symposia, 1983, pp 138-141.

[173] M.S. Leong, P.S. Kooi, Chandra & T.S. Yeo, "Theoretical and experimental investigations of two-dimensional waveguide-excited short backfire antenna structure", IEE Proceedings Pt H, vol 136, no 3, June 1989, pp 263-268.

[174] M. Rayner, A.D. Olver & A.D. Monk, "Radiation characteristics of short backfire antennas", IEE Antennas and Propagation Conference, April 4 1995, pp 59-63.

[175] M. Rayner, A.D. Olver & A.D. Monk, "FD-TD design of short backfire antennas", IEE Proceedings Pt. H, vol. 144, no. 1, Feb 1997, pp 1-6.

[176] K. Yoshiki, Y. Fujii & S. Egashira, "A broadband planar antenna employing waveguide parallel feed circuit", IEEE Antennas and Prop. Symposium Digest, July 1994, pp 1862-1865.

[177] Y. Fujii, K. Yoshiki & T. Abiko, "Waveguide power feeding antenna", Japanese patent H05-175,725A, July 13 1993.

[178] S.V. Savov & H.D. Hristov, "Cavity-backed slot array analysis", IEE Proceedings Part H, vol 134, no 3, June 1987, pp 280-284.

[179] C.A. Balanis, "Antenna theory: analysis & design", John Wiley & Sons, Inc., 1982.

[180] E.H. Fooks & R.A. Zakarevicius, "Microwave engineering using microstrip circuits", Prentice Hall of Australia Pty Ltd, Sydney, 1990.

[181] D.P. Gray, C.B. Ravipati & L. Shafai, "Corporate fed microstrip arrays with non radiating edge fed microstrip patches", IEEE Antennas and Propagation symposia, Atlanta, June 1998, pp 1130-1133.

[182] S.R. Chebolu, K.F. Lee & R.Q. Lee, "Comparison of rectangular and triangular microstrip arrays", IEEE Antennas and Prop. Symposia, 1992, pp 163-166.

[183] D.W. Holst, "Antenna array for grating lobe and sidelobe suppression", U.S. patent 3,811,129, May 14, 1974.

[184] C.M. Hall, "Millimetre-wave microstrip antennas and hybrid types", PhD thesis, School of Electrical Engineering and Science, Royal Military College of Science, Shrivenham, U.K., Feb 1987.

[185] Y.T. Lo, D. Solomon & W.F. Richards, "Theory and experiment on microstrip antennas", IEEE Trans. Antennas and Prop., vol ap-27, no 2, March 1979, pp 137-145.

[186] K.R. Carver & J.W. Mink, "Microstrip antenna technology", IEEE Trans. Antennas and Prop., vol ap-29, no 1, Jan 1981, pp 2-24.

[187] D. Gray and L. Shafai, "Effect of 180 degree delay line in small ehf microstrip array", IEICE Spring Conference 1999, paper B-1-162, p 162.

[188] D. Gray & L. Shafai, "Effect of 180° delay line on 16 x 16 ehf microstrip array", Electronics Letters, vol. 35, no. 18, Sep 2 1999, pp 1499-1501.

[189] Gain and antenna factors for double ridged guide antenna, Model number: 3160-08, Serial number: 1087, EMC test systems, Austin, Texas, Sep 1998.

[190] S.D. Drabowitch & C. Ancona, "Antennas: Volume 2 Applications", Hemisphere Publishing Corporation, Washington, 1988.

[191] A.D. Olver, "Basic properties of antennas", Chapter 1 in *"The handbook of antenna design"*, A.W. Rudge, K. Milne, A.D. Olver & P. Knight, Peter Peregrinus Ltd., London, 1982.

[192] R.E. Collin, "Antennas and radiowave propagation", McGraw-Hill, New York, 1985.

[193] D. Gray and L. Shafai, "Two Planar Array Candidates for LMDS/LMCS Subscriber Terminal", IEEE Antennas and Propagation Symposium Digest, Orlando, July 1999, pp2728-2731.